Title
Methodology for assessing coastal change using terrestrial laser scanning

Author
Olsen, Michael J.

Publication Date
2009

Peer reviewed

UNIVERSITY OF CALIFORNIA, SAN DIEGO

Methodology for assessing coastal change using terrestrial laser scanning

A dissertation submitted in partial satisfaction of the

requirements for the degree of Doctor of Philosophy

in

Structural Engineering

by

Michael James Olsen

Committee in charge:

Professor Falko Kuester, Chair
Professor Scott Ashford
Professor Neal Driscoll
Professor Tara Hutchinson
Professor David Sandwell

2009

The Dissertation of Michael James Olsen is approved, and it is acceptable in quality and form for publication on microfilm and electronically:

Chair

University of California, San Diego

2009

TABLE OF CONTENTS

SIGNATURE PAGE iii
TABLE OF CONTENTS iv
LIST OF FIGURES viii
LIST OF TABLES xv
LIST OF SYMBOLS AND ABBREVIATIONS xvii
ACKNOWLEDGEMENTS xix
VITA xxii
ABSTRACT OF THE DISSERTATION xxiv
CHAPTER 1. INTRODUCTION 1
RESEARCH OVERVIEW 2
RESEARCH REQUIREMENTS 3
RESEARCH GOALS 3
OVERVIEW OF COASTAL MAPPING AND ANALYSIS TECHNIQUES 4
TECHNOLOGICAL BACKGROUND 6
Aerial LIDAR 6
Oblique Helicopter LIDAR 7
Terrestrial Laser Scanning (TLS) 7
Applications of TLS 11
Selection of a Laser Scanner 13
Grazing Angles 17
GPS 23
Differential GPS (DGPS) and Real time Kinematic (RTK) surveying 23
VRS network 23
Software 27
STUDY AREA AND PRIORTIZATION 27
GEOLOGY OF SAN DIEGO COUNTY 30
Coastal Environment and Erosional Processes 31
Wave Erosion 33
Subaerial processes 34
Anthropogenic contributions 36
Geologic Formations 36
The Delmar Formation 39
The Torrey Sandstone formation 41
The Lindavista Formation 43
The Bay Point Formation 43
Ardath Shale 45
DISSERTATION OUTLINE 45

CHAPTER 2. TERRESTRIAL LASER SCANNING OF EXTENDED CLIFF SECTIONS IN DYNAMIC ENVIRONMENTS: A PARAMETER ANALYSIS ... 47
OVERVIEW ... 48
INTRODUCTION ... 49
TLS background ... 52
Error sources in TLS ... 55
APPROACH: FIELD PROCEDURE FOR REGIONAL SURVEYS ... 56
Determining optimal scanning parameters from a calibration survey ... 59
Using a Virtual Reference Station ... 61
Establishing a GPS Base Station as a reference point ... 62
Occupying a fixed control monuments for calibration ... 64
TLS surveying ... 65
Multi-scan, constrained software alignment ... 66
Quality control of scan alignments ... 68
RESULTS AND DISCUSSION ... 70
Calibration study results ... 70
Results of repeat large-scale field surveys ... 77
Verification of field data ... 81
Evaluating the Efficiency of the Survey Methods ... 82
CONCLUSIONS ... 84
ACKNOWLEDGEMENTS ... 85
CHAPTER 3. AUTOMATED, CONSTRAINED POINT-CLOUD ALIGNMENT MINIMIZING WARPING EFFECTS IN MAPPING LONG CLIFF SECTIONS ... 86
OVERVIEW ... 87
INTRODUCTION ... 88
TLS background ... 91
Point Cloud Alignment Background ... 93
Warping Effects in TLS ... 97
Necessity of a New Hybrid Approach ... 103
FIELD METHOD OVERVIEW ... 104
PROCESSING METHODS ... 107
Error Metric ... 107
Workflow Overview ... 109
Initial Alignment (Steps 1-3) ... 109
Scan Editing (Step 4) ... 111
PointReg Algorithm for Point-cloud Registration (Steps 5-8) ... 111
Visual Verification (Steps 9) ... 115
RESULTS AND DISCUSSION ... 117
Software Alignment Without Constraints Using Global Optimization ... 117
Software alignment with constraints ... 122
Performance ... 125
CONCLUSIONS ... 129
ACKNOWLEDGEMENTS ... 130

CHAPTER 4. RAPID RESPONSE TO SEACLIFF EROSION IN SAN DIEGO COUNTY, CALIFORNIA, USING TERRESTRIAL LIDAR 132
OVERVIEW 133
INTRODUCTION 134
METHODS 135
RESULTS 141
Case Study: Torrey Pines Failure at Site TP1 144
CONCLUSIONS 148
ACKNOWLEDGEMENTS 149
CHAPTER 5. FATE AND TRANSPORT OF CLIFF FAILURE SEDIMENT IN THE SOUTHERN OCEANSIDE LITTORAL CELL 150
OVERVIEW 151
INTRODUCTION 152
REGIONAL SETTING 155
METHODS 158
TLS surveying 158
Calculating failure volumes 159
Modeling Beach Elevation Change 161
Modeling Environmental Conditions 163
Failure Site Classification 164
FAILURE DAMAGE POTENTIAL CLASSIFICATION 171
RESULTS 174
Type A Failure Sites 175
EN1 175
Type B Failure Sites 181
EN2 181
TP2 183
TP3 187
TP5 187
Type C Failure Sites 190
DM2 190
TP1 190
TP4 193
TP6 200
Type D Failure Sites 201
DM1 201
SIO1 201
DISCUSSION OF RESULTS 204
CONCLUSIONS 207
ACKNOWLEDGEMENTS 208

CHAPTER 6. TOPCAT: TOPOGRAPHICAL CHANGE ANALYSIS TOOLS FOR ARCGIS® 209
OVERVIEW 210
INTRODUCTION 211
BACKGROUND 212
METHODOLOGY 214
Procedure 214
Additional tools 215
Mechanics 216
Categorization Analysis 222
RESULTS 224
Case Study 1 – Dog Beach, Del Mar, CA 224
Case Study 2 – North Cape Hatteras National Seashore, North Carolina 228
Uncertainty Analysis 232
DISCUSSION 233
Case Study 1 – Dog Beach, Del Mar, CA 233
Case Study 2 – North Cape Hatteras National Seashore, North Carolina 234
CONCLUSIONS 235
ACKNOWLEDGEMENTS 236
CHAPTER 7. CONCLUSIONS AND CONTRIBUTIONS 237
OVERVIEW 238
ADDITIONAL APPLICATIONS OF TLS 241
FUTURE RESEARCH 246
APPENDIX A: Calculating RMS using the point to plane technique 249
APPENDIX B: Least squares approach to solve for the optimal α_B for a given value of α_A…… 252
REFERENCES.. 258

LIST OF FIGURES

Figure 1-1. Plot of mean sea level rise (2.1 mm/year) with the seasonal variability removed and averaged over 6 months. Data obtained from NOAA station 9410170 (NOAA, 2008b)..... 2
Figure 1-2. Spherical scan window for the Leica Scan Station 2..... 9
Figure 1-3. LIDAR data collection workflow..... 10
Figure 1-4. 3D triangulation surface model showing complex overhang features that can be modeled with TLS. (Solana Beach, March 2007)..... 12
Figure 1-5. Schematic showing calculation of incidence and grazing angles for airborne LIDAR and definitions of variables. 20
Figure 1-6. Schematic showing calculation of incidence and grazing angles for TLS 21
Figure 1-7. Grazing angles at mid-height of cliff for airborne and terrestrial LIDAR systems based on geometric configurations. 22
Figure 1-8. Grazing angles at top of cliff for airborne and terrestrial LIDAR systems based on geometric configurations. Note that the cliff top provides the worst-case grazing angles for terrestrial LIDAR and the best for airborne..... 22
Figure 1-9. Locations of base stations and coverage for the CALVRS network (from CALVRS 2008) 25
Figure 1-10. Map of study area showing section divisions. Lagoons are abbreviated on map and are as follows BL = Batiquitos Lagoon, SEL = San Elijo Lagoon, SDL = San Dieguito Lagoon, and LPL = Los Penasquitos Lagoon. 29
Figure 1-11. Schematic illustrating processes contributing to seacliff erosion..... 32
Figure 1-12. Notches in seacliffs at Fletcher's Cove, Solana Beach, CA created through wave-based erosion..... 33
Figure 1-13. Top down cliff erosion from subaerial processes of precipitation and groundwater sapping in Del Mar, CA (Close-up on right)..... 35
Figure 1-14. Biological erosion of Torrey Sandstone at Torrey Pines Reserve (Close-up on right)..... 35
Figure 1-15. (A) Drainage system in Del Mar, CA, which has led to an erosion hotspot (February 2006). (B) Same site (August 2007) after a collapse covered the catch basin..... 37
Figure 1-16. Geologic formations at Torrey Pines Reserve..... 38
Figure 1-17. Typical contact of Torrey Sandstone and Delmar formation..... 42
Figure 1-18. Layer of cobbles separating the Linda Vista formation from the Torrey Sandstone formation. 44
Figure 1-19. Contact between Torrey Sandstone formation and Bay Point formation..... 44

Figure 2-1. Map of study region showing individualized sections. Lagoons are abbreviated on map and are as follows BL = Batiquitos Lagoon, SEL = San Elijo Lagoon, SDL = San Dieguito Lagoon, and LPL = Los Penasquitos Lagoon. Triangles represent survey monuments used for calibration. 50
Figure 2-2. Georeferenced point clouds for regional mapping of Torrey Pines, CA (September 2007). Black semi-circles represent scan setup locations spaced at approximately 50 m. 53
Figure 2-3. Terrestrial laser scanner and RTK GPS field equipment..... 58
Figure 2-4. Calibration survey setup locations spaced 20 m apart at distances of 20, 40 and 50 m from the cliff consisting of the Torrey Pines and Del Mar formations. Notice the different erosion styles between the formations. The Torrey Pines formation erodes by groundwater sapping exacerbated by wind while the Del Mar formation erodes by wave undercutting. 62
Figure 2-5. Verification of Alignment comparing DGPS surveys of "fixed structures." (A) Comparison of DGPS points (green dots with labels) to a georeferenced photograph obtained during scanning, and (B) Comparison of DGPS points (green dots with labels) to the aligned and merged point clouds. 69
Figure 2-6. RMS uncertainty of adjacent scans at varying scan setup spacings for (a) full, (b) quarter, (c) ninth, and (d) sixteenth scanner sampling ratios (γ). Setup spacing pivot points (sp) indicate where closer distances from the cliff produce higher RMS uncertainty. 71
Figure 2-7. Influence of scan sampling ratio (γ) on alignment RMS uncertainty at (a) 20m, (b) 40 m, and (c) 50 m distance (d) from the target during the calibration surveys. 73
Figure 2-8. Aligned point clouds (γ=1) for scans spaced at (A) 80 m at a 20 m distance, (B) 80 m at a 40 m distance, (C) 80 m at a 40 m distance, and (D) 60 m at a 40 m distance. Note the missing cliff top and several occlusions on the cliff in (A), that points appear less bright because of decreased point density at the farther distance in (C), and the optimal coverage of the cliff in (D)..... 74
Figure 2-9. Comparison of RMS uncertainty for field surveys performed at varying distances with results of calibration surveys at 20, 40 and 50 m distances at full resolution (γ=1). Black sample points represents scans performed in the same section (Torrey Pines) as the calibration survey with best fit lines shown as dark lines. Grey sample points represent data from the entire study area, with best fit lines shown as grey dotted lines. 79
Figure 2-10. Estimated time to complete a scan with method described in chapter (solid line) and using reflective targets (dashed line) assuming a scan rate of 4400 points per second..... 83
Figure 2-11. Estimated rate of terrain coverage using the survey method described in this chapter (solid line) and using a target registration

method assuming a scan spacing of 50 m and the scan rate of 4400 points per second..... 83
Figure 3-1. Aligned and merged point cloud dataset. Note the figure is split into (A) North Section and (B) South Section with match line X-X' (Solana Beach, CA, February 2008)..... 89
Figure 3-2. Occlusions requiring multiple setups (A) left scan, (B) center scan, (C) right scan, and (D) combined to minimize occlusions..... 90
Figure 3-3. Example of a failure volumetric and surface change analysis using TLS data aligned using PointReg. Failure site at Torrey Pines State Reserve, CA (a) before failure October 14, 2007, (b) after failure October 29, 2007, with (c) failure analysis highlighting area of failure..... 92
Figure 3-4. Misalignments from erroneous rotations about X or Y axis 98
Figure 3-5. Definitions of variables used to determine warping effects that occur from scanning at oblique angles shown by repeat scans..... 100
Figure 3-6. Error comparisons between repeat scans showing (A) total error, (B) error in Y direction, (C) error in X direction, (D) error in Z direction compared with horizontal angle to surface, ψ, and a comparison of error with (E) range and (F) vertical angle, ϕ. Note that at oblique angles, Δy dominates, whereas at orthogonal angles Δx dominates. Error bars represent the standard deviation of differences between scans in each bin. 102
Figure 3-7. Three scans aligned using backsight registration only, obtained directly in the field. Note the apparent blurriness from the misalignment..... 106
Figure 3-8. Three scans aligned using PointReg to reduce alignment errors. Note the increased clarity as a result of the alignment. 106
Figure 3-9. Schematic illustrating the calculation of the RMS of error between two scans 108
Figure 3-10. Workflow diagram and pseudocode for PointReg scan alignment. Manual processes are illustrated by ellipses while boxes represent automated processes. 110
Figure 3-11. Verification of alignment through 2D cross – section profiles of (a) three unaligned scans (b) three aligned scans. See Figure 2-2 for description of occlusions..... 116
Figure 3-12. Comparison of origin displacement error with distance from fixed center scan for scans collected in a North-South sweep and aligned from the center using unconstrained alignment techniques. Note that the majority of the displacement error is a result displacement in the Easting (X) direction, caused by the propagation of rotational errors about the Z-axis, created by warping biases in each scan. In contrast, because PointReg constrains scans origins, it produces none of these detrimental origin displacement errors..... 119

Figure 3-13. Setup for survey used to analyze the effectiveness and necessary steps for the algorithm. The cliff shown is a texture-mapped, surfaced model using data from the Torrey Pines survey (September 10-11, 2007) aligned with PointReg. 120
Figure 4-1. LIDAR data point cloud baseline of Encinitas, California (December, 2006) 134
Figure 4-2. Field survey equipment and setup 136
Figure 4-3. Data collection and analysis workflow 136
Figure 4-4. Study area location, priority zone mapping, failure locations and coastal accessibility data 138
Figure 4-5. Interaction with data in a virtual environment 140
Figure 4-6. Site TP1 (A) before failure (4/10/2007), (B) during failure (August 4, 2007, photo courtesy of Herb Knufken) (C) two days after failure (August 6, 2007), and (D) after human interference, ~2 months after failure (September 29, 2007) 145
Figure 4-7. Point cloud obtained by LIDAR scans at site TP1 (A) most recent baseline survey (4/11/2007) and (B) two days after failure (8/6/2007) 146
Figure 4-8. Surface change model between rapid response survey on August 23, 2007 and baseline from April 11, 2007 148
Figure 5-1. Schematic illustrating varying mechanisms contributing to seacliff erosion 153
Figure 5-2. Study area map showing locations of failure sites. Note the demarcation line between cliffs with and without talus deposits. Type C failures occurred from subaerial erosion in areas with talus deposits on the North and Type B failures occurred to the South from wave undercutting because of no protective talus deposits. 156
Figure 5-3. Plot of mean sea level with the seasonal variability removed and averaged over 6 months. Plot shows a trend of sea level rise of 2.1 mm/year. Tidal data obtained from NOAA station 9410170 (NOAA 2008b) and are referenced to the NAVD88 datum. Topex/Poseidon data obtained from http://sealevel.colorado.edu and was calibrated by Leuliette et al. (2004) 157
Figure 5-4. Schematic showing elevation measurement locations for beach elevation and maximum failure elevation. Note that the measurement locations for beach elevation are measured relative to the edge of the initial failure mass and are held constant as the failure mass erodes 162
Figure 5-5. Calculation of Total Water Level (NAVD88) using method described in Ruggiero et al. (2008) from (a) Tidal measurements (NOAA Station 9410170) (b) Significant Wave Height (CDIP buoy 100), (c) Wave Runup with 2% proabability of exceedance (calculated using Stockdon, 2006) producing (d) a total water level estimate. 165

Figure 5-6. Comparison of wave data and averaging for missing data at CDIP buoy #100 (CDIP, 2008)..... 166
Figure 5-7. Photographs of failure sites (A) DM1 8/24/2008 (B) DM2 8/24/2008 (C) EN1 a 6/7/2007 (D) EN1b after second failure 9/10/2007 (E) EN2 3/7/2008 (F) SIO1 9/25/2007 (G) TP1a 8/6/2007 (H) TP1b after second failure 7/8/2008 (I) TP2a 9/10/2007 (J) TP2b after second failure 3/4/2008 (K) TP2c after third failure 10/2/2008 (L) TP3 10/14/2007 (M) TP4 10/29/2007 (N) TP5 1/31/2008, and (O) TP6 6/18/2008 167
Figure 5-8. Comparison of failure occurrences with (a) precipitation (NOAA, Station 23188), (b) significant wave height, (c) peak wave period, (d) average wave period, and (e) wave direction from CDIP buoy 100. Red lines denote wave based failures and green lines denote subaerial dominated failures. Dashed lines represent precipitation based failures and dotted lines indicated the presence of groundwater. Dates and times are Coordinated Universal Time (UTC). 169
Figure 5-9. Comparison of typical site profiles at time of failure and varying wave conditions experienced at the site. 170
Figure 5-10. Exceedance probabilities as a function of failure volume, showing classification demarcations. 173
Figure 5-11. Surface comparison of a cliff failure in Encinitas (a) June 07, 2007 (1 day after) and (b) June 22, 2007 (2 weeks after) where blue represents accretion and orange represents erosion compared to scans from April 2005. Continual Monitoring of the failure (c) from a site visit 7/28/2007 showing the failure mass inundated from the waves, and (d) after collapse of vegetation above (9/10/2007)..... 177
Figure 5-12. Cross section of failure site EN1 from an April 2005 LIDAR survey before the failure and a June 7, 2007 LIDAR survey after. The upper portion of the cliff was removed because LIDAR does not penetrate heavy vegetation. 178
Figure 5-13. (A) Failure mass volume of site EN1 with time and (B) comparison of total water level and beach elevation immediately west of failure mass 179
Figure 5-14. Failure mass profiles at site EN1 (A) before first failure and (B) after second failure. Black line representing scans performed on 7/12/2007 are shown in both (A) and (B) for reference. For clarity purposes, scans performed on 9/25/2007, 10/7/2008, and 3/23/2008 were omitted. Note that vegetation was not removed for cross-sections of scans performed between 9/10/2007 through 5/12/2008 but was removed for sediment volume calculations. 180
Figure 5-15. Cross-section analysis for site EN2 before (Oct 10, 2007) and after failure (March 7, 2008). 182
Figure 5-16. Comparison of Site TP2 (a) before failure (6/30/2006) and after significant failures (b) 8/23/2007 (c) 2/17/2008, and (d)

9/23/2008. All surface comparisons are relative to a survey completed on 11/3/2006. 184
Figure 5-17. Plan view schematic showing cliff and platform geometry for Flat Rock, Torrey Pines Reserve. Note that an incoming peak wave direction of 245^{o} to 280^{o} measured clockwise from True North maximizes energy transfer to cliff at failure zone. 185
Figure 5-18. Environmental conditions at time of third failure of site TP2. Time is local San Diego time, divided in 2 hour increments. 186
Figure 5-19. Cross section of failure at site TP5 188
Figure 5-20. Analysis of failure site TP5 showing (A) failure volume, (B) a comparison of beach height immediately west of failure with the total water level, and (C) precipitation levels 189
Figure 5-21. Beach profiles at Site TP1 from TLS data. Note rapid erosion of beach berm between 11/10/2007 and 12/20/2007 with initial winter storms 191
Figure 5-22. (a) Failure mass volumetric change analysis and (b) comparison of beach sand levels to TWL for site TP1. Red diamonds represent TLS surveys and yellow triangles represent field visits. 192
Figure 5-23. Failure site TP4 (a) before failure October 14, 2007, (b) after failure October 29, 2007, with (c) failure analysis highlighting area of failure 194
Figure 5-24. Cross section analysis of failure at site TP4 195
Figure 5-25. Comparison of (a) Failure volume determined from TLS (b) beach elevation and total water level, and (c) precipitation for site TP4. Red diamonds represent TLS surveys and yellow triangles represent field visits. 196
Figure 5-26. Comparison of beach and talus deposit profiles for site TP4 showing increased erosion of talus deposits 25 m to the north and south of failure site and protection of talus deposits at failure site. 197
Figure 5-27. Failure Site TP4 (A) before (Nov 11, 2007) and (B) after (Jan 9, 2008) winter storms showing failure stabilizing talus deposits with erosion of talus deposits away from failure 199
Figure 5-28. Surface change analysis for site TP6 comparing the post failure, June 18, 2008 survey to the pre-failure, April 28, 2008 survey 200
Figure 5-29. Cross section analysis for site SIO1 showing failure mass atop rock platform 202
Figure 5-30. (A) Failure volume change at site SIO1, and (B) comparison of Platform elevation with Total water level. Note that Total water level is for reference only because the waves would dissipate differently upon impact with the platform compared to runup on a beach. 203
Figure 6-1. TopCAT toolbar and user interface run through ESRI's ArcGIS® 215

Figure 6-2. Schematic for compartment creation 218
Figure 6-3. Geometric relationship between average seacliff face retreat and the eroded compartment seacliff volume (figure modified from Young and Ashford, 2006c) 221
Figure 6-4. Location map for case study #1: Dog Beach, Del Mar, California (Elevation basemap from ESRI®) 225
Figure 6-5. Elevation change grid and compartment analysis for Dog Beach, Del Mar, CA (October 2005 – March 2007) 227
Figure 6-6. Location Map for Case Study #2 at Cape Hatteras National Seashore, North Carolina (Elevation basemap from ESRI®) 229
Figure 6-7. Analysis boundaries of DEM for Cape Hatteras National Seashore, North Carolina 229
Figure 6-8. A) A portion of the elevation change grid for North Cape Hatteras National Seashore, North Carolina (Fall 1997 to Fall 1999) and alongshore B) dune and C) Beach volumetric changes induced by Hurricanes Dennis and Bonnie. 230
Figure 7-1. Structural specimen point cloud after failure 242
Figure 7-2. Close-up of surface mesh of failed structural specimen with overlaid texture map. 242
Figure 7-3. (A) LIDAR point clouds of structural specimens on the UCSD Outdoor Shake Table (B) with photodraped surface mesh 243
Figure 7-4. Point cloud dataset for the Hall of the 500 in the Palazzo Vecchio in Florence Italy 244
Figure 7-5. Garden Courtyard of the Palazzo Medici in Florence Italy. 244
Figure 7-6. Display of coastal dataset on Hiperspace tile display wall, a 286 Million Pixel Display 245
Figure 7-7. Display of coastal dataset in a CAVE Virtual Reality Environment (from Hsieh et al. 2007) 245
Figure 7-8. Comparison of (A) Aerial LIDAR dataset (NOAA - LDART 2007 with photographic coloring from photographs from USGS 2008). (B) Terrestrial LIDAR dataset (Feb 2008), and (C) combined for Torrey Pines State Reserve. Note the poor coverage of the airborne LIDAR data on the cliff face and the lack of coverage of the terrestrial LIDAR on the cliff top. 248

LIST OF TABLES

Table 1-1. Advantages and disadvantages of measurement techniques for seacliff erosion studies (modified from Hapke, 2004) 5
Table 1-2. Detailed specification comparison of the I-Site 4400 and Leica ScanStation 2 laser scanners 14
Table 1-3. Comparison of 3D Terrestrial Laser Scanners available in 2006..... 16
Table 1-4. Geologic formations found in study area 38
Table 1-5. Mineralogy of Delmar Formation (Kennedy, 1973) 40
Table 1-6. Mineralogy of Torrey Sandstone Formation (Kennedy, 1973) 42
Table 1-7. Mineralogy of Ardath Shale (Kennedy, 1973) 45
Table 2-1. Resolution settings and corresponding point densities available for the I-Site 4400 scanner..... 60
Table 2-2. Control points used in the calibration of the Scripps Pier monument (UTM NAD 83 Z11N coordinates) 63
Table 2-3. Calibration control monuments for DGPS surveys (UTM NAD 83 Z11N coordinates) 64
Table 2-4. Survey dataset properties and RMS uncertainty between adjacent scans (March 2007- May 2008)..... 78
Table 2-5. Comparison of RMS (cm) of static (fixed) structures in Del Mar between four different surveys to show the repeatability of the survey method. Note that the Aug-07 survey appears to have a ~1.5 cm bias when compared to other scans. 82
Table 3-1. Percentages of point comparisons within tolerances for repeat scans 100
Table 3-2. RMS comparisons for different registration techniques 123
Table 3-3. Time performance comparison (minutes) for scan co-registration using an Intel Core2 Duo 6700@2.66 GHz with 4GB RAM. Lower bounds were estimated based on times for an expert TLS data user to complete the task and upper bounds were estimated based on a novice TLS data user. The ICP and surface alignments were done using I-Site software (I-Site 2008). Each dataset contains approximately 320,000 points. Note that surfacing times are based off of organized point cloud data. Unorganized point cloud data would require substantially more time to create a surface. 127
Table 4-1. Summary of Current (December 21, 2007) Failure Locations (S=Summer and W = Winter)..... 142
Table 5-1. Summary of failure sites and enivornmental conditions at failure (Geologic Units: DM = Delmar formation, TS = Torrey Sandstone formation)..... 168
Table 5-2. Failure Classifications based off exceedance probabilities..... 173
Table 6-1. Comparisons of erosional volumes using 3D volumetric analysis and TopCAT compartmental analysis 226

Table 6-2. Compartmental Analysis from TopCAT for Dog Beach, Del Mar CA (Oct 2005- March 2007)..... 226
Table 6-3. Total volume change analysis from TopCAT for 3.8 km of Cape Hatteras National Seashore, North Carolina (1997-1999)..... 231
Table 6-4. Compartmental Analysis from TopCAT for volumetric alongshore erosion rates for 3.8 km of Cape Hatteras National Seashore, North Carolina (1997-1999)..... 231
Table 6-5. Uncertainty Analysis of total volume from TopCAT for Oregon Inlet, North Carolina (1997 to 1999)..... 233

LIST OF SYMBOLS AND ABBREVIATIONS

Symbol/Abbreviation	*Definition*
%coarse	*% coarse sediment above LCD*
$\vec{n}$	*Normal vector with components a,b,c*
$\vec{v}$	*Vector*
A,B,C,D	*Designators of wave contact at failure site*
A_{cell}	*Area of a cell in a grid*
CDIP	*Coastal Data Information Program*
d	*Distance from cliff, m*
DEM	*Digital Elevation Model*
DGPS	*Differential Global Positioning Systems*
D_i	*Minimum distance from the i^{th} point to the plane*
DM	*Del Mar*
DOF	*Degree of Freedom*
DSAS	*Digital Shoreline Analysis System*
Δ_{zi}	*Difference in elevation for a grid cell*
E	*Eroded Volume*
EN	*Encinitas*
ESRI	*Environmental Systems Research Institute*
g	*Acceleration of gravity, 9.807 m/s^2*
GIS	*Geographic Information Systems*
GPS	*Global Positioning Systems*
h	*Cliff height, m*
H_o	*Significant wave height*
i	*Denotes the index of a variable*
L	*Large boulders (> 0.3 m)*
t	*Time*
LCD	*Littoral Cutoff Diameter*
LIDAR	*LIght Detection and Ranging*
L_o	*Offshore wave length*
M	*Medium sized rocks (0.1 to 0.3m)*
n	*Total number of objects*
NAD83	*North American Datum, 1983*
ncell	*Number of cells*
p	*Point*
NOAA	*National Oceanic and Atmospheric Administration*
OpenGL	*Open Graphics Library*
PE	*Percent Effectiveness*
Qs	*Rate of seacliff coarse sediment yield, m^3/year*
r	*Scan range, m*
R	*Retreat rate, and rotation matrix*
R2%	*Wave runup with 2% probability of exceedance*
RGB	*Red, Green, and Blue Color values*

r_{max}	*Maximum scan range*
r_{min}	Minimum range scans should be filtered
RMS	*Root mean square*
RTK	*Real time Kinematic*
Ru	*Rate of retreat in unprotected regions*
Rv	*Rate of retreat in cells with variable, v*
s	*Scan setup spacing, m*
S	*Small, fine grained sediment (<0.1m)*
SB	*Solana Beach*
SIO	*Scripps Institution of Oceanography*
s_{max}	*Maximum setup spacing, m*
s_p	*Scan spacing producing pivot, m*
T	*Peak wave period*
t	*Time*
TLS	*Terrestrial Laser Scanning/Scanner*
TopCAT	*Topographical Compartment Analysis Tools custom VBA routines in GIS software*
TP	*Torrey Pines*
TWL	*Total Water Level*
UTM	*Universal Transverse Mercator coordinate system*
V	*Error Vector*
VBA	*Visual Basic for Applications*
VRS	*Virtual Reference Station*
w	*Compartment Width*
x,y,z	*Position in 3D space*
ΔR_x	*Erroneous rotation about the X-axis*
ΔZ	*Error in Z direction*
α_i	*Rotation angle for scan i*
β	*Maximum search angle, degrees, and Nearshore beach slope*
ϕ	*Horizontal angle*
γ	*Scanner sampling ratio*
θ	*Angular separation, degrees*
ψ	*Vertical angle*
ρ	*Scan point separation*

ACKNOWLEDGEMENTS

This dissertation required the assistance of several people. First and foremost, I would like to thank my wife Kristen for her support, patience, and encouragement during my work on this research. I also thank my family for their support and teaching me the value of education at an early age.

The field data collection and analysis would not have been possible without the unwavering dedication of Liz Johnstone to this project. I thank Adam Young for his help in introducing me to the project and comments on parts of this dissertation.

Falko Kuester provided substantial guidance and assistance during the completion of this dissertation as my advisor. His visualization and programming advice was invaluable to advance the project. I thank Scott Ashford for making it possible for me to study at UCSD and for his advising during my first two years of study. Neal Driscoll helped immensely in teaching an engineer about geologic processes and in his assistance with project funding and implementation. David Sandwell and Tara Hutchinson served on the dissertation committee for this work and provided insightful comments and ideas, which helped enhance the dissertation. I also thank Steven Bartlett of the University of Utah for his insights and guidance in my educational career.

I also thank Irwin and Joan Jacobs for their generous support of my education through the Jacob's Fellowship. Much of this research was funded via grants from California Seagrant (Project #R/OE-39), the Coastal Environmental Quality Initiative (CEQI) under award #04-T-CEQI-06-0046, and the University of

California, San Diego Chancellor's Interdisciplinary Collaboratories Fund. This material is also based upon work supported by the National Science Foundation under Grant No. 0403433. I would also like to thank Paul and Stacy Jacobs and Friends of CISA3 for their support for point-based modeling research. I am immensely grateful for this financial assistance that made this work possible.

Many people offered immense technical assistance. Scott Schiele and John Dolan of I-Site offered technical support with both the scanner and the software. Travis Thompson established and maintained the CALVRS network, saving us a substantial amount of field setup time. Daryl Rysdyk and Scott Calman assisted in the purchasing of equipment and computer maintenance.

Many others assisted in the rigorous field survey work needed for this project. These include Jessica Raymond, Pat Rentz, John Sorenson, Jillian Maloney, Justin McCullough, Danny Brothers, Jeffery Dingler, David Olson, and Rebecca Samad. Gary Samad provided substantial assistance notifying us of recent seacliff failures and relaying observations from his frequent walks along the beaches. Tung Ju Hseih provided assistance by setting up the virtual reality system to work with LIDAR data. The UCSD Visualization group, GRAVITY, also provided encouragement and assistance to help me complete this dissertation.

PUBLICATIONS OF THE DISSERTATION

Chapter 2, in part, is a reprint of the material as it will appear in the Journal of Surveying Engineering. Olsen, M.J., Johnstone, E., Driscoll, N., Ashford, S.A., and Kuester, F. The dissertation author was the primary investigator and author of this paper.

Chapter 3, in part, is a reprint of the material as it may appear in the Journal of Photogrammetry and Remote Sensing. Olsen, M.J., Johnstone, E., Kuester, F., Ashford, S.A., and Driscoll, N. The dissertation author was the primary investigator and author of this paper.

Chapter 4, in full, is a reprint of the material as it appears in the Proceedings of Solutions to Coastal Disasters, 2008. Olsen, M.J., Johnstone, E., Ashford, S.A., Driscoll, N., Young, A.P., Hsieh, T.J., and Kuester, F., ASCE Solutions to Coastal Disasters, 2008. The dissertation author was the primary investigator and author of this paper.

Chapter 5, in part, is being prepared for submission for publication of the material. Olsen, M.J., Johnstone, E., Driscoll, N., Kuester F., and Ashford, S.A. The dissertation author was the primary investigator and author of this paper.

Chapter 6, in part, is being prepared for submission for publication of the material. Olsen, M.J., Young, A.P., and Ashford, S.A. The dissertation author was the primary investigator and author of this paper.

VITA

2003-2004	Engineer in Training, West Valley City, Utah
2004	Bachelor of Science, University of Utah
2004-2005	Research Assistant, University of Utah
2005	Masters of Science, University of Utah
2005-2009	Research Assistant, University of California, San Diego
2007	Teaching Assistant, Department of Structural Engineering, University of California, San Diego
2009	Doctor of Philosophy, University of California, San Diego

PUBLICATIONS

Olsen, M. J., Bartlett, S. F. and Solomon, B. J., 2007, “Lateral Spread Hazard Mapping of the Northern Salt Lake Valley, Utah, for M7.0 Scenario Earthquake,” Earthquake Spectra, 23(1), pp. 95-113.

Hsieh, T., Olsen, M. J., Johnstone, E., Young, A. P., Driscoll, N., Ashford, S. A., and Kuester, F. (2007). VR-based visual analytics of LIDAR data for cliff erosion assessment. Proc. of the 2007 ACM Symposium on Virtual Reality Software and Technology (Newport Beach, California, November 05 - 07, 2007), S. N. Spencer, Ed., VRST '07, ACM, New York, NY, 249-250.

Olsen, M.J., Johnstone, E., Ashford, S.A., Driscoll, N., Young, A.P., Hsieh, T.J., and Kuester, F. (2008). Rapid Response to Seacliff Erosion in San Diego County, California using Terrestrial LIDAR. Proc. of Solutions to Coastal Disasters, ASCE, Oahu, Hawaii, 573-583.

Olsen, M. J., Johnstone, E., Ashford, S.A., Driscoll, N., and Kuester, F. (2009, In Press). Analysis of parameters for terrestrial laser scanning of long cliff sections in dynamic environments, ASCE Journal of Surveying.

Olsen, M.J., Kuester, F., Chang, B., and Hutchinson, T. (2009, In Press). Terrestrial laser scanning based structural damage assessment, ASCE Journal of Computing in Civil Engineering.

Erickson, G., Olsen, M.J., Bartlett, S. F., Solomon, B. J., and Anderson, L., (accepted with revisions, revising). Probabilistic Liquefaction Potential Mapping of the Salt Lake Valley, Utah. EERI Earthquake Spectra.

Young, A.P., Olsen, M.J., Driscoll, N., Gutierrez, R., Guza, R.T., Flick, R.E., Johnstone, E., and Kuester, F., (Accepted pending revisions). Mapping Seacliff Erosion with Terrestrial and Airborne LIDAR, submitted to the Journal of Photogrammetric Engineering and Remote Sensing

Olsen, M.J., Johnstone, E., Kuester, F., Ashford, S.A., and Driscoll, N. (Under Review). Automated, constrained point-cloud alignment minimizing warping effects in mapping long coastal sections, submitted to the ISPRS Journal of Photogrammetry and Remote Sensing.

Olsen, M.J., Johnstone E., Driscoll, N., Kuester F., and Ashford, S.A. (In Preparation). Fate and Transport of cliff failure sediment in the southern Oceanside littoral cell, to be submitted to Marine Geology.

Olsen, M.J., Young, A.P, Ashford, S.A., and Kuester, F. (In Preparation). *TopCAT – Topographical Compartment Analysis tools for ArcGIS*®, to be submitted to the ASPRS Journal of Photogrammetry and Remote Sensing.

Olsen, M.J., Ponto, K., Kimball, J., and Kuester, F. (In Preparation). Editing 3D laser scans in 2D environments.

FIELDS OF STUDY

Geomatics Engineering
Geotechnical Engineering
Terrestrial Laser Scanning Surveying
Geographical Information Systems
Geologic Hazard Analysis
Earthquake Engineering
3D Scientific Visualization
Coastal Geology

ABSTRACT OF THE DISSERTATION

Methodology for assessing coastal change using terrestrial laser scanning

by

Michael James Olsen

Doctor of Philosophy in Structural Engineering

University of California, San Diego, 2009

Professor Falko Kuester, Chair

Seacliff erosion dramatically alters the coastline of San Diego County through both marine and subaerial mechanisms, threatening development and public safety in the economically important coastal regions. Quantitative analysis of the seacliffs' stability assists public policy makers to determine safe and effective coastline utilization. This dissertation develops concepts, techniques,

and tools drawing from multiple disciplines to provide this essential information of both seasonal and rapid-event erosion.

Terrestrial Laser Scanning (TLS) produces high resolution data to accurately quantify erosion and map hazard areas. Previous work applying TLS to seacliff erosion required additional, time-consuming surveying to georeference TLS surveys, limiting their application to only localized sites. This dissertation presents new methods to georeference TLS data for efficient, quantitative regional mapping and to quantitatively understand sources of uncertainty. The determination of optimal scanning parameters of spacing, distance, and sampling ratio ensures adequate data collection to capture the complex seacliff morphology. A new, automated algorithm for alignment shows how to constrain errors to avoid detrimental misalignment propagation, advancing TLS surveying for application to map long coastal sections. These techniques provide substantial time savings over previous methods, ensure consistent results between repeat surveys, and allow simultaneous study of both small and large scale geologic processes.

The creation of a rapid-response program to observe sites immediately and continually after failure shows the insights TLS can provide in conjunction with wave, tidal, and climate data in understanding geologic processes governing seacliff erosion. The TLS data also showed that minimal wave energy is required to rework failure sediment and suggests that some failure masses can act as a stabilizing force for the cliffs by securing protective talus deposits against the cliff.

The development of automated GIS routines to perform statistical change analysis is also presented. These routines were applied to both cliff and beach studies to show the importance of studying both small and large scale changes to understand geologic processes.

These innovative methods provide a framework for future scientists and engineers to utilize TLS in understanding complex problems by ensuring sufficient data collection, establishing accurate, georeferenced baselines, and providing tools to perform meaningful change analysis.

CHAPTER 1. INTRODUCTION

RESEARCH OVERVIEW

The coast provides a high-energy, dynamic environment vital to the economy of Southern California (Griggs et al., 1985; 2005). Coastal erosion occurs from various geologic processes (Sunamara, 1992) and poses a safety hazard to public infrastructure, tourism, and private land owners who have purchased real estate near the edge of seacliffs. In addition, observed sea level rise (Figure 1-1, NOAA 2008a, Colorado Center for Astrodynamics Research, 2008) will expose seacliffs to higher water levels, exacerbating erosion.

Policy makers have limited data and tools to use to understand and make important decisions regarding these complex processes. Thus, it is requisite for scientists and engineers to produce and analyze the necessary data to understand the geologic processes and effects of control methods so that they can properly disseminate these discoveries.

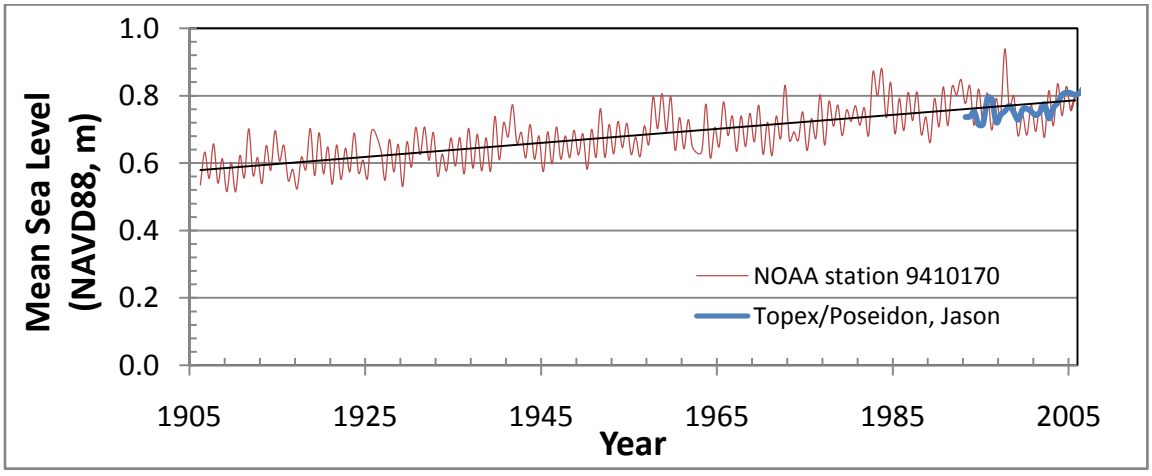

Figure 1-1. Plot of mean sea level rise (2.1 mm/year) with the seasonal variability removed and averaged over 6 months. Data obtained from NOAA station 9410170 (NOAA, 2008b)

RESEARCH REQUIREMENTS

To adequately understand the geologic processes governing seacliff erosion, these processes need to be modeled at the spatial and temporal scales at which they occur. Recent advances in geomatics have now made this endeavor possible by providing new tools to rapidly map features at centimeter-level resolution and accuracy. This progress will make it possible for geologic products to be linked with the processes that create them and revolutionize our understanding of the coastline. By having adequate temporal resolution, the internal mechanisms governing these processes can be discovered and reveal interesting insights to understand better the long term retreat patterns of the coastline. Thus, it is requisite that this data be collected on an unprecedented scale to produce datasets of adequate resolution. This dissertation presents the concepts, techniques, and tools needed for such an undertaking.

RESEARCH GOALS

This dissertation principally aims to develop and unify techniques from multiple disciplines including geomatics, geotechnical engineering, geology, and computer science to understand the complex mechanisms driving coastal erosion. Building upon methods established for site analysis of seacliff erosion, this work seeks to efficiently expand the analysis to a larger scale and on a more frequent basis. Specific research objectives were to:

- Develop efficient and effective survey and software alignment techniques for large-scale Terrestrial Laser Scanning (TLS) mapping

- Produce an accurate georeferenced baseline map for the study region
- Detect temporal change through multiple seasonal surveys
- Evaluate the uncertainty and repeatability of datasets collected (very important for short term studies)
- Develop automated workflows for rapid processing
- Enhance data analysis in Geographic Information Systems (GIS)
- Capture short and long term effects of seacliff failures via rapid response to accurately quantify volumes and understand site characteristics
- Understand failure mechanisms and contribution of environmental factors to these failures
- Quantify speed of reworking processes and feedback mechanisms of recent seacliff failure sediment to coastal change
- Disseminate these results, observations and tools to the public

OVERVIEW OF COASTAL MAPPING AND ANALYSIS TECHNIQUES

Because of importance of California's beaches, the shoreline location and erosion rates have been of much interest to researchers. Hapke (2004) discusses several methods used to perform coastal cliff and bluff retreat measurements, which are summarized in Table 1-1. Crowell, Honeycutt and Hatheway, 1999 discuss similar methods used in shoreline erosion mapping. LIDAR (specifically terrestrial) was chosen for this study because of the ability to capture higher resolution and accuracy data for short-term studies.

Table 1-1. Advantages and disadvantages of measurement techniques for seacliff erosion studies (modified from Hapke, 2004)

Technique	Advantages	Disadvantages
1. Traditional ground surveys	• Very accurate • Easily repeatable	• Poor temporal and spatial coverage • Time consuming/expensive
2. Historical maps	• Inexpensive • Widely available • Very long temporal coverage (1850's – 1979's) • Good spatial coverage	• Low accuracy • Ambiguous cliff/bluff edge position
3. Aerial photographs		
a. Unrectified	• Inexpensive • Widely available • Good temporal coverage (1920's – present) • Good spatial coverage	• Low accuracy • Ambiguous cliff/bluff position in 2D
b. Partially rectified	• Widely available • Good temporal coverage (1920's – present) • Good spatial coverage • Improved accuracy over 3a	• Ambiguous cliff/bluff position in 2D • Hardware/software for processing may be expensive
c. Fully Rectified	• Widely available • Good temporal coverage (1920's – present) • Good spatial coverage • High accuracy • Cliff/bluff edge digitized in 3D	• Time consuming processing • Required software expensive
4. LIDAR		
a. Aerial LIDAR	• Good spatial coverage • Higher resolution and accuracy than aerial photographs • Rapid Acquisition	• Very expensive • Typically no datasets prior to 1990's • Poor coverage of cliff face
b. Oblique Helicopter LIDAR	• Higher resolution and accuracy than aerial photographs • Captures overhangs • Rapid Acquisition	• Very expensive • Typically no datasets prior to the year 2000
c. Terrestrial Laser Scanning	• Very high accuracy • Very high resolution • Captures overhangs and caves • Less expensive than 4a&b	• Difficult spatial coverage • Typically no datasets prior to the year 2000 • Time consuming/expensive
d. Combined LIDAR techniques	• Complete 3D model of seacliffs • Substantial amount of data	• Expensive • Poor temporal coverage • Surveys must be completed nearly simultaneously

TECHNOLOGICAL BACKGROUND

This study utilized the latest in survey technology with a terrestrial laser scanner (TLS) using LIght Detection and Ranging (LIDAR) to capture 3D models. LIDAR is a line of sight remote sensing technique which rapidly sends out laser pulses that reflect off objects back to the scanner. LIDAR technology has been implemented via satellite, airplane, helicopter, and ground based for topographical studies, although satellite LIDAR has not been implemented for seacliff erosion studies. The data were georeferenced by using Real Time Kinematic (RTK) Global Positioning Systems (GPS) using a Virtual Reference System (VRS) to provide differential corrections in real time. Processing of the data were implemented in I-Site Studio 3.0 software, ESRI ArcGIS® software, and through multiple custom algorithms developed in using OpenGL in C++ and Visual Basic for Applications (VBA). This section will provide background information on these technologies and their usefulness in seacliff erosion.

Aerial LIDAR

Aerial LIDAR has been successfully implemented to perform large scale seacliff erosion studies (Young and Ashford, 2006a) and beach erosion studies (Sallenger et al., 2003). Aerial LIDAR is typically performed from a laser scanner mounted on a low flying airplane with a near vertical look angle. It is advantageous because data are rapidly acquired as one continuous dataset. A limitation of aerial LIDAR is that vertical cliffs or complex features such as sea caves are not well resolved as a result of the low data density and/or the poor

incidence angle; in contrast, terrestrial LIDAR can capture data from a more orthogonal angle and improve the resolution of imaging of seacliff erosion. Aerial LIDAR systems are very expensive and require a substantial amount of post-processing for georeferencing involving calibration with control points. Some of these costs can be divided when multiple agencies are interested in the data.

Oblique Helicopter LIDAR

Use of LIDAR mounted on a helicopter allows for an improvement over aerial LIDAR for seacliff erosion analysis because it is performed more orthogonal to the cliff. It is currently being investigated by Rosser et al. (2008) for application to seacliff erosion studies. Complex topography and sea caves still cannot be efficiently captured through this method because the helicopter must be flown above ground away from the cliff. Logistics and costs create substantial difficulty for a typical organization to implement oblique helicopter LIDAR for frequent site and regional surveys.

Terrestrial Laser Scanning (TLS)

TLS performed from the ground produces a near orthogonal view of the cliffs. High speed, phase based scanners compare phase shifts between a modulated laser beam to determine distance to a target at close ranges (<80 m). Time of flight based scanners measure the laser pulse travel time and the angle of return to determine the coordinates of the reflective objects relative to the scanner origin and are more suitable for larger ranges than the phase based

scanners. Scanners operate on a spherical envelope (Figure 1-2). Various laser scanners are currently available with varying speeds (typically 2,000 to 120,000 points per second), maximum scanning resolutions (typically 1 to 100 mm at 50 m), and point measurement accuracies (typically 3 to 50 mm at 100 m). Most scanners concurrently photograph the scene to provide photorealistic RGB values to each scan point. Also, an intensity value is returned, which is the strength of the signal degradation and provides information about the type of material the laser pulse was reflected from. Because LIDAR is a line of sight technology, multiple scans must be merged together to form a complete model. Systems are being developed for stop and go scanning and continuous scanning (Barber 2008) to efficiently cover large areas.

A typical LIDAR data acquisition workflow is shown in (Figure 1-3). In addition, Bernardini and Rushmeier (2002) discuss a typical processing pipeline from acquiring the data to post processing for computer visualization and graphic purposes. Scans need to be collected from several locations, and the alignment of these scans is achieved through by direct georeferencing or software methods (Alba and Scaioni, 2007). Direct georeferencing (Scaioni, 2005) methods use reflective targets that have known coordinates to align the scans together or survey the control points where the scanner is set up. These coordinates can be obtained through GPS, Total Station, or other survey devices. Indirect alignment through software registration determines the optimal alignment of a scan based on similar features in neighboring scans to merge the scans together.

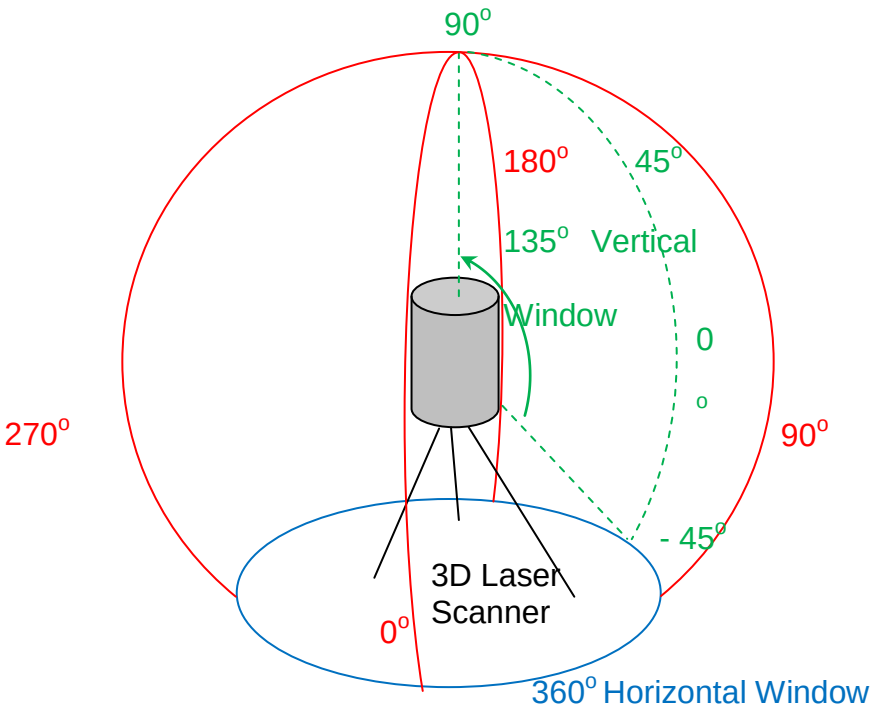

Figure 1-2. Spherical scan window for the Leica Scan Station 2

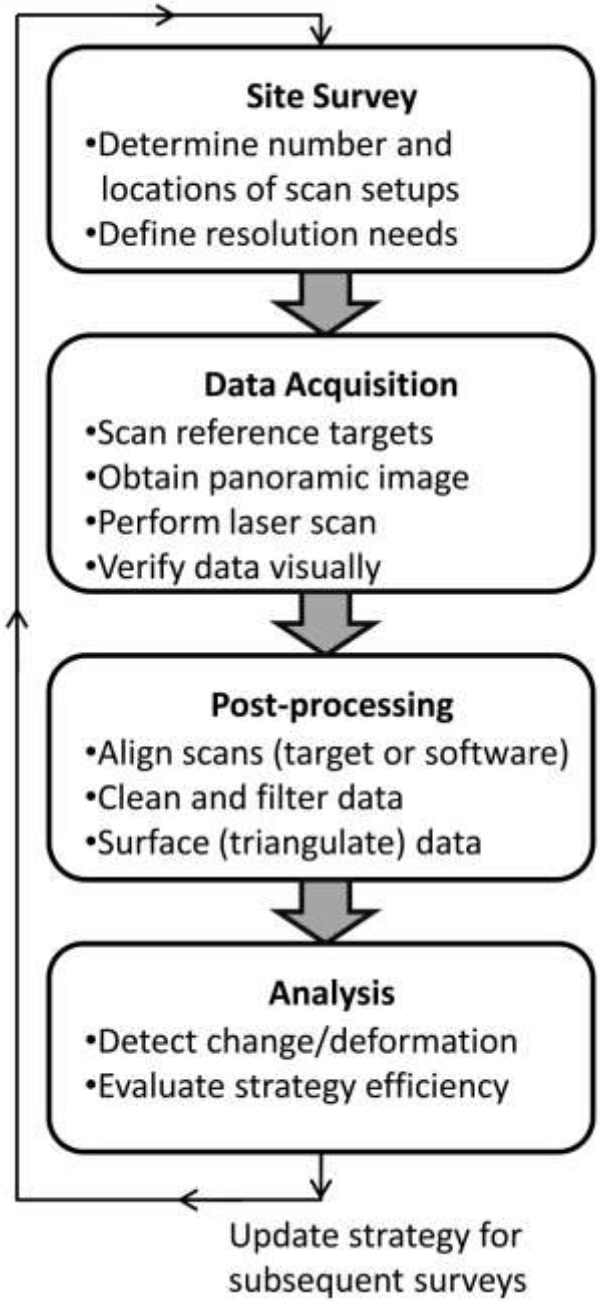

Figure 1-3. LIDAR data collection workflow

Once scans are aligned and merged, datasets are edited to remove artifacts. The data can also be filtered to remove noise or provide a more uniform point sampling throughout the scan. 3D surface meshes (Figure 1-4) can then be created by triangulating the point cloud to provide reference models to perform calculations and analysis. These meshes can model complex overhang features, such as sea caves, that cannot be captured with aerial LIDAR datasets.

Applications of TLS

Due to its efficiency for data collection, TLS has been successfully implemented for a wide variety of applications ranging from 3D modeling of small objects to large-scale terrain mapping. However, a specific laser scanner will not be suitable for all applications because each application requires a different range, level of accuracy, level of detail (resolution), and/or data size, and many challenges in each of the applications differ.

One of the first applications of laser scanning was reverse engineering and part inspection where objects are scanned and compared to CAD models to verify that they are within specification (Son et al., 2002). TLS has also gained popularity in use for historical preservation by scanning historic buildings and sites and works of art. Levoy et al. (2000) started the Digital Michelangelo Project to model and study Michelangelo's David statue and has developed many useful tools for application of TLS to cultural heritage. Bernardini et al. (2002) used TLS to analyze Michelangelo's Pieta statue.

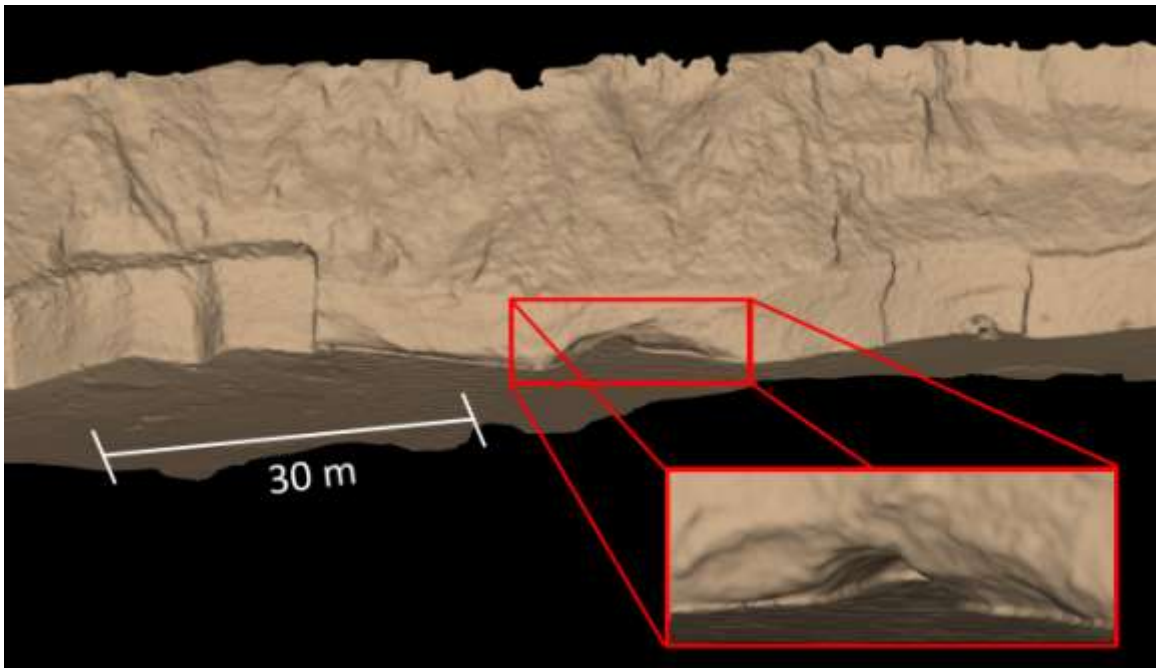

Figure 1-4. 3D triangulation surface model showing complex overhang features that can be modeled with TLS. (Solana Beach, March 2007).

Guarnieri (2005) presents the application of a 3D model to joint cultural heritage and structural analysis problem by exporting the TLS models to finite element analysis software to perform static and dynamic stress analysis on a full 3D model as opposed to cross sections. Dal Piaz et al. (2007) looked at using TLS to model a historical structure to analyze its stability. Monserrat (2008) modeled full 3D deformations of objects by moving targets between surveys and compared the TLS results to survey results using a Total Station. Girardeau-Montaut (2005) used TLS to observe changes at building sites and inside facilities for monitoring purposes. Hori et al. (2007) used TLS to determine the accuracy of original structural drawings to the as-built conditions.

TLS has also been implemented for several geologic studies. Alba et al. (2005) updated hazard maps by using TLS to monitor rock falls. Kayen et al. (2006) used TLS to model both ground and structural deformations following the 2004 Nigata Earthquake, showing its usefulness in quickly ascertaining post hazard damage. Scaioni et al. (2007) applied TLS to analyze a landslide threatening a village and also to a rock quarry.

TLS has proven to be an efficient tool for seacliff erosion studies (Collins and Sitar, 2004; Lim et al., 2005; Rosser et al., 2005; Collins et al., 2007; Young and Ashford, 2007). This dissertation builds upon their methods to allow TLS surveys to be performed more efficiently to increase spatial and temporal coverage.

Selection of a Laser Scanner

Laser scanners generally are designed for specific purposes or environments. In addition, caution must be used when comparing specifications because manufacturers tend to use their own specifications. For example, the accuracies of scanners vary nonlinearly with distance and some manufacturers publish accuracies at 50 m and others at 100 m. Also, accuracies are influenced by the surface being scanned. Direct georeferencing scan alignment techniques (Litchi, 2005) have inherent error, which influences the overall accuracy of the TLS survey. For example, the accuracy of a survey grade GPS unit is typically 1.0 cm in the horizontal and 2.0 cm in the vertical. Thus, a scanner with a millimeter level accuracy will no longer be of millimeter accuracy if GPS is used

for the scan georeferencing. This dissertation was completed using both I-Site 4400 and Leica Scanstation 2 laser scanners (see comparison in Table 1-2).

Table 1-2. Detailed specification comparison of the I-Site 4400 and Leica ScanStation 2 laser scanners

Parameter	I-Site 4400	Leica Scan Station2
Type	Time of flight pulsed rangefinder	Time of flight pulsed rangefinder
Wavelength	905 nm	532 nm
Beam divergence	1.4 mrad	-
Spot Size @ 0 m	21.6 mm	6 mm
Maximum Range:	500m @90% albedo	300m @90% albedo
Minimum Range	3 m	-
Measurement Rate	Ave. 4,400 points per second	Maximum 50,000 points per second
Min. angular point Separation	0.108°	0.0002°
Max Sampling	9 cm @ 50 m	1mm @ 300m
Angular accuracy	+/- 0.04°	+/- 0.0034°
Lab Position accuracy	20 mm @ 1- 50 m	6mm @ 1-50 m
Field Positional Accuracy	50 mm @ 1-500m	-
Angular scanning range	80° vertical, 360° horizontal	135° vertical, 360° horizontal
Laser Class	Class 3R laser product	Class 3R laser product
Output	X,Y,Z,R,G,B,Intensity	X,Y,Z,R,G,B,Intensity
Camera Type	Line scanning digital panoramic	1 MP 24^o x 24^o digital
Pixel Resolution	37 MP max for angular scanning range	64 MP max for angular scanning range
Dual Axis Tilt Compensator Range	+/- 3^o0'0"	+/- 0^o5'0"
Dual Axis Tilt Compensator Resolution	0^o0'20"	0^o0'1"
Optical Backsight Res.	0^o0'20"	Not Available

Criteria that should be weighted in the selection of a scanner for seacliff erosion include:

1. Type of laser – How well does the laser reflect off topographical surfaces?
2. Spot size – What will be the size of the laser spot on the target? Do features smaller than this need to be modeled?
3. Speed – How many points does it collect per second? How much setup and processing time is involved?
4. Field of View – How wide is the scan view?
5. Accuracy – What level of measurement error is acceptable?
6. Resolution – What point density is achievable/required?
7. Range – How much coverage is needed in a single scan?
8. Georeferencing – Does the scanner have a calibrated GPS mount for georeferencing? Or are external targets required?
9. Mobility, durability – Is the scanner designed for field operation?
10. Photography – Does the scanner use an internal or external camera? What steps need to be taken calibrate the photograph to the data if it is external? Is the photograph taken simultaneously or as an additional data collection procedure?
11. Software – What software package is used for aligning and meshing the scans? What features are available?
12. Effects on humans – Is it eye safe?

Table 1-3. Comparison of 3D Terrestrial Laser Scanners available in 2006

Manufacturer	System	Type	Range	Nominal Accuracy	Points per sec.
I-SITE	4400	Panoramic Camera	500 m	20 mm @ < 500m	4,400
OPTECH	ILRIS-3D	Camera Scanner	800 m	3mm @ <100m	2,000
LEICA	HDS 3000	Panorama Scanner	300 m	6mm @ 50 m	4,000
Trimble/ Mensi	GS 200	Hybrid Scanner	700 m	-	5,000
REIGL	LMS Z 390	Hybrid Scanner	300-800 m	6 mm	8,000-12,000
Z+F	IMAGER 5003	Panorama Scanner	52 m	5 mm	-
FARO	LS 880	Phase	76 m	3 mm	120,000

Table 1-3 shows a comparison of some of the many scanners that were currently available on the market at the time of scanner purchase, but by no means is considered comprehensive.

After careful consideration in evaluating several laser scanners, the research team selected the I-Site 4400 Scanner to perform the field work for this project. Although its accuracy was lower than that of other scanners, several features made it the ideal scanner for work where surveys needed to be completed rapidly during limited low tide opportunities. A simultaneous, built-in camera eliminates the need for additional setup and time required with most other scanners. The camera in the I-Site scanner is capable of a higher resolution photograph (37 MP) than most of the other scanners (6-12 MP). The I-Site 4400 scanner has a dedicated, calibrated GPS receiver connection, while

most other scanners require swapping of the GPS receiver and the camera for each scan. This swapping not only increases the setup time at each point, but it allows for more contact with the instrument which leads to increased error. The I-Site scanner automatically rotates to get a full field of view, while some other scanners must be manually rotated to capture the same view. Another advanced feature of the I-Site scanner is the wide-range (up to 3^{o}) level compensator which corrects the data for an unlevel setup. This is critical on a sloped beach where a level setup is difficult to obtain and would be a time-consuming process. Finally, optical backsight capabilities provide the ability to directly georeference the data without targets, thus reducing processing time.

Grazing Angles

For LIDAR, the location of the scanner relative to the cliff and the geometry of the cliff can influence the ability to retrieve return pulses from the laser. Simple geometry can be used to determine the angle of incidence (θ, angle between the laser beam and surface normal) and grazing angle (γ, angle between the laser beam and cliff surface. Lower incidence angles and higher grazing angles indicate that the reflection is more direct with the surface. While the geometry and calculations would be the same between the airborne and terrestrial scanners, the equations can be simplified differently. For these derivations, all elevations are relative to the cliff base. Figure 1-5 shows the setup and calculation for airborne LIDAR and Figure 1-6 shows the setup and calculation for terrestrial LIDAR. First, the cliff slope can be calculated by:

$$\alpha = \tan^{-1}(h/w) \qquad (1\text{-}1)$$

The angle of the cliff surface normal from horizontal (η) can be calculated from:

$$\eta = 90^o - \alpha \quad (1\text{-}2)$$

Next the angle of the laser beam from vertical (δ) is calculated by:

$$\delta = \left| \tan^{-1}(x + \Delta w)/(Z - \Delta h) \right| \qquad (1\text{-}3)$$

For the terrestrial LIDAR, the scanner is typically at the same elevation as the base of the cliff, so Z ~ 0. Thus δ would be negative for TLS without the inclusion of the absolute value function. The beam angle from horizontal can be calculated as:

$$\phi = |90^o - \delta| \quad (1\text{-}4)$$

The definition of the incidence angle is the angle between the normal and the beam angle. Thus,

$$\theta = \eta - \phi \qquad (1\text{-}5)$$

Note that ϕ is upward/positive from horizontal for Z> Δh (airborne) and negative from horizontal for Z≤ Δh (terrestrial scanning). So for airborne LIDAR (Z> Δh):

$$\theta = (90^o - \alpha) - (90^o - \delta) \qquad (1\text{-}7a)$$

$$\theta = \delta - \alpha \qquad (1\text{-}8a)$$

And for terrestrial (Z≤ Δh):

$$\theta = (90^o - \alpha) + (90^o - \delta) \qquad (1\text{-}7b)$$

$$\theta = 180^o - \alpha - \delta \qquad (1\text{-}8b)$$

The grazing angle can then be calculated by:

$$\gamma = 90 - \theta \quad (1\text{-}9)$$

So for airborne LIDAR (Z> Δh):

$$\gamma = 90^o - \alpha - \delta \quad (1\text{-}10a)$$

And terrestrial (Z≤ Δh):

$$\gamma = \alpha + \delta - 90^o \quad (1\text{-}10b)$$

Additionally, for TLS (Z≤ Δh), the calculations can be simplified by assuming the scanner is directly horizontal from the cliff base and using the angle of the laser beam from horizontal, ω, instead of δ. ω is simply calculated by:

$$\omega = 90^o - \delta \quad (1\text{-}11)$$

or:

$$\omega = \left| \tan^{-1} (Z - \Delta z) \Big/ (x + \Delta x) \right| \quad (1\text{-}12)$$

By forming a triangle between the scanner, a point directly horizontal from the scanner on the cliff base (Z = 0), and the point of reflection, and using the identity that the sum of the three angles of a triangle add up to 180^o, the grazing angle can be calculated:

$$180^o = \omega + (180^o - \alpha) + \gamma \quad (1\text{-}13)$$

$$\gamma = \alpha - \omega \quad (1\text{-}14)$$

And the incidence angle can be calculated by:

$$\theta = 90^o - \gamma = 90^o - (\alpha - \omega) = 90^o - \alpha + \omega \quad (1\text{-}15)$$

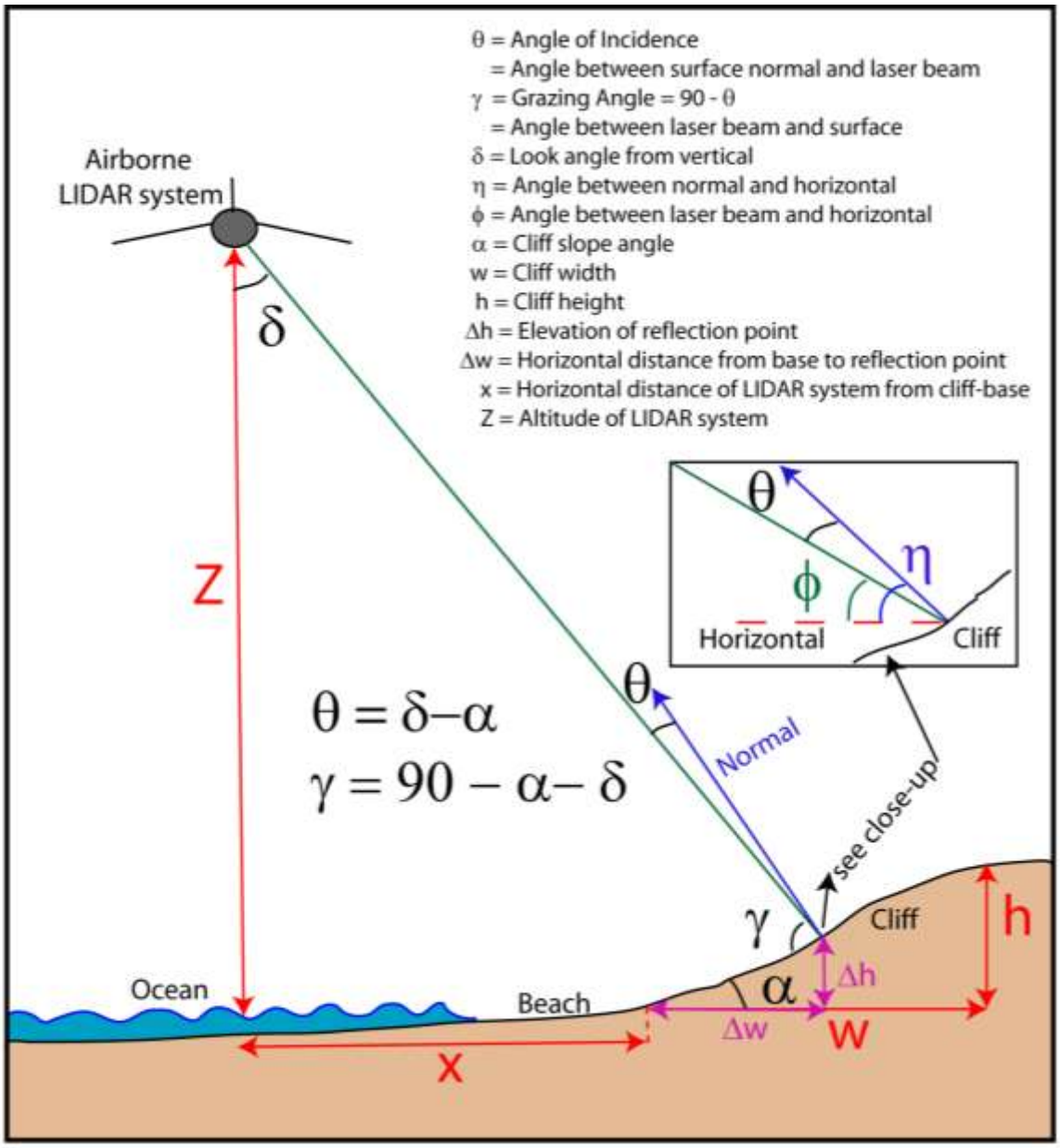

Figure 1-5. Schematic showing calculation of incidence and grazing angles for airborne LIDAR and definitions of variables.

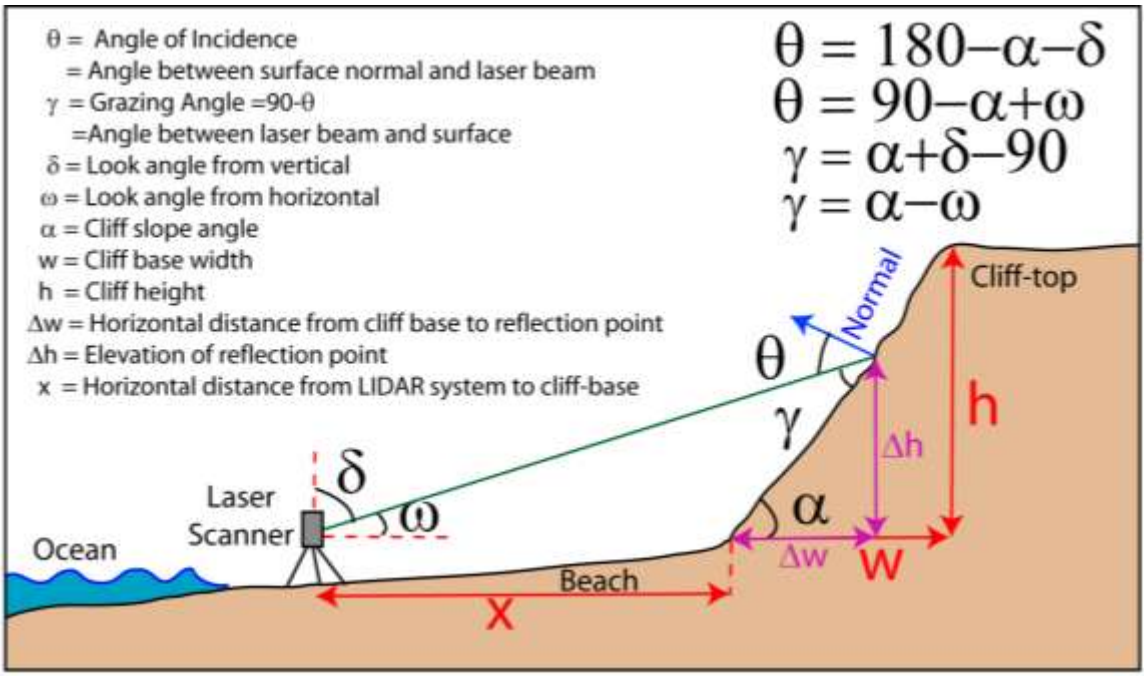

Figure 1-6. Schematic showing calculation of incidence and grazing angles for TLS

Figure 1-7 and Figure 1-8 show the grazing angles based on various configurations of cliff geometry and scanner position. In general, airborne LIDAR has better grazing angles for gentle cliff slopes, while terrestrial LIDAR has better grazing angles for steep cliff slopes. Figure 1-7 shows the grazing angles for the mid-height of the cliff, while Figure 1-8 shows the worst-case scenario for terrestrial LIDAR at the top of the cliff. Note that for low values of x/h, scanning is performed too close to the cliff, reducing grazing angles. Also, the airborne appears consistent between plots, however, for a fixed airplane position, δ would vary between the mid-height of the cliff and the top, so a different δ value should be calculated for each position.

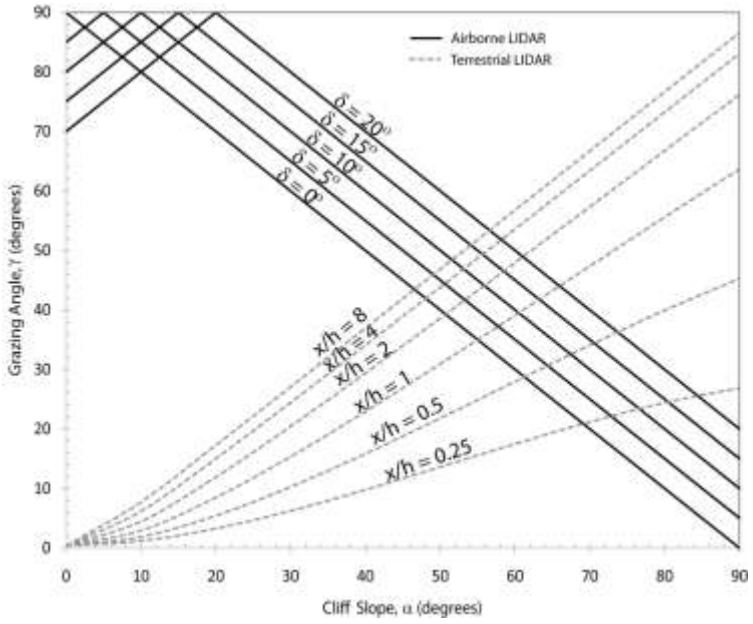

Figure 1-7. Grazing angles at mid-height of cliff for airborne and terrestrial LIDAR systems based on geometric configurations.

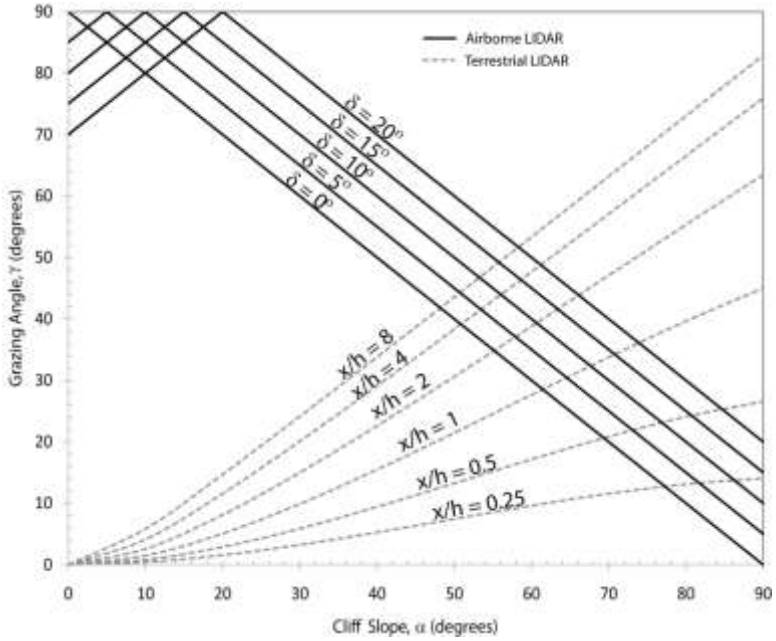

Figure 1-8. Grazing angles at top of cliff for airborne and terrestrial LIDAR systems based on geometric configurations. Note that the cliff top provides the worst-case grazing angles for terrestrial LIDAR and the best for airborne.

GPS

Differential GPS (DGPS) and Real time Kinematic (RTK) surveying

For DGPS, a base station can remove some of the error in the measurement due to ionospheric disturbance. By occupying a known location with a GPS receiver (base station) and another location to be surveyed with another GPS receiver (rover), the error induced by the ionosphere can be reduced by correcting the measured position at the known location to the correct location and applying that same correction to the point taken at the survey site. RTK GPS uses additional satellites to allow for data to be collected accurately in real time.

VRS network

This study utilizes the CALVRS (California Virtual Reference Station, 2008) system to provide the necessary differential correction factors transmitted from a base station. A VRS system links data from several different base stations on a network to interpolate the correction values between base stations (Figure 1-9). The GPS receiver obtains the correction values using a cellular phone as an internet connection to a webserver computer. This means that the user is not dependent on line of sight radio signal as with a traditional base station setup, but can use the method wherever they have cellular phone coverage within the VRS network. In addition, this network is continually monitored so it can immediately remove a base station from the network if moves

out of tolerance (e.g., something disturbs the base station). The surveyor can seamlessly continue to acquire quality data by using the other base stations instead of the erroneous corrections transmitted from the disturbed base station.

A further advantage of using a VRS system is the field efficiency from the ease of implementation. Using the VRS network removes the necessity of setting up a transient base station, a time-intensive process to setup and that introduce errors from inconsistent setups between surveys. The rover unit is able to initialize quickly because the webserver is continually running and is able to communicate quickly with the rover via the internet connection. Finally, this network reduces equipment costs by not needing an additional GPS receiver to serve as the base station.

Figure 1-9. Locations of base stations and coverage for the CALVRS network (from CALVRS 2008)

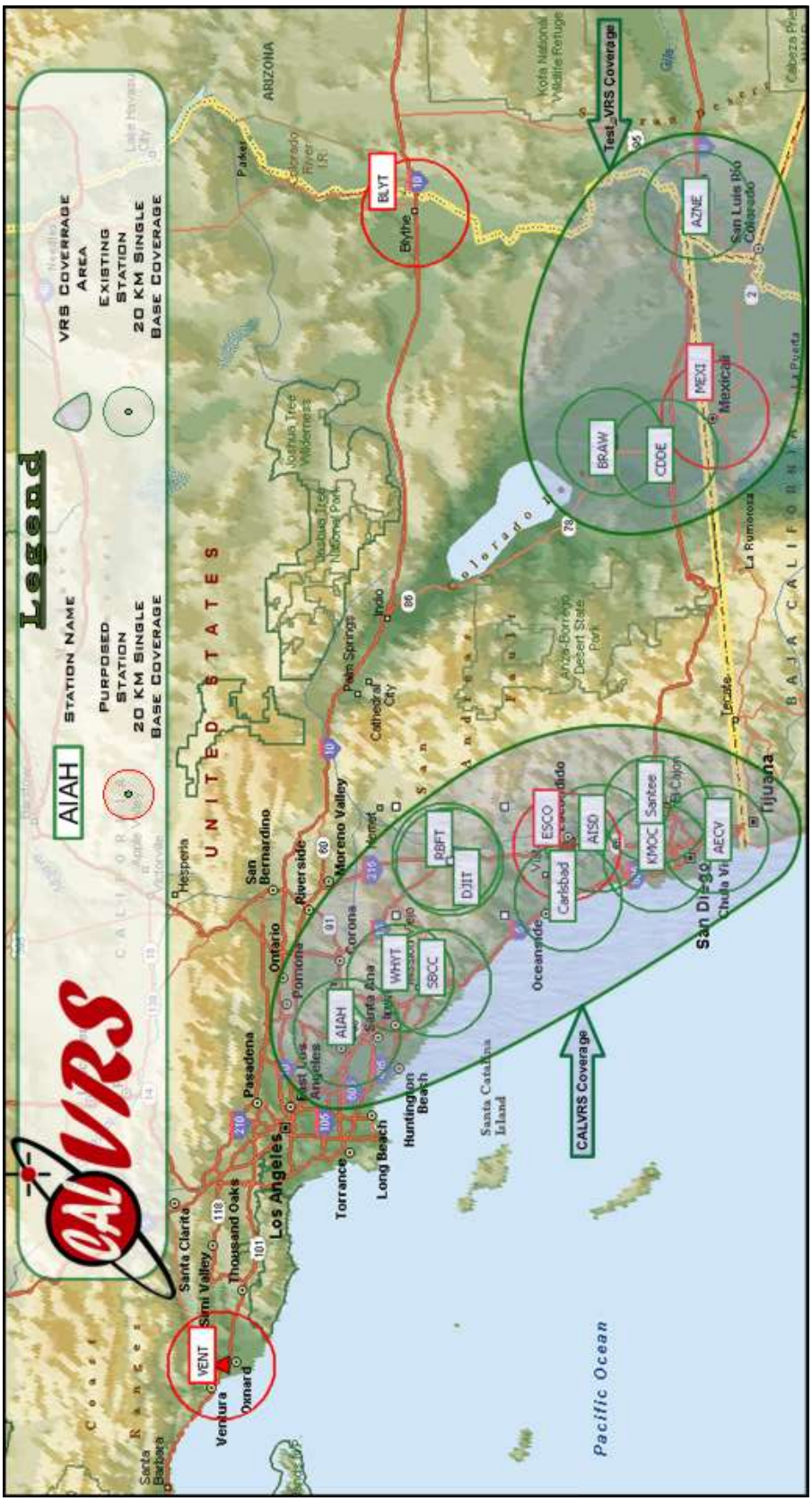
Legend
VRS COVERAGE AREA
EXISTING STATION 20 KM SINGLE BASE COVERAGE
AIAH
STATION NAME
PURPOSED STATION 20 KM SINGLE BASE COVERAGE
CALVRS
Test_VRS Coverage
CALVRS Coverage
UNITED STATES
ARIZONA
CALIFORNIA
BAJA CALIFORNIA
Pacific Ocean
VENT
BLYT
AIAH
WHYT
SBCC
RBFT
DJIT
ESCO
CRSB
AISD
KMOC
SNTE
AECV
BRAW
CDDE
MEXI
AZNE
Los Angeles
San Diego
Tijuana
Mexicali
Riverside
Moreno Valley
Palm Springs
Blythe
Oceanside
Carlsbad
Santee
Chula Vista
Ventura
Oxnard
Simi Valley
Santa Clarita
Thousand Oaks
Pasadena
Torrance
Long Beach
Huntington Beach
Ontario
Pomona
San Bernardino
Hesperia
Indio
Cathedral City
Yuma
Parker
Lake Havasu City
Needles
Santa Barbara
Santa Catalina Island
Joshua Tree National Park
Anza-Borrego Desert State Park
Kofa National Wildlife Refuge
Gila
San Luis Río Colorado
La Rumorosa
Ensenada
Tecate
Colorado River
San Andreas Fault
Coast Ranges

Software

Several software packages were used to perform the analysis of the complex datasets. I-Site Studio 3.0 (I-Site, 2008) was used for data editing, surfacing, and volumetric analysis of failures. ArcGIS® (ESRI, 2008) provided a GIS environment to perform spatial analysis. Utilizing Visual Basic for Applications within ArcGIS®, allowed for new analysis techniques to be developed in the GIS environment.

As TLS is a recent technology, much of the software available for analysis does not provide all the necessary tools for a complete study and/or is very expensive. The large size of TLS datasets limits their use in many software applications. Many customized routines were developed in the C++ language to efficiently process the data to perform tasks such as filtering, scan alignment and georeferencing, volumetric analysis, cross-sectioning, and generating surface models. These programs were enhanced using the Open Graphics Library (OpenGL) to provide a 3D visualization environment to interactively compare and analyze the TLS datasets.

STUDY AREA AND PRIORTIZATION

This study focuses on the seacliffs for the northern portion of San Diego County from Scripps Pier to Batiquitos Lagoon in Encinitas covering 17 km of seacliffs. The study area is divided into several sections (Figure 1-10) including: Scripps, Black's Beach, Torrey Pines, Del Mar, Solana Beach, and Encinitas. These sections are based on natural breaks in the seacliffs from lagoons or

canyons. Although there are some differences in the geology of each section, the above sections contain similar sediments and geologic formations.

To map erosion or any form of change in a region requires systemic and informed surveying to capture the most information in areas that undergo the most change. This study utilized a priority mapping effort to determine what areas would be scanned during the limited survey times (i.e. low tide cycles) to maximize the data collection efforts. To determine which areas to establish as priorities, the research team should consider which areas or sites undergo substantial change, are of the most value to the study, and require a higher level of detail. Areas undergoing the most change should be surveyed most frequently so that the changes can be captured and accurately modeled. In situations where a section requires substantial survey time because of the topographical complexity, the research team should consider their capabilities (i.e. insufficient scanner resolution/accuracy or processing equipment) of modeling those complexities. For example, LIDAR cannot penetrate heavy vegetation to obtain data on the cliff below, so areas with dense vegetation were given low priority.

Figure 1-10. Map of study area showing section divisions. Lagoons are abbreviated on map and are as follows BL = Batiquitos Lagoon, SEL = San Elijo Lagoon, SDL = San Dieguito Lagoon, and LPL = Los Penasquitos Lagoon.

GEOLOGY OF SAN DIEGO COUNTY

The sediments of San Diego County consist of several well-sorted, cemented marine terraces that have formed as a result of sea level rise and fall in combination with tectonic activity throughout the ages (Kennedy, 1973). These deposits are nearshore marine, beach, estuarine, lagoonal and continental dune facies which have cemented and compacted over time to form sedimentary rocks. Underlying these marine sediments are volcanic materials formed during the Mesozoic era such as Granite, and some metamorphic rocks (AASP, 1973).

The seismically active County of San Diego contains four major strike-slip faults oriented northwest to southeast and several other smaller faults. Along the San Diego Coast, uplift has been estimated at rates of 19 to 24 m during the past 80,000 years (Gastil, 1977).

In addition to the active tectonics in the region, the cycling sea level rise and fall through geologic time has created an active coast in San Diego County as both ocean wave erosion and subaerial processes transport sediment along the coast. The erosion of cliffs along the coast is so significant that one can easily observe dramatic changes in one's lifetime. This erosion threatens the developed coastline where several homeowners have purchased valuable real estate, but the erosion is a necessary process to preserving the beach and the nearshore processes associated with it.

Coastal Environment and Erosional Processes

Sediment transport along a coast can be modeled using the concept of a littoral cell, which is a segment of a coast line containing a complete cycle of littoral transportation and sedimentation. The study area is located in the Oceanside littoral cell which extends from Dana Point to the La Jolla Submarine Canyon (Nordstrom and Inman, 1973). The alongshore transport of sand by wave energy in the Oceanside littoral cell is generally in the North to South direction. The sand budget in this littoral cell has been in a deficit from damming of coastal rivers (Flick, 1994; Inman and Masters, 1991), and as a result, there is less sand on the beach. This, in turn, has accelerated cliff erosion because beaches act as a buffer zone to protect the seacliffs.

Seacliff erosion is a function of both the material (Benumof and Griggs, 1999) and physical processes (Benumof et al., 2000). Both wave and subaerial erosional process contribute to the erosion of the seacliffs in San Diego County (Sunamara, 1992). Earthquakes also cause dynamic accelerations that can cause the cliffs to fail. Sea level rise results in a transgression of the ocean surface. This, in turn, results in a redistribution of sediment as sediment near the shore is eroded and transported offshore. As the sea level lowers, the ocean regresses, and sediment is then pushed back onto the shore. These processes can be observed throughout the study area where sea level fluctuations have led to the creation of several marine terraces.

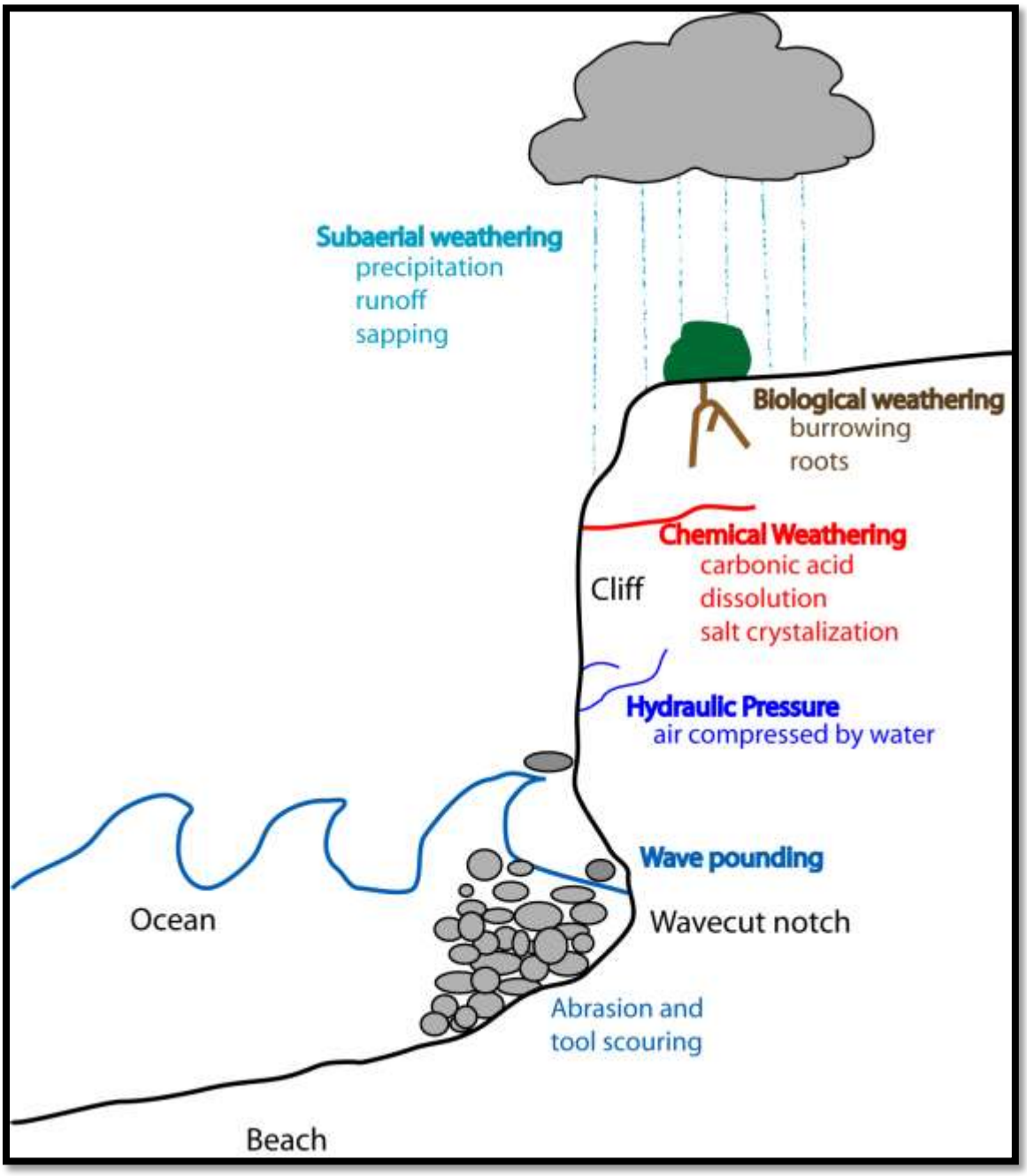

Figure 1-11. Schematic illustrating processes contributing to seacliff erosion

Wave Erosion

Wave erosion plays a significant role in the destabilization of the cliffs through erosion of the base. As wave energy hits the cliffs, notches and sea caves develop (Figure 1-12). The impact of these waves are more dramatic during the winter when the waves break closer to shore and less energy is dissipated by the beach. Waves also pick up sands and gravels which work similar to sandpaper as they grind against the cliff, causing abrasion. During high energy storms, the waves can thrust cobbles against the base of the cliff. After a substantial amount of erosion, gravity failures can occur from the notches and sea caves that develop, creating a steep cliff face. The stability of such sections was analyzed in Young and Ashford (2008).

Figure 1-12. Notches in seacliffs at Fletcher's Cove, Solana Beach, CA created through wave-based erosion.

Subaerial processes

In contrast to wave based erosion, subaerial processes erode the cliff from the top of the cliff toward the base (Emery and Kuhn, 1982) and tend to flatten the cliff. Runoff from precipitation erodes the cliffs from the top of the cliff downward as gullies and canyons form at locations of concentrated water flow. Figure 1-13 shows this process in combination with groundwater seeping through the cliffs. Groundwater transport through the highly permeable sandstone mixes with the calcium carbonate cement in the soil to form carbonic acid, accelerating erosion through chemical weathering. Groundwater sapping can be observed at many sites throughout the study area. Additionally, the formation of tensile cracks allows water to seep into the cliff, causing weathering and adding additional weight to the soil. This water then creates hydrostatic pressure, pushing the crack apart.

Biological weathering occurs when plants grow in cracks, break down weak sediment, and push slabs apart until failure occurs (Figure 1-14). Plants on the seacliff can also add additional weight to the cliff, leading to instability. Attempts to stabilize the cliffs by using plants has often created negative impacts because the plants are add to the weight of the slope, and pull more water through the soil. As plants draw water out of the soil, their roots cause piping, removing soil around the roots. Animals and insects burrowing in the soil loosen the soil and create channels for water flow into the soil, exposing more surface area to water.

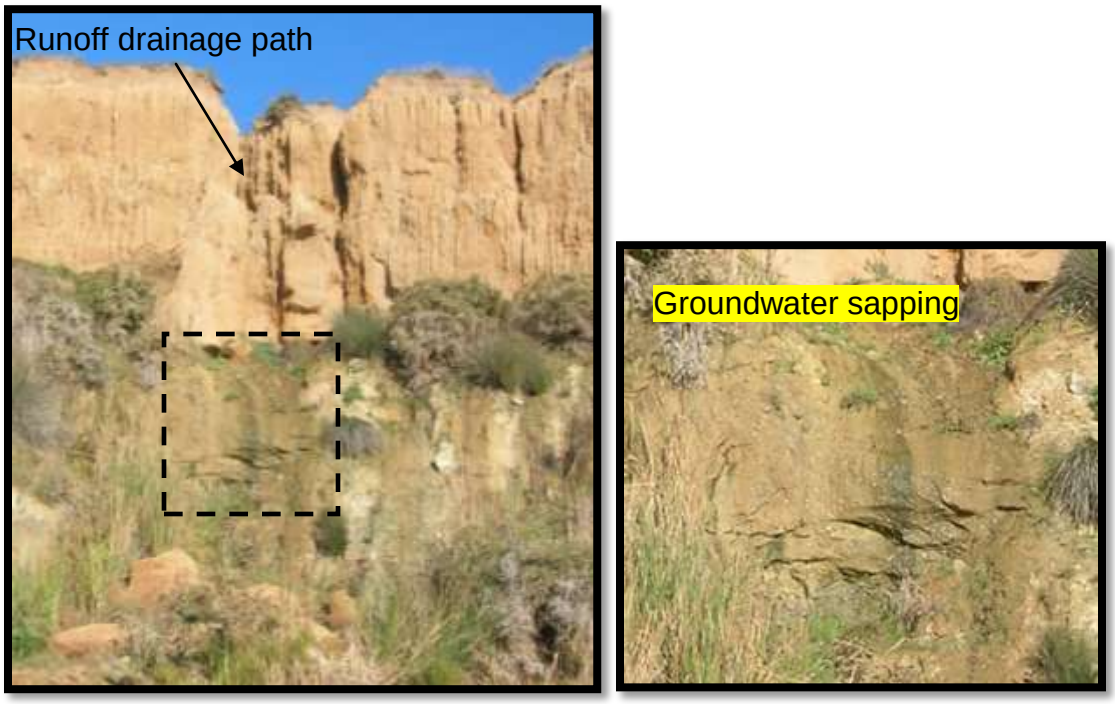

Figure 1-13. Top down cliff erosion from subaerial processes of precipitation and groundwater sapping in Del Mar, CA (Close-up on right)

Figure 1-14. Biological erosion of Torrey Sandstone at Torrey Pines Reserve (Close-up on right)

Anthropogenic contributions

Human development has dramatically advanced the erosion of sea cliffs (Kuhn and Shepard, 1980; Moore et al., 1999). Development of storm drainage for roads and developments led to concentrated water flows on to the cliffs accelerating erosion (Figure 1-15). Many drainage pipes placed in or on the cliff have also broken, causing concentrated erosion spots. Overwatering of plants also contributes to erosion. In addition, bluff grading close to the edge of the slope also initiates slope failures (Robinson, 1988). The terrace deposits consist primarily of weakly cemented sands (Kennedy, 1975), so as the top layers which have undergone the most cementing are removed, the bluffs become more permeable and thus more susceptible to erosion. Grading can also remove an erosion resistant cap that protects the weaker sediment from erosion.

Geologic Formations

The study area is constructed of sedimentary rocks that are part of the La Jolla Group (Kennedy, 1973), which are geologically divided into formations. Table 1-4 lists the formations found in the study area and key attributes of each formation such as age. The primary formations seen along the majority of the coast are the Delmar and Torrey Sandstone formations. Figure 1-16 shows the relationship of these formations to the beach environment. As each of these formations erode differently, their composition will be discussed in further detail.

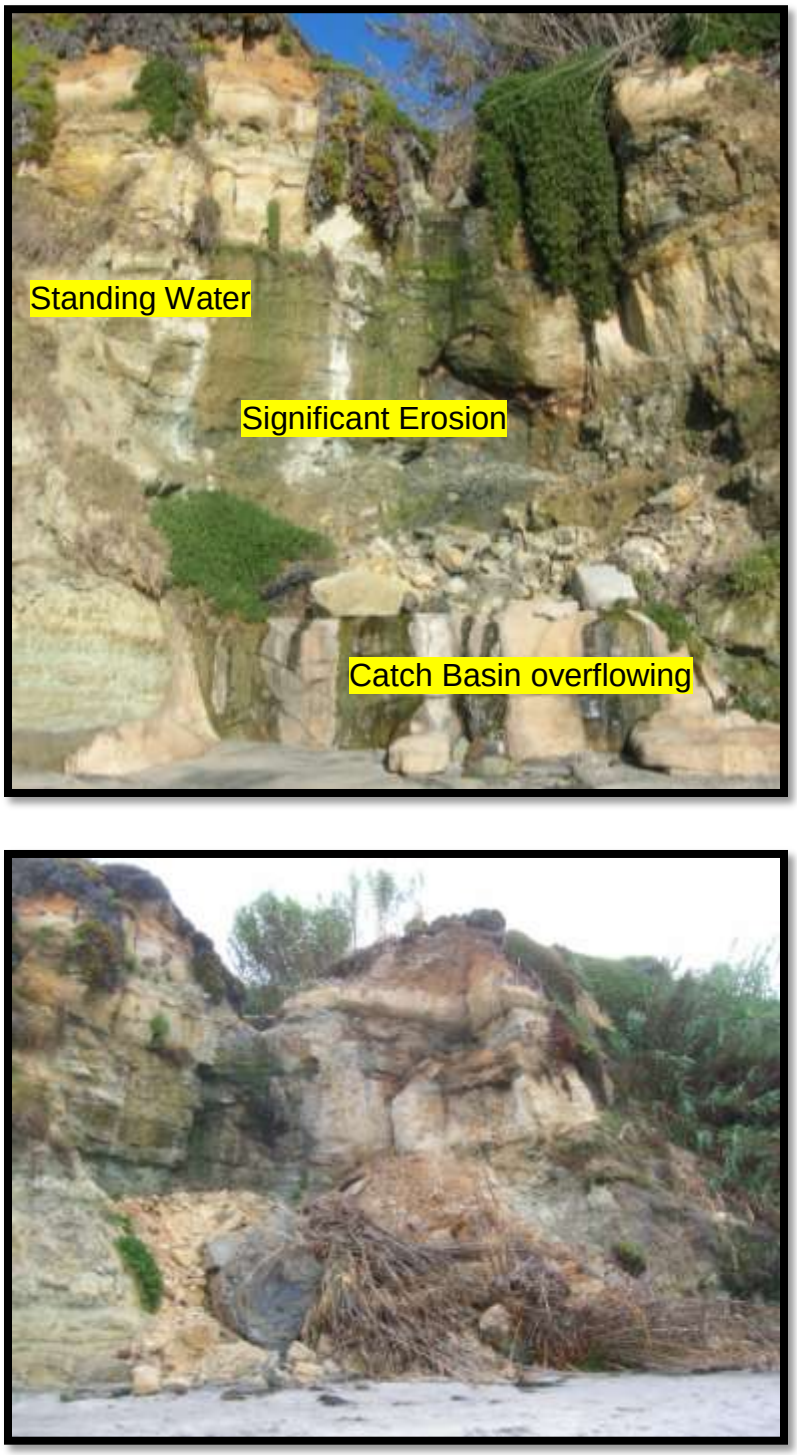

Figure 1-15. (A) Drainage system in Del Mar, CA, which has led to an erosion hotspot (February 2006). (B) Same site (August 2007) after a collapse covered the catch basin.

Figure 1-16. Geologic formations at Torrey Pines Reserve

Table 1-4. Geologic formations found in study area

Formation	Geologic Age	Age (years) (Grine, 2005)	Soil types	Depositional Environment
Delmar	Middle Eocene	48,000,000	Claystone, siltstone, mudstone	Estuarine lagoonal
Torrey Sandstone	Middle Eocene	48,000,000	Sandstone	Tidal flat
Lindavista	Middle Pleistocene	1,000,000	Sandstone, cobble layers	Marine terrace
Bay Point	Upper Pleistocene	120,000 to 40,000	Sandstone	Marine/Non-marine Terrace
Ardath Shale	Middle Eocene	-	Siltstone, claystone	Marine slope facies

The Delmar Formation

The Delmar Formation rests on older plutonic basement rocks (Kennedy, 1973) and was deposited in an estuarine lagoon environment with substantial energy fluctuations. While it consists mostly of mudstone and siltstone, or finer grained particles, it contains some layers of sandstone up to 3 m thick. These layers were deposited in a quiescent marine environment, as they are fine particles and would settle out at lower velocities. Several of these mudstone layers in the Delmar Formation have a greenish hue, indicating sulfate reduction in the underwater in swampy environments. The mineralogical composition is described in Table 1-5. Several fossils cemented throughout the Delmar formation create erosion resistant layers. These fossils are predominately bioherms and biostromes of oysters and other mollusks (AAPS, 1973). The shell fossil layers indicate high energy deposition in a tidal environment. In addition, rapid bedding changes are frequent throughout the Delmar formation, which would be a result of tides, storms, and floods. Several finer grained layers contain worm holes and bioturbation where the cross bedding was disturbed. These worm holes indicate that the sediment here was deposited in a lower energy environment where these creatures could thrive.

The sandstone layers within the Delmar formation were deposited as a result of channel fill deposits. The Delmar Formation also contains several cuts of siltstone and shalestone into the sandstone from channels cutting through the sand. Some of these layers create weak sliding planes. They also can create

perched groundwater causing sapping in the sandstone layers in the Delmar formation. The Delmar Formation can be considered heavily consolidated and tends to coarsen upward. However, there are several areas where there are fine grained layers between the coarse grained layers due to fluctuations in the marine environment. Cross-bedding observed in the Del Mar formation is a result of barrier beaches created from channel migration or a lagoon isolated from the tidal inlet and the open sea. The sandstone layers of the Delmar Formation contain several mud clasts, indicative of current motion ripping up the mud from the surface of the channel, carrying it, and depositing it with the sand.

Many outcrops of the Delmar formation are undercut by waves, forming wave notches and sea caves, creating instability of the cliff. In some areas with the Torrey Sandstone eroding through subaerial processes above the Del Mar formation, miniature alluvial fans form at the base protecting the cliff from undercutting.

Table 1-5. Mineralogy of Delmar Formation (Kennedy, 1973)

Mineral	Percent Composition (%)
Quartz	80-85
Plagioclase Feldspar	10-15
Biotite	3-5
Hematite, topaz, pyroxene, tourmaline, chlorite, glaucinite	Trace

The Torrey Sandstone formation

The Torrey Sandstone formation was a barrier beach deposited along a submerging coastline (Kennedy, 1973), providing a barrier to the lagoon where the Delmar formation was formed. Thus, very few fossils are found within it; however, the trace fossil Ophiomopha can be found at many levels in the sandstone (AAPS, 1973). With time, the sand that now is the Torrey Sandstone transgressed over the Delmar sediment. The Torrey Sandstone consists of poorly consolidated sandstone consisting of medium to coarse grained quartz that is well sorted with some feldspar (Table 1-6). This suggests that the primary source of the minerals is the plutonic rock of the Southern California batholith (Kennedy, 1973). It is naturally white, but as it is exposed to the elements in the atmosphere, it chemically weathers and turns a tan/light brown or pinkish color from iron oxide staining. The sandstone exhibits large-scale cross-bedding (AAPS, 1973).

The erosional patterns of the Torrey Sandstone are particularly interesting. As water flowed through the sandstone, it left calcium carbonate which cemented areas of the sandstone, similar to the formation of stalactites and stalagmites in a cave. These cemented areas are more resistant to erosion, creating holes and caves in the sandstone. As these areas erode, carbonic acid forms which accelerates the erosion of weaker sections. This creates a honeycomb pattern on the outcrop. The sandstone is very permeable and porous which has caused some problems with groundwater on unprotected slopes (Kennedy, 1973).

Table 1-6. Mineralogy of Torrey Sandstone Formation (Kennedy, 1973)

Mineral	Percent Composition (%)
Quartz	85
Potassium Feldspar	5-10
Biotite	3-5
Plagioclase Feldspar	1
Hematite, epidote, chlorite, zircon, tourmaline, pyroxene, and amphibole	Trace

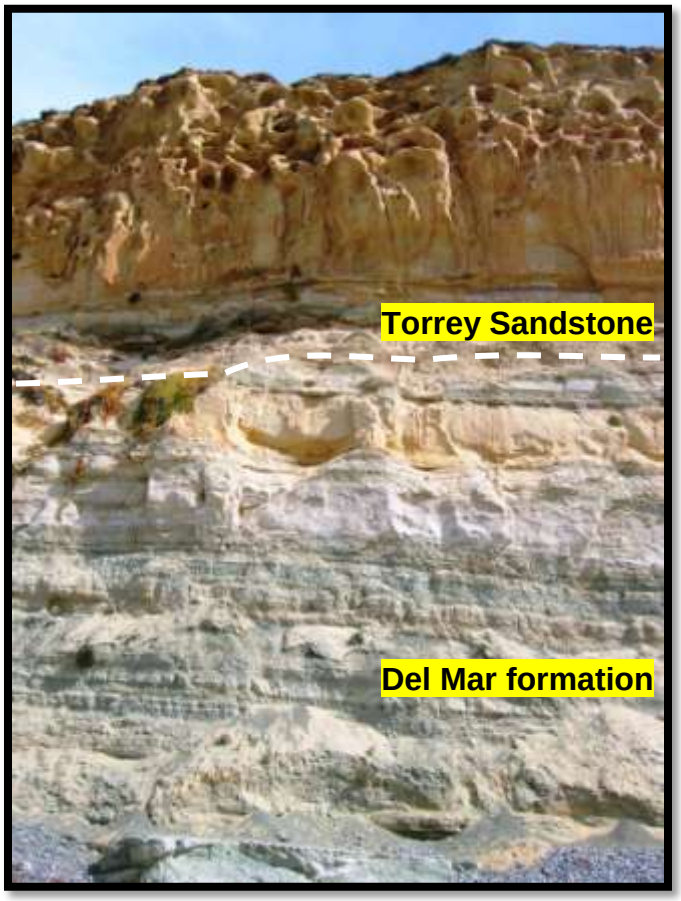

Figure 1-17. Typical contact of Torrey Sandstone and Delmar formation.

The Lindavista Formation

The Lindavista Formation is a very hard, interbedded red sandstone and conglomerate. Its red color results from ferruginous cement, mainly hematite, in the Lindavista formation (Gastil, 1977). Where the Lindavista formation overlays the Torrey Sandstone, it acts as a cap rock protecting the softer Torrey Sandstone. These beach cobbles form the base of the Lindavista formation and mark an abrasion surface (Figure 1-18) during a transgression of the ocean. When the ocean regressed, the Lindavista was formed as a result of the deposition of material eroded from the older sedimentary rocks within the San Diego embayment (Gastil, 1977) transported both in the ocean and in rivers. Thus, it is both a near-shore marine and non-marine deposit (Reed, 1990). Fossils from streams and marine shells can be found in this formation.

The Bay Point Formation

The Bay Point Formation (Figure 1-19), found at the north end of the Torrey Pines Reserve, contains poorly-cemented, light-brown sandstone. The formation was both deposited in the ocean and subaerially on an abraded wave cut terrace, similar to that of the Lindavista formation. The layers of the Bay Point Formation below 33 m above current sea level contain shells, which indicate that they were deposited in an ocean environment. Above that elevation, there are no shells, so indicating a different depositional environment from sediment being washed down slopes by rivers. It is a relatively young formation and has not consolidated, thus it is prone to landslides.

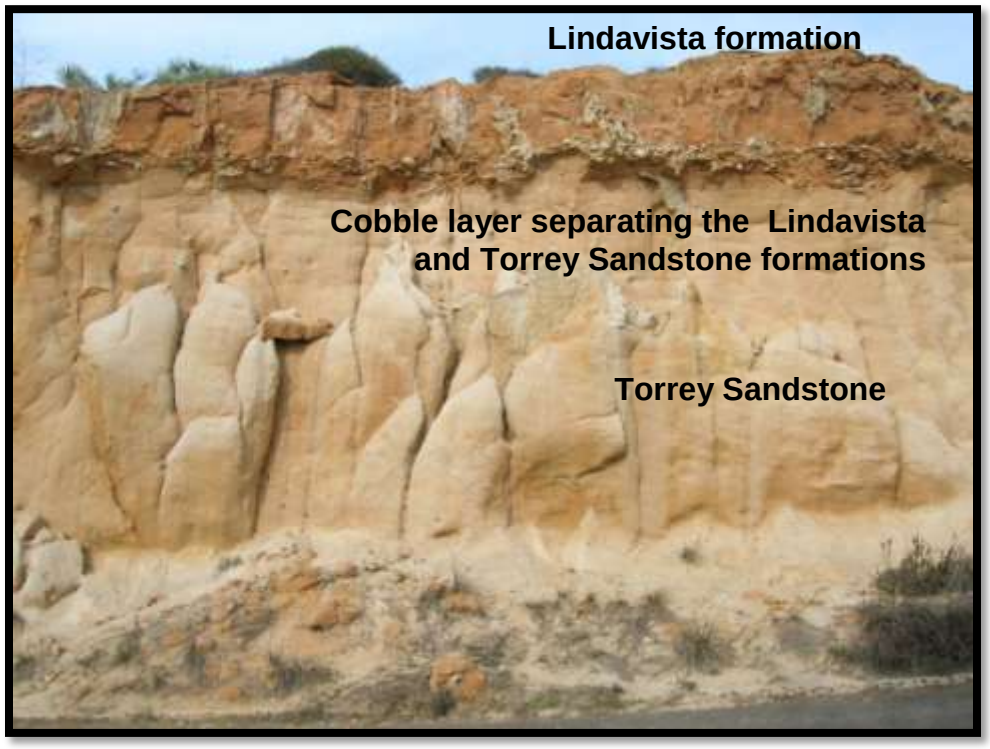

Figure 1-18. Layer of cobbles separating the Linda Vista formation from the Torrey Sandstone formation.

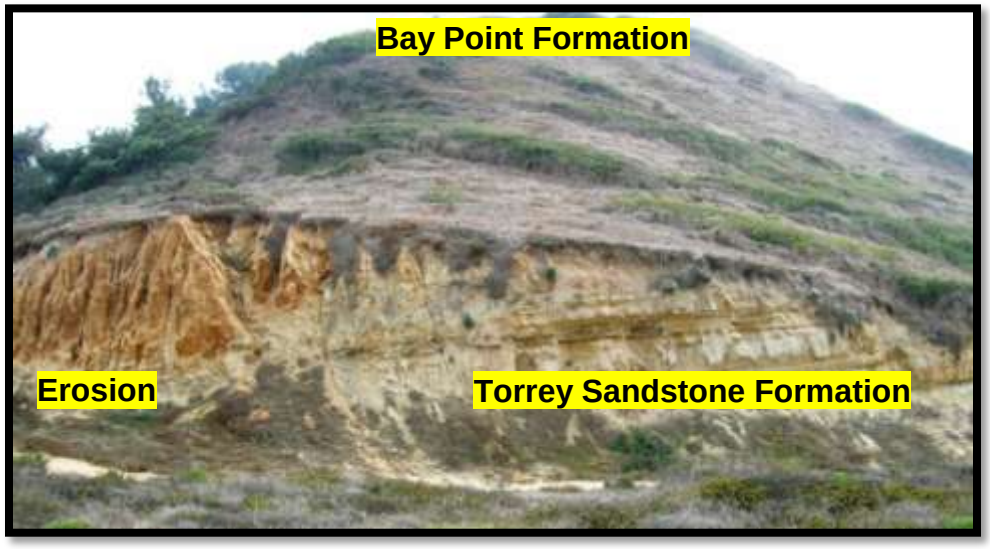

Figure 1-19. Contact between Torrey Sandstone formation and Bay Point formation.

Table 1-7. Mineralogy of Ardath Shale (Kennedy, 1973)

Mineral	Percent Composition (%)
Quartz	70-75
Orthoclase Feldspar	15-20
Biotite	5-10
Plagioclase Feldspar	5
Microcline, tourmaline, zircon, pyroxene, and hematite	Minor

Ardath Shale

The Ardath shale is primarily a weakly fissile siltshale with layers of expansible claystones that at this site comprise up to 25% of the unit (Kennedy, 1973). Landslides are very common in this material. It also contains thin beds of medium grained sandstone and concreted beds with mulluscan fossils (AAPS, 1973). The Ardath Shale consists of slope facies that formed on the marine continental shelf offshore from the Torrey barrier beach. The Ardath Shale consists mostly of quartz, as shown in Table 1-7. It is generally impermeable, so it can trap water in layers above it.

DISSERTATION OUTLINE

Now that a background on the geology and technology necessary for this study has been established, the remainder of the dissertation will discuss new methodologies necessary to perform large-scale seacliff erosion analysis using TLS. Chapter 2 will discuss a new survey approach to ensure accurate alignments of long cliff sections that is a hybrid between the direct

georeferencing and software alignment approaches that have been performed previously for 3D laser scanning of objects or sites. It will also discuss methods to determine optimal scanning parameters of scan spacing, distance, and resolution to ensure optimal quality data is collected. Chapter 3 will discuss the intricacies of the automated software alignment algorithm developed using least squares to batch process the substantial amounts of field data collected following the procedure of Chapter 2. It will also discuss the influence of warping caused by typical software alignments.

Chapter 4 will discuss the development of a rapid response program to obtain data on seacliff failures as soon as possible after they occur. The development of a coastal database and prioritization of the study are will be discussed. Chapter 5 will show more detailed results of the methodology of Chapter 4 and discuss the insights obtained from the rapid response endeavor. Chapter 6 will then discuss the development of a VBA program, TopCAT (Topographical Change Analysis Tools), developed to automate the change analysis of 3D datasets in a GIS environment. The applications of TopCAT to regional seacliff, beach, and dune erosion are presented. Chapter 7 will then summarize the conclusions and contributions of the dissertation and discuss continuing work necessary for further applications of TLS and seacliff erosion.

CHAPTER 2. TERRESTRIAL LASER SCANNING OF EXTENDED CLIFF SECTIONS IN DYNAMIC ENVIRONMENTS: A PARAMETER ANALYSIS

OVERVIEW

Substantial erosion of the unstable seacliffs along the economically important coastline of San Diego County, California, threatens existing developments and public safety. Time-series mapping of the seacliffs and beaches provides valuable information about seasonal and rapid- event erosion. With high resolution terrestrial laser scanning (TLS) georeferenced using real-time-kinematic global positioning systems, it is possible to establish reliable comparisons of time-series surveys for quantitative change analysis of seacliff morphology. This chapter introduces new field survey methods for georeferencing TLS surveys collected in dynamic environments where conventional control methods cannot be effectively implemented for large-scale mapping. Specifically, the quality control of scan alignment and the identification of optimal surveying parameters of point separation/density, distance from target, setup spacing, and efficiency are discussed for long cliff sections. These TLS surveys, performed several times along an approximately 17 km segment of seacliffs in San Diego County show an average root mean square uncertainty of 7.9 cm between adjacent scans approaching the nominal 7.2 cm accuracy of the survey equipment.

INTRODUCTION

New procedures for terrestrial laser scanning (TLS) with real-time-kinematic (RTK) Global Positioning Systems (GPS) are presented for regional mapping of cliff topography that markedly reduce manual processing and eliminate reliance on previous datasets for data alignment. Procedures are also presented to determine optimal surveying parameters for TLS. For clarity, a consistent nomenclature is used to describe these parameters. Spacing, *s*, refers to the distance between scan setup locations. Distance, *d*, refers to the horizontal distance from the scanner to the cliff. / Finally, the scanner sampling ratio (γ) represents the resolution at which a scan is performed relative to the maximum resolution capabilities of the scanner. This ratio influences the point separation (distance between points on the target surface) and likewise the point density (number of points on the target surface). It should be noted that the final point density on the target is always higher because of overlap between multiple scans. The TLS surveys for this study repeatedly imaged 17 km of seacliffs in San Diego County, CA from La Jolla to Encinitas, to understand better the processes governing seacliff retreat. The region was divided into sections based on natural breaks in the seacliffs from lagoons or points of limited beach access, as shown in Figure 2-1. While the project involved regional mapping of seacliffs, the new approaches can be applied to a variety of similar mapping projects using TLS.

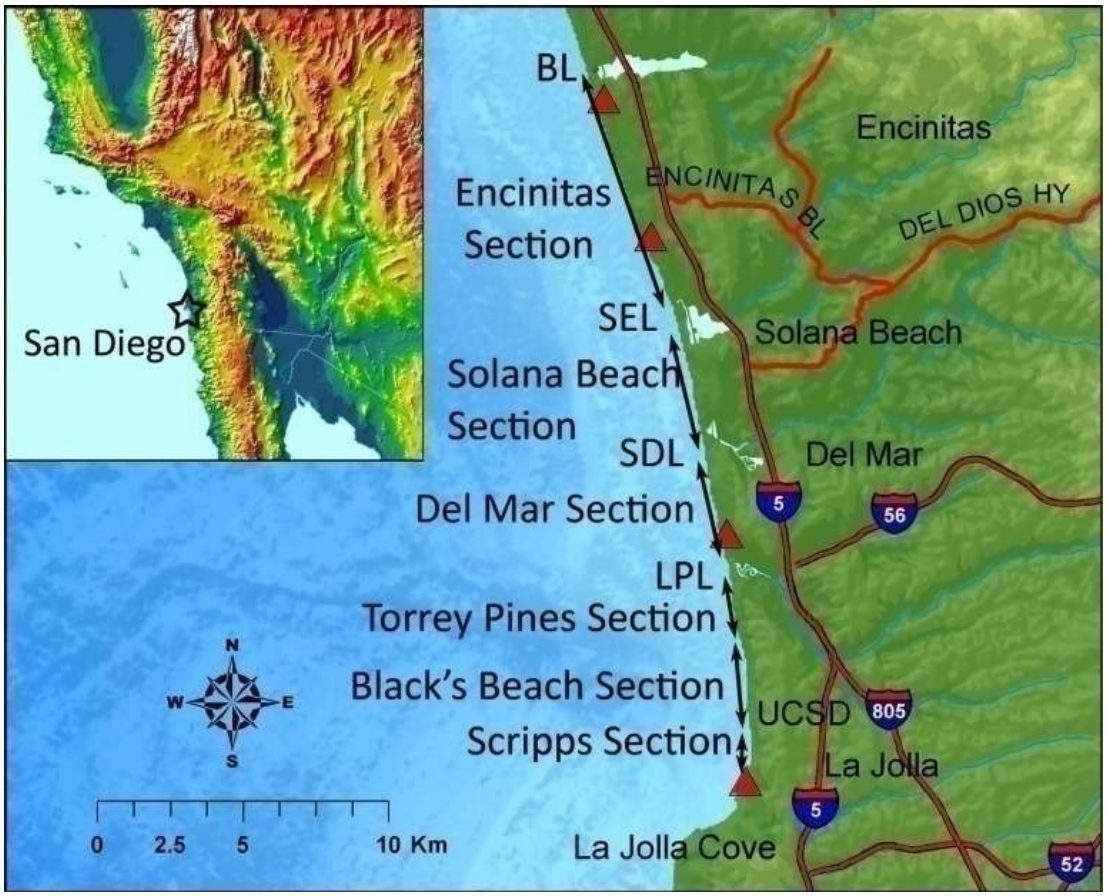

Figure 2-1. Map of study region showing individualized sections. Lagoons are abbreviated on map and are as follows BL = Batiquitos Lagoon, SEL = San Elijo Lagoon, SDL = San Dieguito Lagoon, and LPL = Los Penasquitos Lagoon. Triangles represent survey monuments used for calibration.

Seacliff erosion occurs through both marine and subaerial processes (Sunamura 1992). Marine processes include wave erosion of the cliff base, often creating notches and unstable, cantilever cliff sections. Subaerial processes include erosion from precipitation and surface runoff from cliff tops forming gullies and canyons, eroding the upper slope. Seacliff erosion tends to happen as episodic events where large sections of the cliffs fail on to the beach. In San

Diego County, these failures often threaten developed structures and public safety in this highly used and economically important coastal region (Griggs et al. 2005). Additionally, the seacliffs can provide much needed sediment to the beaches (Haas 2005; Young and Ashford 2006a,2006c), which are vital resource to the economy of Southern California. Furthermore, the heavy municipal development on the cliff tops along the coastline in this region requires accurate quantification of aggregate retreat rates for effective coastal management solutions. To gain a broader understanding of the processes that occur, quantitative analysis of the stability of seacliffs and erosional trends is essential. Such information can only be obtained by establishing a reference baseline model of the cliff location and geometry for future comparisons. Methods of data collection such as digital photogrammetry (i.e., Moore et al. 1999; Hapke and Richmond 2000), aerial Light Detection and Ranging (LIDAR) (Young and Ashford 2006a) and oblique helicopter LIDAR (Rosser et al. 2008) are not generally feasible for repeated coastal cliff surveys due to greater expense, difficult logistics, lower resolution, and/or the ability to capture the cliff face topography (including complex sea caves) in sufficient detail. As substantial change from seacliff failures greater than 30 m^3 can be observed monthly throughout the study area, such information must be obtained on a regular basis before becoming overprinted by subsequent natural processes or anthropogenic control efforts.

TLS background

TLS (also called terrestrial LIDAR), a line-of-sight remote sensing technique, rapidly transmits a light source to a target which subsequently reflects the light back to the scanner, producing a 3D point cloud model. High-speed, phase-based scanners compare phase differences between a modulated laser beam to determine distance to a target at close ranges (typically <80m). Time-of-flight scanners measure the laser pulse travel time to determine the coordinates of the survey scene relative to the scanner. Time-of-flight scanners are more suitable for longer range applications (>50m) such as this study where data needs to be acquired on a large scale. Use of RTK GPS allows point clouds to be transformed into a georeferenced, global *X, Y, Z* coordinate system (Figure 2-2).

The ability to capture centimeter accuracy data at high-resolution and the rapid response capability afforded by TLS makes it the ideal tool for quantitative mapping of seacliff erosion. TLS has various applications in civil and survey engineering and has proven to be an effective tool to study topography for coastal studies (Collins and Sitar 2004; Lim et al. 2005; Rosser et al. 2005; Collins et al. 2007; Young and Ashford 2007). While these studies show the effectiveness of TLS for studying seacliff geomorphology, they required time-intensive processes for data alignment and thus were only performed on small segments of the coast (typically less than 1 km) and. This study builds upon their efforts to produce a method applicable for large sections (several kilometers) of

Figure 2-2. Georeferenced point clouds for regional mapping of Torrey Pines, CA (September 2007). Black semi-circles represent scan setup locations spaced at approximately 50 m.

seacliffs, which presents new challenges to be addressed because the typical control methods cannot be effectively and efficiently applied.

Several scans must be linked together and georeferenced in order to map regional features. Collins and Sitar (2004; 2007) discuss several common methods used to georeference TLS for localized studies of cliff failures and landslides. One method locates the scanner using known control monuments. While feasible in a static urban environment, dynamic factors of coastal environments including seasonal beach height fluctuation and daily beach width changes from tides render this method unrealistic for large-scale mapping. Another method places target reflectors as control points at locations that have been surveyed that can be used to georeference the data with at least 3 control targets per scan. This method provides repeatable results between surveys provided the target locations remain fixed or are re-surveyed during each scan.

A difficulty mentioned by Collins and Sitar (2004) is some targets or target locations placed on the cliff can be lost during cliff collapses and new targets need to be introduced in subsequent surveys. In addition, placement of targets can be difficult and dangerous on near-vertical seacliffs such as those of San Diego County. Also, there is substantial public resistance to any alterations to the natural beach environment.

A common practice used for site surveying uses temporary reflector targets spread throughout the scan scene that are subsequently co-registered between scans. The use of such targets is possible in regional mapping, however, either substantial numbers of targets are required or the targets need to be re-positioned as the mapping progresses, which can be very time and labor intensive. Also, in coastal locations with unconsolidated sediment, the targets can sink or be disturbed by wind or waves during scanning, creating increased uncertainty in the alignment during data processing.

Lim et al. (2005) and Rosser et al. (2005) used a total station to obtain control points on the cliff, which are manually matched to comparative points in the point clouds to georeference the TLS surveys. Limitations of this method for large-scale application in sandy beach environments include requiring substantial field and manual user processing time, difficulty in maintaining survey control on a sandy beach environment (Lim et al. 2005 and Rosser et al. 2005 were both performed on hard, rocky coasts), potential safety hazards, and requiring very high resolution scans to adequately find matching tie points in the point cloud.

Young and Ashford (2007) performed terrestrial laser scanning for a portion of the study area from 2004-2005. The data was georeferenced during post processing using common baseline features (e.g. seawalls, buildings, etc.) between surveys, limiting application to developed areas of the coast. Such a technique requires substantial processing time to manually select and register baseline features together. Thus, new methods are requisite to efficiently and accurately survey large sections of coastline.

Error sources in TLS

Error sources in TLS depend on the laser characteristics, target characteristics, the scanner setup, and the alignment of scans. Lichti et al. (2005) discuss an error budget for the direct georeferencing of TLS and common artifacts from laser scanning. Direct georeferencing errors occur in the ability to resolve coordinates for the scanner origin, leveling, and backsighting. An important error source to consider for topographical mapping is the increasing spot size of the laser beam with range which reduces accuracy, removes the ability to model small variability which is averaged over the spot size, and creates artifacts in the point cloud. Scaioni (2004) discusses the theoretical increase in error from the spot size with distance from the target using simulated data.

While TLS may be able to produce a high accuracy model from a single setup, improper alignments can produce much larger error when attempting to globally align several scans. For example, a small rotation from an incorrect alignment between scans or unlevel setup can have a minimal effect on a

localized area. However, in regional mapping, a small rotation during post processing alignment in software can be amplified as scans are merged together leading to an increasing offset with distance and can be several meters in magnitude over a 1 kilometer range. These large alignment errors can be reduced by adequate data collection through the selection of appropriate parameters in the data collection to avoid error propagation.

APPROACH: FIELD PROCEDURE FOR REGIONAL SURVEYS

The field survey equipment (Figure 2-3) used for this study combines an I-Site 4400 laser scanner, a tablet PC controller, a survey-grade Trimble 5800 RTK GPS unit, and a cell phone, all transported on a rugged wagon. The scanner is nominally accurate to 2 cm at 50 m in a controlled lab test environment and 5 cm for general topographical scanning for its range of 5-500 m (I-Site 2008). The RTK GPS is nominally accurate to 2.2 cm (Trimble 2008). Overall, this amounts to a worst case potential of 7.2 cm of uncertainty for each point measurement. This scanner is not the most accurate scanner available; however, several features such as optical backsight capability, a wide range level/tilt compensator, internal 37 Mega Pixel scan-line camera, a calibrated GPS receiver connection directly above the scanner origin, and long range capability of 500 m made it an appropriate scanner for coastal studies where surveys need to be completed rapidly and repeatedly in a dynamic environment. The scanner requires six minutes to perform a 180 degree scan at its highest resolution (9.4 cm point separation at 50m), which typically captures a cloud of approximately

0.5 million X,Y,Z points. The scanner simultaneously uses a high resolution scan-line camera to photograph the target, which directly maps RGB values to each scan point. The scanner also measures the return signal strength, or intensity values, which can be useful in programmatically determining the nature of the target (e.g., whether the pulse was returned from a man-made concrete structure such as a sea wall or from vegetation). The level/tilt compensator of the scanner determines the angle (maximum range of 3^{o}, detectible within 20" increments) at which the scanner is unlevel by performing a 360^{o} preview rotation before the scan is acquired and adjusts the data so that they are appropriately leveled. The self leveling markedly reduces field setup time because the scan does not have to be manually leveled at each new origin.

To properly georeference TLS data, each point cloud must be appropriately constrained along six degrees of freedom (DOF) including translation in the *X*, *Y*, and *Z* directions and rotation about the *X*, *Y*, and *Z* axes. The objective of this field procedure is to constrain as many DOFs in the field as possible to minimize data alignment processing. The field procedure builds upon the procedures developed by I-Site (2008) and other scanner manufacturers and involves:

- Surveying using the optimal scanning parameters of point separation (i.e. γ), scan spacing (*s*), and target distance (*d*)
- Using a Virtual Reference Station (VRS) network or establishing a GPS Base Station as a reference point for RTK GPS surveying

Figure 2-3. Terrestrial laser scanner and RTK GPS field equipment

- Occupying control monuments with the RTK GPS receiver for calibration
- Performing TLS surveying by obtaining RTK GPS points at each scan origin to translate the scanner origin to its real-world *X*, *Y*, *Z* coordinates, leveling the scanner via a level compensator to constrain rotation about the *X* and *Y* axes, and backsighting the scanner to an estimated (cannot be accurately marked in dynamic environments) previous location or reference point to constrain rotation about the *Z*-axis.
- Perform a multi-scan, constrained software alignment to correct for backsight error
- Use quality control methods to verify accuracy of point cloud alignments

Determining optimal scanning parameters from a calibration survey

Choosing the appropriate spacing between scan setups (*s*), distance (*d*) from the target, and sampling ratios (γ) for TLS is a delicate balance between collecting enough information to capture the topography and avoiding excess redundant data, which can overload data processing. The spacing of the scans can be highly variable, as relatively flat cliff surfaces allow for increased spacing, whereas complex cliff topography requires closely spaced scans to avoid data gaps from shadowing. A simple rule for maximum scan spacing can be obtained from the following equation based on the Pythagorean theorem:

$$s_{max} = \sqrt{r_{max}{}^2 - d^2 - h^2} \qquad \textbf{(2-1)}$$

where:

s_{max} = the maximum scan setup spacing,

r_{max} = the maximum scanner or filtered data range,

d = the typical cliff distance, and

h = the average cliff height.

The scanner used for this study has low, medium, and high resolution settings (Table 2-1) which are based on an angular separation between scan lines, not the actual sampling ratio on the target surface. At the highest sampling ratio, the angular separation between points is 0.108^{o}. The point separation for

any scanner is a function of distance from the target (and thus will vary across the scan scene) and can be calculated by:

$$\rho = d \cdot \tan\theta \qquad \textbf{(2-2)}$$

where:

ρ = point separation on the target,

d = distance from the target, and

θ = angular separation.

Some scanners allow the user to specify a desired resolution at a particular range but are still limited by a minimum possible angular separation and accuracy limitations. Scanning near the target at close spacings increases point density at the expense of broad data coverage. The reverse is true for scanning at far distances from the target at far spacings. To understand the effects of these variables in field data collection and the repeatability of the survey method described previously, several calibration surveys were performed.

Table 2-1. Resolution settings and corresponding point densities available for the I-Site 4400 scanner

Resolution setting	Scanner sampling ratio, γ	Angular separation, θ	Point separation, ρ, at 50 m (cm)
LOW	1/16	0.432^{o}	37.7
MED	1/4	0.216^{o}	18.8
HIGH	1/1	0.108^{o}	9.4

Figure 2-4 shows a typical setup for a calibration survey where scans were performed at a 20 m spacing at distances (*d*) of 20, 40, and 50 m from the cliff. From these surveys, scan spacings (*s*) at 20, 40, 60, 80, and 100 m (and 120 m for the surveys 40 m from the cliff) apart were aligned separately to illustrate their effects on scan alignments and repeatability from different setup spacings (*s*) and distances (*d*) from the target. The scans were performed at the highest sampling ratio (Table 2-1) and then filtered to include only points on every 2^{nd}, 3^{rd}, and 4^{th}, scan line and row to simulate 1/4, 1/9, and 1/16 sampling ratios (γ), respectively. All datasets were filtered to 200 m from the scanner origin to remove distant sections of lower point density and less accuracy from a larger spot size.

Using a Virtual Reference Station

This study utilizes the CALVRS (California Virtual Reference Station 2008) system to provide the necessary correction factors transmitted from a base station for RTK GPS. A VRS system links data from several different base stations on a network accessible through a cell phone to interpolate the correction values between base stations. Although any form of RTK GPS could be used, a virtual reference station eliminates the need to set up a dedicated base station at the site, provided the site has sufficient cell phone signal strength. Thus, the VRS network requires less equipment, reduces setup time, and provides more quality control (i.e. multiple base stations providing correction factors) than conventional RTK GPS surveying.

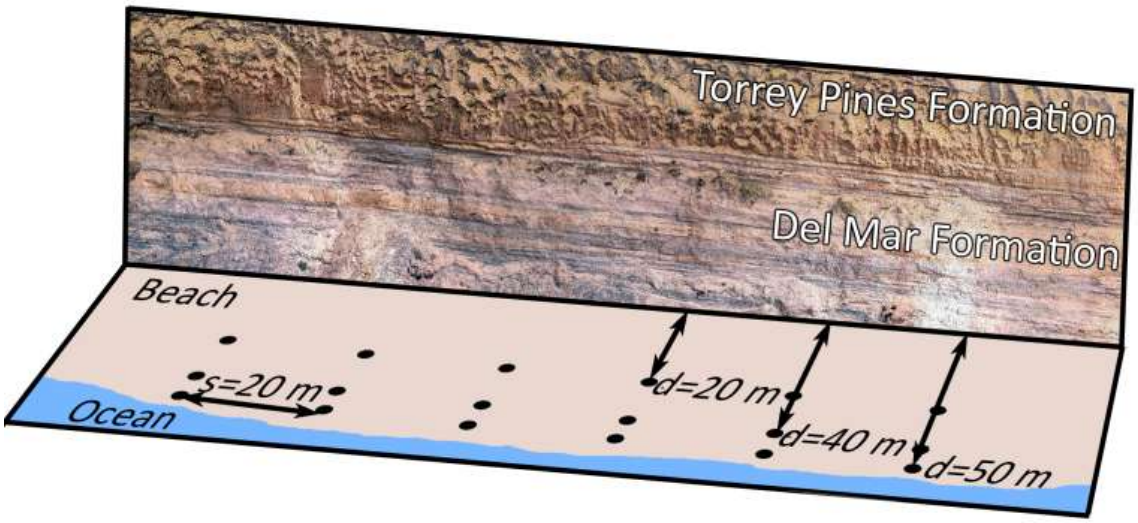

Figure 2-4. Calibration survey setup locations spaced 20 m apart at distances of 20, 40 and 50 m from the cliff consisting of the Torrey Pines and Del Mar formations. Notice the different erosion styles between the formations. The Torrey Pines formation erodes by groundwater sapping exacerbated by wind while the Del Mar formation erodes by wave undercutting.

Establishing a GPS Base Station as a reference point

If a VRS network is available, this method is not recommended. Also, if a permanent base station can be established, the error induced in the GPS measurements will be reduced because setup is only done once compared to a mobile base where different users set it up on different days, leading to a slight offset in position.

For differential GPS, a base station is required to remove some of the error in the measurement due to effects in the ionosphere. By occupying a known location with a GPS receiver (base station) and another location to be

surveyed with another GPS receiver (rover), the error induced by the ionosphere can be reduced by correcting the measured position at the known location to the correct location and applying that same correction to the point taken at the survey site.

The ideal base station should be located somewhere where it can be safely left unattended and in a position that it can broadcast via radio to the rover. The base station for the surveys was set up at the top of Scripps pier, as this allowed for a good line of site for much of the coastline. A monument needed to be calibrated on the pier for the reference, and the necessary monuments are listed in Table 2-2. This was accomplished by setting up a temporary base station above a nearby monument (DC1313) which was recently vertically and horizontally calibrated. Several measurements were obtained at the new monument above the pier, and the average of those were used as the final coordinates. Several nearby monuments were used to calibrate the data to other control points while using the temporary base station. The monuments that

Table 2-2. Control points used in the calibration of the Scripps Pier monument (UTM NAD 83 Z11N coordinates)

Monument	Location	Northing	Easting	Elevation
DC1507	Mt Soledad	3,633,553.469	477,099.148	247.500
Annie	Del Mar	3,644,907.775	475,584.962	42.179
DC1313	Scripps	3,636,391.642	476,214.558	9.303
-	Scripps Pier	3,636,567.632	475,943.585	12.950

had the least discrepancy were used (DC1507 and Annie). This base station was used for all surveys until June 2007 in this study, and thereafter, the field surveys were performed using the CALVRS network. As will be discussed in the uncertainty section of this chapter, the results agree well between the two methods.

Occupying a fixed control monuments for calibration

Each section surveyed (Figure 2-1) is calibrated using RTK GPS on fixed, control monuments (Table 2-3) so the data are consistent between surveys in areas that are repeatedly scanned. Two monuments (preferably one at each end of the scan region) are employed because the coast is essentially linear along a NW-SE axis. In areas where the region expands along two axes, a third monument should be used to calibrate the scans in and out of the plane.

Table 2-3. Calibration control monuments for DGPS surveys (UTM NAD 83 Z11N coordinates)

Section	Monument	Northing	Easting	Elevation
Torrey Pines/ Black's Beach/ Scripps	DC1313 (Scripps)	3,636,391.642	476,214.558	9.303
	Annie (Del Mar)	3,644,907.775	475,584.962	42.179
Del Mar and Solana Beach	Annie (Del Mar)	3,644,907.775	475,584.962	42.179
	SD-0660 (Swami's)	3,655,144.190	472,710.187	3.323
Encinitas	SD-0660 (Swami's)	3,655,144.190	472,710.187	3.323
	SD-0700 (Grand View)	3,659,812.551	471,041.397	4.776

TLS surveying

The coordinates of the scanner origin are obtained during the scan via RTK GPS centered directly over the scan origin. Laser scan data for each setup are in positions relative to the scanner origin, so a coordinate for the origin allows the data to be correctly translated in the *X*, *Y*, and *Z* directions, constraining three DOF in the alignment process. Because of the extreme difficulty in identifying and re-occupying the exact same position (to cm accuracy) on the beach, real time survey methods must be used, with RTK GPS, providing the most efficient solution. Temporary or permanent markers are ineffective when on a mobile platform because there is no downward optical site to identify the exact setup location and markers are easily disturbed by waves or people on the beach. The dual axis/tilt compensator of the scanner ($\pm 3^{o}$ determined within 20" for the scanner in this study) constrains the DOF associated with rotation about the X and Y axes. Generally laser scanners do not have such a wide range for level compensation, and would need to be leveled manually. Because the beach sand elevations can be highly variable, leveling the scanner mounted on a wagon is a tedious and difficult task; hence, a wide-range level compensator is valuable.

Aligning the scanner to a known location (e.g. backsighting) can remove the DOF associated with rotation about the *Z*-axis by calculating a bearing between the scanner origin and the backsight coordinates. Typically a previous scan location provides a convenient backsight. Unfortunately, because the there are no monuments and the previous position cannot be determined using

markers to centimeter accuracy when using a mobile platform on the sandy beach, it must be approximated. Estimating the backsight without a fixed reference point typically places the scan within 0.25^{o} of rotation about the *Z*-axis of its correct position. As most scanners do not have backsighting capabilities, the *Z*-axis rotation angle can also be estimated by a digital compass (within 0.1^{o}, if calibrated with the scanner). Alternatively, the scanner can be aligned approximately northward and a fictitious point due north can be used as the backsight coordinates. The scan can then be manually rotated about the *Z*-axis (centered at the scanner origin) in software to a rough alignment (quickly within $1\text{-}2^{o}$).

Multi-scan, constrained software alignment

Because the final DOF with rotation about the *Z*-axis is not completely resolved in the field, a software alignment is required for proper alignment. The scan origins are first translated to the RTK GPS coordinates obtained for their origins and level corrections are applied. The backsight estimate is then used to approximate the rotation about the *Z*-axis. A scan point cloud alignment algorithm should then be implemented using the leveling and origin coordinate constraints from the field procedure to find the optimal rotation for a scan about the Z-axis at its origin to minimize the backsighting error. The point cloud alignment algorithm must have several capabilities to avoid detrimental global error propagation. First, the algorithm must not depend on one scan being completely fixed because all of the scans probably have some backsighting error

that must be eliminated, because of the difficulty in marking a backsight target on the beach. In addition, aligning adjacent scans to a single, fixed scan can lead to the propagation of misalignments because of warping effects in scans. Secondly, the algorithm must constrain five of the six DOF's (translation *X, Y, Z* and rotation *X, Y*) and only allow for rotation about the *Z*-axis (centered at the scanner origin) to avoid misalignments. Thirdly, points should only be compared in areas where both scans have dense point coverage. Finally, it is important that the alignment be performed using neighboring scans on each side of every scan because pairwise point cloud registrations can misalign the scan with its other neighbor, whereas a multi-neighbor alignment better distributes the error between neighboring scans.

These requirements are not met in most available software packages. An automated algorithm, developed by the author, is available at *http://lidarweb.ucsd.edu/coastalstudy/softwaretools.html*, which incorporates these requirements. This algorithm determines neighboring scans by searching through the survey database of GPS coordinates (*X, Y, Z, scan ID*, and *backsight ID*), and batch processes the scan alignment procedure. The algorithm simultaneously rotates adjacent scans about their Z-axis and compares the distance from the points in one scan to planes formed by neighboring points in the adjacent scans to determine the optimal rotational angles for each of the scans, producing the lowest RMS distance between common features in scans. This algorithm will be discussed in further detail in Chapter 3.

Quality control of scan alignments

To ensure the accuracy of the scans, several methods of quality control can be employed. Scans can be compared to their neighboring scans to evaluate the root-mean-square (RMS) distance between the points in one scan and the plane formed by the nearest three neighbors in the second scan. Sometimes results can appear adequate mathematically because a localized minimum can be obtained in software alignments. By viewing 2D cross-sections of the cliff from neighboring scans simultaneously, misalignments become apparent that can be indiscernible in 3D. To ensure misalignments do not propagate globally through the aligned scans, annual RTK GPS surveys (Figure 2-5) can be performed on “fixed” structures such as stairwells, seawalls, and fences. Certainly these objects will move over time as waves disturb them, but during short time periods, they can be assumed to be fixed, especially during the calmer summer months. Obtaining RTK GPS points on features of highest curvature are easy to quickly visually compare to the TLS data. This also provides more tie points in georeferencing datasets from different sources. These surveys can be rapidly completed and do not have the constraint of requiring low tides. Because of possible movements of the “fixed” structures with time, it is recommended to repeat these surveys annually after the winter season. After obtaining repeat surveys of an area, surveys can be compared in areas with minimal change to ensure a successful alignment. This study utilized all of these methods to verify the accuracy of the TLS surveys.

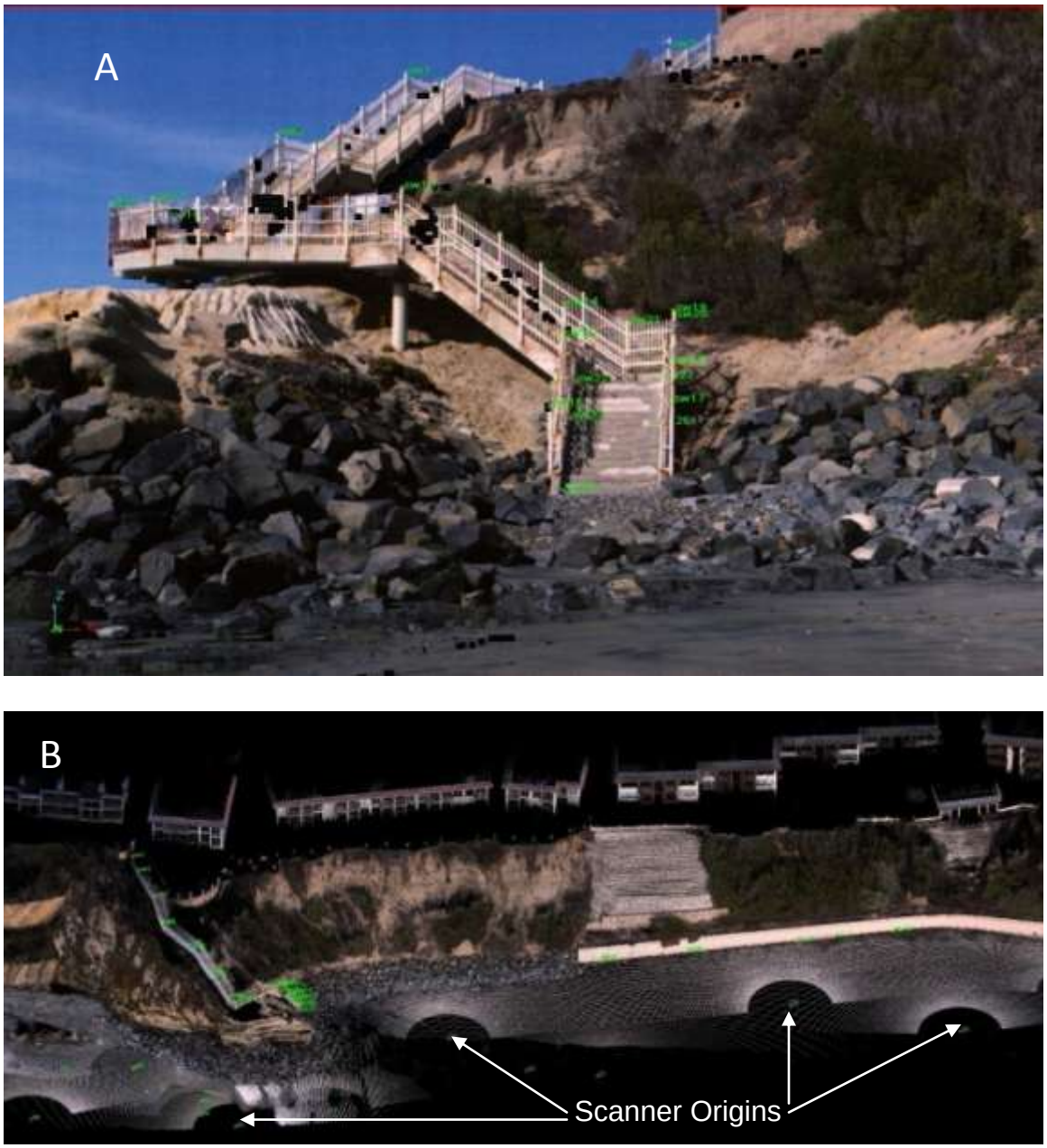

Figure 2-5. Verification of Alignment comparing DGPS surveys of "fixed structures." (A) Comparison of DGPS points (green dots with labels) to a georeferenced photograph obtained during scanning, and (B) Comparison of DGPS points (green dots with labels) to the aligned and merged point clouds.

RESULTS AND DISCUSSION

Calibration study results

For each scan spacing and cliff distance during the calibration experiments performed on the Torrey Pines section, the alignment uncertainty was evaluated by calculating the root mean square (RMS) uncertainty between neighboring scans. The RMS uncertainty metric used in this study compares distances of the points of one scan to a plane formed by their nearest neighbors in another scan to predict where the scans should be relative to one another.

Figure 2-6 shows the relationship between scanning distance (*d*), setup spacing (*s*), and the sampling ratio (γ). The three curves in Figure 2-6 drawn for full, quarter, ninth, and sixteenth resolution represent the distances from the cliff (20, 40, and 50m) at which the scans were performed. For a given sampling ratio, there are three zones. First, at close spacings (<50 m for γ =1) between setups, the RMS uncertainty is mostly dependent on the accuracy of the equipment. While the RMS is lowest in this region, it requires the most time. At large spacings (>70 m for γ = 1), the RMS is heavily dependent on the poorer point overlap and shadowing effects of the topography, causing data gaps. Additionally, at this spacing, scans are performed more obliquely to the cliff surface. In between, is the optimal zone (50-70 m for γ = 1) for efficiency (provided it meets the desired accuracy of the project) where the distance curves converge and the RMS is optimized.

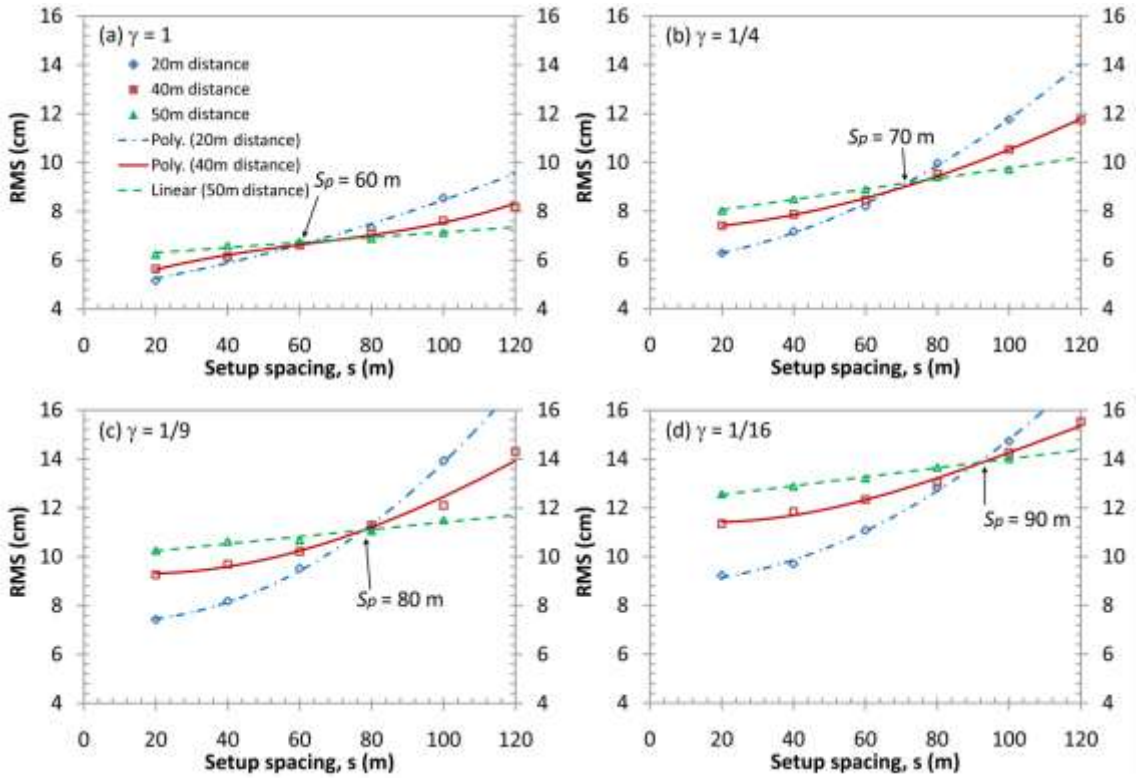

Figure 2-6. RMS uncertainty of adjacent scans at varying scan setup spacings for (a) full, (b) quarter, (c) ninth, and (d) sixteenth scanner sampling ratios (γ). Setup spacing pivot points (sp) indicate where closer distances from the cliff produce higher RMS uncertainty.

Comparing the distance curves for different sampling ratios shows that resolution is more critical at higher spacings, and lower sampling ratios increases RMS. The spacing where these curves pivot (s_p, where surveys closer to the cliff produce a higher RMS than further surveys) tends to increase with decreasing sampling ratio. The curves also become more linear with increasing distance from the cliff. Additionally, Figure 2-7 shows that at close distances, the RMS is heavily dependent on the setup spacing, whereas, at far distances, the curves converge, showing that the RMS is more a function of the sampling ratio than

scan spacing for long-distance scans. Curves for closer spacings increase at higher distances, whereas curves for higher spacings decrease with higher distances. These curves show a sharp drop off between γ = 1/16, γ = 1/9, and γ = 1/4, but less of a drop between γ = 1/4 and γ = 1. This shows that the lower sampling ratios do not adequately resolve features on the topography, which are mostly resolved for γ = 1/4 and better resolved at γ = 1. While the scanner cannot sample more than this, the flattening of the curves suggests that the highest sampling ratio sufficiently resolves the topographical features within its accuracy limits.

Sample results of the calibration experiment with various scanner spacing and distance from the cliffs with γ = 1 are shown in Figure 2-8. Figure 2-8A shows scans spaced at 80 m with a distance of 20 m from the cliff. The scans show high point density on the cliff; however, they have several large shadow zones, including at the cliff top, as a consequence of being too close to the cliff. Figure 2-8B shows scans at the same spacing (80 m) but at a distance of 40 m from the cliff. Note there is less shadowing at a 40 m distance but also a lower point density. Figure 2-8C shows scans at the same spacing (80 m) that are 50 m from the cliff, showing less point density than the 40 m curves. Figure 2-8D illustrates scanning near the optimal spacing of 60 m with a distance of 40 m from the cliff where shadowing problems are eliminated and a sufficient point separation is maintained.

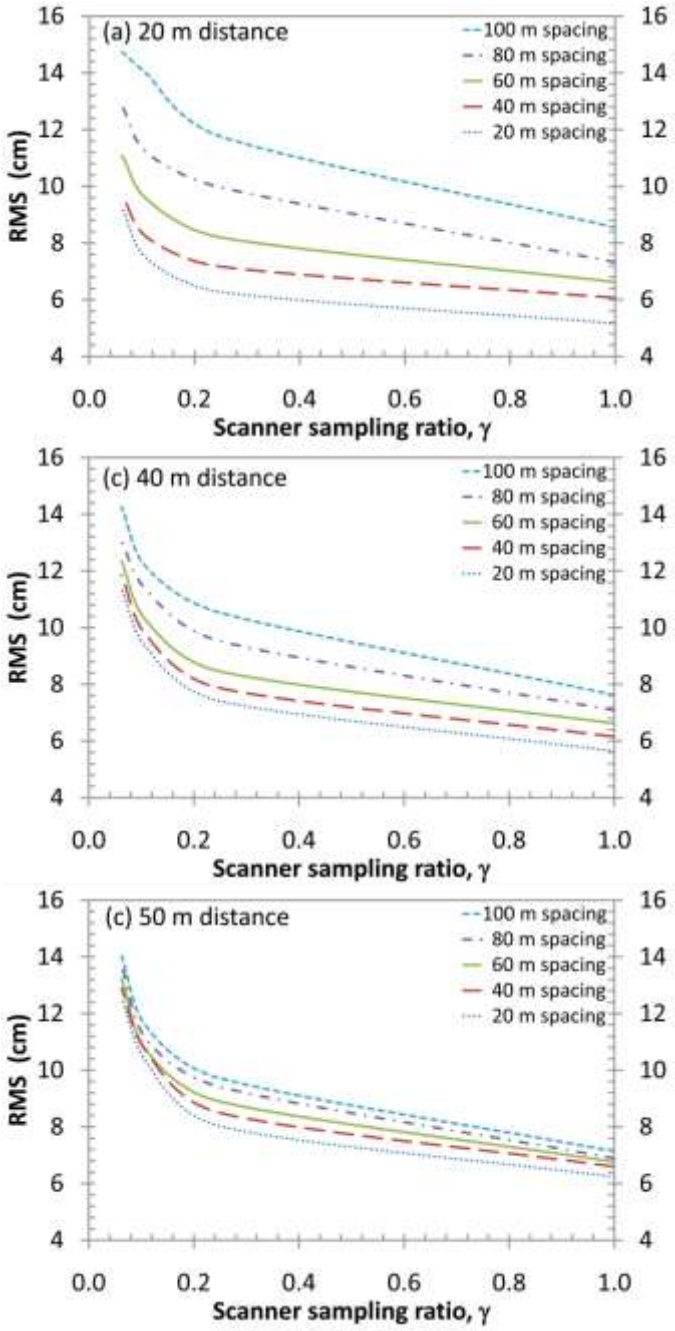

Figure 2-7. Influence of scan sampling ratio (γ) on alignment RMS uncertainty at (a) 20m, (b) 40 m, and (c) 50 m distance (d) from the target during the calibration surveys.

Figure 2-8. Aligned point clouds (γ=1) for scans spaced at (A) 80 m at a 20 m distance, (B) 80 m at a 40 m distance, (C) 80 m at a 40 m distance, and (D) 60 m at a 40 m distance. Note the missing cliff top and several occlusions on the cliff in (A), that points appear less bright because of decreased point density at the farther distance in (C), and the optimal coverage of the cliff in (D).

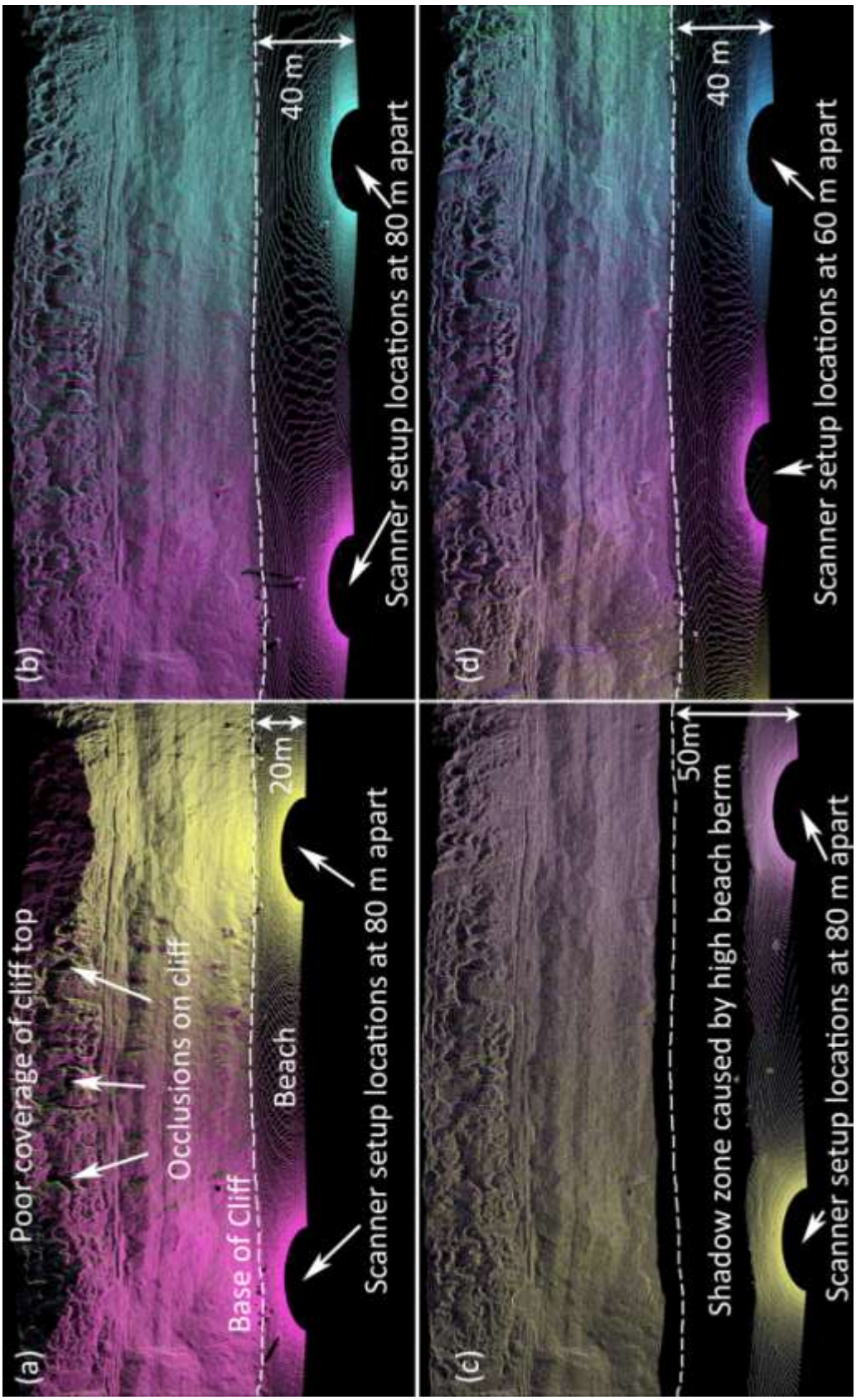
(a)
Poor coverage of cliff top
Occlusions on cliff
Base of Cliff
Beach
20m
Scanner setup locations at 80 m apart
(b)
40 m
Scanner setup locations at 80 m apart
(c)
50m
Shadow zone caused by high beach berm
Scanner setup locations at 80 m apart
(d)
40 m
Scanner setup locations at 60 m apart

When working in a dynamic coastal setting, the survey team often has minimal flexibility in determining the scanning distance from the cliff because of tide cycles and resulting limited beach width. Thus, a closer spacing is required when the tide forces scanning to be performed closer to the seacliffs. Fortunately, the distance from the cliff (within 20-50 m) appears to have the largest increase in RMS at large scan spacings, so if the survey team works within the optimal zone, the data quality should not be compromised. As shown in Figure 2-6, for this particular scanner, the optimal spacing for the highest sampling ratio would be from 50-70 m to limit the RMS to below 7.2 cm (5 cm error from the scanner and 2.2 cm error from the RTK GPS). Above this, the RMS tends to steepen rapidly with increased spacing. Scans should be performed about 30-40 m from the cliff, if possible, to allow the scan window to capture the cliff top (up to 70m) and minimize topographic shadowing from being too close to the cliff.

While the optimal range of parameters for scanning for a location is illustrated by the calibration survey, there are times when a different spacing should be employed. Areas of complex topography such as sea caves will require closer spaced scans at different angles to capture occluded features. Also, care should also be taken to scan with a tighter spacing around acute angle corners where the scanning direction switches considerably to ensure sufficient overlap for alignment of the point cloud datasets. Finally, if increased morphological resolution is desired, the scanning should be performed closer to

the cliff and at closer intervals. However, this will increase the time cost associated with scanning.

Further, to use the calibration scans to assess the repeatability between surveys, two sets of four scans of the same section were aligned separately with the near-optimal scanning parameters (γ = 1, *d* = 40 m, *s* = 60 m) to simulate two independent surveys. The RMS difference between these two datasets was 6.2 cm, which agrees with the RMS the calibration curves. This shows that the survey method not only reduces alignment uncertainty between neighboring scans but between surveys, as well.

Results of repeat large-scale field surveys

Table 2-4 shows the results of the RMS uncertainty between neighboring scans calculated from the alignment of several regional seacliff studies. The overall average RMS uncertainty of 7.9 cm approaches the limitations of the equipment for field conditions (7.2 cm). Figure 2-9 shows a comparison RMS uncertainty of the individual scans from the field datasets to the calibration curves. Data from the Torrey Pines section where the calibration survey was performed are shown as plus marks; whereas all field data from the entire study area are shown as grey circles. The field data shows the same general trends as the calibration data, however, the RMS values are higher and show much more spread. While the trendline for the Torrey Pines field data is slightly higher than the calibration curves, there is a larger difference when compared to the entire survey region showing that there are morphological effects that contribute to the

RMS uncertainty in other sections. The topography can have very complex features, which increases error from shadowing and less consistency between datasets for alignment.

Table 2-4. Survey dataset properties and RMS uncertainty between adjacent scans (March 2007- May 2008)

Segment	*Survey Date*	*Length (km)*	*# Scans*	*Average Scan Spacing (m)*	*# Points (Millions)*	*RMS (cm)*			
						Ave.	*Max*	*Min*	*Std Dev*
Encinitas	May-08	4.3	67	64	19.004	8.6	12.3	6.4	1.3
	Oct-07	4.9	89	55	22.374	8.6	13.8	5.6	1.7
Solana Beach	Feb-08	2.9	66	44	17.948	8.2	10.0	5.4	1.0
	Mar-07	2.9	117	25	38.635	6.9	10.4	4.0	1.2
Del Mar	Apr-08	2.6	39	67	12.273	8.8	12.6	6.1	1.8
	Jan-08	2.8	46	61	7.645	8.3	13.6	5.7	2.0
	Aug-07	2.5	60	42	14.965	7.3	10.4	4.9	1.5
	Mar-07	2.5	66	38	16.321	7.8	12.3	4.8	1.8
Torrey Pines	Apr-08	1.8	47	38	17.662	7.1	9.8	4.6	1.1
	Mar-08	1.8	42	43	13.364	7.3	11.4	5.9	0.9
	Sep-07	1.7	79	22	33.515	6.4	8.7	4.7	1.0
	Apr-07	1.5	36	42	13.428	6.6	10.6	4.6	1.4
Black's Beach	Feb-08	4.4	81	54	19.346	9.7	13.5	6.0	1.6
	May-07	3.3	54	61	13.500	8.8	12.7	5.5	2.2
Scripps	Mar-08	0.6	14	43	4.530	7.5	9.2	6.3	0.9
	Sep-07	0.6	12	50	5.441	7.7	9.0	6.0	1.2
	May-07	0.4	11	36	4.420	7.5	8.8	6.2	0.9
Totals	**-**	**41.5**	**926**	**-**	**274**	**-**	**-**	**-**	**-**
Overall	**-**	**-**	**-**	**45**	**-**	**7.9**	**13.8**	**4.0**	**1.4**

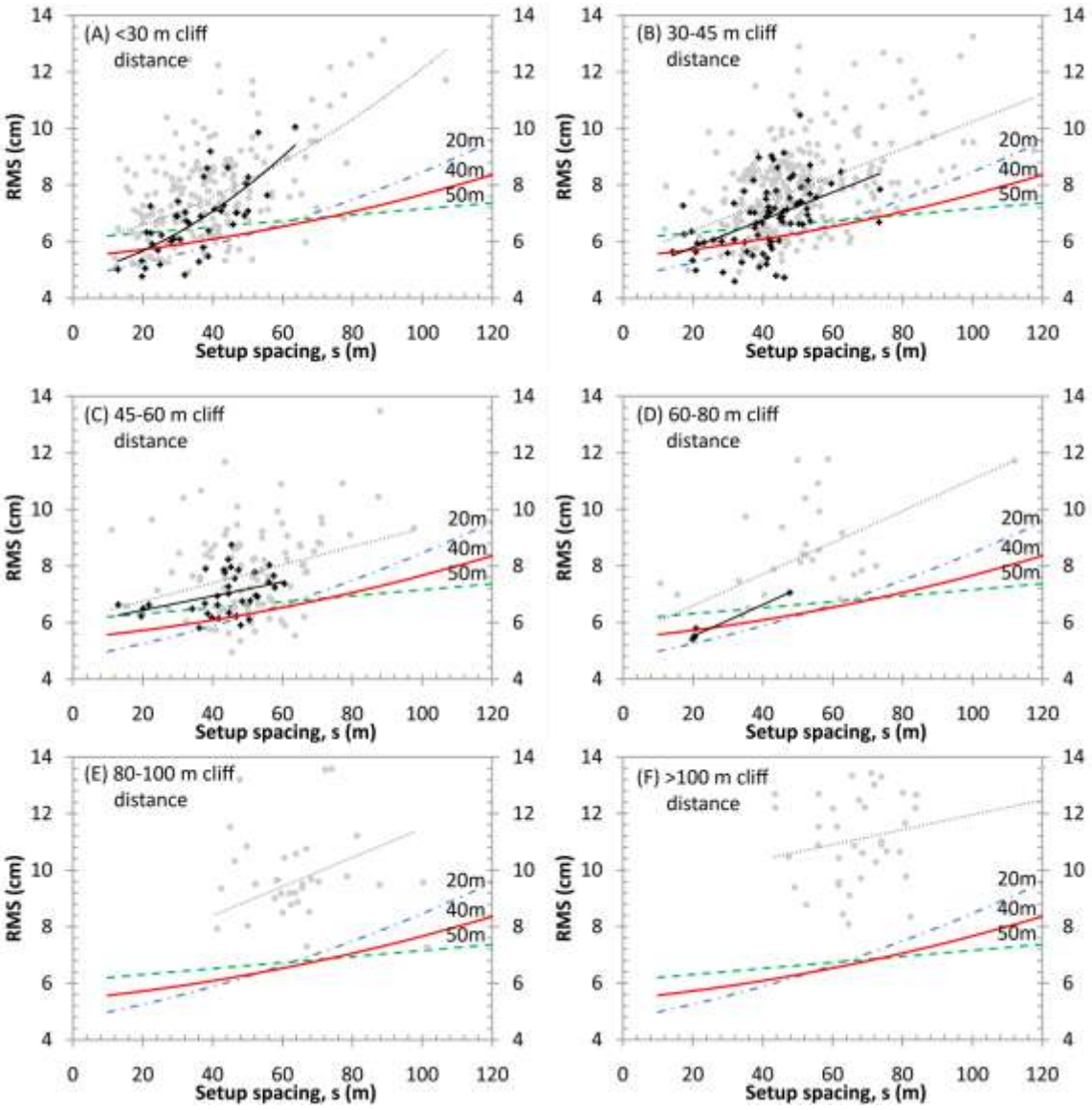

Figure 2-9. Comparison of RMS uncertainty for field surveys performed at varying distances with results of calibration surveys at 20, 40 and 50 m distances at full resolution (γ=1). Black sample points represents scans performed in the same section (Torrey Pines) as the calibration survey with best fit lines shown as dark lines. Grey sample points represent data from the entire study area, with best fit lines shown as grey dotted lines.

There are several other reasons why these RMS difference values are higher than results from the calibration survey. First, some of these surveys include areas of heavy vegetation, which can move during scans. Also, points can be collected on varying parts of the vegetation, making correspondence between scans difficult. Where possible, these points were eliminated from the dataset, however, this also reduces the number of points available for the alignment process. The maximum RMS values in Table 2-4 occur from scans in these vegetated areas; 10% of the field scans have an RMS larger than 10 cm with their neighboring scans, and 68% of those were in areas of dense vegetation covering the majority of the cliff face, so less data were available for alignment. Second, some areas required scanning far from the cliff to obtain data on the entire cliff face (Figure 2-9e and f), which results in a lower point density. 28% of the scans with an RMS greater than 10 cm were in areas of tall cliffs (> 100 m), so they were performed at a far distance from the cliff for complete coverage, which resulted in a lower point density. Third, the calibration surveys were carefully controlled and the scan spacings were measured, which was not done during the field surveys where scan spacing is often estimated during scanning. Fourth, there is always some possible equipment error such as high interference for the RTK GPS readings or atmospheric conditions affecting the laser time measurements. Finally, the scanner platform can settle slightly as the scan is being performed in the wet, loose sand.

Verification of field data

The field data was verified through the procedures discussed in the approach section. By comparing scans to RTK GPS surveys performed on “fixed” structures, the RTK GPS points were found generally to be within 10 cm of the scan points for those structures. Because of a typical point separation of 10 cm on the structures, their equivalent location in the point cloud could not be better resolved. Thus, using control points for scan alignment, as has been done for seacliff erosion studies, would not be advisable without a larger point density. However, using the RTK GPS points as a check to ensure there was not any large global propagation of misalignments proved effective. Examination of cross-sections throughout the entire span of each dataset showed much less than 10 cm error between adjacent scans (typically undetectable), except in approximately 10% of the field scans where the RMS was slightly larger than 10 cm, and occurred in areas of heavy vegetation or areas with extremely tall cliffs forcing the survey team to scan far from the target.

The repeatability was verified by comparing the results of points representing structures from the four surveys of the Del Mar section. The results shown in Table 2-5 show that the RMS between surveys is very similar to the RMS between adjacent scans during a survey so that comparison analysis can be performed without alignment biases between surveys.

Table 2-5. Comparison of RMS (cm) of static (fixed) structures in Del Mar between four different surveys to show the repeatability of the survey method. Note that the Aug-07 survey appears to have a ~1.5 cm bias when compared to other scans.

Jan-08	7.2	-	8.5
Aug-07	8.6	8.5	-
Mar-07	7.0	6.7	8.4
Survey Date	**Apr-08**	**Jan-08**	**Aug-07**

Evaluating the Efficiency of the Survey Methods

To compare the efficiency of the survey methods to target based approaches, a theoretical evaluation (Figure 2-10) was performed based on the speed and characteristics of the I-Site 4400 scanner used for the project assuming it were capable of performing scans at any resolution. At high sampling ratios, the scan time is governed by the maximum speed at which the laser can fire (4400 points per second). At low sampling ratios, the scan time is governed by setup time. For the method proposed in this chapter, approximately 4 minutes is required to move the scanner, roughly level it at the new site, perform the backsight and preview for the level compensator and start the scan. For target based registration using a Leica ScanStation 2 scanner requires at least 15 minutes per scan setup. Thus, as shown in Figure 2-11, that increase in setup time dramatically influences the amount of terrain that can be covered in the scans.

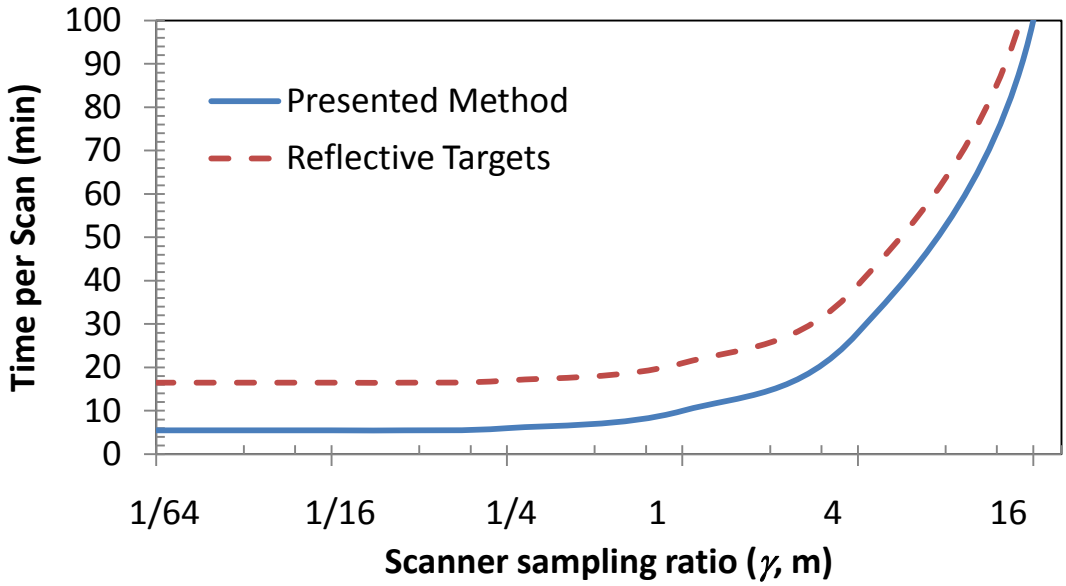

Figure 2-10. Estimated time to complete a scan with method described in chapter (solid line) and using reflective targets (dashed line) assuming a scan rate of 4400 points per second

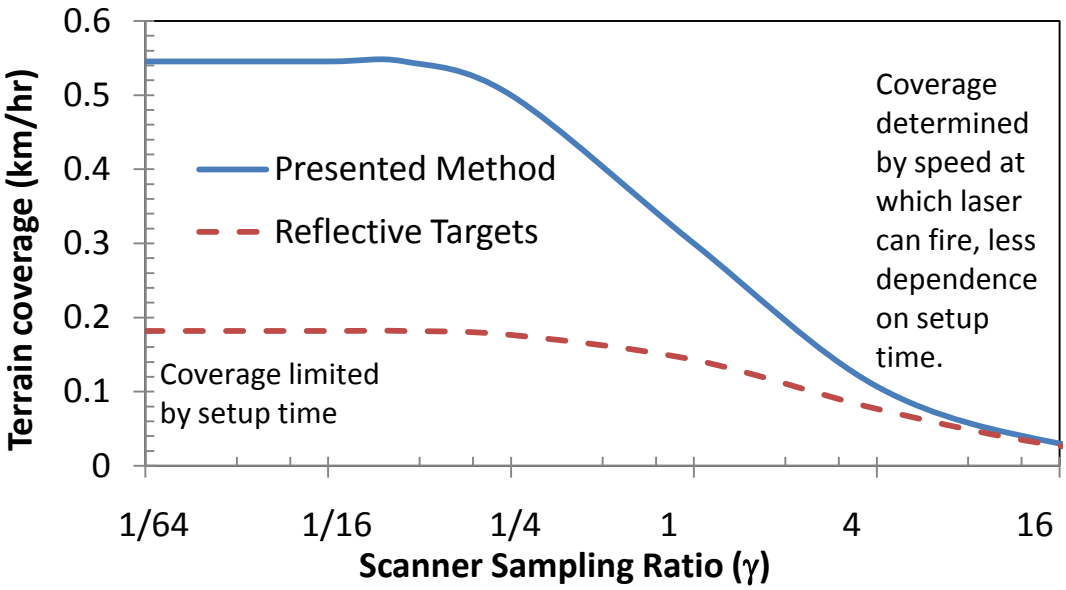

Figure 2-11. Estimated rate of terrain coverage using the survey method described in this chapter (solid line) and using a target registration method assuming a scan spacing of 50 m and the scan rate of 4400 points per second.

CONCLUSIONS

By using consistent methods which minimize data alignment processing to perform field work, regional TLS surveys can be efficiently georeferenced for comparative studies and mapping. The methods outlined in this chapter show how to perform TLS for large, dynamic sections and how to ensure the data are accurately georeferenced both between adjacent scans in a survey and between surveys without requiring time-intensive control surveys, which may not be possible in such environments. Accurately georeferenced data are essential to compare time series data sets to observe real change as opposed to apparent change from misaligned data. Data acquired with such techniques provide a reliable baseline for subsequent erosion monitoring and analyses.

Furthermore, understanding the influence of scan setup spacing (s), cliff distance, (d), and sampling ratio (γ) on alignment RMS through calibration surveys ensures that quality data are collected consistently and efficiently so that features are adequately resolved in the data. Additionally, it provides a simple test to assess the repeatability between surveys. The optimal parameters presented in this study are a function of seacliff morphology and the type of scanner used; thus, it is recommended that researchers implement these calibration methods on test sections of their study areas to determine the optimal parameters based on their equipment and the seacliff morphology. While trends will be similar, the scanner characteristics and seacliff morphology will produce different RMS values than those presented herein. Fortunately, the described

calibration survey is simple to implement and can be performed quickly. Because of additional factors and complexities possible in typical field scanning, the optimal parameters should be used as an upper limit for spacing, *s*, and distance, *d*, and a lower limit for the scanner sampling ratio, γ, to ensure adequate field data collection.

ACKNOWLEDGEMENTS

This research was funded via a grant from California Seagrant (Project #R/OE-39) and the Coastal Environmental Quality Initiative (CEQI) under award #04-T-CEQI-06-0046. Pat Rentz and Jessica Raymond of Scripps Institution of Oceanography assisted in the TLS surveys. Scott Schiele and John Dolan from I-Site provided technical assistance for this work. Travis Thompson of CALVRS assisted in using the CALVRS network. I would also like to thank the reviewers and editorial staff whose valuable comments and insight enhanced this chapter.

Chapter 2, in part, is a reprint of the material as it will appear in the Journal of Surveying Engineering, 2009. Olsen, M.J., Johnstone, E., Driscoll, N., Ashford, S.A., and Kuester, F. ASCE, 2009. The dissertation author was the primary investigator and author of this paper.

CHAPTER 3. AUTOMATED, CONSTRAINED POINT-CLOUD ALIGNMENT MINIMIZING WARPING EFFECTS IN MAPPING LONG CLIFF SECTIONS

OVERVIEW

This chapter presents new techniques and a corresponding open source application to automate 3D point cloud alignment for large-scale datasets collected in dynamic environments where typical controls used for scanning objects or localized sites cannot be efficiently employed. To produce georeferenced datasets comparable between surveys, parameters such as origin coordinates and leveling information must be incorporated as constraints in the point cloud alignment process for each scan to avoid propagation of misalignments from warping. These warping effects occur when performing long-range scans on nearly linear surfaces because the laser pulse reflects obliquely at the edges of the scan and more orthogonal at the center, and are quantified herein. Unfortunately, existing global alignment algorithms do not apply the appropriate constraints and thus are subject to these warping effects unless 360^{o} coverage completely surrounding the object is obtained. Such coverage is not feasible for scanning long, linear segments, such as seacliffs. Further, existing methods require substantial user interaction to produce accurate alignments, which is now reduced through an automated algorithm which can efficiently determine neighboring scans. This new method seeks to simultaneously minimize error between adjacent scans in a survey, minimize error between surveys, and provide data georeferenced to real world coordinate systems. Comparison of the application of the new methods with the existing methods to seacliff erosion studies in Southern California are presented to

highlight the necessity of constraints and the efficiency of this automated method to produce georeferenced, topographical datasets that are comparable for change analysis.

INTRODUCTION

Terrestrial laser scanners (TLS) have been proven to be an efficient tool for topographical surveying such as localized seacliff erosion studies (Collins and Sitar 2004; Lim et al. 2005; Rosser et al. 2005; Collins et al. 2007; Young and Ashford 2007). Lim et al. (2005) and Rosser et al. (2005) used external direct georeferencing methods to perform the scan alignment for localized site studies. Collins et al. (2005; 2007) used reflective target registration. Young and Ashford (2007) used structures such as houses and seawalls as common alignment tie points between surveys. These previous techniques can be difficult to implement in a dynamic coastal environment where survey work can only be completed during small time windows of low tide, and thus, they severely limit data coverage. While, aerial LIght Detection and Ranging (LIDAR) is commonly used for topographical analysis, it tends to have poor coverage on vertical faces and misses complex topography such as caves which are important to seacliff studies.

For this seacliff erosion project, multiple time-series surveys consisting of multiple scans are performed to quantify seacliff erosion for a 20 km segment of coastline. Figure 3-1 shows an example of multiple TLS scans merged for a

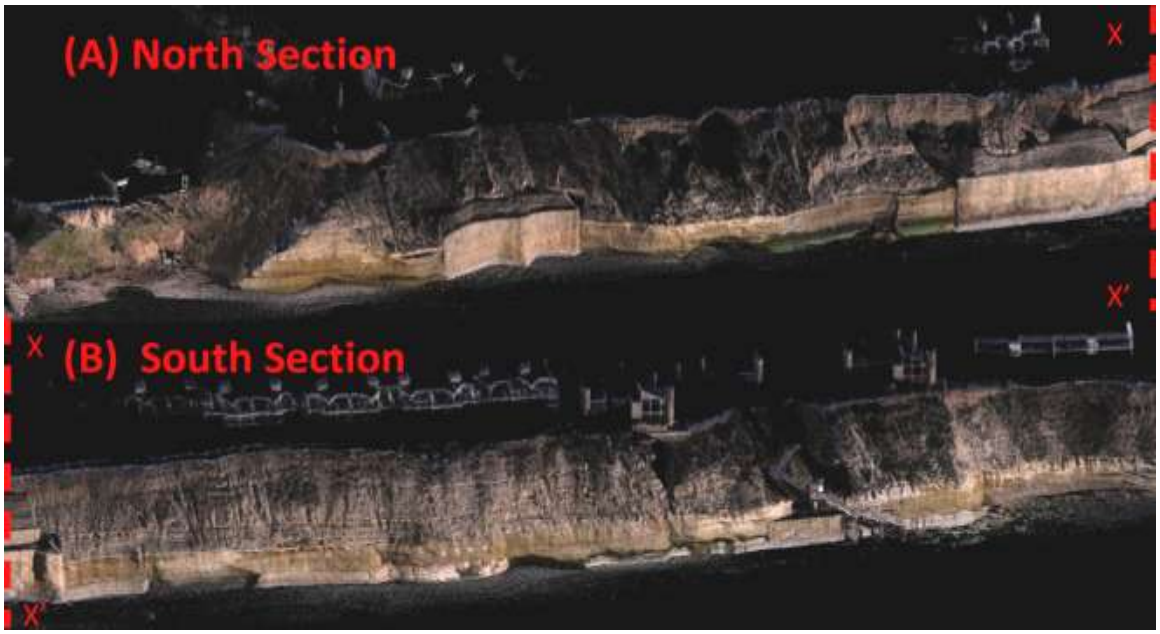

Figure 3-1. Aligned and merged point cloud dataset. Note the figure is split into (A) North Section and (B) South Section with match line X-X' (Solana Beach, CA, February 2008)

survey of Solana Beach, CA and aligned using the techniques described in this chapter. Figure 3-2 shows an example of the need for multiple scans to be merged to complete a survey because of occlusions occurring in each scan. For accurate change comparison, each survey must be an independent measure and not reliant on a past survey for alignment, otherwise uniform change would be considered error. Additionally, to ensure compatibility with other datasets such as aerial LIDAR, photogrammetry, etc., the datasets need to be georeferenced into a real world coordinate system. While previous work focuses on co-registration of scans in a survey or co-registering different surveys, this new approach seeks to expand the contributions of previous work by providing an algorithm that does all of the following to ensure accurate change assessment:

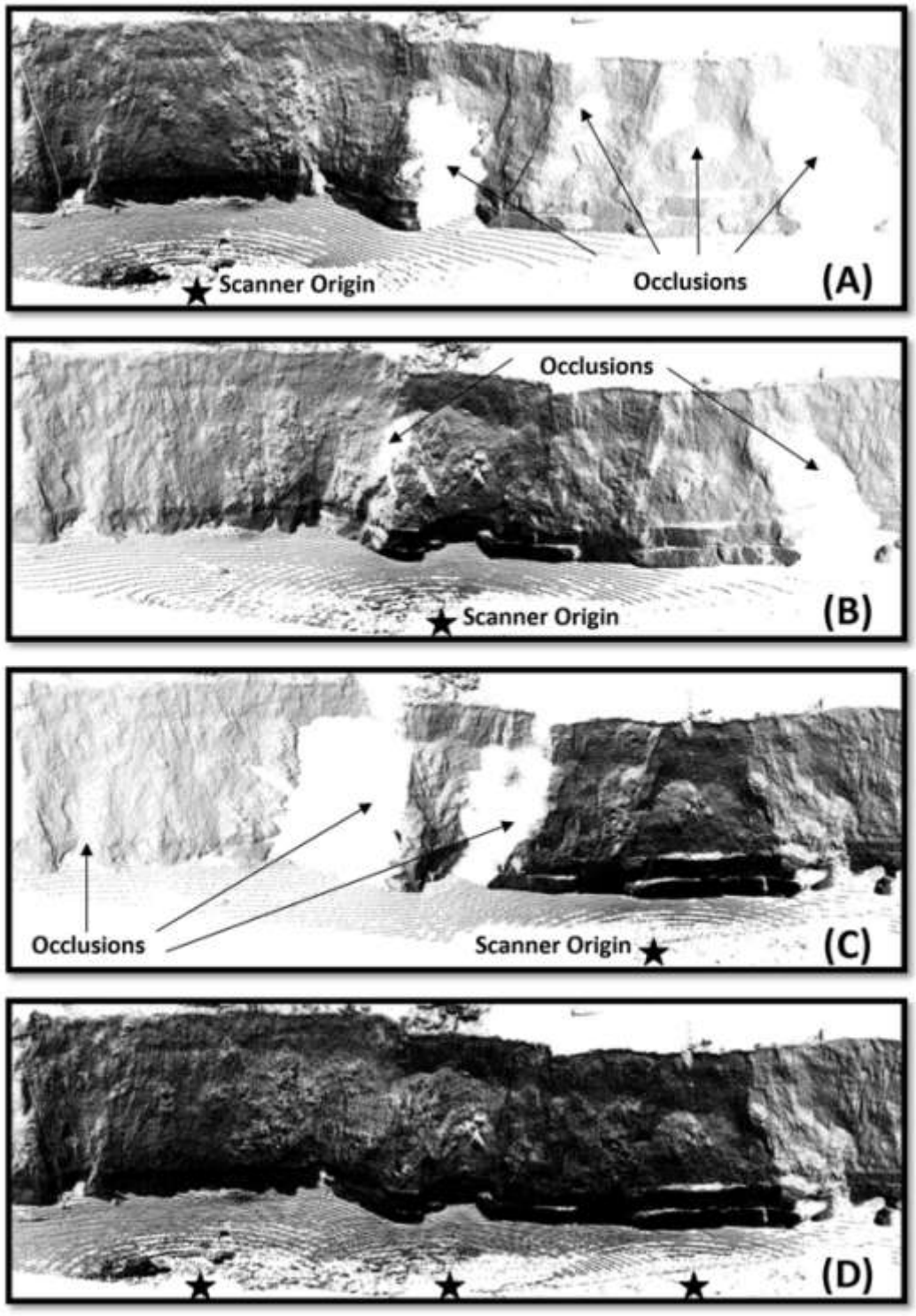

Figure 3-2. Occlusions requiring multiple setups (A) left scan, (B) center scan, (C) right scan, and (D) combined to minimize occlusions

1. Increase scan alignment accuracy by using constraints to prevent warping,
2. Automate the alignment procedure to decrease user-interaction time,
3. Decrease error between adjacent scans in a single survey,
4. Decrease error between multiple time-series surveys,
5. Provide independent time-series surveys (i.e., one survey is not dependent on another for alignment), and
6. Simultaneously georeference the data to a real world coordinate system.

By developing such a methodology, datasets are immediately compatible and comparable to analyze change such as cliff failure volumes. Figure 3-3 shows an example of surface change analysis before and after a failure using data aligned using *PointReg.* For adequate change surveys such as Figure 3-3, each survey must be independent so that near uniform retreat at a site can be accounted for. Such change analysis will provide key insights into many geologic processes occurring on the coastline.

TLS background

TLS scanners use LIDAR (LIght Detection And Ranging) that employs laser pulses to rapidly model objects. Topographic coordinates are determined from either a measurement of the phase shift in a modulated laser pulse or the time of

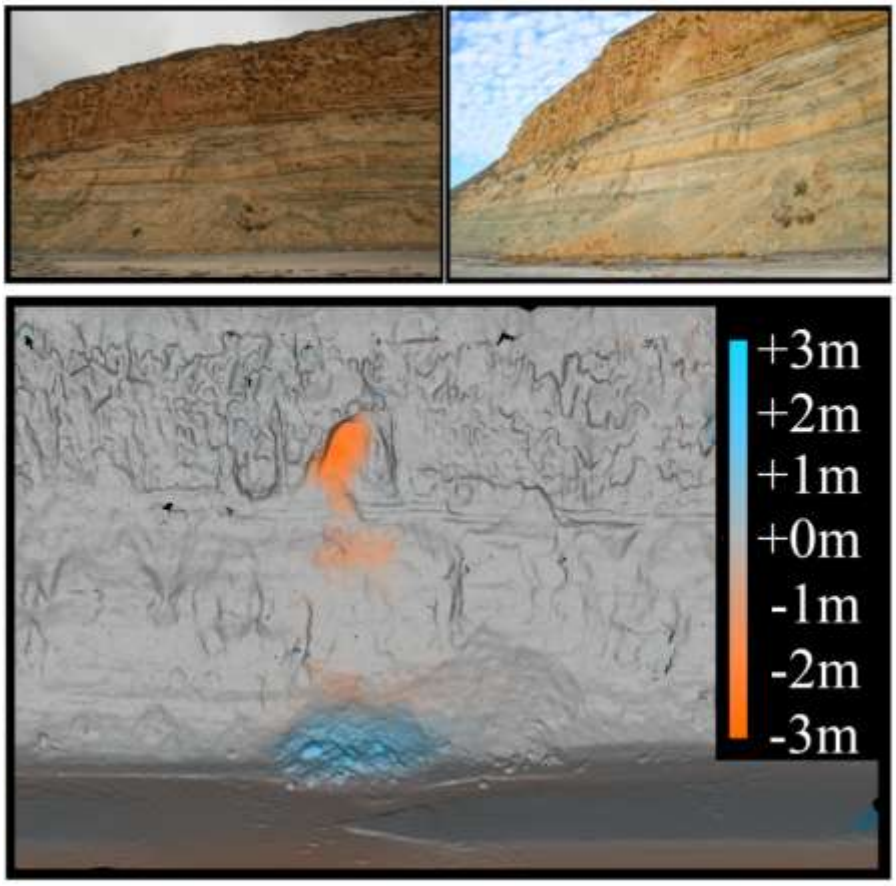

Figure 3-3. Example of a failure volumetric and surface change analysis using TLS data aligned using *PointReg*. Failure site at Torrey Pines State Reserve, CA (a) before failure October 14, 2007, (b) after failure October 29, 2007, with (c) failure analysis highlighting area of failure.

flight (the travel time) of the laser pulse and the pulse's return angle. This information is returned as a point cloud dataset of *X,Y,Z* coordinates relative to the scanner origin (typically defined as 0,0,0). Because of line-of sight requirements, the target topology for a section of complex topography (Figure 3-1) cannot be collected using TLS from a single scan location or in one continuous sweep. For example, effects such as shadowing or occlusions

(Figure 3-2) from objects blocking other objects lead to data gaps, which are filled in with additional scans. The inability to have a continuous data stream increases the complexity in gathering and processing data as it requires an algorithm to register point clouds from adjacent scans for alignment. Additionally, for surveys to be comparable for change analysis, the scans must be georeferenced to a common, real-world coordinate system.

Point Cloud Alignment Background

Various point cloud and surface registration alignment methods exist and some of the most common methods are discussed below, including Iterative Closest Point (ICP), 3D surface, minimal perturbation, and target. Some methods rely on a fixed reference scan to align the other scans or fixing the scans as they are aligned. Other methods align scans in a pair-wise approach by finding the optimal alignment of a scan with one of its neighbors. These pair-wise alignments can be improved by global optimizations. Several of these methods were developed for manufacturing, reverse engineering, or local site alignments, as opposed to being developed for quantitative morphological surveys in a dynamic coastal environment, which necessitates a different approach. In addition, most processing tools are either private processing algorithms or are available as part of expensive commercial packages, thus limiting use.

The ICP method developed by Besl and McKay (1992) selects random points in one scan and finds a “matching point” for each point in a second scan

and evaluates the residuals. The “matching points” are the closest points found in the second scan respective to points in the first scan. The optimal alignment is determined by the translation and rotation of one scan to fit the other scan that produces the lowest Root Mean Square (RMS) error value between the scans. An inherent disadvantage to this method is caused by the scanning procedure where the point field distribution in each scan is different so exact matching points are not captured in adjacent scans. Bernardini and Rushmeier (2002) provide a detailed discussion of several methods developed to improve the ICP method and its application to scanning objects. Zhang et al. (1994) introduce parameters such as a distance threshold to reduce inconsistent point pair matching.

3D least squares surface registration methods (Gruen and Akca, 2004; Chen and Medoni, 1992) have been developed to provide a better fit than the traditional ICP methods. Later, these methods were generalized to allow for multiple registrations (Akca and Gruen, 2007) that provide excellent results by averaging the alignment error between adjacent scans. These methods, however, require the triangulation of the point clouds for the creation of a surface mesh prior to the alignment. Creating a satisfactory surface mesh can be a time consuming process for an unstructured 3D point cloud, especially when modeling complex topography with large shadow zones.

While not developed for TLS, Miller et al. (2008) present a method to match DEM surfaces derived from aerial LIDAR and photogrammetry for coastal

change assessment. By using a robust surface matching technique, which removes outliers resulting from change, error can be reduced between two DEMs for comparison. While this method could be adopted to align two TLS surveys, it would still require a method to align the scans in each survey before the surveys can be co-registered.

Aman (2004) developed a minimum perturbation method for scans that have no favorable starting positions and a singular value decomposition is used to find the optimal translations and rotations between datasets based on an estimated global geometric shape. This method was developed for localized objects to bring one scan into the coordinate system of another fixed reference scan rather than translating and rotating all scans into a real world coordinate system. This method works well for objects where a rough geometric shape can approximate the data, as opposed to complex topography found in coastal environments.

To reduce the error created from the single neighbor or pair-wise alignment of scans described above, Pulli (1999) developed a global optimization technique, which can reduce some of the alignment error for the global model by relating a scan to multiple neighboring scans. The user performs ICP pair-wise alignments for all overlapping scans. The global alignment then uses this information to minimize errors between inconsistencies in pair-wise alignments. The methods described in Pulli (1999) and Ikemoto et al. (2003) were designed and work efficiently for features scanned continuously surrounding the target

object, such as a statue. Therefore, they are limited in application to regional seacliff topography because complete 360^{o} coverage surrounding the seacliffs is not feasible. When scans are performed on a regional scale, very few scans have actual correspondence with one another because of they are spaced far apart (typically 50m), reducing the effectiveness of a global optimization. Furthermore, high computational complexity for global optimization becomes an issue for extensive scans covering several kilometers, because information from all datasets has to be considered concurrently. In addition, global optimization requires the initial scan to be initially fixed into place, otherwise, when attempting to align scans continuously around an object, it would continue in an infinite loop as adjustments propagate. The algorithm does not present nor allow for application of all necessary constraints because the global optimization requires the flexibility to move the scans to perform the optimization.

An example of an existing software packages which readily implement these algorithms is SCANALYZE (2002), which incorporates the ICP and point to plane pair-wise matching followed by a global optimization (Pulli, 1999) and has been used successfully on several projects (e.g. Levoy et al., 2000) scanning objects where 360^{o} coverage was possible. However, it does not allow constraints to be defined, requires organized data structures, and works on limited formats, not easily exportable from other software packages, requiring additional conversion steps. Additionally, these alignment methods are manual and must be tediously applied on a scan by scan basis.

Target methods, similar to direct georeferencing, are very common and effective, yet time-consuming, for use with 3D laser scanning (Collins and Sitar, 2004) and are incorporated in proprietary software (e.g. Leica Geosystems, 2008; Innovemetric, 2008). Scans are generally aligned by setting up three or more common targets between scans or by placing targets over control points and using the targets to define the coordinates of the points within the scan. As discussed in Akca and Gruen (2007) these methods are time consuming in the field if targets cannot be permanently placed and thus are difficult to use over large areas. Typically each target can require 15 minutes to setup, 5 minutes to scan, and additional field help. In addition, if coordinates are not obtained for each target and a chain of targets is used to link scans together for a large area survey, alignment errors can propagate because target alignment will be reliant on other target alignments. These methods work well for point cloud alignment in localized site scans where minimal setup is required (Guarnieri, 2005), but implementation requires careful control and spacing of the targets. Schuhmacher and Bohm (2005) discuss comparisons between target based field methods, surveying control points with a Total Station, and software based alignment methods. Lichti et al. (2005) present error budget analysis for direct georeferencing.

Warping Effects in TLS

Particularly on a regional scale, slight misalignments can be detrimental and lead to extreme global misalignments over a long range. For example,

assuming scans of a linear feature are performed in the *Y* direction looking toward the *X* direction (Figure 3-4), if a leveled scan is erroneously rotated by 0.1^{o} about the X-axis by an algorithm, and each subsequent scan is then registered to that fixed scan, a misalignment of 0.2 m in the *Z* direction is introduced at 100 m from the scanner origin as a result of that single misalignment. This leads to successive misalignments that propagate through the data linked from the original scan.

In addition to warping that can occur from linking multiple scans, Scaioni (2004) presents a discussion on theoretical error for a single scan from biases from scanning at non-orthogonal angles because of spot-size variations, which explains some of the errors that occur in software alignments. To illustrate the amount of warping that occurs when scanning linear features, five repeat scans were performed from the same setup location approximately 35 m from the cliff

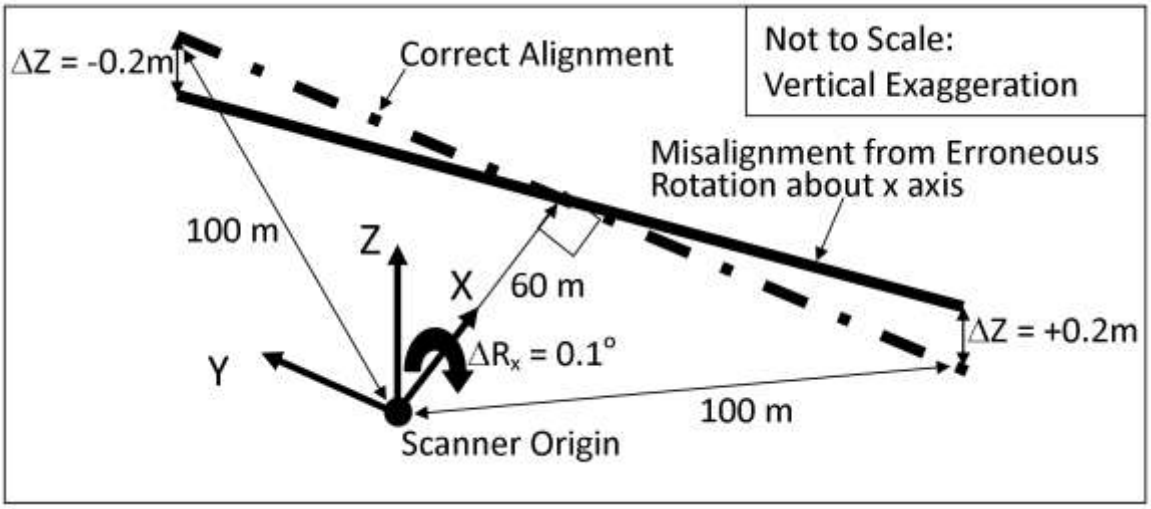

Figure 3-4. Misalignments from erroneous rotations about X or Y axis

using an I-Site 4400 laser scanner. This scanner is nominally accurate to 2 cm at 50 m under lab conditions and 5 cm for its range of 5-500 m for field conditions. Because the scanner operates on a repetitive grid format, the laser fires at the same angular increments for each scan. Thus, multiple scans at the same location can be averaged to produce a more accurate point cloud (I-Site, 2008). These repeat scans can quantify the warping that occurs at the edges of the scans of linear features, where scanning is performed at more oblique angles to the surface. The maximum deviation from the average of the scans was recorded for each grid point. Table 3-1 shows the percentage breakdown of comparable scan points and error thresholds. Points that were not on the cliff face, including points created from people or birds passing in front of the scanner, were removed prior to the analysis. Note that very few points (<2%) are above a 0.5m error threshold and 83% of the points are within 0.1 m. Figure 3-5 describes the variables used to analyze the error distribution. ψ represents the horizontal angle and ϕ represents the vertical angle at which the laser is fired for a scan point. The range or distance is represented by *r.* The horizontal angles were categorized from -80^{o} to $+80^{o}$ in 5 degree increments to statistically illustrate the warping effect.

The average error for each category with error bars representing the standard deviation of points within the category are plotted in Figure 3-6. Because the scan target surface is roughly a linear feature in the north-south

Table 3-1. Percentages of point comparisons within tolerances for repeat scans

Error (m)	Num Pts	Percent
>0.50	438	0.1
0.25-0.50	5,261	1.5
0.10-0.50	54,253	15.5
0.05-0.10	95,768	27.4
0.01-0.05	151,034	43.2
<0.01	42,821	12.2
Total	**349,575**	**100**

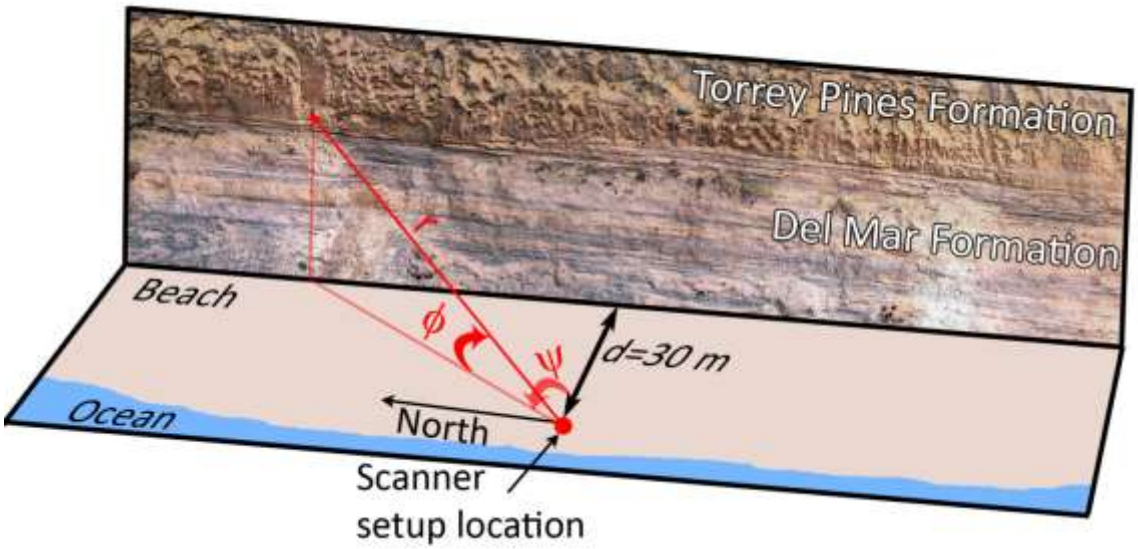

Figure 3-5. Definitions of variables used to determine warping effects that occur from scanning at oblique angles shown by repeat scans

and south of the scanner location. Figure 3-6A shows the total error increases with ψ for a linear target surface. Similarly, the standard deviation also increases dramatically with the more oblique angles, showing more uncertainty in these measurements taken at oblique angles. Figure 3-6B shows that at these oblique angles, the majority of the error results from error in the Y (northing) direction. This is because the laser spot extends in a distorted fashion along the Y axis, and thus the resulting measurement will be averaged over a larger, oblique surface area. Figure 3-6C shows that the error in the X direction is fairly consistent, regardless of ψ. This error results from the length of the laser pulse and the measurement accuracy of the scanner, rather than the angles. Figure 3-6D shows that the Z values are well resolved and actually tend to be more accurate at more oblique horizontal angles. This occurs because for small Y values, the vertical angle, ϕ, is more oblique for the upper cliff and is less oblique for larger Y values. Figure 3-6E shows the increase in average error and standard deviation with range. However, this error probably results because larger range points were scanned at more oblique angles than from the range itself. Figure 3-6F shows the increasing error as a function of vertical angle, although this is not as substantial as the influence of ψ. Additionally, note that the warping error is symmetric for the linear sea cliffs (Figure 3-6A-D), and thus the averaging method implemented in *PointReg* is effective in minimizing these warping effects.

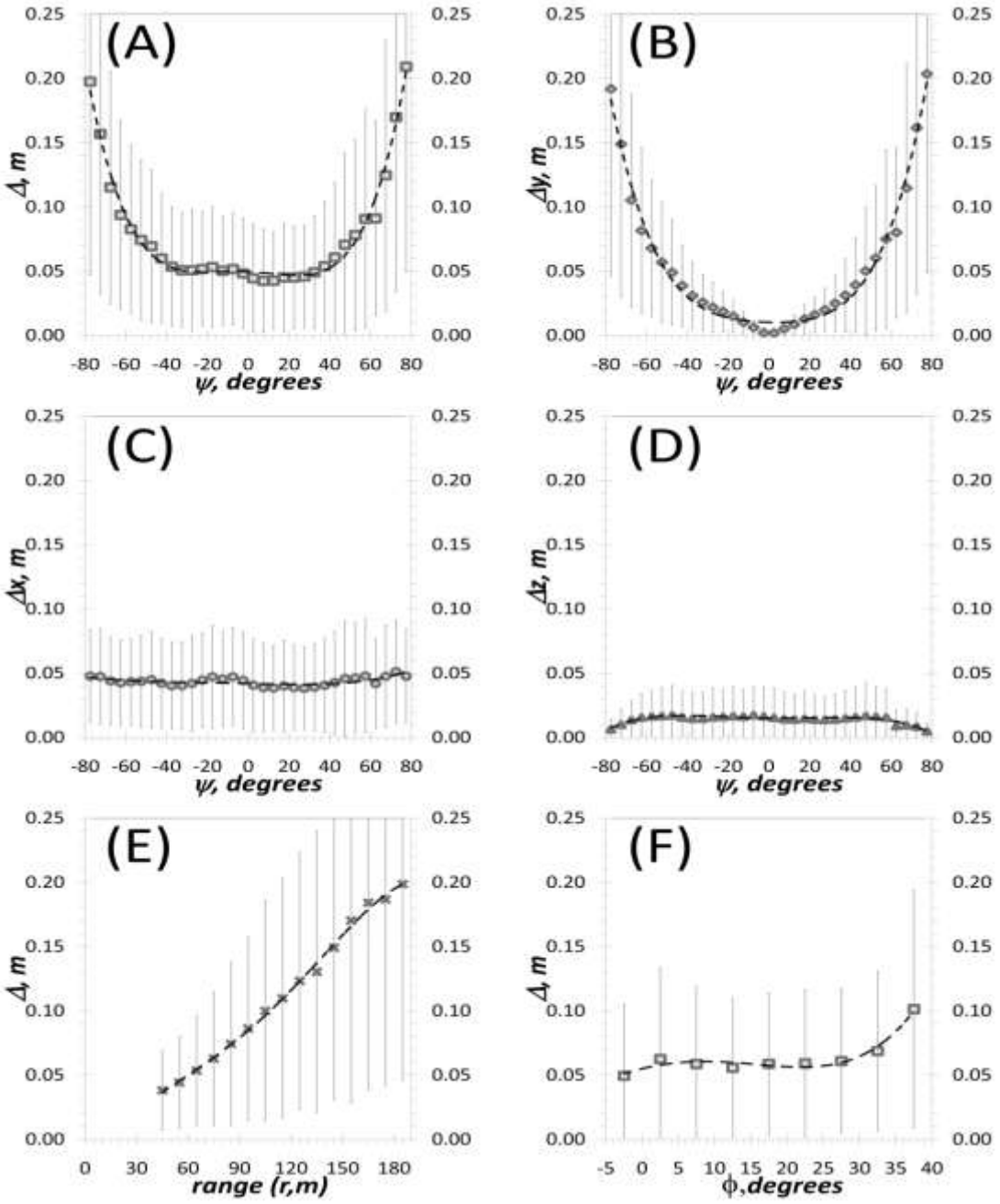

Figure 3-6. Error comparisons between repeat scans showing (A) total error, (B) error in Y direction, (C) error in X direction, (D) error in Z direction compared with horizontal angle to surface, ψ, and a comparison of error with (E) range and (F) vertical angle, ϕ. Note that at oblique angles, Δy dominates, whereas at orthogonal angles Δx dominates. Error bars represent the standard deviation of differences between scans in each bin.

Necessity of a New Hybrid Approach

As will be shown in this chapter, constraints are necessary to produce an accurate model of large-scale objects because of propagating errors that occur from warping in scans of long, nearly linear objects. This chapter presents a hybrid approach to georeference scan data by simultaneously collecting constraint information in the field with the laser scan data and then performing a constrained software alignment to minimize alignment error. To align scans in a survey, this new alignment procedure assumes point cloud information is being collected in combination with a set of base-parameters required for subsequent data processing and alignment and as such is independent of the chosen scanner platform. The needed base parameters include real world *X,Y,Z* coordinates for the scanner origin and a level/tilt compensation to constrain the data about the *X* and *Y* axes. For direct georeferencing, backsight information is required to constrain rotation about the *Z* axis. For this hybrid approach, the backsight is estimated in the field because of the difficulty in precisely marking reference points on the sandy beach. The backsight estimate is then corrected at the software level using information from neighboring scans.

An advantage of this method for coastal change surveys is that it does not rely on previous surveys to align datasets. Thus, if uniform change is observed across a site, that can be quantified and would not be minimized when co-registering two surveys. Additionally, the data are available in a real-world coordinate system so that it can be automatically integrated with other spatial

data such as photogrammetry, airborne LIDAR, etc. It is important to note the difference between co-registering two scans into a common coordinate system and simultaneously georeferencing them to a real-world coordinate system.

FIELD METHOD OVERVIEW

To optimize this approach, data collection should follow the field procedure outlined in Chapter 2, which will be briefly summarized in this section. This field method requires minimal additional field time (approximately two minutes per scan) compared to the time already required for mobilization (approximately 1.5 hours per survey day) and scanning (approximately six minutes per scan). A modest increase in field time translates into a marked reduction in processing time as well as an improved alignment between neighboring scans. Additionally, the method was developed for dynamic environments for which conventional control is difficult to implement. For example, beach levels commonly fluctuate by meters throughout the year, making control points impossible for repeat surveys. Furthermore, cliffs are near-vertical, posing a safety hazard when attempting to place reflective targets on or above the cliff.

The field method involves completely constraining five of the six degrees of freedom for data alignment in the field so the alignment is only dependent on a single degree of freedom, which is nearly constrained in the field. Translation of the data in the *X, Y*, and *Z* (up) directions is accomplished by acquiring RTK GPS (Real Time Kinematic Global Positioning Systems) coordinates accurate to 2.2

cm to represent the scanner origin. Base corrections to produce accurate RTK GPS measurements were obtained using the California Virtual Reference Station (CALVRS 2008) network. Occupying known control points or other survey methods can also be used to obtain the coordinates but requires additional setup time. When surveying in dynamic environments such as coastal environments, static control points are difficult, if not impossible, to use. Rotation of the data about the *X* and *Y* axes is constrained by using a scanner with a dual axis level/tilt compensator. The final degree of freedom, rotation about the *Z*-axis, is nearly accomplished in the field by backsighting, or targeting the scanner to a known point before scanning to calculate a bearing at which to align the data. In dynamic locations such as sandy, coastal beaches without control monuments, it can be difficult to precisely mark a backsight target, thus some rotation about the *Z*-axis is required to minimize error and improve the data fit (see Figures 3-7 and 3-8), and thus a hybrid approach estimating the backsight in the field and then correcting the estimate at the software level by using neighboring scans, discussed in the next section. The approximate backsighting can be performed in the field using a scanner with backsight capabilities or a digital compass to align the scans to an estimated reference point. Additionally, it can be estimated by manual rotations in software.

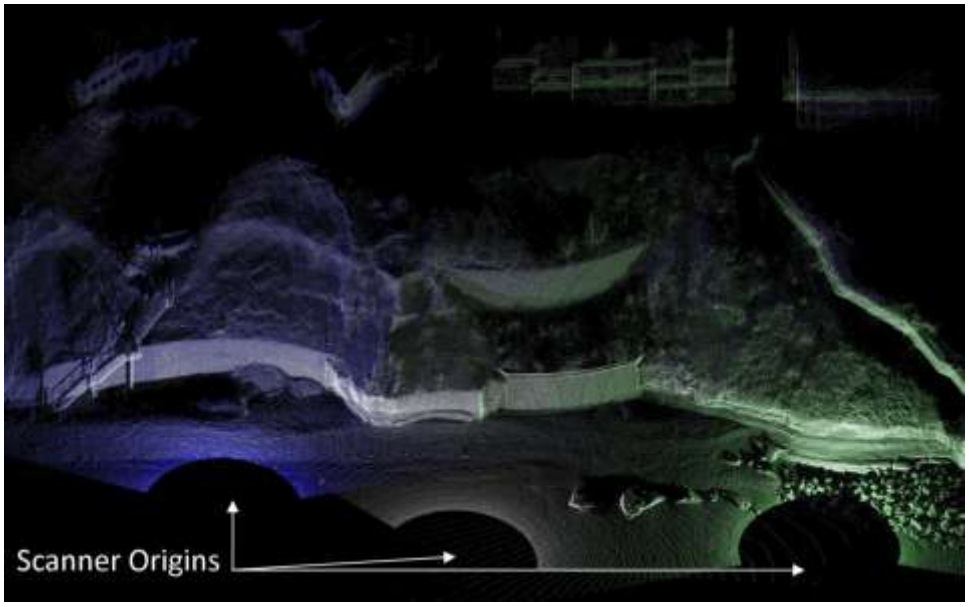

Figure 3-7. Three scans aligned using backsight registration only, obtained directly in the field. Note the apparent blurriness from the misalignment.

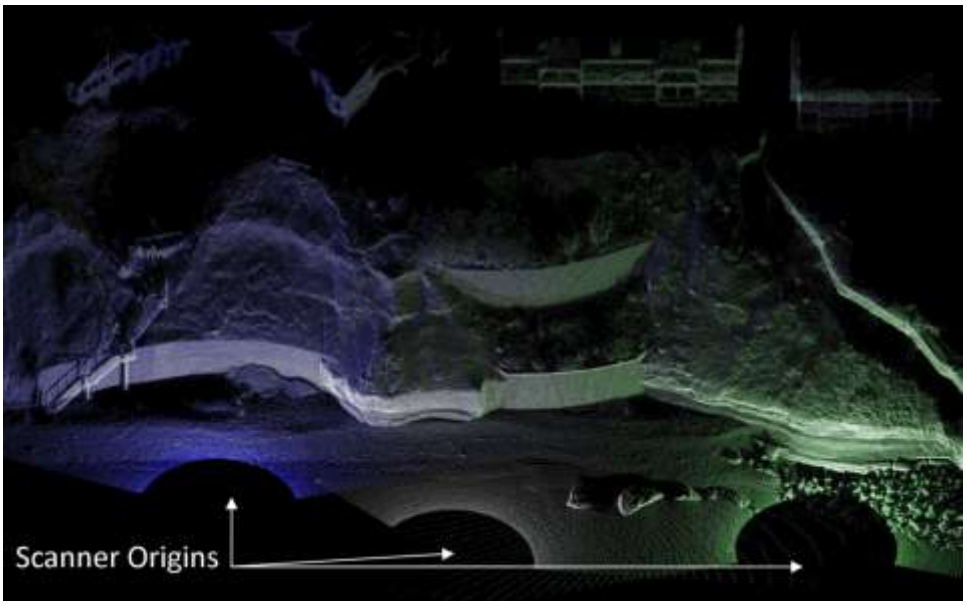

Figure 3-8. Three scans aligned using *PointReg* to reduce alignment errors. Note the increased clarity as a result of the alignment.

PROCESSING METHODS

Error Metric

Quantifying the accuracy of an alignment of two scans is difficult because both scans will not include points from the same spatial location and the actual coordinates of the points collected are unknown. However, the most likely fit can be found by evaluating the RMS of the errors, commonly used in the discussed methods. The procedure to calculate the RMS between two scans (scans A and B) for this study is illustrated in Figure 3-9 and shown in pseudocode in Figure 3-10. For a complete mathematical discussion of the algorithm, the reader is referred to Appendix A. The points of each scan are divided into cube subsets of user specified dimensions (typically 1m x 1m x 1m) similar to the boxing structure acceleration method discussed in Akca and Gruen (2005). These cube subsets organize the data to decrease computational time and ensure that points are not compared to unrelated distant points. The algorithm finds the cubes containing a sufficient number of user specified points, based on the typical scan point density of each scan. Data correlation then ensures that the registration is performed only on the areas with a large point density for two scans, enhancing accuracy. Next, a sampling of those points in the cube is selected for the comparisons between scans. This is repeated for all cubes with sufficient points to approximate the overall topography of the entire scan window.

The distance from each selected point from scan A to where that point would correlate with scan B is calculated by assuming that the point ($p_A = (x_a, y_a,$

z_a)) from scan A is coplanar with the nearest three points (p_1, p_2, p_3) from scan B in the same cube. The distance from point, p_A, to the plane formed by the points p_1, p_2, and p_3 is then computed. While this is not entirely accurate, it is generally acceptable from a practical standpoint in areas where the topography does not contain extreme complexity. This is similar to comparing the point to a surface mesh rather than a point cloud, although it only represents one triangle in the mesh and does not require the time consuming process of generating a clean and accurate mesh for each scan prior to alignment. The sum of the squares of the residuals is then used as the RMS measure.

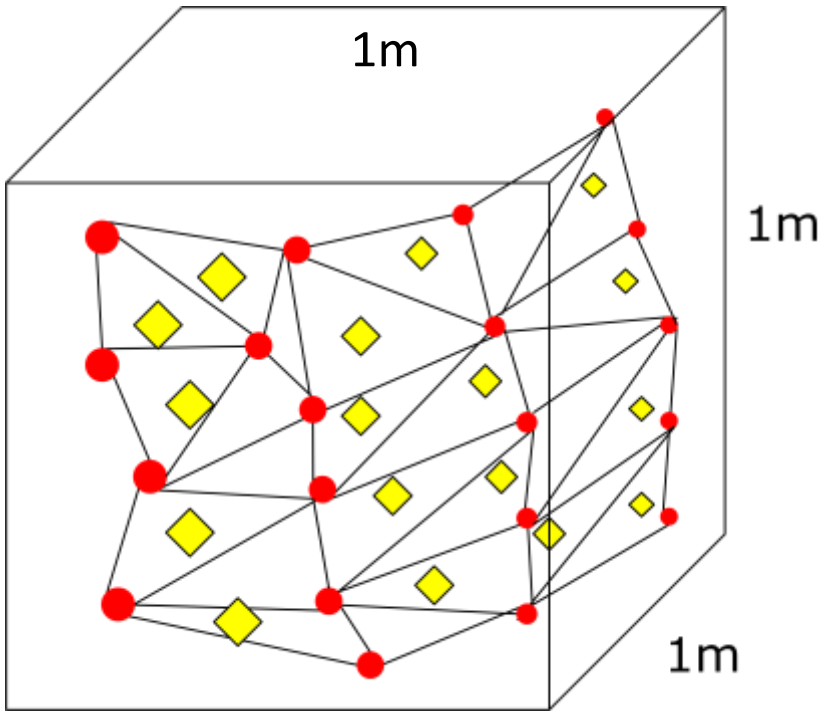

Figure 3-9. Schematic illustrating the calculation of the RMS of error between two scans

Workflow Overview

Scan alignment requires data preprocessing to ensure that the best points are used for the alignment. The *PointReg* algorithm presented in this chapter automates most procedures required for the scan alignment and thus, requires minimal user-guided pre and post processing. The workflow is presented in Figure 3-10, showing which steps are automated in boxes and which are manually applied in ellipses. Note that all of the manual techniques would be required for adequate results using any surface matching technique. Major steps of this workflow will be discussed in detail in the following sections.

Initial Alignment (Steps 1-3)

Most scanners collect data relative to the scanner origin defined as (0,0,0). To translate the data to a global coordinate system, each scan origin is translated by the X,Y,Z coordinates of the setup location, applying any corrections of the height offset from the coordinates obtained from a RTK GPS receiver centered directly above the scanner origin or from another survey technique. Registration and rough alignment of the data by backsight registration can be performed instantaneously for all scans in a survey (e.g. I-Site, 2008) by linking scans to relative scanner and backsight coordinates. If the scanner or software does not have backsighting capabilities and a digital compass is not available, then the data can be manually rotated about the *Z*-axis so it is roughly aligned within approximately 1-2^{o}. This rough alignment allows for a quick, visual

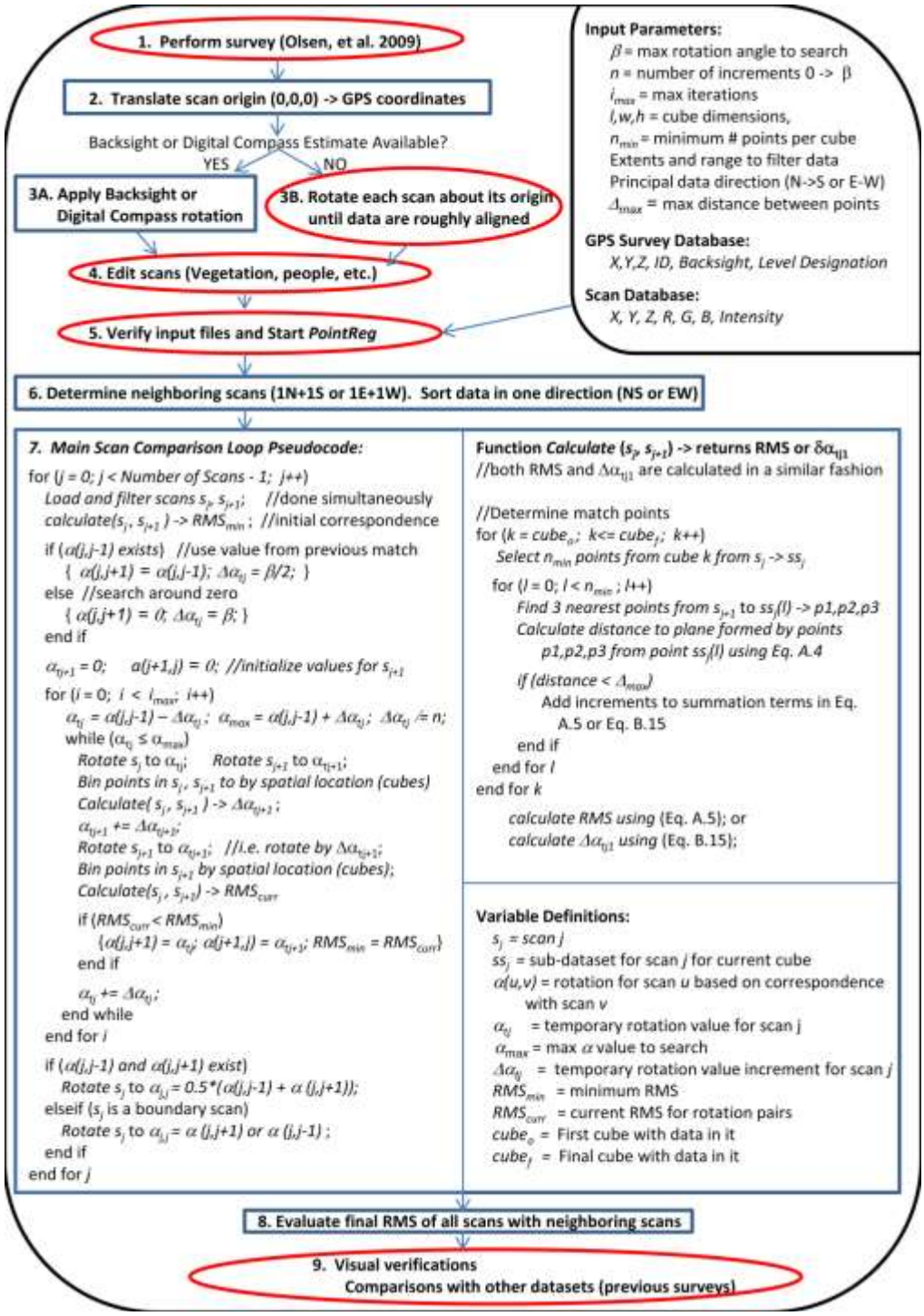

Figure 3-10. Workflow diagram and pseudocode for PointReg scan alignment. Manual processes are illustrated by ellipses while boxes represent automated processes.

inspection of the dataset to verify that no major errors were incorporated into the data or significant data gaps exist from over-spacing the scans.

Scan Editing (Step 4)

To ensure that the registration is performed only on objects consistent between scans, any moving objects in the scans should be eliminated. Beaches are a public and heavily frequented location, thus resulting in people, vehicles, and animals passing in front of the scanner as data are being acquired. Heavy vegetation should be eliminated from the scans because points are reflected off of different parts of the surface and possible movements of the vegetation between scans will result in significant inconsistencies between acquired points. However, redundant or close points between datasets should only be removed after completion of the registration process. Note that these filtering and editing steps would be required for a successful alignment using any software registration. This step can be performed before the initial alignment, if desired.

***PointReg* Algorithm for Point-cloud Registration (Steps 5-8)**

PointReg was developed to perform the point cloud registration appropriately for topographical point clouds collected in uncontrollable environments. The *PointReg* algorithm assumes that the scan data is within 1^{o} - 2^{o} of rotation about the *Z*-axis of the scan origin, is level, and has a coordinate for the origin of each scan. *PointReg* determines the optimal rotation angle of a scan based on multiple neighboring scans instead of just one, eliminating the

problem of a small offset from an erroneous alignment to get the best fit between two scans propagating through the dataset. With this technique, it is not necessary to fix any of the scans for reference.

PointReg operates on a simple survey text file of the scanner origin coordinates (*X,Y,Z*) the scan ID, the scan backsight ID, and a leveling identifier, which can be directly exported from a survey controller. Using this survey database, it automatically formulates the filenames for the files with the scan data if the data was collected using a consistent naming convention. *PointReg* significantly reduces user-input processing time by searching through this survey text file and automatically determining neighboring scans to register together based on the proximity of RTK GPS coordinates. A minimum distance and maximum distance between scanner origins can be set to avoid registering scans that are too close together or too far apart. For example, if two scans were taken from almost the same location, they would appear to have a good fit at many rotations about the *Z*-axis because of their similarity and the proximity of the rotation origins. The distance threshold eliminates this problem. The simple data structure and automation allows the user to quickly declare a few input parameters and let the program run autonomously in batch mode rather than the user having to manually apply it to each set of scans. The algorithm marches from North to South or East to West and registers each scan with the next scan to the South or the East. This ensures that each scan (with the exception of the two boundary scans) is matched against 2 scans on opposing sides to minimize

the warping effects. It also allows for better matching because once a scan has been matched with one neighbor, that rotational angle can be used as a starting point for the match with the second neighbor.

PointReg also provides several automated filtering options that are implemented upon data loading. While loading data, the limiting factor is reading the data from the hard disk. Thus, by performing these filters upon data loading, they do not add increased processing time, as the processer remains relatively free during data loading. First, *PointReg* performs basic filtering options by *X,Y,Z* extents. This is important to seacliff alignment where points on the beach are less satisfactory for alignment because they are planar and can be automatically filtered by specifying a minimum elevation. Second, the data can also be filtered by range to remove points far from the scanner origin that are less accurate and spaced farther apart. The amount of filtering required depends on the desired accuracy and type of 3D scanner used, and can be set as a parameter in the input gui. As distance increases from the scanner, the accuracy of the data decreases and points beyond a certain range will be undesirable. This maximum range is a function of the type of 3D scanner used and the size and amount of topographical features within the line of sight. For this study, the I-Site 4400 scanner has a resolution of approximately 18 cm at 100 m, so points farther than this were removed because of the large point spacing and hence are less desirable for alignment purposes. If there are too many data gaps (scans or RTK GPS data), this range may need to be increased in order to have sufficient

overlap to register scans. However, because both accuracy and resolution decrease with increasing range, the alignment inherits those inaccuracies. To minimize gaps in the data, the following equation, based on the Pythagorean theorem, calculates the minimum range that should be used in filtering the data to preserve sufficient overlap to avoid occlusions (Figure 3-2):

$$r_{min} = \sqrt{d^2 + s^2 + h^2} \qquad (3\text{-}1)$$

where, r_{min} is the minimum range to filter the data, *d* is the typical distance from the cliff at which the scans are performed, *s* is the typical spacing between scans, and *h* is the average height of the cliff.

As previously discussed, with the appropriate surveying and backsighting, the data merely needs to be slightly rotated about the *Z*-axis (centered at the scan origin) to be aligned to its proper location (Figures 3-7 and 3-8). *PointReg* (see pseudocode in Figure 3-10) evaluates the combinations of rotations of two datasets (scans A and B) to find the best rotation pair that produces the lowest RMS error. Unfortunately, a direct solution is not possible because both scans must be rotated from their initial positions, as opposed to keeping one scan fixed. However, an iterative approach can be used to determine the rotational angle, α_A, required for scan A and then a least squares technique can be used to determine the optimal rotational angle of scan B, α_B, given α_A. The math for this least squares approach is given in Appendix B. The first scan is rotated about the *Z*-axis centered at its origin from an angle $\alpha_A = -\beta$ (typically $1^o - 2^o$) to $\alpha_A = +\beta$ in 2*n* increments of $\Delta\alpha_A = \beta / n$. If a value for α_A has already been found for

scan A using another neighboring scan, the search window is reduced to focus around α_A +/-$\beta/2$. At each increment, matching point pairs are updated and the optimal angle, α_B, to rotate scan B given the current α_A is solved for. The pair of α_A and α_B that produces the lowest RMS is selected. The user also specifies the number of required iterations. Upon each iteration, the search window and increment steps are refined. This iterative approach allows the solution to converge rapidly; thus, few iterations are required to produce a satisfactory alignment (Figure 3-8). The two rotation angles found for scan A based on its two neighbors are then averaged for the final rotation angle. While more complex weighting schemes could be implemented, the warping illustrated in Figure 3-6 is nearly symmetric, so averaging produces excellent results, especially since the two rotation angles predicted from the neighboring scans tend to be very similar. *PointReg* then marches through the survey dataset to ensure that each scan is aligned to two neighboring scans on opposing sides. Once all scans have rotation angles, then *PointReg* outputs new files with the adjusted scans and evaluates the final error between neighboring scans for the final global model.

Visual Verification (Steps 9)

Although results may look good mathematically, the data still should always be visually inspected for quality control purposes. Long, linear structures such as seawalls work well for verification of scan alignments where a misaligned structure can be readily identified from a map perspective. Figure 3-7 shows an

area with a misaligned seawall, stairwell, and buildings that are properly aligned using *PointReg* in Figure 3-8. Another visual verification of alignment can be done by comparing RTK GPS points obtained on “fixed structures” appearing in the scans. Comparison of scans to previous surveys or datasets is also an effective method to verify data alignment if there is substantial correspondence. Because there are areas in coastal environments that have not undergone significant change between recent surveys, these areas can be compared to confirm both datasets are in the proper location. Scan origins will be different, so any misalignments from one dataset will occur along a portion of another dataset that would be less affected by a misalignment from rotations. Such methods provide an efficient way to quickly detect large misalignments. Visual verification by examining cross sections (Figure 3-11) allows for a finer view of the scan’s alignment. A misaligned scan may appear aligned when viewed from a normal 3D view but will appear misaligned in a 2D cross section view.

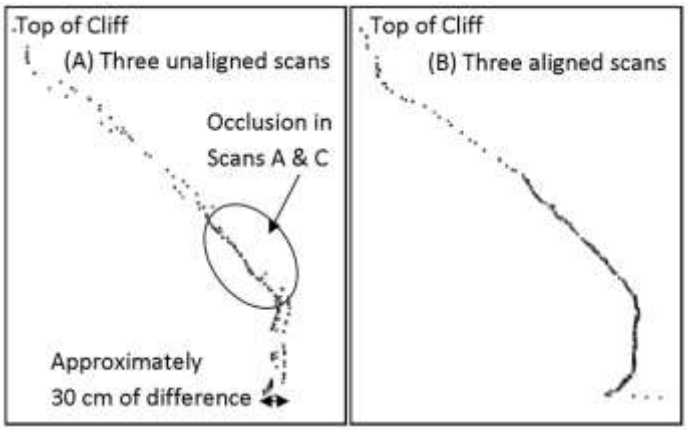

Figure 3-11. Verification of alignment through 2D cross – section profiles of (a) three unaligned scans (b) three aligned scans. See Figure 2-2 for description of occlusions.

RESULTS AND DISCUSSION

Successful application of this algorithm producing repeatable results between multiple surveys is shown for multiple coastal surveys in Chapter 2. This discussion will demonstrate the necessity of several unique features of the algorithm and compare the performance of the algorithm to common techniques.

Software Alignment Without Constraints Using Global Optimization

Figure 3-12 shows the error induced at scan origins after performing a software alignment without constraining any DOF's. This problem will occur with currently available alignment software and illustrates the necessity of constraints for large-scale data collection. This error is induced from the warping described in the previous section. The data represent a 1.4 km test section at Torrey Pines, CA Data collection was performed facing East (+X) and marching from North to South (-Y) with approximately 40 m between scans covering a 180^{o} view of the seacliffs. Figure 3-13 shows the locations for a section of the survey to illustrate the survey pattern. Initial scan alignment was done using GPS information, however, as warping occurred from the center, these scans needed to be translated for a better fit with the merged model before the alignment algorithms could be used. The 6DOF software alignment was performed by co-registering and then fixing the two center scans, to simulate a fixed reference scan for a starting point. Accurate alignment for these scans was verified by comparison to several surveys, guaranteeing that any introduced errors would be

a result of the alignment technique itself and not of a bad initial condition. All scans were edited and filtered to a 100 m range, as discussed above.

Pair-wise alignments were repeatedly performed multiple times to ensure that the best fit was found between the neighboring scans. Scans were then aligned using a global alignment technique (Pulli, 1999), which operates by fixing the scan with the most overlapping scans and adding additional scans outward from the original fixed scan. The new origins of each scan as a result of the translation and rotation of the alignment process were compared to the original RTK GPS coordinates obtained for the scan origins. The substantial errors shown in Figure 3-12 shows current global optimization techniques do not apply the constraints necessary to prevent this warping problem from occurring because they do not initially constrain the scan, they only constrain it relative to its neighbors. Global optimization succeeds in removing this warping error when it completely surrounds an object, which would be impractical for seacliff studies for long coastal sections. Because *PointReg* constrains the scans to their origins, it does not suffer from these alignment propagations, and has no error in the origin location. Additionally, the global alignment technique required substantial user input (3 hours) to pre-align the data from 36 scans and to re-iterate the alignment after the initial pair-wise alignments fell victim to localized minimums, creating erroneous alignments of up to 20 m. The alignments were visually inspected and produced acceptable RMS errors before comparing origin displacements.

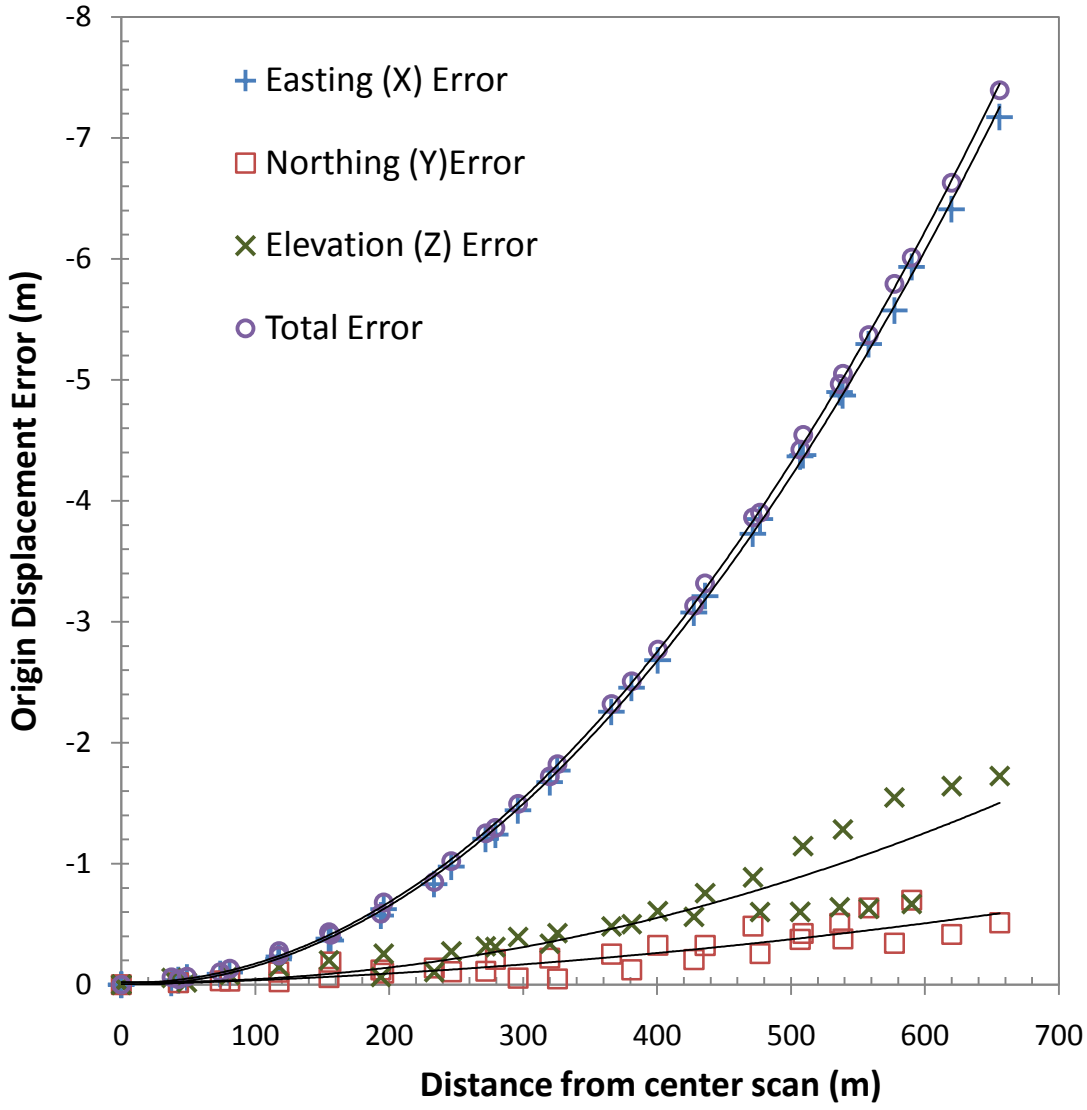

Figure 3-12. Comparison of origin displacement error with distance from fixed center scan for scans collected in a North-South sweep and aligned from the center using unconstrained alignment techniques. Note that the majority of the displacement error is a result displacement in the Easting (X) direction, caused by the propagation of rotational errors about the Z-axis, created by warping biases in each scan. In contrast, because PointReg constrains scans origins, it produces none of these detrimental origin displacement errors.

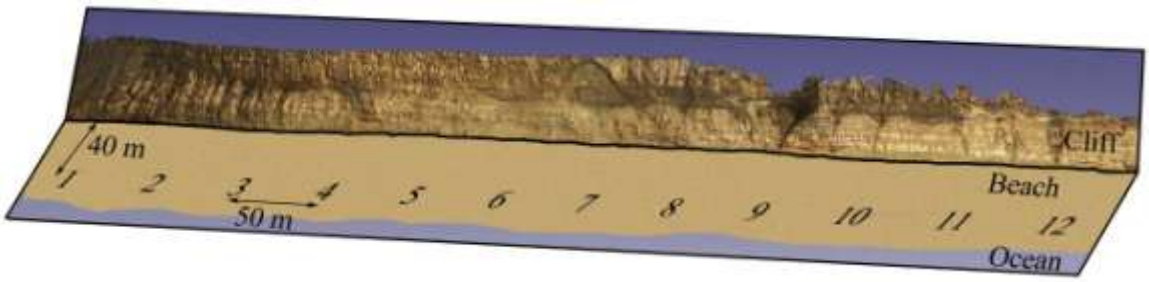

Figure 3-13. Setup for survey used to analyze the effectiveness and necessary steps for the algorithm. The cliff shown is a texture-mapped, surfaced model using data from the Torrey Pines survey (September 10-11, 2007) aligned with *PointReg.*

Figure 3-12 provides insight on how warping occurs when attempting to scans over a large region when performing a traditional software alignment. The overwhelming majority of the error resides in incorrect easting values, showing that the major contribution to misalignments is the incorrect rotation about the *Z*-axis, which would lead to large displacements in the Easting direction. With the target primarily being scanned in the north-south direction with slight variability in the easting direction, there is limited data to constrain it. The northing direction shows less displacement as a result of substantial data being available along the north-south axis to serve as a constraint. The bifurcation of the Z- direction error results from larger error in the northern scans compared to the southern scans. The northernmost scans showed more error in the *Z*-direction because the cliffs were taller in the northern direction, creating more uncertainty in the alignment from increased shadowing and complexity

This bias in the –X (West) direction occurs when scanning a near-linear feature in the north south direction facing east because the edges of a 180^{o} scan will be at a more oblique angle compared to the more orthogonal scanning of the center of the scan. Thus, the spot-size would be more oblique at these angles and result in more measurement error. These edges are what provide the overlap needed for point cloud alignment. While for repeat scans discussed in Section 1.2 on warping, the measurement error is principally in the *Y* (North) direction, this measurement error translates into alignment error in the *X (East)* direction during the alignment process. This occurs because as points at the overlapping edges of scans are brought closer together to minimize distance, the measurement error in the *Y* direction causes some rotation about the *Z* axis, which, in turn, leads to alignment error in the *X* direction. Thus, while at an initial glance, the results may appear inconsistent, each section is actually discussing a different type of error.

Interestingly, there is no bias between the alignment of scans from the center northward, and from the center southward. This illustrates why averaging the rotation values found using both neighboring scans on each side of the scan is effective. With a pair-wise alignment with one neighboring scan, these biases will cause a slight, incorrect clockwise rotation. Contrarily, the pair-wise alignment with the neighboring scan on the other side will cause a slight, incorrect counter-clockwise rotation. By averaging these rotation angles, *PointReg* effectively eliminates this bias error, thus avoiding large misalignments

caused by global error propagation. Additionally, Figure 3-12 shows that these biases are minimized for small distances, thus *PointReg* effectively constrains these biases locally where they are minimized.

Software alignment with constraints

To contrast the error from software alignments without constraints, Table 3-2 compares several possible methods using constraints to align the point clouds obtained from a linear progression survey of the seacliffs (Figure 3-13). The scans were spaced at 50 m approximately 40 m from the cliff. These scans, initially approximately 320,000 points each, were filtered by range and elevation to 200,000 points. Approximately 25,000 points per scan were used for in the actual alignment in Point Reg. Alignments were performed using scans that were properly field constrained and with only one changing degree of freedom, the rotation about the *Z*-axis. The first column shows the accuracy from the backsighted (estimating the backsight targets) and leveled field data without any software alignment. Single neighbor registration methods are evaluated consisting of the paired method and the fixed method. The paired method consists of registering each scan with a neighbor. For example, Scans 1 and 2 are registered together, Scans 3 and 4 are registered together and likewise until the end of the linear segment. As shown in Table 3-2, this produces good agreement between the scans that are co-registered; however, the results are poor for adjacent scans that were not paired together for the registration, such as Scans 2 and 3.

Table 3-2. RMS comparisons for different registration techniques

		Single Neighbor Alignment		Multiple Neighbor Alignment	
Scans	**Field Method**	**Pair Method**	**Fixed Method**	**ICP Method**	***PointReg* Method**
1&2	0.0870	0.0449	0.0455	0.1184	0.0734
2&3	0.1210	0.0963	0.0510	0.1144	0.0689
3&4	0.1529	0.0509	0.0668	0.1042	0.0586
4&5	0.1112	0.1174	0.0609	0.1212	0.0773
5&6	0.1803	0.0524	0.0858	0.1158	0.0728
6&7	0.0958	0.0799	0.2412	0.1060	0.0598
7&8	0.1993	0.0525	0.0728	0.1150	0.0689
8&9	0.1685	0.0969	0.0722	0.1301	0.0798
9&10	0.1303	0.0598	0.0664	0.1211	0.0736
10&11	0.0880	0.0952	0.0742	0.1167	0.0734
11&12	0.1116	0.0598	0.0588	0.1054	0.0618
Summary Statistics					
Average	0.1314	0.0733	0.0814	0.1153	0.0699
Max	0.1993	0.1174	0.2412	0.1301	0.0798
Min	0.0870	0.0449	0.0455	0.1042	0.0586
Std Dev	0.0386	0.0247	0.0542	0.0078	0.0070

The fixed method involves fixing a paired registration at each end of the linear segment and then registering each adjacent scan to a fixed neighbor until they converge in the center. For example, in this study, Scans 1 and 2 are registered together as in the paired method. Scan 3 is then registered to Scan 2, which remains fixed. This is repeated until the center is reached. On the opposite side, Scans 11 and 12 are registered together and Scan 10 is registered to a fixed Scan 11. This is repeated to the center, where on the left side Scan 6 is registered to Scan 5 and on the right side Scan 7 is registered to Scan 8. If

this method were to be effective, Scans 6 and 7 would have good agreement, even though they were not registered together. As a result of the previously discussed warping, there is considerable error (0.24 m) between Scans 6 and 7 (Table 3-2). An alternative would be to fix the center scans (6&7) and work outward, which would produce good mathematical agreement and low RMS values. However, because applying this method from the outside to the center does not work, the low RMS would not be a guarantee of accurate alignment and the model would still experience warping. The results from the single neighbor alignment methods show that a multiple neighbor registration is needed.

The quality of alignment of the multiple neighbor registration is shown by two methods to compare the ICP point to point method and the point to plane method used in *PointReg*. The standard deviations of the RMS between adjacent scans shown in Table 3-2 for these two methods, is much lower than for the single registration method. This shows that the multiple registration method evenly distributes the alignment error, preventing warping. The ICP method has a higher RMS than the *PointReg* method because the ICP method assumes that points from different scans are the same point in actuality, which tends to pull points closer together during alignment and over predicts the RMS because this assumption generally is not true. In a perfect world, where scanner location could be repeated precisely, then the distribution of points in the cloud would overlap. However, in a beach environment, where the Z component changes by meters throughout the year, it is very difficult to locate the scanner in the exact

same location. The inherent problem with the point to point method in this environment is the point distribution varies from scan to scan and when aligning adjacent scans. The end result is that the points between scans are warped in attempt to minimize the RMS error. That is, we introduce error into overlapping areas of adjacent scans that is larger by the point to point method than the point to plane method (Table 3-2).

Performance

To evaluate the performance of *PointReg*, the 12 scan survey used in the previous section (Figure 3-13) were aligned using several registration techniques available in I-Site Studio 3.0 (I-Site, 2008). The performances of these methods are compared to *PointReg* in Table 3-3. It should be noted that the time required is heavily dependent on the user's experience level and the equipment used. Thus, Table 3-3 presents a range of values. Four cases were evaluated in I-Site Studio 3.0 to compare to *PointReg*. First using the ICP algorithm with 6 DOF, second using the ICP algorithm with 3 DOF using GPS origin and backsight information, third using the surface matching with 6 DOF and fourth using the surface matching with 3 DOF using origin and backsight information. Total times per scan were evaluated in addition to the time required for the 12 scan dataset. Further, times were estimated for a typical survey of 50 scans covering 2.5 km. It is important to note that in conventional software, the user must manually determine adjacent scans to match together. While the matching itself may not require user interaction, the user will often wait until it is complete and then move

onto the next. In contrast, *PointReg* performs all of the computations in a batch process, so the user can work on another task while the computations are being performed, enhancing productivity. The only tasks that are not automated are the setup and editing. Additionally, because of improper matching pairs from rough initial alignments, registration may need to be repeated multiple times for the scans using other techniques, whereas *PointReg* performs an iterative sweep and updates point pairs during the sweep to eliminate this problem. Note that for the ICP and surface 3 DOF or 6 DOF methods to correct for warping, a global alignment algorithm would then need to be performed after implementing the initial pair-wise alignments and would require additional time beyond that presented in Table 3-3. Further, the ICP and surface 6 DOF methods would then require additional time to georeference the data into a real world coordinate system.

Table 3-3. Time performance comparison (minutes) for scan co-registration using an Intel Core2 Duo 6700@2.66 GHz with 4GB RAM. Lower bounds were estimated based on times for an expert TLS data user to complete the task and upper bounds were estimated based on a novice TLS data user. The ICP and surface alignments were done using I-Site software (I-Site 2008). Each dataset contains approximately 320,000 points. Note that surfacing times are based off of organized point cloud data. Unorganized point cloud data would require substantially more time to create a surface.

	Setup (load program, input files) for all scans	Data loading per scan	Editing time per scan	Filtering (Range and Extents) per scan	Initial Alignment per scan	Surf-acing per scan	Co-reg per scan	Total Time per scan	Total time (12 scans)	Total time (50 scans, 2.5 km)
ICP 6 DOF	0.5 - 1.0	0.1	0.5 - 5.0	0.5 - 1.0	5.0 - 10.0	0	0.8 - 2.0	**6.9 - 18.1**	**83 - 218**	**346-906**
ICP 3 DOF using GPS origin information	0.5 - 1.0	0.1	0.5 - 5.0	0.5 - 1.0	0.05 - 0.10	0	0.6 - 1.4	**1.8 - 7.6**	**22 - 92**	**88 - 381**
Surface 6DOF	0.5 - 1.0	0.1	0.5 - 5.0	0.5 - 1.0	5.0 - 10.0	0.2 - 0.4	0.5 - 1.0	**6.8 - 17.5**	**82 - 211**	**341 - 876**
Surface 3DOF using GPS origin information	0.5 - 1.0	0.1	0.5 - 5.0	0.5 - 1.0	0.05 - 0.10	0.2 - 0.4	0.3 - 0.7	**1.7 - 7.3**	**20 - 89**	**83 - 366**
***PointReg* 1DOF**	1.0	0.1	0.5 - 5.0	0 *during data loading	0.05 - 0.10	0	0.2	**0.9 - 5.4**	**11 - 65**	**44 - 269**

CONCLUSIONS

Alignment strategies and tools needed to align point cloud datasets are developed for regional topographic mapping, providing an approach to evaluate and reduce alignment uncertainty. This method applies the scanner origin coordinates and leveling constraints necessary to prevent successive propagations of misalignments throughout the mapped region that can be created through global optimizations because of scan warping. These constraints are crucial for repeat surveys, ensuring that rates of change between datasets are calculated based on real change and not misalignments. For example, in a volumetric comparison for cliff erosion, if scans are uniformly misaligned by 0.1 m for 1 km in an area with 30 m high cliffs, the volume estimate would be off by 0.1m*1,000m*30m = 3,000 m^3. These misalignments are more substantial than common range measurement errors because range measurement errors will include positive and negative errors spread throughout, smoothing out the overall error. Misalignments produce propagating biases and calculations using these datasets will contain substantial preventable error. This warping is created because the seacliffs are nearly linear features so the edges of the scans occur at oblique angles, causing more uncertainty in the laser measurement.

This alignment method was also developed for topographical datasets, which must be collected quickly in dynamic environments and thus offers improvements for topographical survey alignments over current point cloud

alignment techniques developed for high-density datasets in controlled environments. Since the user is not required to surface or interpolate the data prior to alignment and the *PointReg* algorithm automatically determines which scans to register together, it can be efficiently implemented in a common survey workflow. Additionally, the method performs the alignment based on multiple scans (generally two scans on opposing sides is sufficient) as opposed to being able to only register scans together in a pair-wise fashion. Alignments based on multiple scans allows for a better alignment between subsequent scans because it ensures that the error in a scan alignment is averaged between its neighbors instead of fitting one neighbor well and poorly with the other. Being a simplified approach, this method is easy to implement and reduces the complexity of the scan alignment problems and still yields accurate and repeatable results.

The *PointReg algorithm is* available for free public use at http://lidarweb.ucsd.edu/coastalstudy/softwaretools.html. All tools operate unorganized point clouds in a clear-text ASCII file format allowing for straight forward data conversion from arbitrary scanner/software systems.

ACKNOWLEDGEMENTS

This research was partially funded via a grant from California Seagrant (Project #R/OE-39), the Coastal Environmental Quality Initiative (CEQI) under award #04-T-CEQI-06-0046, and the University of California, San Diego Chancellor's Interdisciplinary Collaboratories Fund. The above support is greatly appreciated. I also thank Pat Rentz and Jessica Raymond for their assistance in

the TLS surveying. I also thank Scott Schiele (I-Site), John Dolan (I-Site), and Travis Thompson (CALVRS) for their technical assistance.

Chapter 3, in part, is a reprint of the material as it may appear in the Journal of Photogrammetry and Remote Sensing. Olsen, M.J., Johnstone, E., Kuester, F., Ashford, S.A., and Driscoll, N. The dissertation author was the primary investigator and author of this paper.

CHAPTER 4. RAPID RESPONSE TO SEACLIFF EROSION IN SAN DIEGO COUNTY, CALIFORNIA, USING TERRESTRIAL LIDAR

OVERVIEW

Seacliff erosion plagues the coastline of northern San Diego County, California through both marine and subaerial processes. Heavy development on seacliffs and the economic value of beaches in San Diego County, California place a heavy emphasis on maintaining a healthy and safe beach. This chapter illustrates the development of a rapid response program to study and document seacliff erosional processes utilizing a terrestrial LIght Detection And Ranging (LIDAR) system in combination with interactive visualization techniques to publically present this research. One of the cliff failures currently being studied as part of this rapid response program is described in this chapter to demonstrate the insights that can be gained by observing the temporal change of a failure mass using frequent site monitoring.

Figure 4-1. LIDAR data point cloud baseline of Encinitas, California (December, 2006)

INTRODUCTION

Heavy development on the cliff tops of the coastline of San Diego County, California has produced a demand for accurate quantification of seacliff retreat rates and an understanding of the erosional processes. Seacliff failures threaten not only private cliff top structures but also threaten public safety and infrastructure due to the high levels of beach usage in San Diego County, California. Additionally, the cliffs in this region can provide a significant amount of sediment to the beaches (Haas, 2005; Young and Ashford, 2006), which are of particular importance to the Southern California economy.

Terrestrial LIDAR (LIght Detection And Ranging) has been proven to be an effective tool to study cliff failures and morphology (Collins and Sitar, 2004; Young and Ashford, 2007). Terrestrial LIDAR scanners use a laser based on time-of-flight or phase-based measurements to determine the distance of a sample point from the scanner. LIDAR systems capture topological characteristics at high resolution, producing a detailed point cloud (Figure 4-1).

These point cloud datasets contain XYZ coordinates, RGB color, and return signal intensity information. A single scan can swiftly collect approximately one million points in about six minutes, densely covering about 40-70 meters of coastline, depending on the complexity of the topography. The survey system (Figure 4-2) consists of five main components: a LIDAR scanner, a laptop controller, GPS receiver, GPS controller, and a cell phone. Volumetric quantification of the failure mass can be calculated by comparing surveys before and after a failure event.

METHODS

This research program (see Figure 4-3 for workflow) focuses on the continual monitoring of seacliffs in northern San Diego County, California from Scripps Pier, La Jolla to Encinitas, an area which contains approximately 20 km of seacliffs. Priority study areas (Figure 4-4) are initially determined by searching through historical documents, photographs, surveys, and field investigations to determine erosional hotspots. Coastal accessibility data (Figure 4-4) for these locations are then stored in a GIS database which includes information about the quality of the access and the ease to transport the field equipment. Having this information readily available in a GIS database allows the investigation team to rapidly respond to a failure before waves wash away the deposited material.

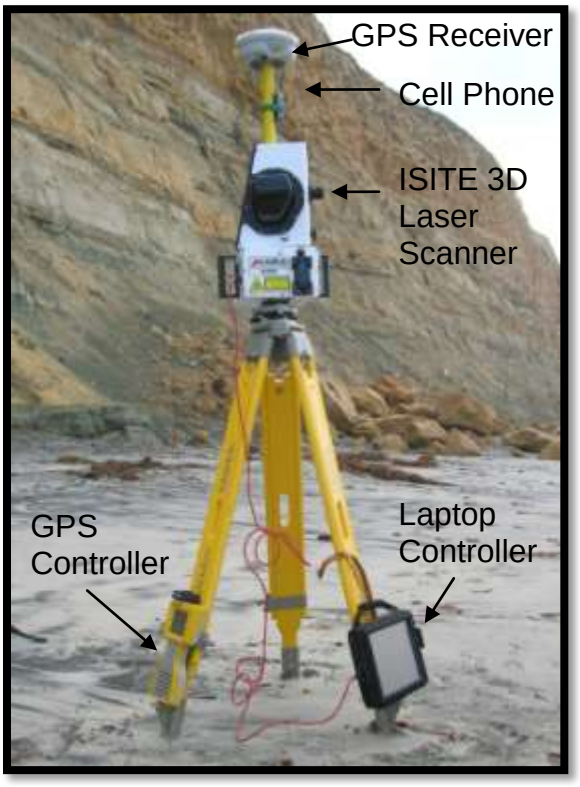

Figure 4-2. Field survey equipment and setup

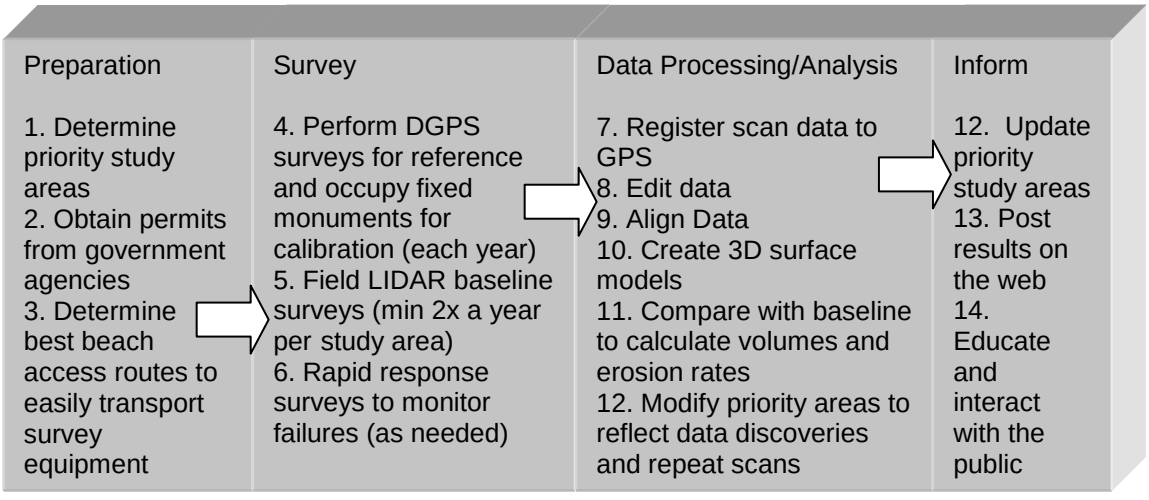

Figure 4-3. Data collection and analysis workflow

The first step in determining topographic change consists of establishing a baseline as reference for comparisons. The field crew performs bi-yearly scans in each of the sections shown in Figure 4-4 with an I-Site 4400 3D terrestrial laser scanner to document the differences in erosion between the winter and summer seasons. This also ensures that a recent survey is available for comparison when an event occurs. Erosional hot-spots are identified and surveyed more frequently (monthly or bi-weekly) to track the change that occurs. These sites and their priority levels are shown in Figure 4-4.

Georeferencing the LIDAR data to UTM NAD83 Zone 11 Coordinates utilizes Differential GPS (DGPS) survey methods described in Chapter 2, allowing for a comparison of previous and future datasets. This process involves:

- Establishing a DGPS Base Station as a reference point or using a Virtual Reference Station (VRS) network
- Occupying fixed control monuments for calibration of the survey
- Performing DGPS surveys of “fixed” structures for verification of scan alignment
- Obtaining DGPS points for each scanner location and backsighting (aligning) to the previous location

This project utilizes the California Virtual Reference Station (CALVRS) network where a cellular phone obtains base station correction information from the CALVRS network via the internet. This information is relayed to the DGPS

survey controller in the field providing real time kinetic GPS measurements with centimeter accuracy. Utilizing the CALVRS network eliminates a DGPS base station setup and thus allows the investigation team to respond more quickly to an event. Additionally, utilizing a cellular phone provides better signal coverage when compared to a DGPS base station radio signal requiring line of sight.

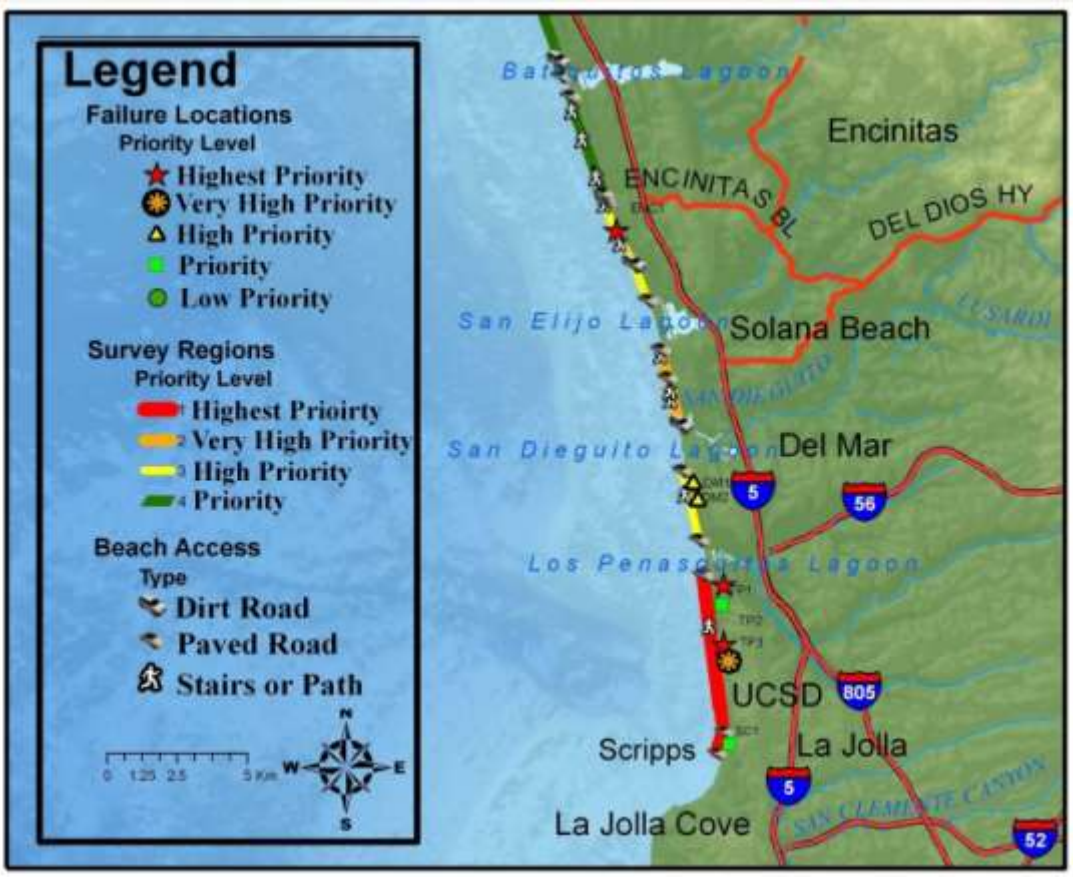

Figure 4-4. Study area location, priority zone mapping, failure locations and coastal accessibility data

Following the survey methodology described above, the scan data can be quickly imported into the I-Site Studio 3.0 software developed by I-Site Inc. (2007) and immediately georeferenced (typically within 30 cm accuracy) with the scanner origin and backsight GPS information. This allows for a quick, superficial investigation of the data to verify there are no major problems with the data or large survey data gaps. Further refinement to correct for backsighting errors is then performed to georeference the data within about 6-7 cm accuracy (limits of the DGPS and the scanner) as described in Chapter 3. After georeferencing the scan data, the point clouds are converted to 3D surface models (Figure 4-8) and compared to a previous survey for change detection. If rapid post slide response is possible, then the envelope defined by the pre and post slide surfaces can be used to determine the total landslide volumes before the sediment is eroded away by wave action. The distance between surfaces can be calculated and displayed in a color coded fashion, allowing for easy identification of erosional hot-spots (Figure 4-8). After indentifying erosional hot spots, the priority maps are updated to focus on areas with recent landslides or high erosion rates for the next survey.

The examination, classification, and editing of the datasets is also performed in a virtual reality (VR) environment (Figure 4-5) discussed in Hsieh et al. (2007). This virtual environment allows the user to swiftly navigate the data space, scale, annotate or otherwise modify it. The user can analyze the data at different spatial and temporal scales and fuse different visual representations.

The user can assume arbitrary vantage points, which allows local and global phenomena to be swiftly identified and studied, while literally walking through the datasets. This interaction with the dataset assists in the discovery of the involved erosion processes and provides insights that cannot be seen in the typical 2D environment. Most importantly, this virtual reality environment allows the investigation team to collaboratively compare sequential datasets, examine the cause of failure, and evaluate the potential of continual failure at that location almost immediately after the field surveys are performed.

In addition to the availability of this data for public display in the VR environment, a website dedicated to the study of seacliff erosion in northern San Diego County, California (http://lidarweb.ucsd.edu/coastalstudy/), provides an immediate dissemination mechanism of survey results to the public within a day of acquisition. Additionally, the website provides a channel of communication for the public to inform the survey team of any recent failures they observe. Efforts

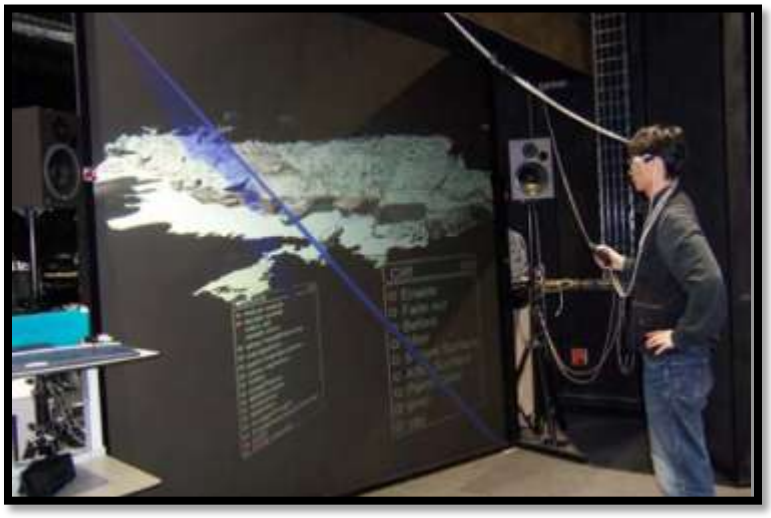

Figure 4-5. Interaction with data in a virtual environment

are underway to publish and distribute pamphlets during field surveys to educate the public about the dangers of cliff failures and how they occur. Field surveys have provided a unique opportunity to educate the public about coastal hazards and to discuss the results directly with those who regularly use the beach. It also serves as a grassroots effort to raise awareness and to encourage the public to become part of a human sensor network that helps identify existing or pending failures. The website allows them to quickly inform the research team of failures they see, providing a constantly improving notification system.

RESULTS

Several failures (Table 4-1) were observed during the initial implementation of the rapid response program during the summer of 2007 and are currently the focus of this research project. These failures and their priority levels are stored in the GIS database discussed previously (Figure 4-4). All of the above failures occurred during the calmer summer months. After their initial failure, however, most of the sites in Table 1 showed minimal change until December 2007 when the harsher winter waves quickly reworked the failure mass sediment. Table 1 shows the original failure volumes and the current volume of the failure mass on the beach determined from the most recent scans performed in mid-December 2007.

Continuous study of some of these failures such as sites EN1 and TP2 will be published in subsequent papers when they can be more fully analyzed and

Table 4-1. Summary of Current (December 21, 2007) Failure Locations (S=Summer and W = Winter)

Failure	DM1	DM2	EN1	SIO1	TP1	TP2	TP3	TP4
Location	Del Mar 9th St	Del Mar 13th St	Encinitas J St	Scripps	Torrey Pines 1km N of Flat Rock	Torrey Pines Flat Rock	Torrey Pines 200m S of Flat Rock	Torrey Pines 200m S of parking lot
Failure Date	8/21/2007 +/- 7 days	Summer 2007	6/6/2007	9/2/2007 +/- 7 days	8/4/2007	8/23/2007 +/- 1 day	9/30/2007 +/- 3 days	10/20/2007 +/- 5 days
Initial Priority Survey Date	8/28/2007	8/28/2007	6/7/2007	9/12/2007	8/6/2007	8/24/2007	10/5/2007	10/29/2007
Initial Failure Volume m^3	88	24	139	30	31	79	28	168
Current Failure Volume* m^3	39	19	45	30	25	46	0	104
Amount of Change Observed	S: Slight W: Major	S: Slight W: Slight	S: Major W: Major	S: None W: None	S: Minor W: Slight	S: Major W: Major	S: Minor W: Major	S: Slight W: Major
Waves reach failure	S: No W: Some	S: Some W: Some	S: Yes W: Yes	S: No W: No	S: No W: Some	S: Some W: Yes	S: Some W: Yes	S: Some W: Yes
Probable Cause of Failure	Groundwater	General Instability	Undercutting /Groundwater	General Instability	General Instability	Undercutting	General Instability	General Instability

studied and thus will not be elaborated in detail in this chapter. This chapter will discuss the failure currently being monitored at site TP1 in Torrey Pines State Reserve, California as an example to illustrate potential benefits available from a rapid response to a failure and subsequent observations.

Case Study: Torrey Pines Failure at Site TP1

The failure at site TP1 (Figure 4-6) occurred during the late afternoon of August 4, 2007 at Torrey Pines State Reserve and was fortuitously photographed as it occurred by Herb Knufken, a Docent of Torrey Pines State Reserve. The rapid response researchers were quickly notified of this failure through his photographs via email from the Torrey Pines State Park Rangers. Although the failure could not be surveyed until two days after the failure occurred, August 6, 2007, the failure mass can be assumed to be untouched by wave action during those two days as evidenced by the dusty sand layer from the collapse about 5 mm thick covering the beach in that area. The failure was also contained on the high berm of the back beach (typical of a summer beach profile) which prevented the incoming waves from interfering with the failure mass. The failure mass consisted mostly of sandstone rocks larger than 15 cm in diameter with a few large (> 50 cm) boulders.

Figure 4-7A shows approximately 1 million points with a typical point density of 8 cm from the most recent baseline LIDAR survey of Torrey Pines performed in April 2007. The rapid response survey to this failure on August 6,

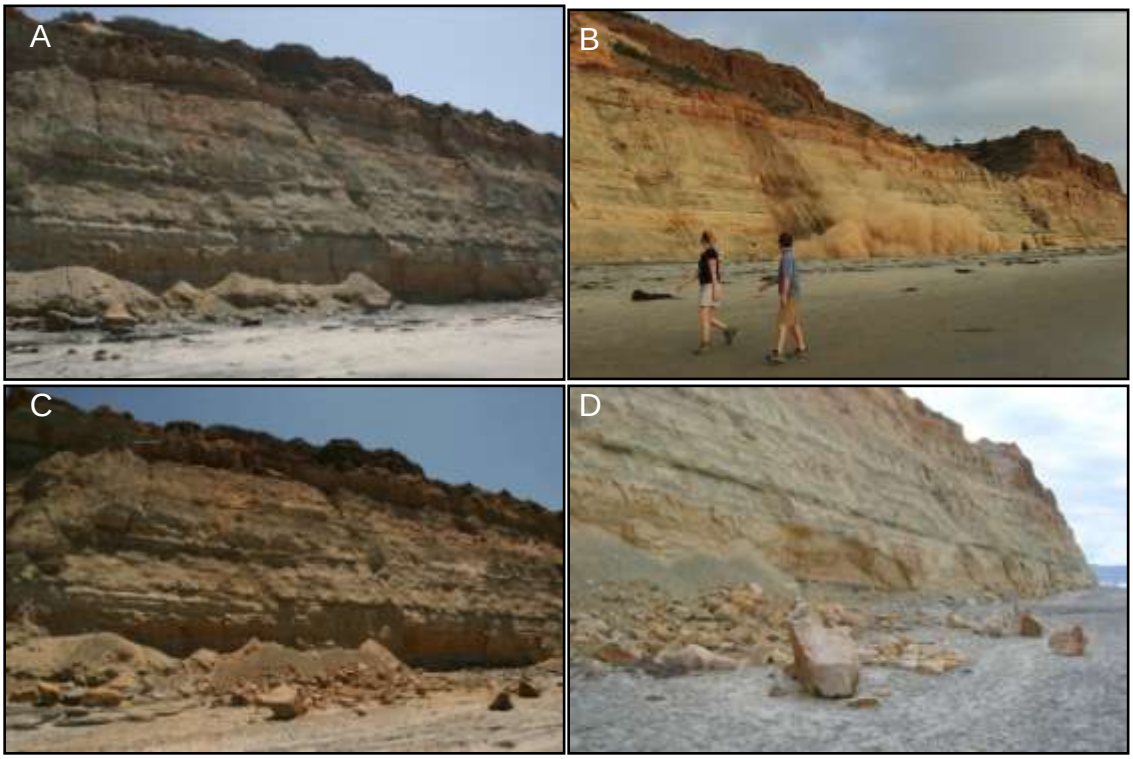

Figure 4-6. Site TP1 (A) before failure (4/10/2007), (B) during failure (August 4, 2007, photo courtesy of Herb Knufken) (C) two days after failure (August 6, 2007), and (D) after human interference, ~2 months after failure (September 29, 2007)

2007 (Figure 4-7B) contains approximately 4 million points at a typical point density of 5 cm on the cliff surface. The root mean square (RMS) of error between the unchanging portions of these two surveys is 4.9 cm. The original failure volume was determined to be 31 m^3 and the surface area of the cliff significantly affected by the failure was 316 m^2 (Figure 4-8), although the most substantial change occurred on the upper 16 m^2 portion of the cliff showing 1-2 m of change (Figure 4-8).

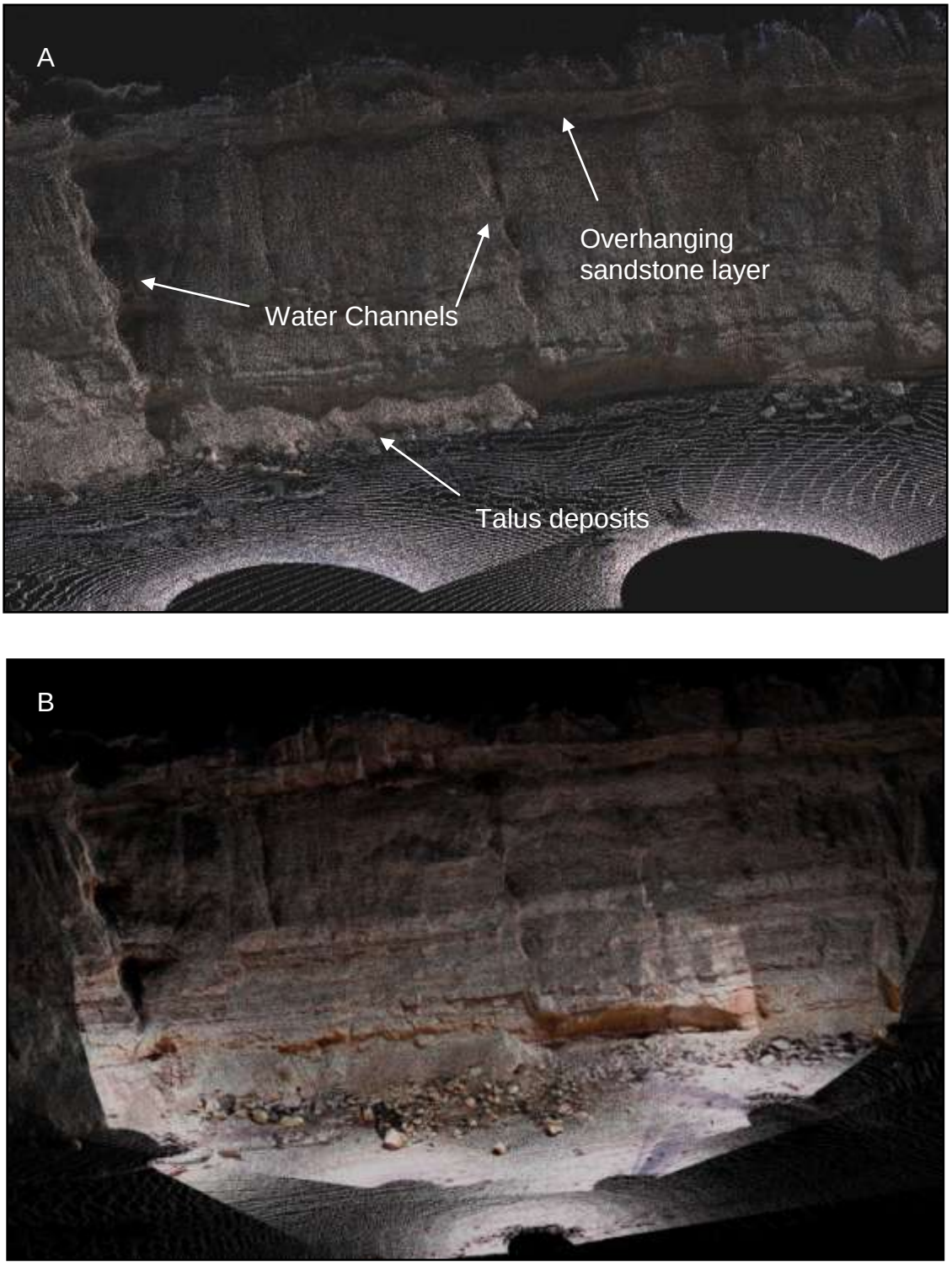

Figure 4-7. Point cloud obtained by LIDAR scans at site TP1 (A) most recent baseline survey (4/11/2007) and (B) two days after failure (8/6/2007)

The talus deposits at the base of the cliff in the April 2007 survey show evidence of continual erosion of the upper cliff. Concentrated water channels can be seen on both sides of the failure location. The failure (Figure 4-7 and 4-8) occurred on the upper portion of the cliff when an overhanging, weakly cemented sandstone layer collapsed due to continual erosion of the weaker layers below it. Groundwater sapping was not observed at the site; however, the site does show evidence of streaks from water runoff along the cliff face. Thus, it is assumed that the erosion of the sediment below the sandstone layer was probably the result of rain and runoff along the cliff face. The continual undercutting left the above sandstone layer unsupported until it failed and slid down the cliff face on August 4, 2007.

Subsequent visits showed minimal change in the failure mass other than the disappearance of the dusty sand layer due to heavy foot traffic in the area. On August 24, change in the site occurred when rocks were moved and organized into a pile by visitors to the beach. The site was then rescanned to model this change, so any further change could be documented. The volume remained constant at 31 m^3 in subsequent surveys until incoming winter waves eroded the protective beach berm in December 2007 and waves begin to erode approximately 6 m^3 of the failure mass. The smaller rocks (< 0.2 m in diameter) were washed away and larger boulders remained. Monitoring of the site will continue throughout the winter months where it is anticipated that the winter waves will remove more of the failure mass and cause more erosion at the site.

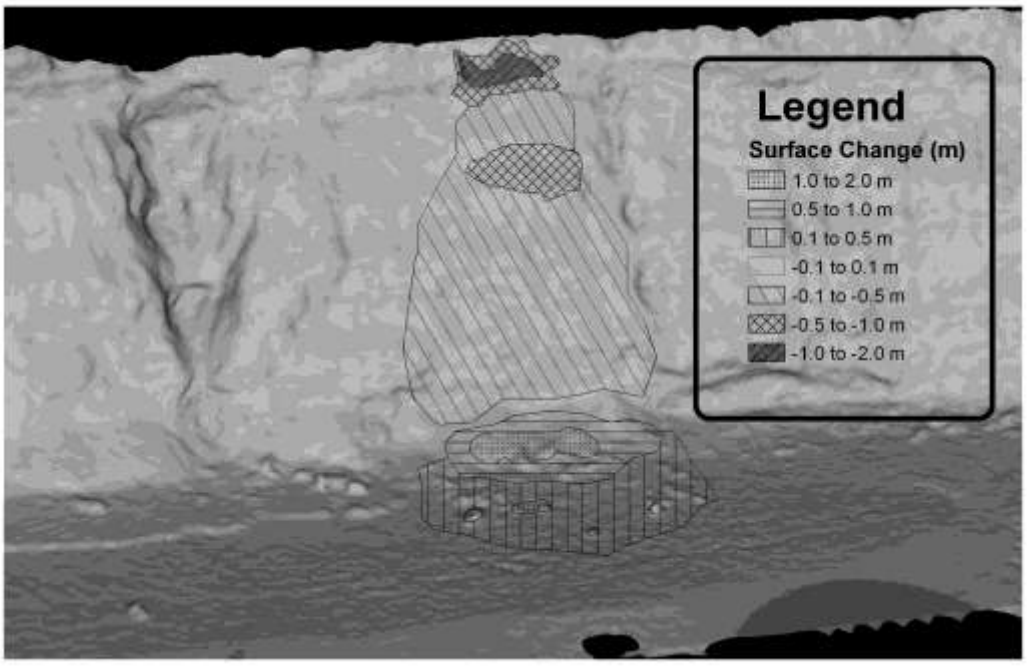

Figure 4-8. Surface change model between rapid response survey on August 23, 2007 and baseline from April 11, 2007

CONCLUSIONS

Rapid response to seacliff failures offers a unique opportunity to study the erosional patterns and boundary conditions needed for the formulation of a theoretical model that can properly capture and eventually predict these events. Responding immediately to an erosional event provides the ability to obtain data before waves remove talus deposits and rework them into the beach. It also allows researchers to pinpoint specific failure mechanisms and the sequence of events at sites that undergo multiple failures. Utilizing tools such as LIDAR and Virtual Reality, rapid processing of this data enhances public educational efforts. Proper education and accurate information will inherently lead to the best

solutions for coastal management. The research team will use the images and results produced from this analysis and the visualization enhancements to educate and assist the public, city councils, and government agencies responsible for the future of the coastline. The high resolution data from this study is used to calculate short-term (and eventually long term) cliff retreat rates which will help government agencies determine appropriate cliff setbacks for safe public and private land use. This research endeavor provides a useful and reliable tool to investigate the geologic processes that shape the California coast and accurately quantify seacliff erosion that occurs.

ACKNOWLEDGEMENTS

This research is supported by the California Seagrant and the California Environmental Quality Initiative (CEQI). Scott Schiele and John Dolan of I-Site and Travis Thompson of CALVRS provided technical support for this project. We appreciate all those who alert us to the locations of new failures, especially Gary Samad, who has alerted us of several failures and provided valuable information. We also thank Herb Knufken for the photographs of failure TP1 in action which informed us of that failure.

This chapter, in full, is a reprint of the material as it appears in Rapid Response to Seacliff Erosion in San Diego County, California using Terrestrial LIDAR, 2008. Olsen, M.J., Johnstone, E., Ashford, S.A., Driscoll, N., Young, A.P., Hsieh, T.J., and Kuester, F., ASCE Solutions to Coastal Disasters, 2008. The dissertation author was the primary investigator and author of this paper.

CHAPTER 5. FATE AND TRANSPORT OF CLIFF FAILURE SEDIMENT IN THE SOUTHERN OCEANSIDE LITTORAL CELL

OVERVIEW

Erosion and collapse of unstable seacliffs along the economically important coastline of San Diego County, California, threatens existing development and public safety. Time-series mapping of the seacliffs and beaches provides valuable insight into the processes responsible for cliff erosion as well as reworking and transport of the failed material. High-resolution terrestrial laser scan (TLS) data provides reliable, quantitative data for analyzing seacliff morphology; the data are georeferenced using real-time-kinematic global positioning systems to accurately capture spatial relationships over time. Through an ongoing “rapid response” program operational since in Spring 2007, eleven substantial seacliff failure sites were mapped pre-collapse, immediately post-collapse, and repeatedly after the failure to constrain processes causing cliff failure and estimate the rate at which failed material is reworked. Comparison of the TLS data with wave (Coastal Data Information Program, CDIP, Scripps 2008), tidal (National Oceanic and Atmospheric Administration, NOAA, 2008c), and climate data (NOAA, 2008b) highlights the contributing mechanisms to the seacliff failures and the rapid reworking of the failed seacliff material. Failure sites were categorized based on the amount of wave contact (i.e., wave size) at the site to assess differences in the rates of sediment reworking. These classifications were determined by whether typical waves, minor storm waves, and/or major storm waves reached the site. For example, unconsolidated failed material on the beach itself was reworked by the average wave field at sites with

waves reaching the failure on a near daily basis. Conversely, other failures with less wave contact were only reworked by the largest waves during severe storm events. Finally, at sites where the failure material consists of large boulders, there are feedback mechanisms at play where the failed material protects the cliff base by stabilizing talus deposits, similar to rip-rap stabilization techniques. Such a feedback causes failures due to wave undercutting and notching to migrate laterally and might explain the long-term linear retreat of the seacliffs that minimizes the development of embayments and promontories.

INTRODUCTION

Several mechanisms contribute to the destabilization of seacliffs (Figure 5-1). Subaerial erosion breaks the cliff up from the top down and tends to relax or diminish the slope (Weissel and Driscoll, 1998). These processes are accelerated by chemical weathering caused by carbonic acid further dissolving the weakly cemented sandstone. Wave based erosion tends to create notches at the base of the cliff and creates vertical cliff faces when failures occur from wave cutting. The rate of cliff erosion is so rapid that one can easily observe dramatic changes on short time scales (10-20 years). While seacliff erosion threatens the development of the coastline (Griggs et al. 2005), it is a necessary and natural cycle that provides vital sediment (Haas, 2005; Young and Ashford, 2006a) to the beach, which then can act as a buffer to the nearshore processes that act to erode cliffs from the bottom up.

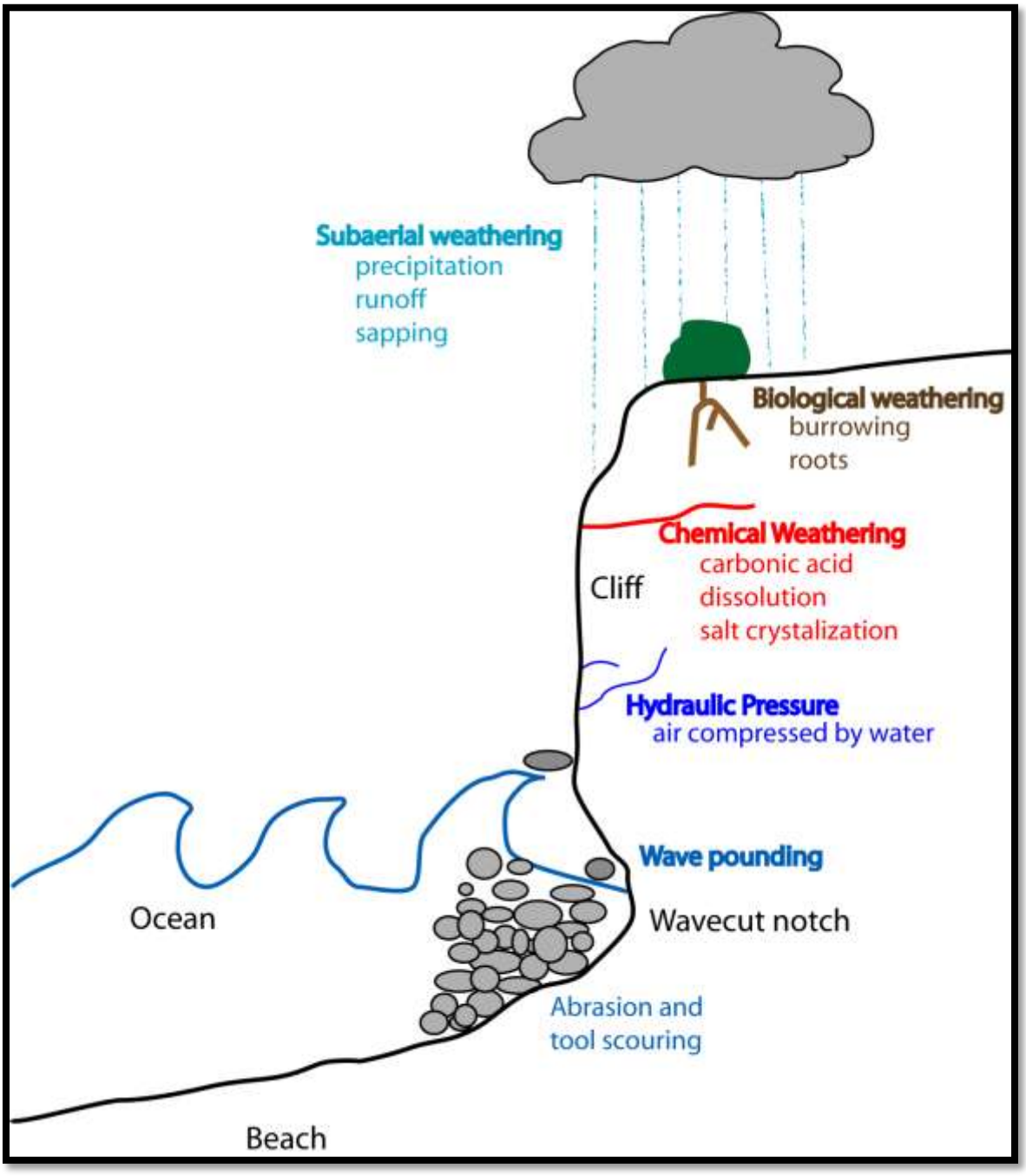

Figure 5-1. Schematic illustrating varying mechanisms contributing to seacliff erosion

Previous methods for analysis of seacliff retreat such as digital photogrammetry (i.e., Moore et al. 1999; Hapke and Richmond 2000), aerial Light Detection and Ranging (LIDAR) (Young and Ashford 2006) and oblique helicopter LIDAR (Rosser et al. 2008) have yielded important results, yet they have limitations for repeated coastal cliff surveys due to greater expense, difficult logistics, lower resolution, and/or the ability to capture the cliff face topography (including complex sea caves) in sufficient detail. Substantial change from seacliff failures greater than 30 m^3 can be observed monthly throughout the study area, and the corresponding data must be obtained on a regular basis before becoming overprinted by other events. Once temporal and spatial processes are understood, it is possible to characterize boundary conditions and processes that lead to cliff erosion.

Terrestrial LIDAR (LIght Detection And Ranging) has been proven to be an effective tool to study seacliff failures and morphology (Collins and Sitar, 2004; Rosser et al., 2005; Lim et al., 2005; Young and Ashford, 2007). Terrestrial laser scanning (TLS) uses time-of-flight or phase-based measurements to determine the distance of a sample point. TLS captures topological characteristics at high resolution, producing a detailed point cloud containing *X, Y, Z* coordinates, RGB color, and return signal intensity information. Typical scanners scan at rates of 2,000 – 50,000 points per second. A single scan with the I-Site scanner used for this study can acquire approximately 0.5-1 million sample points on the cliff and beach in about six minutes, densely

covering (~100 points per m^2) about 70 meters of coastline, depending on the complexity of the topography and efficiency of the surveyors. The aforementioned previous studies using TLS have shown the effectiveness of TLS to capture geometry for high-resolution 3D modeling at two time steps, one before and one after substantial failures. This study builds upon their work and reveals additional insights obtained through a "rapid response" program with repeated mapping of a site after a failure occurs, and tracking the dispersion of failure sediment. As the coastal environment is dynamic, continual observation is necessary to understand and assess coastal change.

REGIONAL SETTING

This study focuses on seacliff erosion and failure along the northern portion of San Diego County from Scripps Pier to Batiquitos Lagoon in Encinitas covering 20 km of coastline (Figure 5-2). The study area is divided into several sections based on natural breaks in the seacliffs by lagoons or canyons: Scripps, Black's Beach, Torrey Pines, Del Mar, Solana Beach, and Encinitas. Although there are some differences in the geology of each section, the above sections predominantly contain similar sediment and geologic formations. The two major geologic formations within this study area are the Delmar Formation and the Torrey Formation. The Delmar Formation is composed of fine-grained clays and silts with occasional sands deposited in an estuarine lagoonal environment. Strongly cemented shells within fine-grained, cohesive clay make this material more resistant to erosion than the overlying Torrey Formation. The

Torrey Formation consists of weakly-cemented, coarser-grained sandstone from barrier beach deposits formed along a submerging coastline (Kennedy, 1973). When meteoric water permeates the sandstone, the cement is dissolved and the sandstone begins to crumble. Wind erosion accentuates these areas of differential erosion and produces a honeycomb-like morphology.

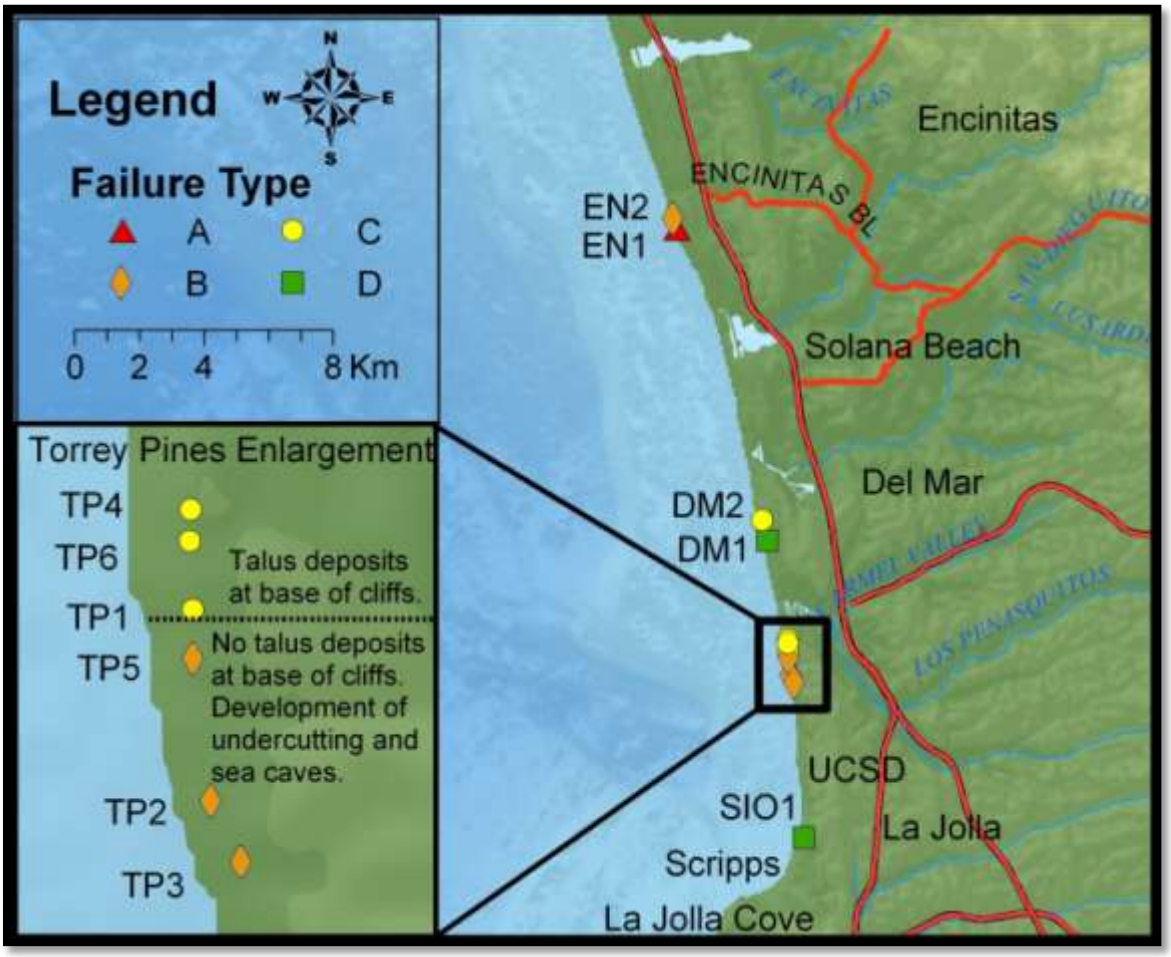

Figure 5-2. Study area map showing locations of failure sites. Note the demarcation line between cliffs with and without talus deposits. Type C failures occurred from subaerial erosion in areas with talus deposits on the North and Type B failures occurred to the South from wave undercutting because of no protective talus deposits.

The sediments of San Diego County consist of several well-sorted, cemented marine terraces that have formed as a result of sea level rise and fall in combination with tectonic activity throughout during California's geologic history (Kennedy, 2008). These deposits include nearshore marine, beach, estuarine, lagoonal and continental dune facies which have undergone cementation and compaction over thousands to millions of years to form sedimentary rocks. Due to the cycling sea level rise and fall through geologic time, the coast of San Diego County is particularly active as both ocean wave erosion and subaerial processes transport (Sunamura 1992) and rework the sediment along the coast. Figure 5-3 shows the rise of sea level over the last century.

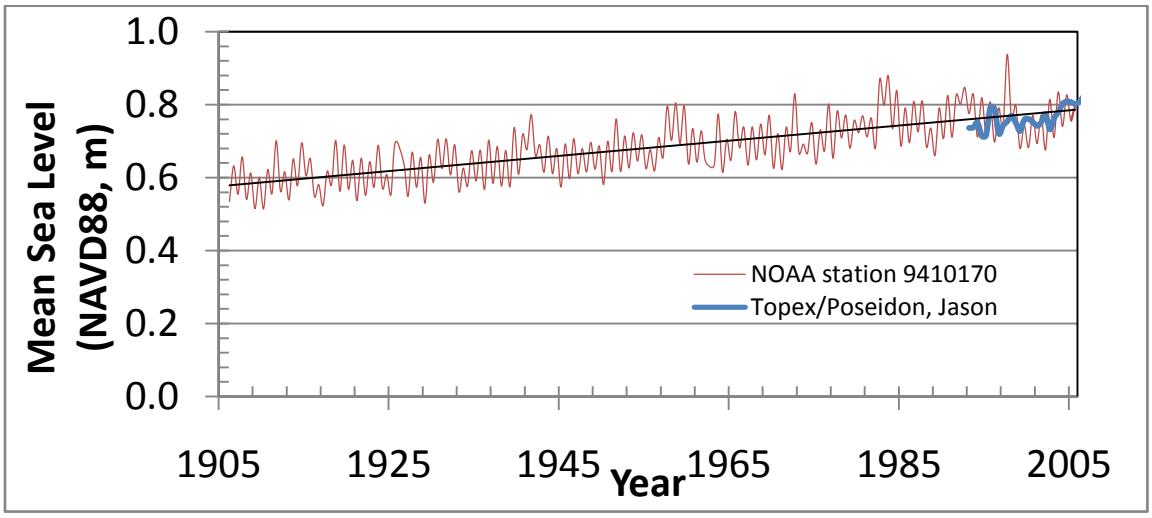

Figure 5-3. Plot of mean sea level with the seasonal variability removed and averaged over 6 months. Plot shows a trend of sea level rise of 2.1 mm/year. Tidal data obtained from NOAA station 9410170 (NOAA 2008b) and are referenced to the NAVD88 datum. Topex/Poseidon data obtained from http://sealevel.colorado.edu and was calibrated by Leuliette et al. (2004).

San Diego has a Mediterranean type climate with little rainfall throughout the year (NOAA, 2008c), especially during the summer months. Substantial development on the cliffs, however, has created increased surface runoff and groundwater from urban landscaping and irrigation. Heavy vegetation also covers many parts of the cliff.

METHODS

Several data sources were required to asses change at the failure sites. First, TLS was used to create geometric models of the seacliffs and failure masses. Changes in geometric conditions were assessed by determining failure volumes and evaluating changes in beach elevation. These geometric changes were compared to environmental data observed near the sites to understand the rates at which they occurred. Based on the environmental data, the failure sites were then classified based on differences in wave contact. The methodology for each of these analysis steps will now be discussed in greater detail.

TLS surveying

This study is builds on and expands the rapid response effort described in Olsen et al. (2008) where laser scans and site investigations were performed as soon as possible after a seacliff failure to obtain accurate failure volumes before wave reworking. The study area is prioritized in a GIS database based on the most recent observations through the study area. Regional baseline scans are performed at least twice a year (more in high priority areas) to quantify seasonal

variability. The Torrey Pines section was marked as the highest priority section because of multiple failures and thus was scanned most frequently (4-6 times per year). Thus, it was more likely that additional failures would be discovered in that section. The methods used to perform and georeference these surveys to UTM Zone 11 NAD 1983 coordinates are discussed in Chapters 2 and 3. In addition to periodic surveys, frequent photographic surveys are performed, allowing the research team to bracket failure dates.

Calculating failure volumes

A comparison of 3D cliff surface models can determine the initial volume of the failure. This is done by creating a surface of the initial conditions of the cliff from the most recent survey and the conditions of the cliff after the failure and comparing the volumes. This can then be compared to the volume calculated from the failure mass on the beach. Caution must be used in the algorithm used to calculate the volume because it must be orthogonal to the cliff. If an algorithm performs the calculation by a look in the Z (Elevation) direction toward the XY (Northing-Easting) plane, the volume can be erroneous if there is an overhang in the cliff because it may not be accounted for in a XY plane volumetric analysis. If a rapid response effort was performed and the team arrives soon after the failure, the volumes calculated from the failure mass and the volume of sediment lost from the cliff should be equivalent. Because often the failure is broken up with space between blocks, it can have a larger volume than that calculated from the

cliff measurement. If waves have reached the failure, its volume on the beach may not agree with the volume derived by differencing.

Failure volumes were not differentiated between soil type and size to determine whether the sediments would remain on the beach during beach sorting processes. These volumes will be determined as part of a continuing study as they require grain size analysis and observation of the failure sites for several years to determine volume of large rocks that were part of the failure that could not be determined in this study because they were buried under sand at times during the study and need to be evaluated over two winter seasons.

Volumetric analysis on a dynamic beach environment requires a systematic approach to calculate failure volumes. Depending on site morphology, different methods need to be implemented to produce consistent results. The following methods were used to create triangulated surfaces for the different types of failure sites. These methods assume that unless the failure is on a fixed platform, all failure volumes are relative to the current surrounding beach level, thus any sediment derived from the failure that is below the current beach datum becomes part of the beach and no longer is considered part of the failure volume. The methods use for volume calculations are:

1. Failure on slump or pre-existing failure
    A. Define failure boundaries
    B. Create surface of failure mass
    C. Remove areas previously covered by beach sand

D. Create surface of initial conditions (e.g. the cliff that will not erode until the fresh failure volume erodes). Obtain this data from the most recent scans.

E. Create a surface of the current beach levels based on failure boundaries.

F. Merge surfaces D and E together to form the comparison surface

G. Calculate the volume differences between B and E

2. Failure mass on a nearly planar beach

A. Define failure boundaries

B. Create surface of failure mass

C. Remove areas previously covered by beach sand

D. Select points on beach (not part of failure mass)

E. Fit a plane to selected points

F. Calculate volume difference between B and E

3. Failure occurs on a rock platform

A. Define failure boundaries

B. Create surface of the failure mass

C. Create surface of the platform from the most recent baseline scan

D. Calculate the volume between B and C

Modeling Beach Elevation Change

Beach elevations were also plotted for failure sites. Figure 5-4 shows the locations at which beach elevations were determined along the centerline of the

failure mass. These measurement locations are based off of the original failure location and do not change as the failure mass erodes, so that a representative beach elevation can be shown. The beach elevation at the immediate western edge of the failure is plotted for all surveys. Additionally, where available, beach elevations 5m, 10m, 15m, and 20m west of the failure elevation are plotted to show the changes in beach berms. The maximum failure elevation is also recorded for each TLS survey. As the failure erodes, the maximum failure elevation becomes closer to the beach elevation, although it should be noted that beach elevations are taken from the west (ocean-facing) side of where the maximum failure elevation is taken, so the failure elevation will be higher because the beach slopes upward to the East.

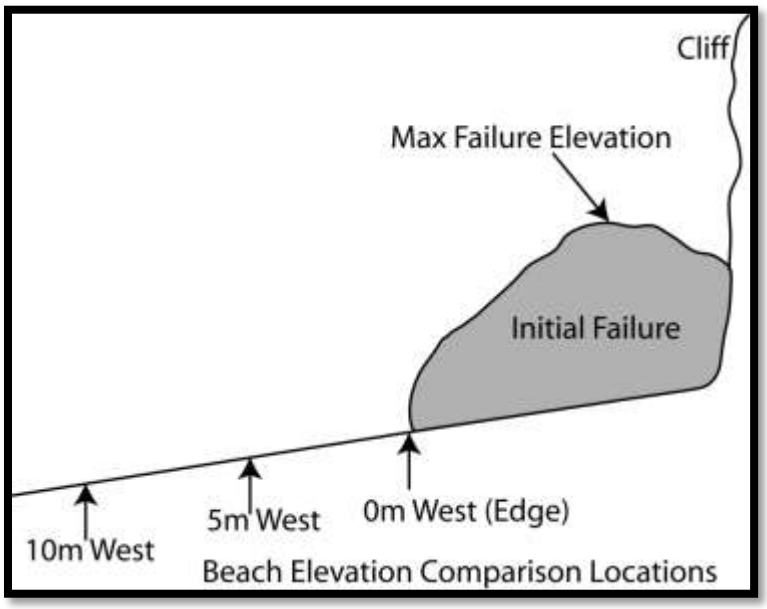

Figure 5-4. Schematic showing elevation measurement locations for beach elevation and maximum failure elevation. Note that the measurement locations for beach elevation are measured relative to the edge of the initial failure mass and are held constant as the failure mass erodes.

Modeling Environmental Conditions

Environmental conditions (Figure 5-5) are critical to understanding seacliff erosion and the reworking of failure sediment into the beach environment. Precipitation data were obtained from NOAA station 23188 (NOAA, 2008c) at the San Diego Airport. Wave height, period, and directional information were obtained from the CDIP off shore buoy 100 (Scripps, 2008). To fill a data gap from buoy TP100 during the period between 12/5/2007 and 12/12/2007, data from the Mission Beach (station 93) and Oceanside (station 45) buoys were averaged to approximate data for the missing time period. A comparison of these datasets for the month of December (Figure 5-6) shows reasonable agreement. Tidal information was obtained from the NOAA tidal gage 9410170 (NOAA, 2008b). These data were converted into the total water level (TWL) to compare the TWL to the beach height using the method outlined in Ruggiero (1996; updated in 2001 and 2008). The TWL is calculated as the sum of the tidal level and the runup level from the wave height and beach slope. The runup level can be estimated using the following empirical equation (Stockdon et al., 2006):

$$R_{2\%} = 1.1\left(0.35\beta(H_O L_O)^{1/2} + \frac{\left[H_O L_O(0.563\beta^2+0.004\right]^{1/2}}{2}\right) \quad (5\text{-}1)$$

where:

$R_{2\%}$ = the wave runup elevation with a 2% probability of exceedance,

β = the foreshore beach slope,

H_O = the offshore wave height, and

$L_O = (g/2\pi)T^2$ = the offshore wave length,

where T = the peak wave period, and

g = the acceleration of gravity (9.807 m/s^2).

Erosion of the failure mass occurs when the TWL is larger than the beach height. A typical beach slope of β = 0.05 measured and verified with multiple TLS surveys was used for the runup calculations in Figure 5-5.

Failure Site Classification

Failure sites are shown in Figure 5-7 and site characteristics are outlined in Table 5-1. Figure 5-8 shows a comparison of the failure dates with the environmental conditions. This provides insight into the potential cause at the time of failure. The failure sites were divided up into four major categories (Figure 5-9) based on annual wave contact with the failure. The classification was developed to assist in the prioritization of sites for repeat surveys and to understand sediment redistribution patterns. These sites were classified by:

(**A)** Consistent wave contact on a nearly daily basis (EN1)

(B) Intermittent wave contact during minor and major storms (EN2, TP2, TP3, TP5)

(C) Wave contact during major storm events only (TP1, TP4, TP6 and DM2)

(**D)** Rare wave contact (DM1 and SIO1)

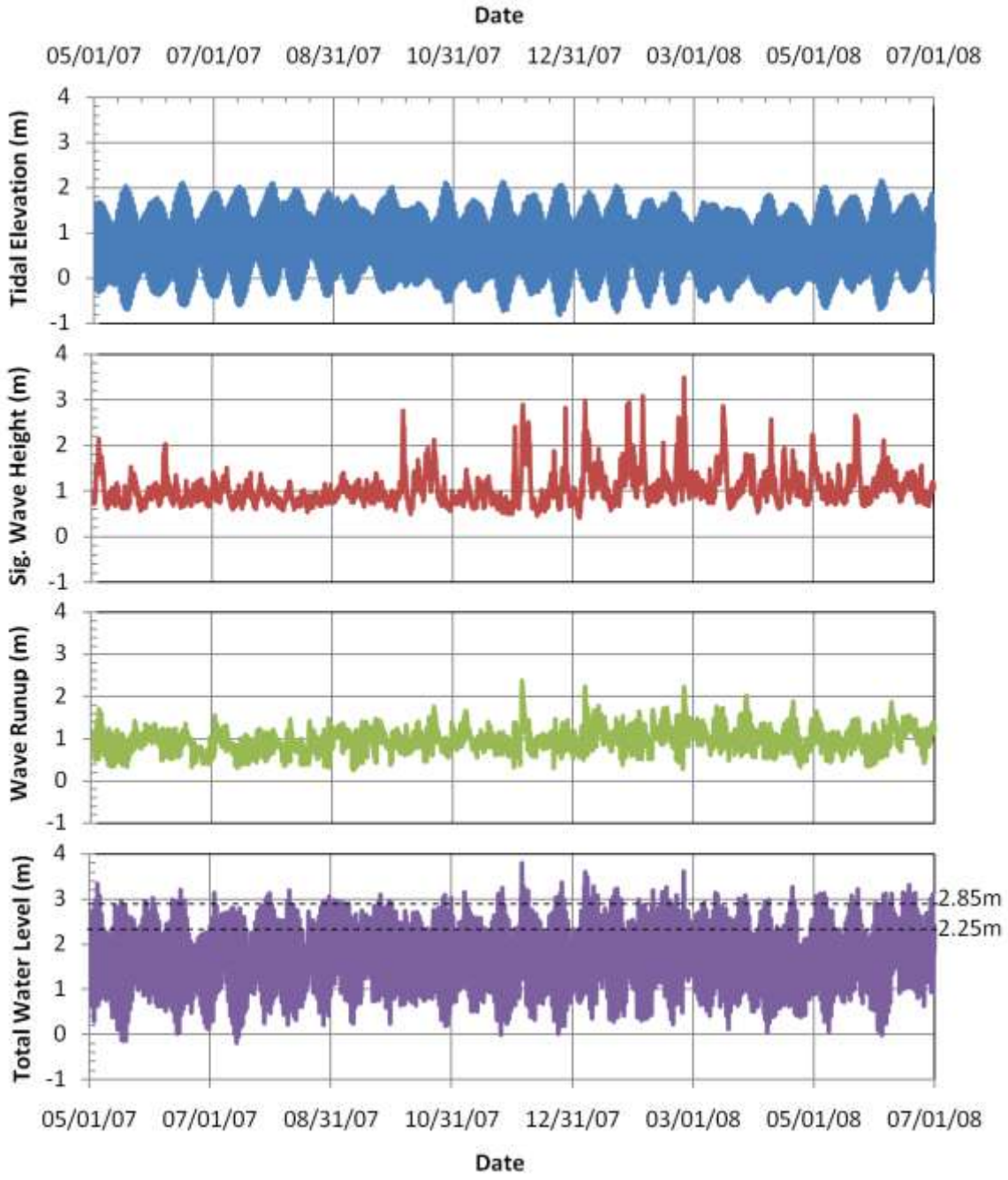

Figure 5-5. Calculation of Total Water Level (NAVD88) using method described in Ruggiero et al. (2008) from (a) Tidal measurements (NOAA Station 9410170) (b) Significant Wave Height (CDIP buoy 100), (c) Wave Runup with 2% proabability of exceedance (calculated using Stockdon, 2006) producing (d) a total water level estimate.

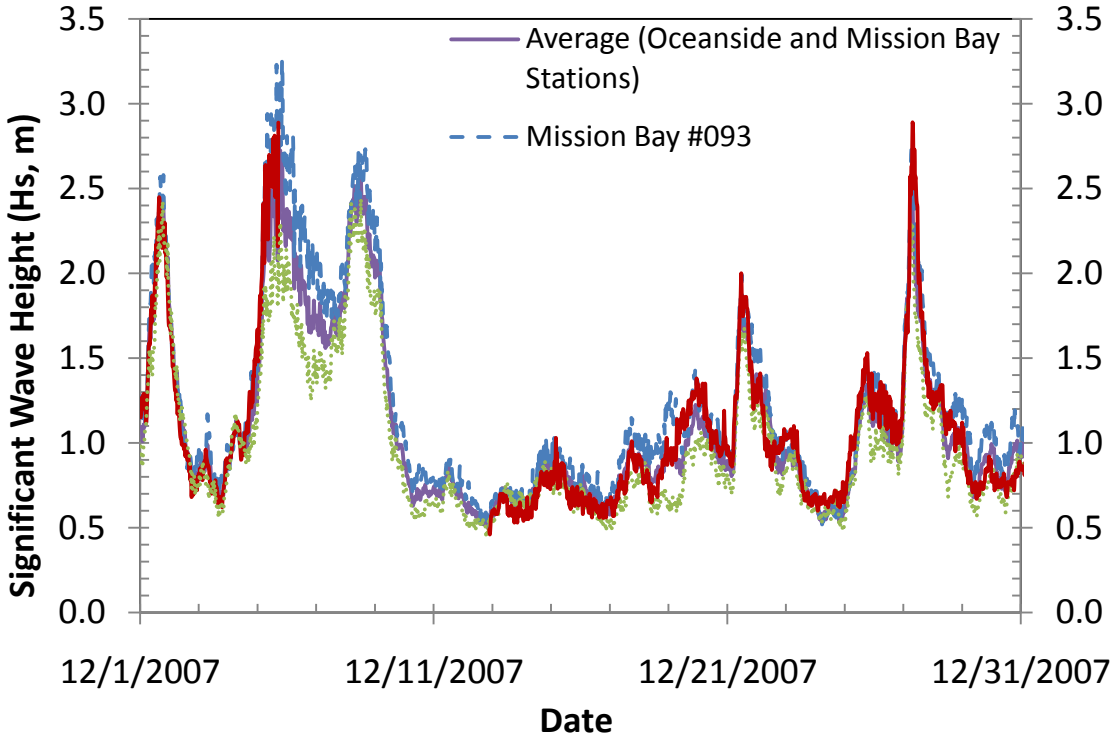

Figure 5-6. Comparison of wave data and averaging for missing data at CDIP buoy #100 (CDIP, 2008)

Type A failure sites occur in areas where the waves directly impact the cliff regularly throughout the year and thus would typically be wave-based failures. The sediment from these sites is quickly reworked and distributed along the beach. These sites are where the beach elevation is typically lower than the mean TWL plus one standard deviation (2.25 m for the study period). Type B sites have intermittent contact with waves throughout the year when minor storms create larger waves and also typically occur as a result of wave based erosional processes. These sites are where the beach elevation is typically

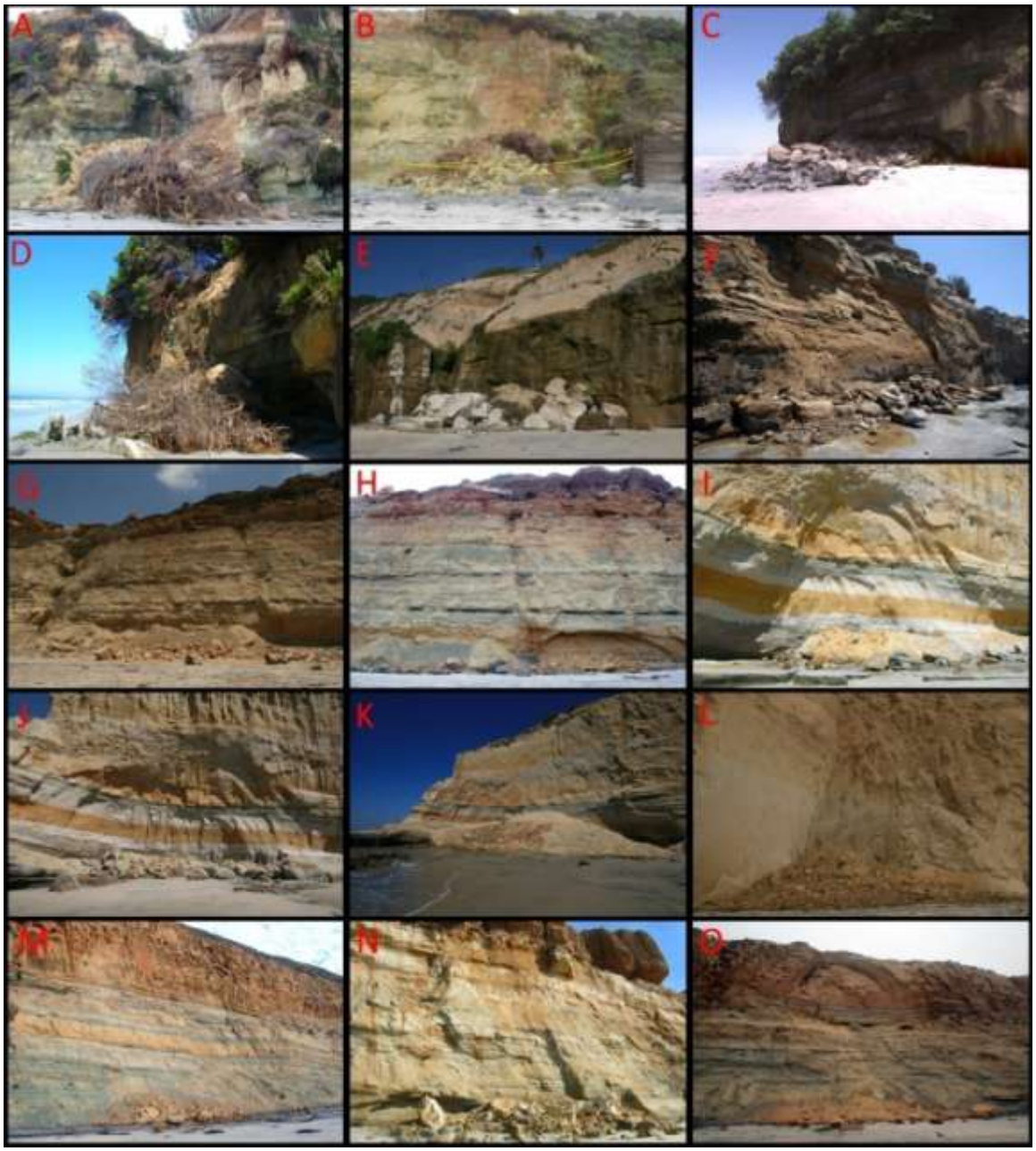

Figure 5-7. Photographs of failure sites (A) DM1 8/24/2008 (B) DM2 8/24/2008 (C) EN1 a 6/7/2007 (D) EN1b after second failure 9/10/2007 (E) EN2 3/7/2008 (F) SIO1 9/25/2007 (G) TP1a 8/6/2007 (H) TP1b after second failure 7/8/2008 (I) TP2a 9/10/2007 (J) TP2b after second failure 3/4/2008 (K) TP2c after third failure 10/2/2008 (L) TP3 10/14/2007 (M) TP4 10/29/2007 (N) TP5 1/31/2008, and (O) TP6 6/18/2008

Table 5-1. Summary of failure sites and enivornmental conditions at failure (Geologic Units: DM = Delmar formation, TS = Torrey Sandstone formation)

Failure site	Type	Geologic Unit	Failure date	Initial post-failure survey date	Initial Failure Volume m^3	Environmental factors at failure: Talus Deposits	Waves	Ground-water	Prec.	Probable cause of failure
EN1a	A-SL	DM	6/6/2007	6/7/2007	139	N	Y	Y	N	Undercutting /Groundwater
EN1b	A-S	TS	Sept 2007	9/10/2007	30	N	Y	Y	N	Retrogressive failure
EN2	B-L	DM	Feb 2008	3/7/2008	177	N	Y	Y	N	Undercutting /Groundwater
TP1	C-M	TS	8/4/2007	8/6/2007	31	Y	N	N	N	General Instability
TP2a	B-M	TS	8/23/2007 (+/- 1 day)	8/24/2007	79	N	Y	N	N	Undercutting
TP2b	B-M	TS	2/10/2008 (+/- 5 days)	2/17/2008	50	N	Y	N	N	Undercutting
TP2c	B-S	TS	9/22/2008	9/23/2008	445	N	Y	N	N	Retrogressive
TP3	B-S	TS	9/30/2007 (+/- 3 days)	10/5/2007	28	N	Y	N	N	Wave impact
TP4	C-M	TS	10/20/2007 (+/- 5 days)	10/29/2007	168	Y	Slight	N	Y	Precipitation
TP5	B-M	TS	1/28/2008 (+/- 1 day)	1/31/2008	120	N	Y	N	Y	Precipitation
TP6	C-M	TS	6/16/2008 (+/- 1 day)	6/18/2008	77	Y	Y	N	N	General Instability
DM1	D-S	TS	8/21/2007 (+/- 7 days)	8/28/2007	88	N	N	Y	N	Groundwater
DM2	C-S	TS	Summer 2007	8/28/2007	24	N	N	Y	N	General Instability
SIO1	D-M	TS	9/2/2007 (+/- 7 days)	9/12/2007	30	N	N	Y	N	Groundwater

lower than the mean TWL plus two standard deviation (2.85 m for the study period), but larger than the mean plus one standard deviation (2.25 m). Type C sites experience wave contact only during large winter storms because of protection by a beach berm during summer or a rock platform. These sites show little to no change in failure volumes, with the only change during large storm events when the wave runup is sufficient to reach the failure. These failures are

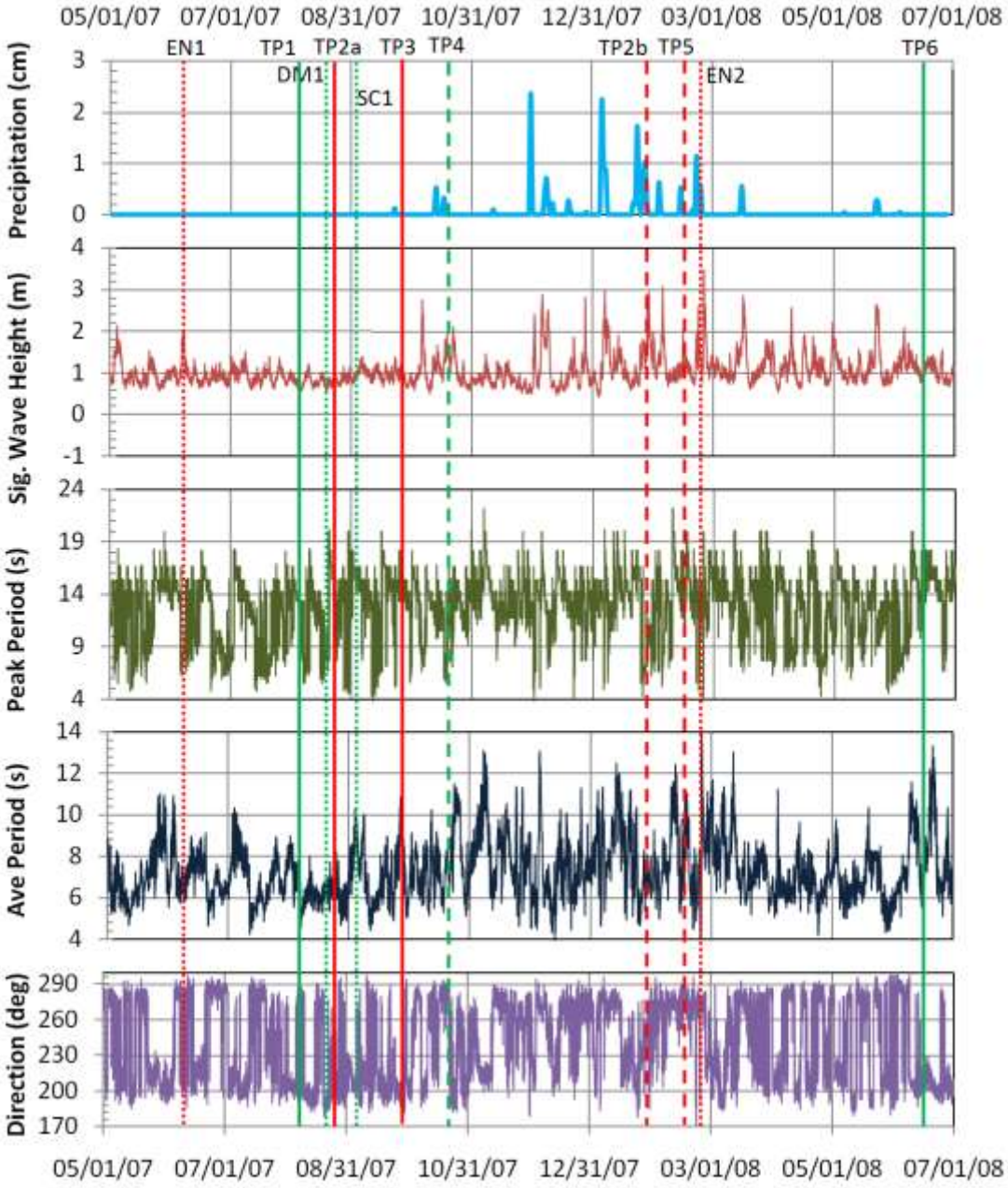

Figure 5-8. Comparison of failure occurrences with (a) precipitation (NOAA, Station 23188), (b) significant wave height, (c) peak wave period, (d) average wave period, and (e) wave direction from CDIP buoy 100. Red lines denote wave based failures and green lines denote subaerial dominated failures. Dashed lines represent precipitation based failures and dotted lines indicated the presence of groundwater. Dates and times are Coordinated Universal Time (UTC).

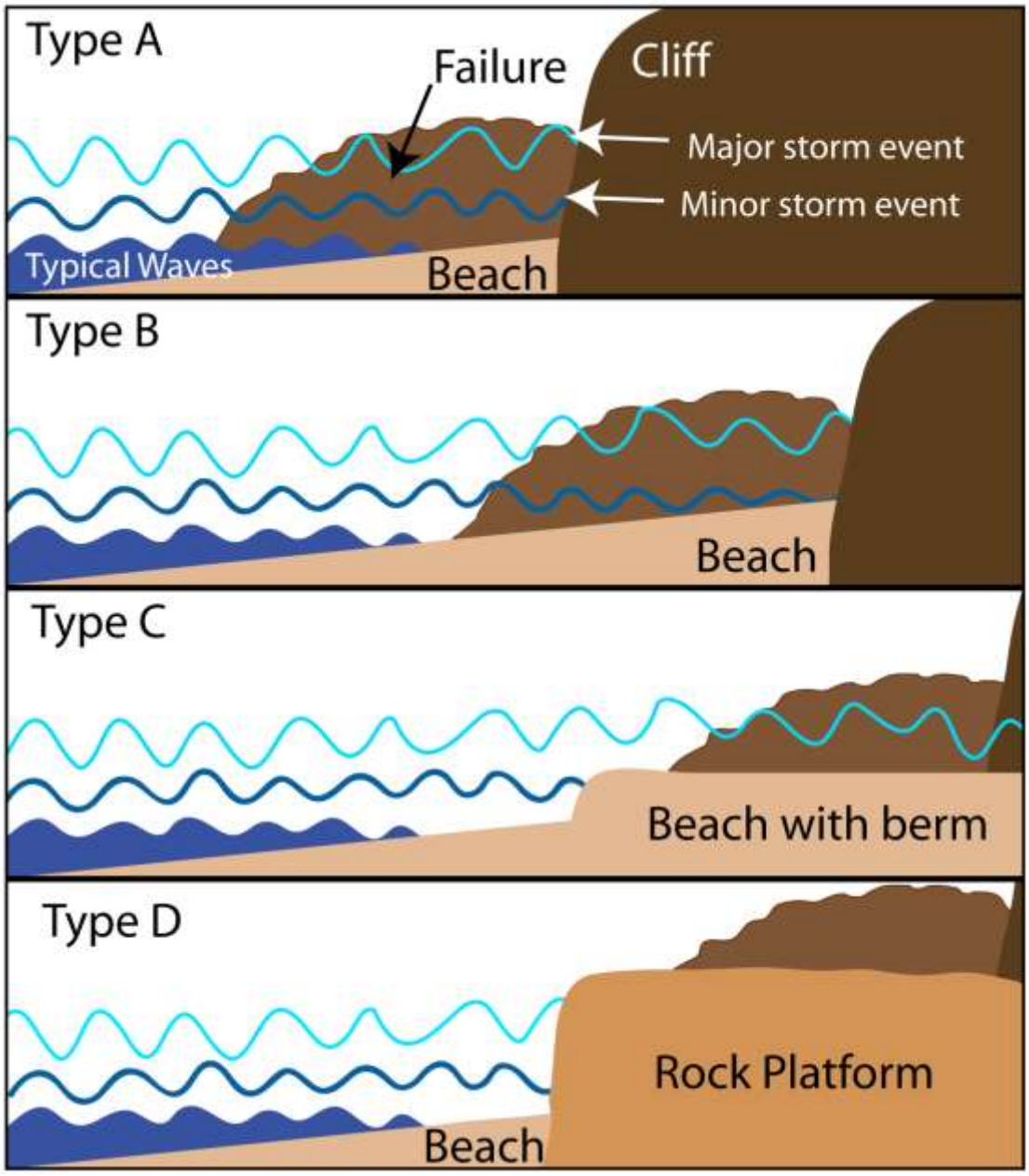

Figure 5-9. Comparison of typical site profiles at time of failure and varying wave conditions experienced at the site.

for the most part caused by subaerial processes, although they can occur as a result of extreme wave events. These are sites where the beach elevation is typically higher than the mean TWL plus two standard deviations (2.85 m for the study period), but are still accessible during large wave events. Type D sites have rare contact with waves because failure mass falls on an elevated rock platform. These failures are predominantly caused by subaerial processes.

A secondary identifier describing the dominate failure material size was added to characterize further failures types as follows:

S = mostly small grained particles (sands, gravels, small rocks up to 0.1 m in size)

M = mostly medium sized rocks up to 0.3 m in size, and

L = mostly large rocks and boulders > 0.3 m in size.

The material size plays a significant role in determining whether it will be reworked by waves as a failure with larger rocks will require more wave energy to be reworked.

FAILURE DAMAGE POTENTIAL CLASSIFICATION

To assess damage potential of seacliff failures, an initial, simple classification of potential damage from a failure based on its size in volume (V) was conducted using the rapid response data in Table 5-1 and Table 5-2. Because smaller seacliff failures are more frequent than large failures (Young and Ashford, 2007), an exponential model was selected for the analysis and

provided a better fit to the data than normal distribution and other models. Equation 5-2 shows the exceedance probability for an exponential distribution:

$$p(V > V_i) = e^{-\lambda V_i} = e^{-V_i/E(V)} \qquad (5\text{-}2)$$

where:

p(V>Vi) = the probability of the failure volume (V) exceeding a volume (V_i),

E(V) = the mean failure volume = 106 m^3 for this dataset, and

λ = *1/E(V)* = 0.00942 m^{-3}*, for this dataset.*

To evaluate effectiveness of the exponential distribution, the model (Figure 5-10) was compared to the percent of all failure volumes (*V*) exceeding each individual failure volume (V_i). The model provided a very good (r^2 = 0.95) fit with the data. Demarcations using exceedance probability thresholds of Minor (p>0.75, V_i>30m^3), Moderate (0.25>p>0.75, 30m^3<V_i<150m^3) and Major (p<0.25, V_i>150m^3) were created. The subsequent classification of each individual failure can be seen in Table 5-2.

Several factors about the data used for the development of this model should be noted. First, this model was created based on data from one year during a dry period. Seacliff failures tend to be larger and more frequent during high rainfall and storm events. Additionally, the data used for this classification model was based off a rapid response surveys that, due to resource constraints,

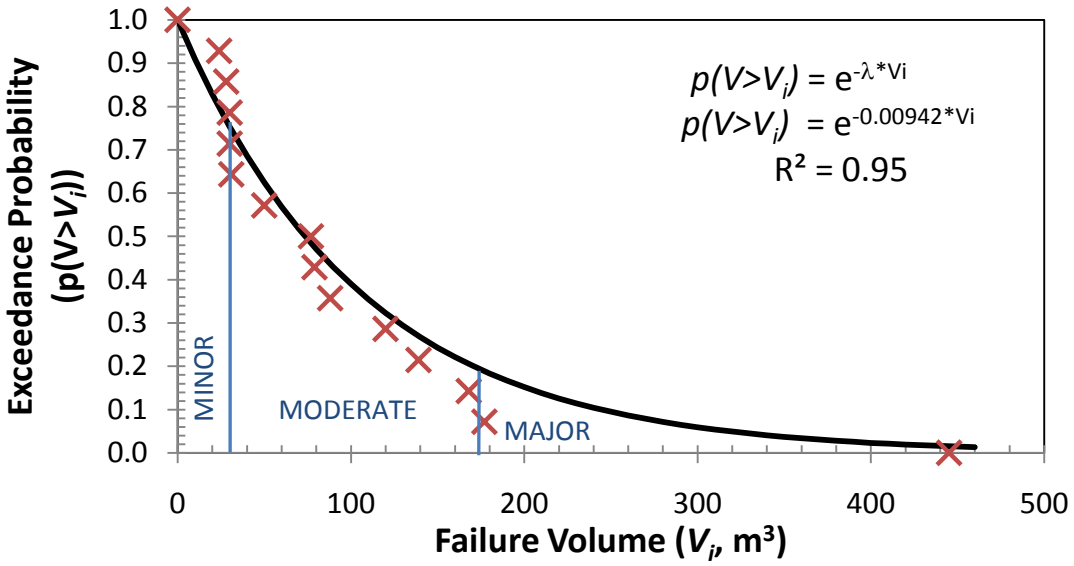

Figure 5-10. Exceedance probabilities as a function of failure volume, showing classification demarcations.

Table 5-2. Failure Classifications based off exceedance probabilities.

Failure Site	V_i (m^3)	# Sites V> V_i	% Sites V> V_i	p(V> V_i)	Classification
DM1	88	5	36	0.44	Moderate
DM2	24	13	93	0.80	Major
EN1a	139	3	21	0.27	Moderate
En1b	30	11	79	0.75	Major
EN2	177	1	7	0.19	Minor
SIO1	30	10	71	0.75	Major
TP1	31	9	64	0.75	Moderate
TP2a	79	6	43	0.48	Moderate
TP2b	50	8	57	0.62	Moderate
TP2c	445	0	0	0.02	Minor
TP3	28	12	86	0.77	Major
TP4	168	2	14	0.21	Minor
TP5	120	4	29	0.32	Moderate
TP6	77	7	50	0.48	Moderate

were only done on failures that were estimated to be 25 m^3 or larger. Thus, failure events smaller than 25 m^3, which occur on a regular basis in the study area, were screened from the analysis. Also, many factors can contribute to the potential damage that can occur because of a seacliff failure. This classification system only looks at the size or volume of the failure. Potential other factors include, but are not limited to, proximity of structures to the cliff edge, proximity of people to the cliff, number of people in the vicinity of the failure, nature and size distribution of failure material, and the potential of the cliff to fail (including frequency of wave contact, precipitation, and groundwater at the site). While the analyses of such parameters are well beyond the scope of this dissertation, it is an important endeavor for future research.

It is important to note that although the classification provides initial guidelines for damage potential, a “Minor” failure can still have disastrous consequences. For example, during this study period, a tourist was killed by a $4m^3$ failure.

RESULTS

Failure types A-D (Figure 5-9) were all observed throughout the study area. Here in the results, details of the individual sites are discussed (Figure 5-2, Figure 5-7) in light of failure type and rate of reworking, and unique observations from field investigations.

Type A Failure Sites

EN1

This failure (Figure 5-11) occurred during June 6, 2007, as a result of tension failure caused by a combination of wave undercutting creating a large sea cave and a substantial amount of groundwater sapping both adding weight to the rock above the sea cave and potentially weakening the rock (Figure 5-12). The timing of the failure correlates with a minor wave storm event (Figure 5-8). Groundwater expulsion occurs along the contact between the Del Mar and Torrey formations, because the claystones acts as an aquitard and thus creates a region of dense vegetation. This failure is continually impacted by waves (both summer and winter) except during low tide (Figure 5-13). Volumetric analysis for the failure, as shown in Figure 5-11 and Figure 5-13, show the impact of the waves on the slide mass. When scanned on the day after failure, the slide volume was 139 m^3. The original volume was most likely larger as it was exposed to waves for a day. Volume estimates could not be computed from the cliff because the cliff was obscured prior to the failure by heavy vegetation. Within two weeks of the failure (Figure 5-13), the slide volume dropped to 47 m^3, as most sand, gravel, and rocks smaller than 0.5 m in diameter were eroded unless they were close to the cliff and on top of large rocks. Thus, this site was given a secondary designation, *S*. Newer, small piles of sediment were observed a top the old failure (Figure 5-14), resulting from the unstable, upper cliff. Boulders as large as 1m in dimension had moved between the surveys. Beach

heights had also increased by 0.3 m between these surveys, although it is difficult to attribute whether this records additional sediment sourced from the slide or seasonal beach height fluctuations (Figure 5-14). Figure 5-14 shows the centerline profile of the site obtained from all laser scans. Note the rapid decrease between the first two surveys after failure and the eventual rise of the beach to cover the failure mass.

A survey performed one month after the failure showed the slide had a volume of 37 m^3. The summer wave energy was not sufficient to rework the larger rocks and did not reach the loose sediment sitting on top of those rocks. Subsequent site visits did not show much change until about three months after the initial failure, a substantial amount of vegetation and about 30 m^3 of sediment from the unstable upper cliff collapsed. Subsequent site visits showed a continual increase in sediment on top of the large rocks remaining from the first failure, caused by the instability of the upper slope. This new sediment was too high to be reached by typical waves (Figure 5-13). Eventually during the winter months where the TWL (Figure 5-13) was high enough to reach the sediment, it was quickly washed away, once again leaving only larger rocks (>1/3 m) on the beach.

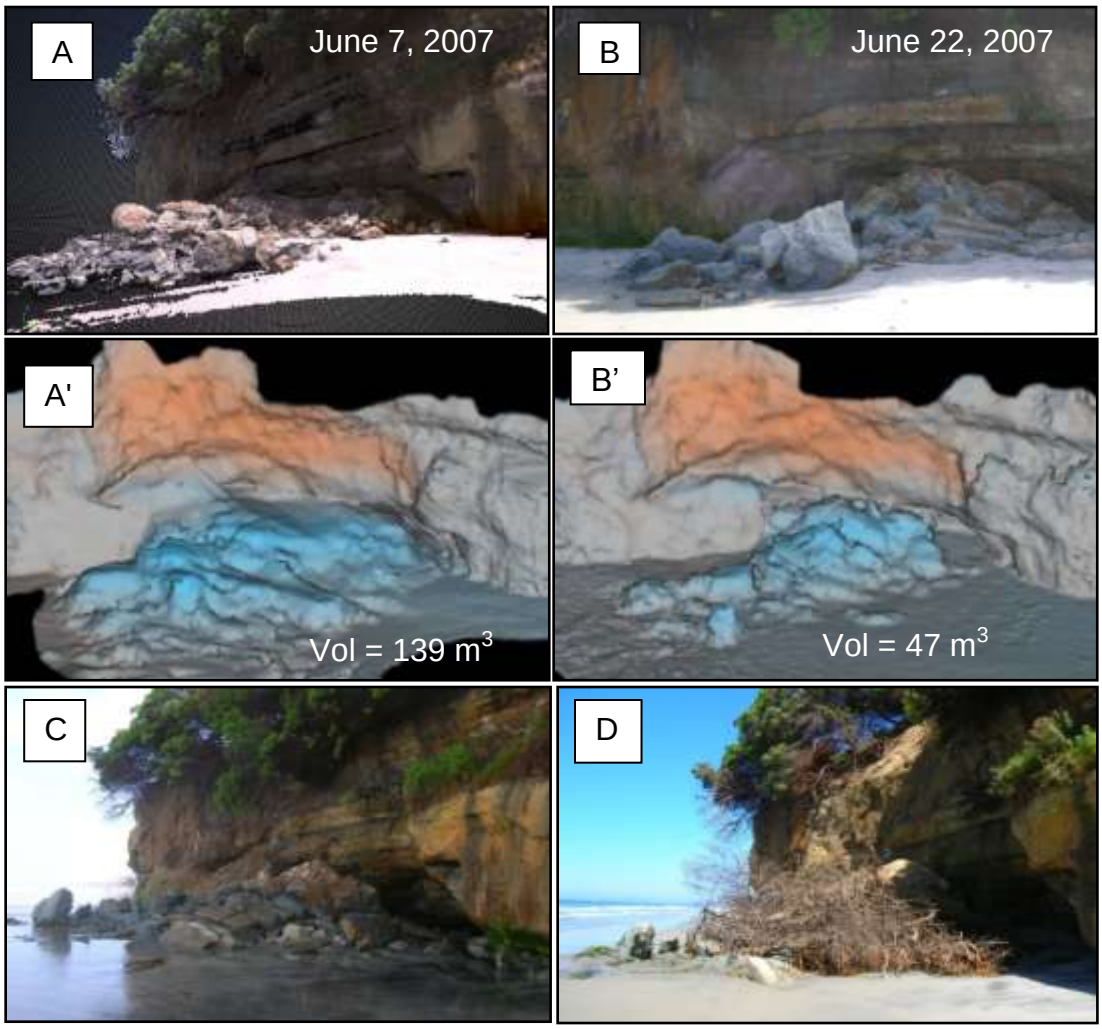

Figure 5-11. Surface comparison of a cliff failure in Encinitas (a) June 07, 2007 (1 day after) and (b) June 22, 2007 (2 weeks after) where blue represents accretion and orange represents erosion compared to scans from April 2005. Continual Monitoring of the failure (c) from a site visit 7/28/2007 showing the failure mass inundated from the waves, and (d) after collapse of vegetation above (9/10/2007)

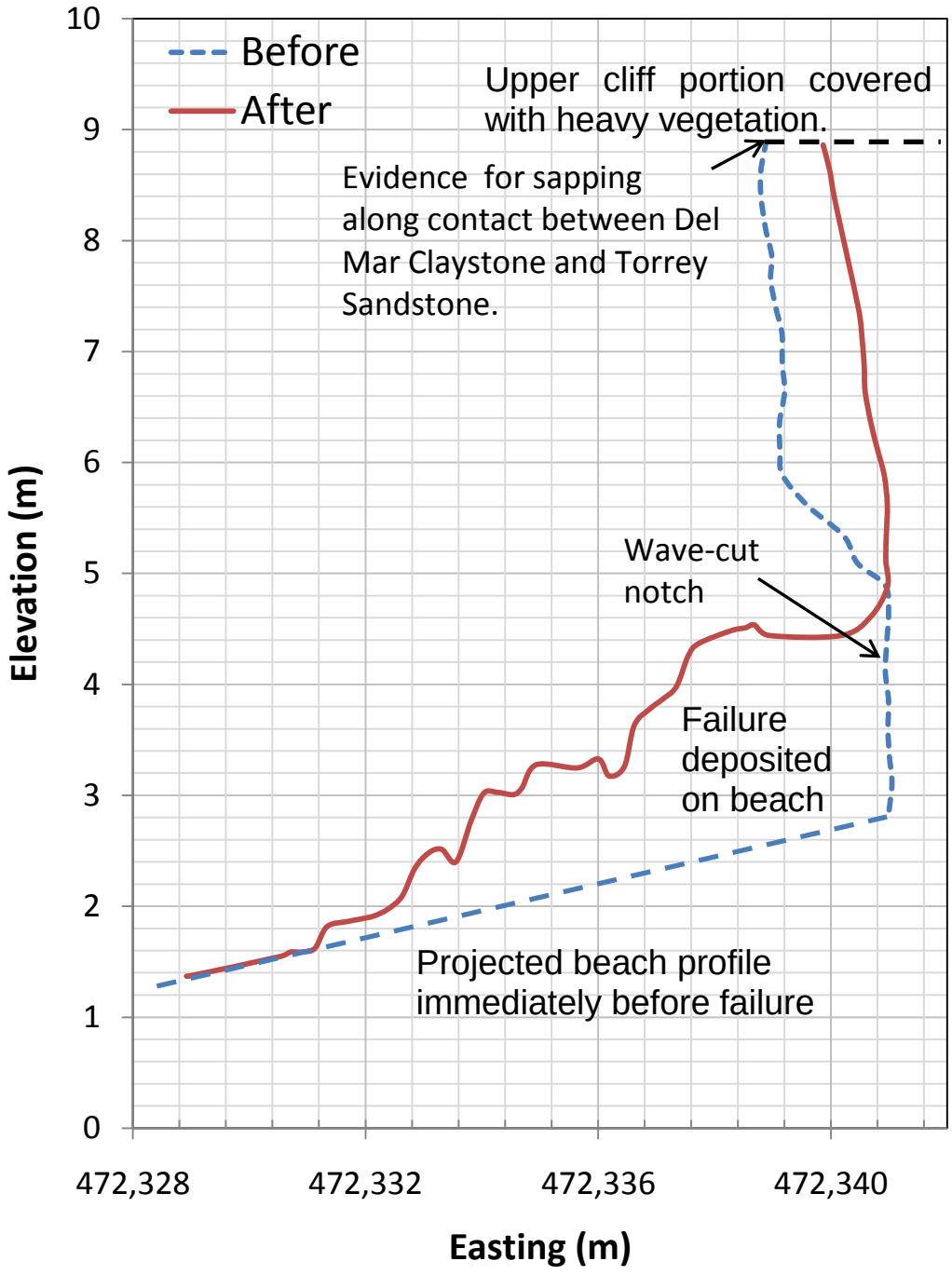

Figure 5-12. Cross section of failure site EN1 from an April 2005 LIDAR survey before the failure and a June 7, 2007 LIDAR survey after. The upper portion of the cliff was removed because LIDAR does not penetrate heavy vegetation.

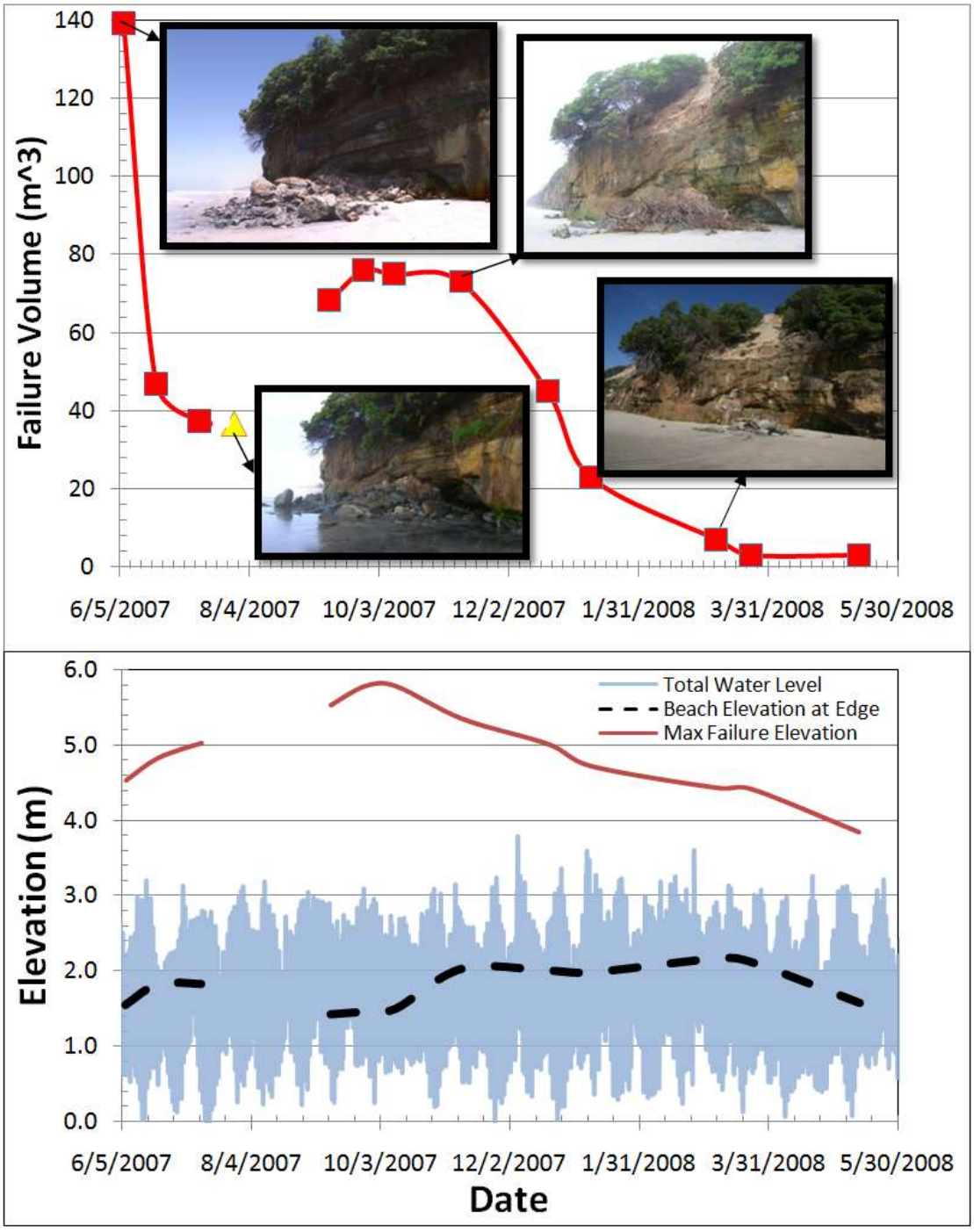

Figure 5-13. (A) Failure mass volume of site EN1 with time and (B) comparison of total water level and beach elevation immediately west of failure mass

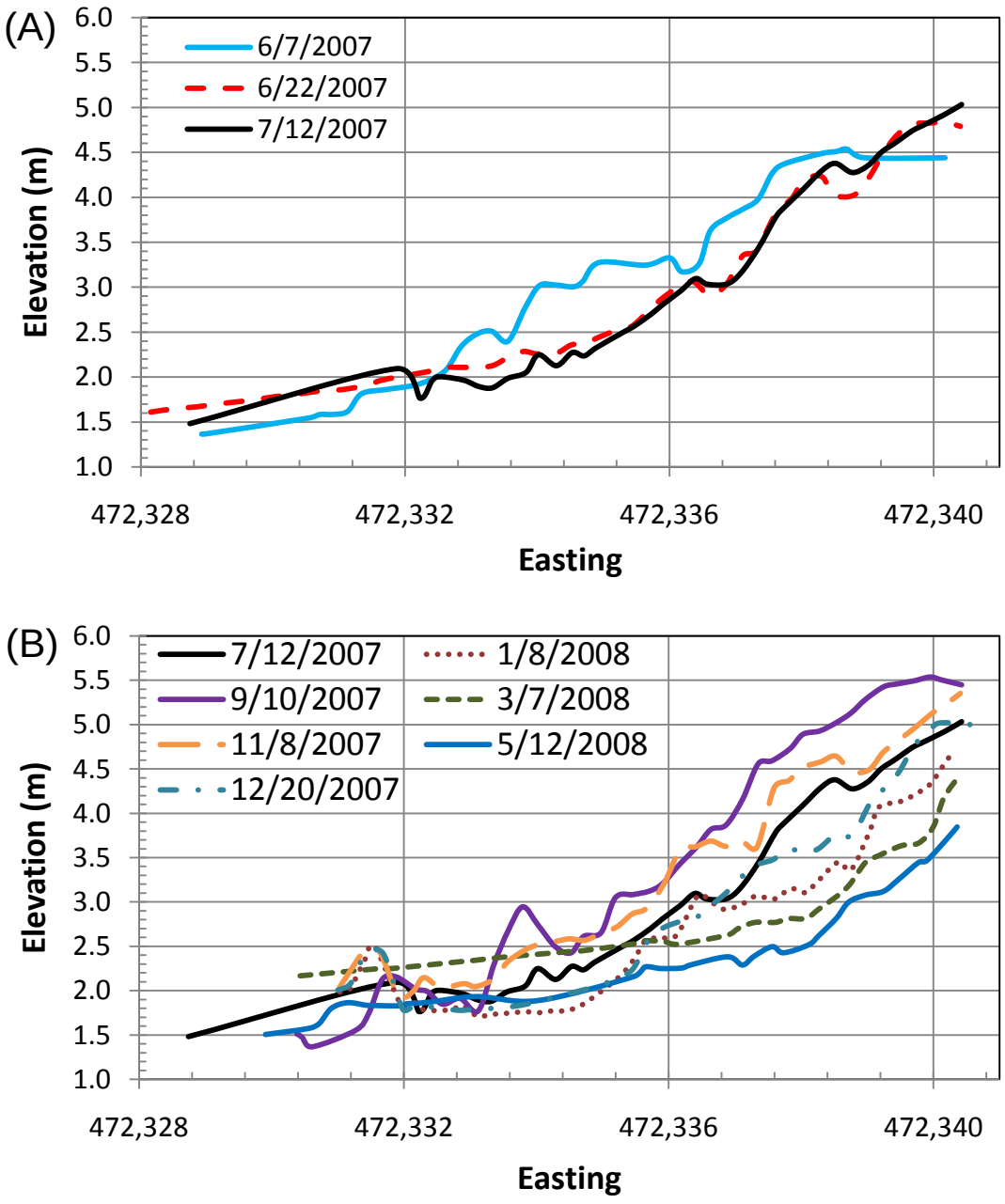

Figure 5-14. Failure mass profiles at site EN1 (A) before first failure and (B) after second failure. Black line representing scans performed on 7/12/2007 are shown in both (A) and (B) for reference. For clarity purposes, scans performed on 9/25/2007, 10/7/2008, and 3/23/2008 were omitted. Note that vegetation was not removed for cross-sections of scans performed between 9/10/2007 through 5/12/2008 but was removed for sediment volume calculations.

Type B Failure Sites

EN2

The failure at Site EN2 was discovered during a routine visit to site EN1 on March 7, 2008. The failure was estimated to have occurred during the end of February 2008 because the vegetation that had fallen with the failure was still green when surveyed in March. Figure 5-8 shows that a major wave event and some precipitation occurred in this time period. Figure 5-15 shows a cross section comparing the cliff profile before (Oct. 2007) and after (March 2008) failure. This failure also appears to be triggered by tension caused by a wavecut notch. Substantial groundwater sapping is again observed along the contact of the Delmar and Torrey formations as evidenced by the vegetation at the edge of the cliff, although not nearly as much vegetation as site EN1. The failure mass was approximately 177 m^3 in volume, when originally surveyed. Comparing the cliff from the March 2008 surveys and the October 2007 surveys yielded a volume change of approximately 200 m^3. A precise number could not be obtained because the failure covered the bottom of the cliff, so the basal shape of the cliff scar had to be estimated. The beach elevation was approximately 3m on the western boundary of the failure mass when surveyed in March, so the failure mass has been mostly out of the range of waves since it was discovered.

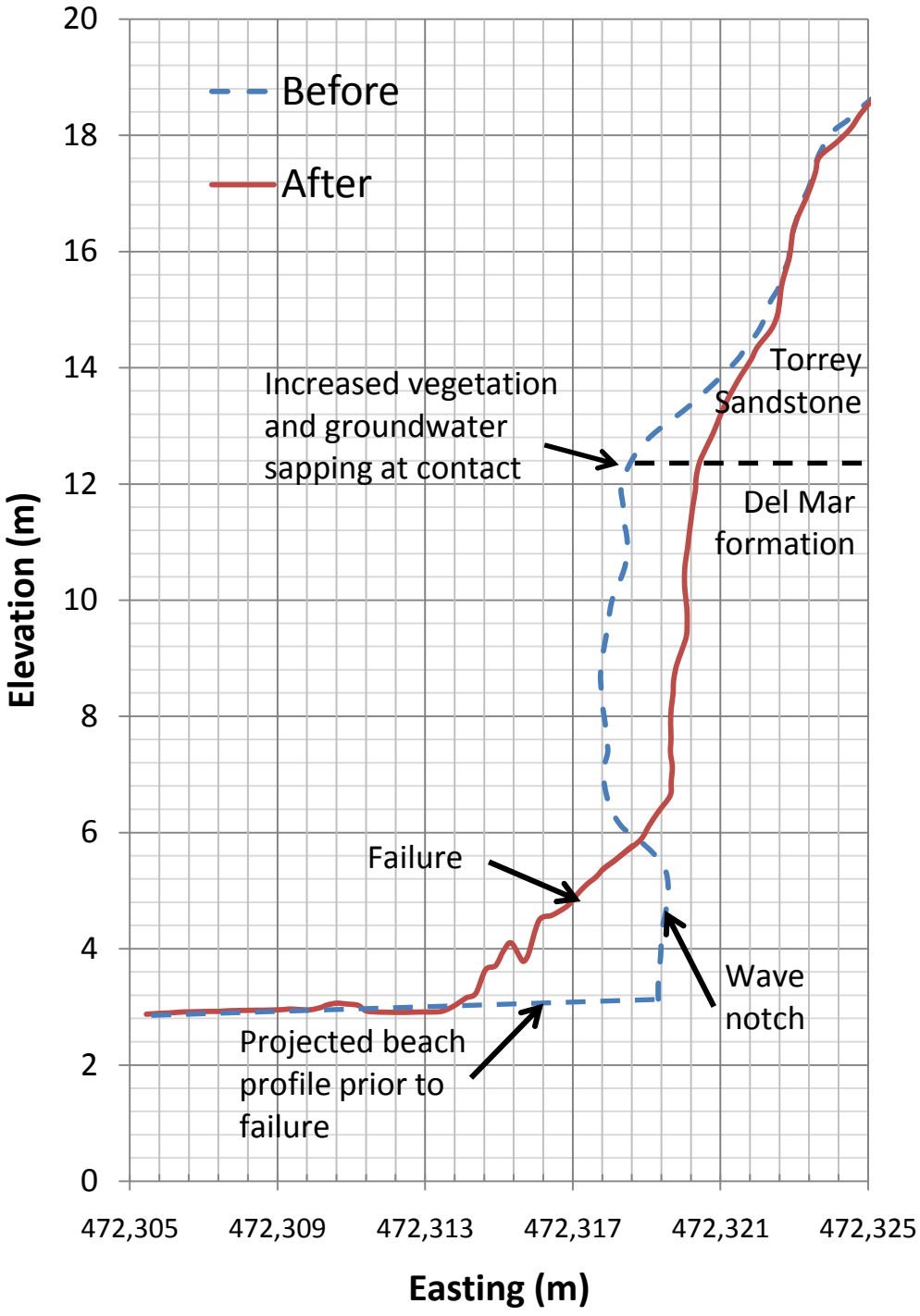

Figure 5-15. Cross-section analysis for site EN2 before (Oct 10, 2007) and after failure (March 7, 2008).

TP2

The failure at site TP2 (Figure 5-16) occurred within a day of August 23, 2007 on the South side of Flat Rock at Torrey Pines State Reserve. This is site is of substantial concern because the failure mass landed on a pedestrian pathway commonly used to access the southern end of Torrey Pines due to limited beach access during high tides. The researchers were notified of this failure by people who frequently walk this section of the beach while performing a site investigation for TP1. This failure (8/23/2007) had an original volume of 79 m^3. Within 20 days, the failure volume had dropped to 58 m^3. Site visits at high tide showed that the waves only reached one side of the slide mass as they were blocked by exposed platforms surrounding the failure. A survey performed 1.5 months following the failure showed the failure volume had increased to 74 m^3, which indicates that although the waves were eroding part of the failure, there was additional sediment being supplied to the failure by continued cliff erosion . This survey showed minor movement of rocks less than 0.33 m in diameter from the waves. The beach sand levels in the small cove area in front of the failure mass increased 0.2 m during this time. In contrast, on the north side of Flat Rock the sand levels decreased (up to 0.5 m) during this same time period. Thus, sediment derived from the failure was trapped in this small cove and caused small beach inflation. Additional rock and sediment accretion was commonly observed during site visits. In early February 2008, a second collapse of 50 m^3 occurred at this site (Figure 5-16) during a major wave event (Figure 5-8).

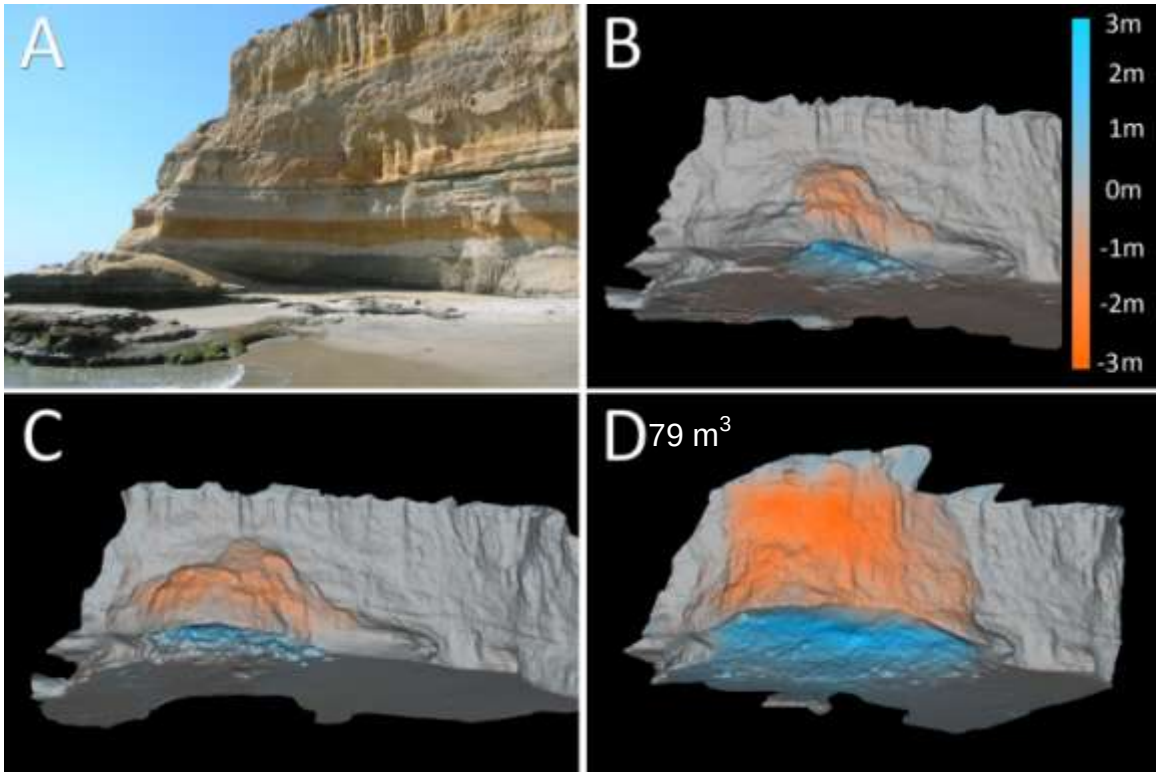

Figure 5-16. Comparison of Site TP2 (a) before failure (6/30/2006) and after significant failures (b) 8/23/2007 (c) 2/17/2008, and (d) 9/23/2008. All surface comparisons are relative to a survey completed on 11/3/2006.

The first two collapses occurred on the lower portion of the cliff, creating a substantial overhang. On September 21 or 22, 2008, the upper overhang collapsed, adding 445 m^3 of material to the existing failure. Figure 5-17 shows a map of the failure site at Flat Rock, derived from the TLS data. Flat Rock and other exposed rocks act as barriers protecting the cliff from the waves. However, waves approaching from a direction of 245˚ and 280˚ clockwise from true North will directly impact the cliff. As observed in the wave field (Figure 5-18), prior to the failure, there was a substantial amount of time where low-period (frequent)

waves were travelling in this direction, maximizing their impact on the cliff. This failure most likely occurred during a surge of low-period waves as the tide was receding that were from a direction of about 245˚, which thus focused on the cliff base.

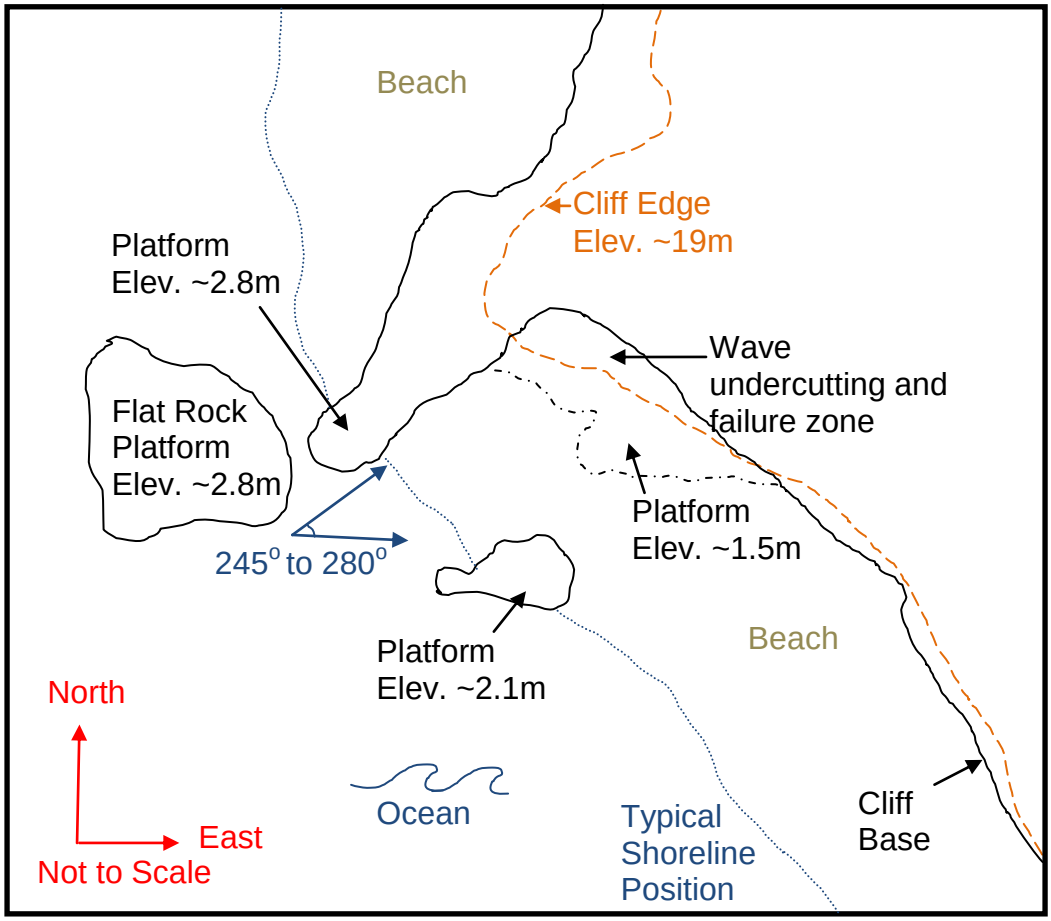

Figure 5-17. Plan view schematic showing cliff and platform geometry for Flat Rock, Torrey Pines Reserve. Note that an incoming peak wave direction of 245° to 280° measured clockwise from True North maximizes energy transfer to cliff at failure zone.

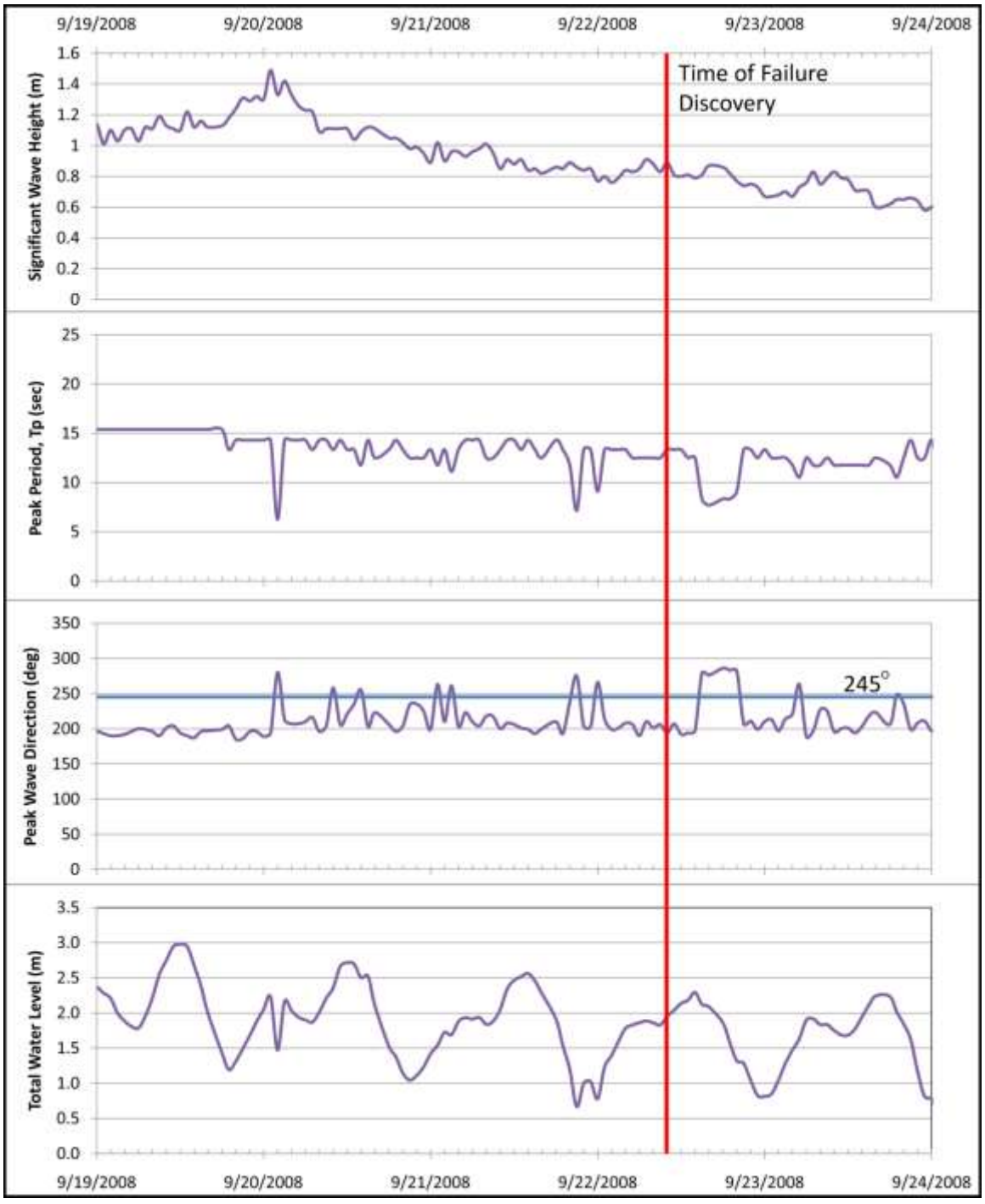

Figure 5-18. Environmental conditions at time of third failure of site TP2. Time is local San Diego time, divided in 2 hour increments.

TP3

Site TP3 has undergone a substantial amount of erosion since it was first surveyed in November 2006, where a failure mass of 97 m^3 was observed on the beach at the site. This failure mass was the remains of a collapse of part of a column-like feature in January 2006. Shortly after the November 2006 survey sometime between the end of December 2006 and the beginning of January 2007, the rest of the columnar shaped feature collapsed on the beach. Most of this failure mass eroded during the winter months.

A continuation of the failure of this site occurred at the end of September 2007. Because of high tide cycles, the site was inaccessible prior to the survey on October 12, 2007. An elevated beach berm prevented waves from reaching this failure. Scans completed on October 12, 2007 showed that the total failure volume on the beach was 128 m^3, accumulated from multiple failures over several years. Comparisons of the November 2006 survey with the October 2007 surveys showed that about 134 m^3 had eroded from the cliff at this site between the surveys, including the collapse of a column like feature in the cliff. Most of this material was removed from the failure mass by waves, so only the largest cemented sandstone boulders remained.

TP5

The failure at site TP5 occurred with the collapse of an overhang on the upper portion of the cliff (Figure 5-19) following a minor wave storm and precipitation event in January 2008 (Figure 5-20). Because this site was directly

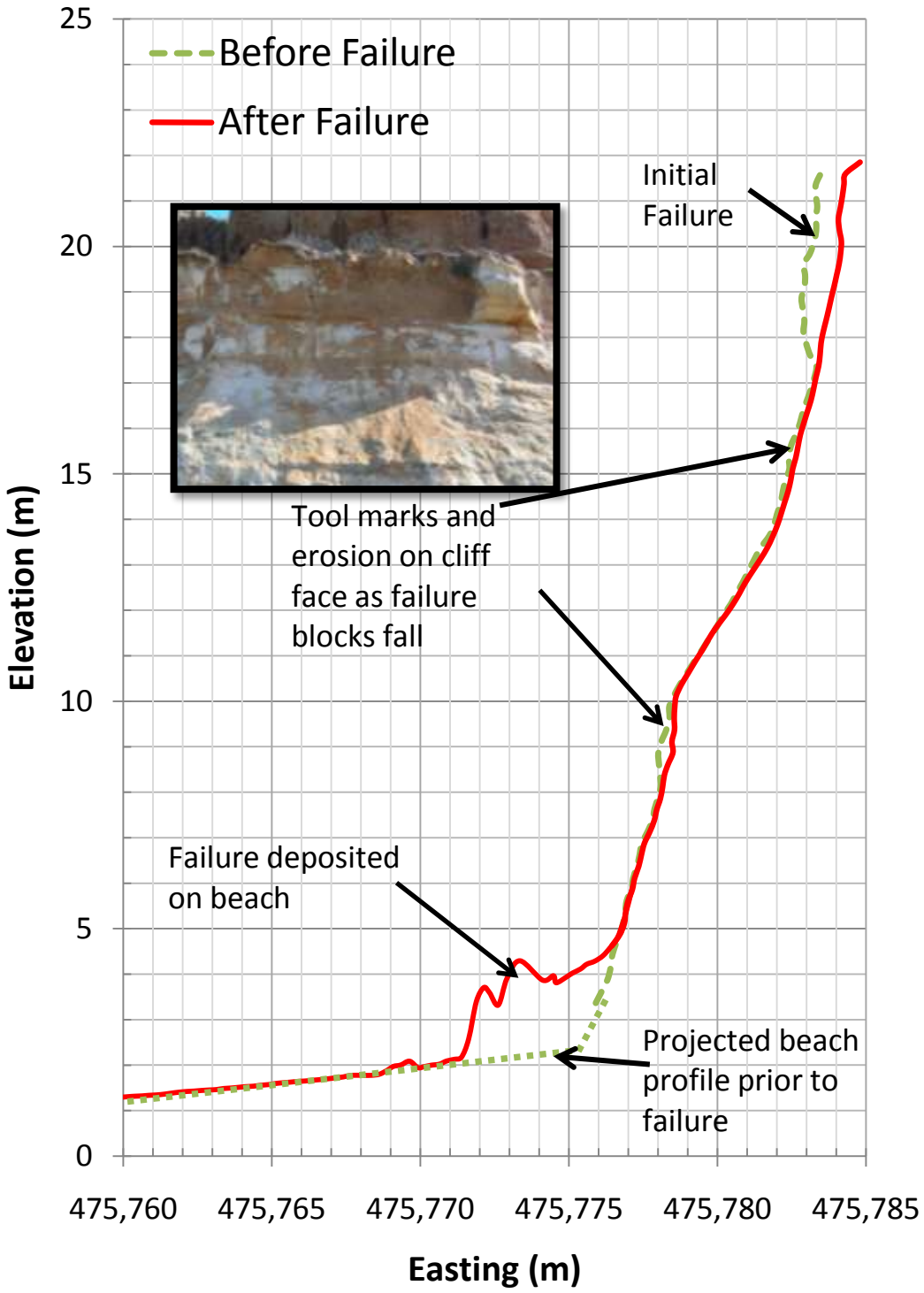

Figure 5-19. Cross section of failure at site TP5

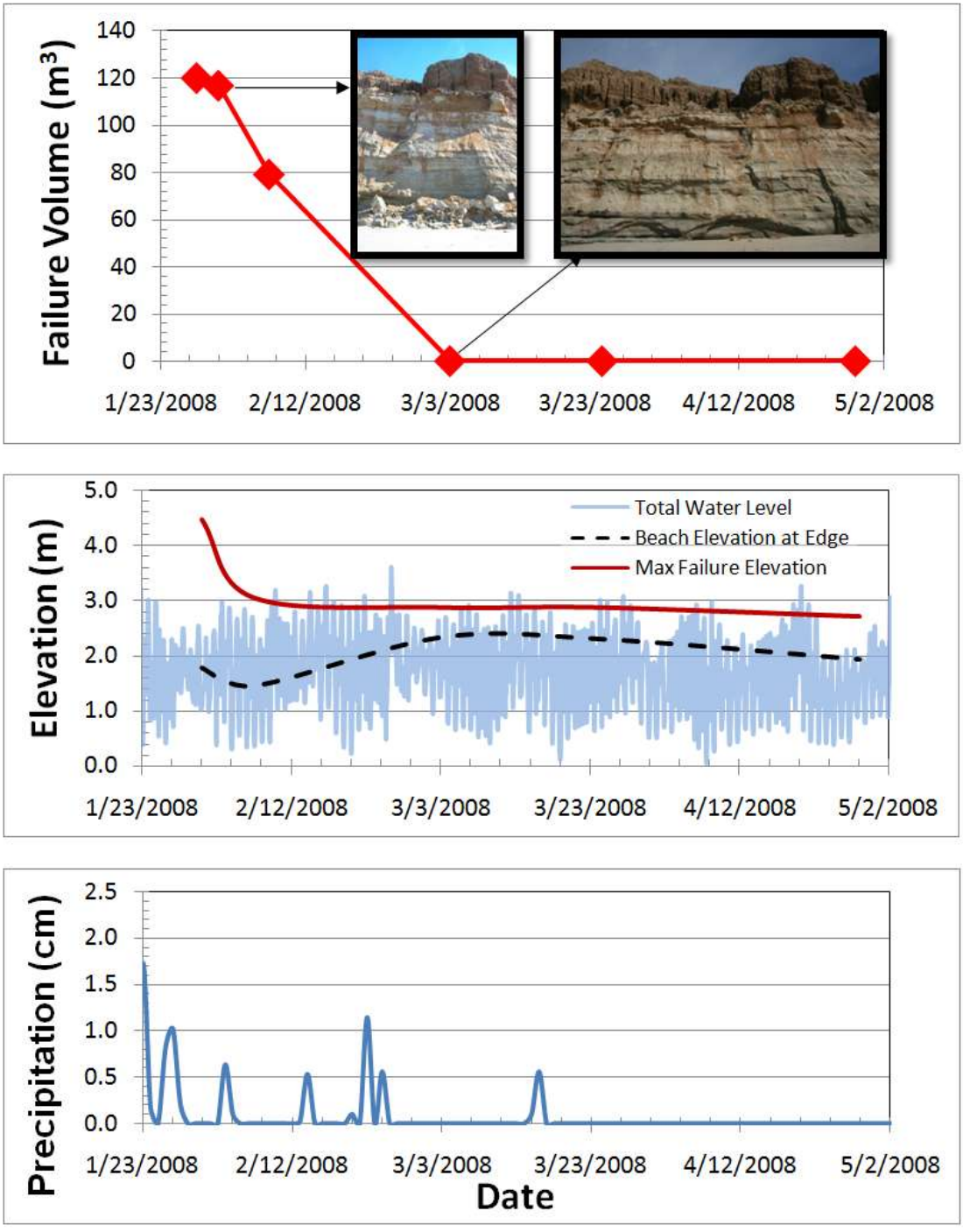

Figure 5-20. Analysis of failure site TP5 showing (A) failure volume, (B) a comparison of beach height immediately west of failure with the total water level, and (C) precipitation levels

in the reach of waves at the time of failure, it was quickly reworked along the beach (Figure 5-20). In addition, rising beach levels covered the larger rocks of the failure mass within a couple months of its occurrence.

Type C Failure Sites

DM2

The failure at Site DM2 occurred in summer 2007 and was discovered during a seasonal survey. Most of the failure mass was loose sand and gravel material. The failure volume was calculated to be 25 m^3 and remained constant during surveys until this sediment was quickly reworked by the first winter storms that reached it in late November 2007.

TP1

Preliminary results and observations from site TP1 were discussed in detail in Chapter 4. The site remained consistent in failure volume until late December 2007 when waves had eroded the protective beach berm (Figure 5-21) and reworked all the fine sediment from the failure mass (Figure 5-22). Larger rocks were pushed against the cliff and talus deposits during winter events. Immediately to the side of these rocks and talus deposits a smaller failure occurred in May 2008 (Figure 5-7L) from the collapse of an adjacent sea cave. The south edge of site TP1 is a boundary between the talus deposits found to the North and the sea caves and wave undercutting found to the South of Torrey Pines.

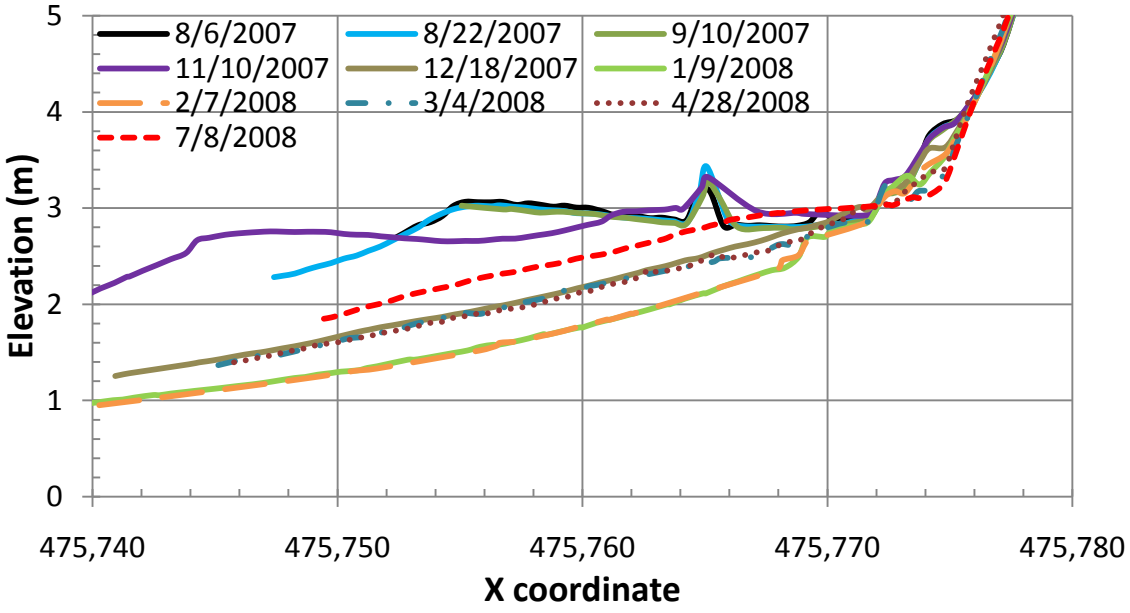

Figure 5-21. Beach profiles at Site TP1 from TLS data. Note rapid erosion of beach berm between 11/10/2007 and 12/20/2007 with initial winter storms

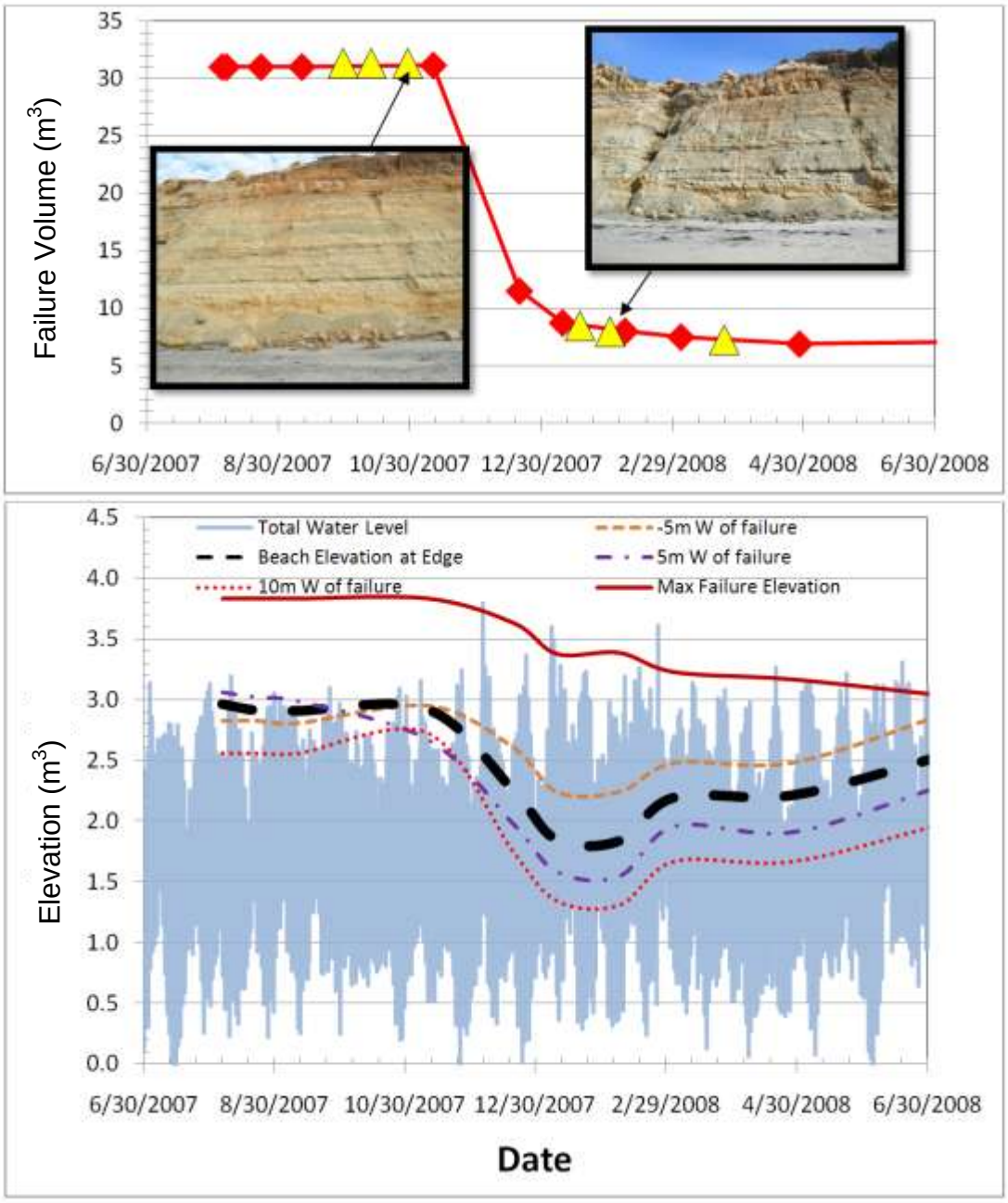

Figure 5-22. (a) Failure mass volumetric change analysis and (b) comparison of beach sand levels to TWL for site TP1. Red diamonds represent TLS surveys and yellow triangles represent field visits.

TP4

This failure occurred on approximately October 20, 2007 (Figure 5-23) during a storm event with minor waves and precipitation (Figure 5-8). The failure mass landed on a beach berm; however, large waves were still able to reach the base of the failure after it occurred. The failure block occurred on the upper portion of the cliff (Figure 5-24) and impacted the top of the talus deposits, causing a small loss in the top of the talus deposits. As soon as the larger winter waves reached the failure, much of the failure was eroded (Figure 5-25).

Analyzing the cross sections (Figure 5-26) of the beach and talus deposits at this failure site shows that after the major waves reworked the finer sediment from the failure, the larger failure boulders (>0.5 m in diameter) were pushed up against the talus deposits and acted as a protection to the cliff, similar to riprap stabilization techniques. The failure also acted similar to a retaining wall, collecting talus deposits behind it that would otherwise land on the beach and be reworked (Figure 5-26). Observing the seacliff on the sides of the failure mass showed substantial erosion of talus deposits during the winter, leaving the cliffs exposed to wave energy and impact (Figure 5-27). Thus, the failure temporarily acted as a barrier to erosion during the winter months. The mild winter did not have substantial wave energy to rework and transport the large boulders. During extremely large winter storms, these large boulders might be eroded. After February 2008, beach levels began to increase and bury portions of the failure mass (Figure 5-25).

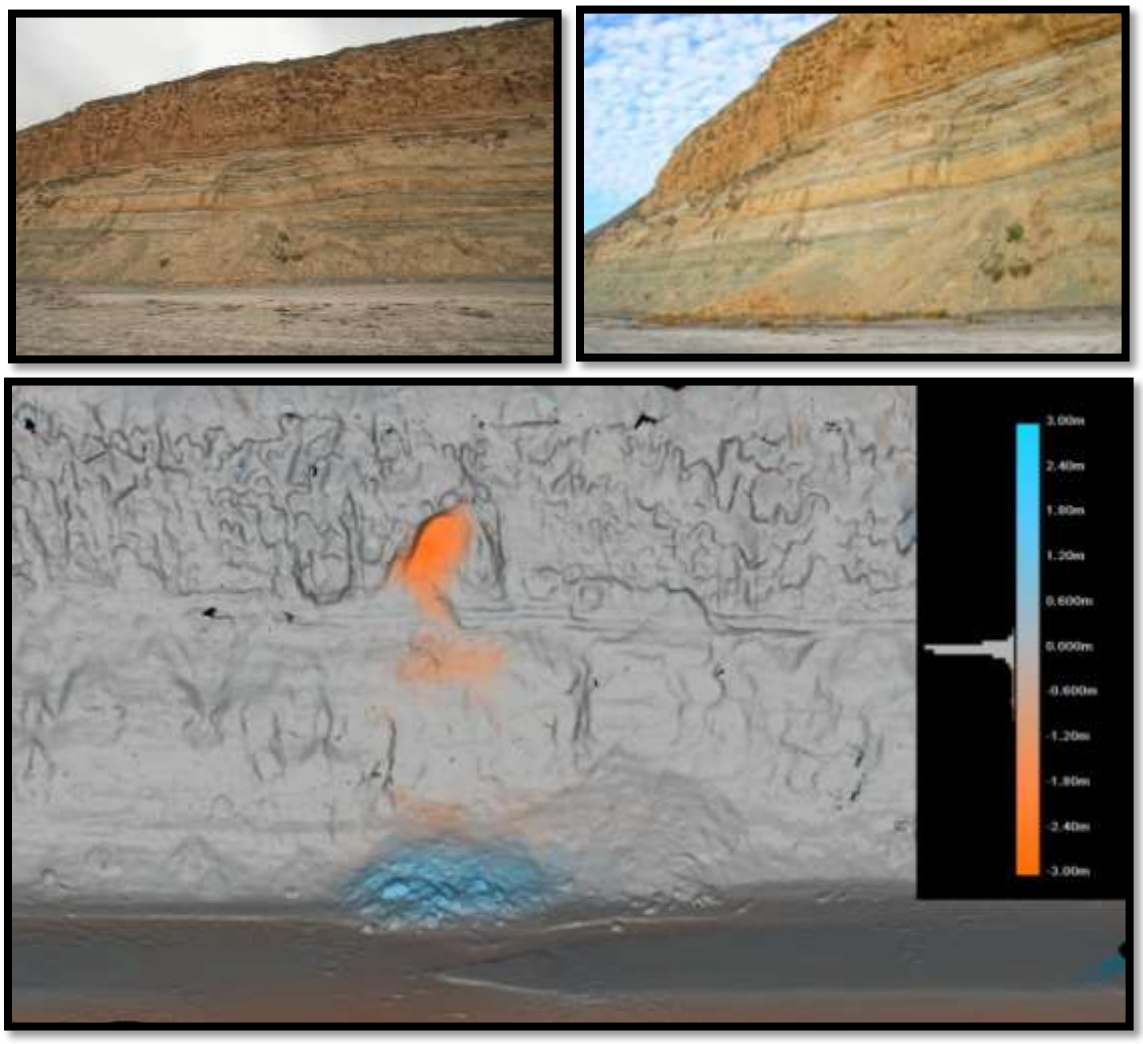

Figure 5-23. Failure site TP4 (a) before failure October 14, 2007, (b) after failure October 29, 2007, with (c) failure analysis highlighting area of failure

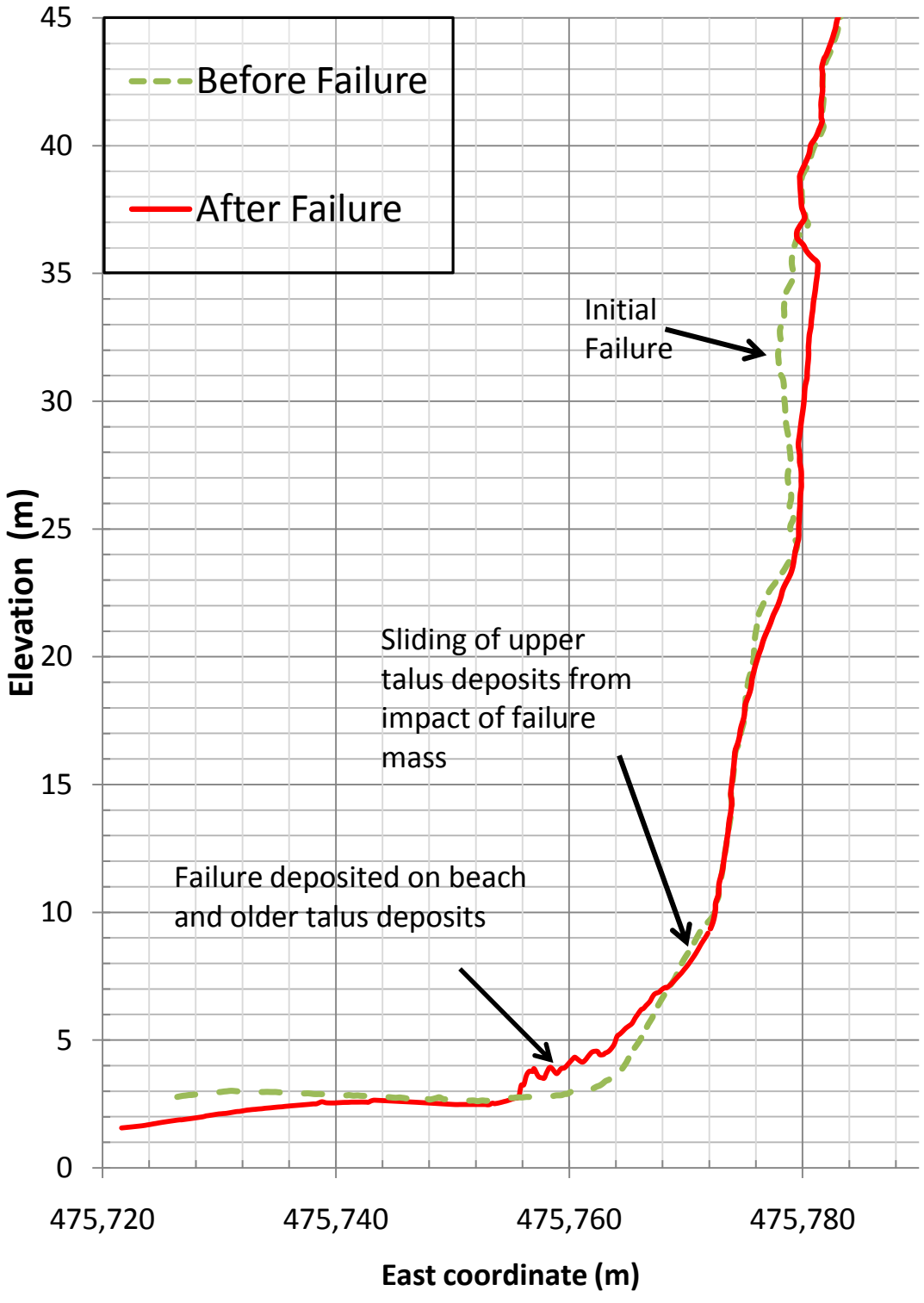

Figure 5-24. Cross section analysis of failure at site TP4

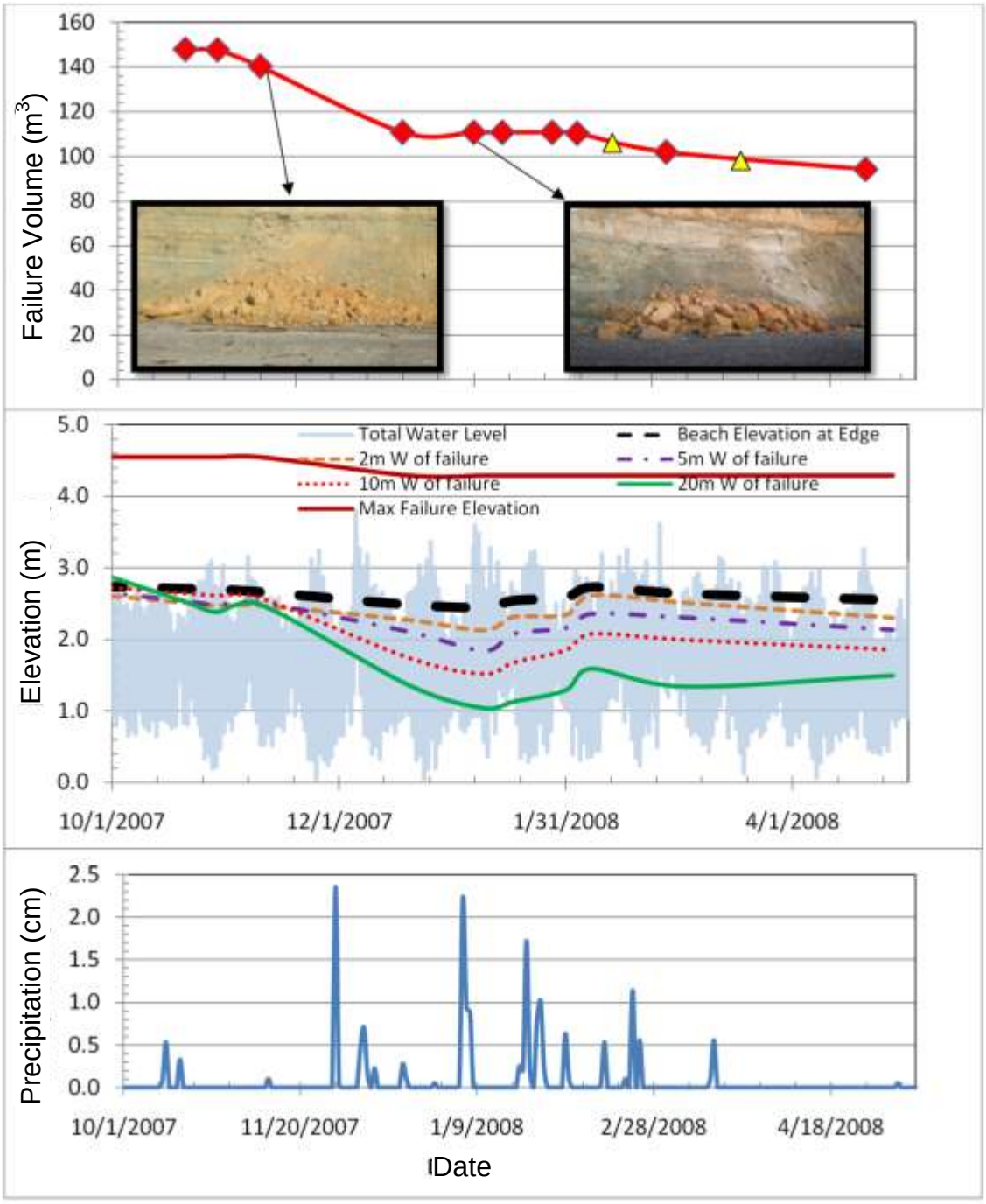

Figure 5-25. Comparison of (a) Failure volume determined from TLS (b) beach elevation and total water level, and (c) precipitation for site TP4. Red diamonds represent TLS surveys and yellow triangles represent field visits.

Figure 5-26. Comparison of beach and talus deposit profiles for site TP4 showing increased erosion of talus deposits 25 m to the north and south of failure site and protection of talus deposits at failure site.

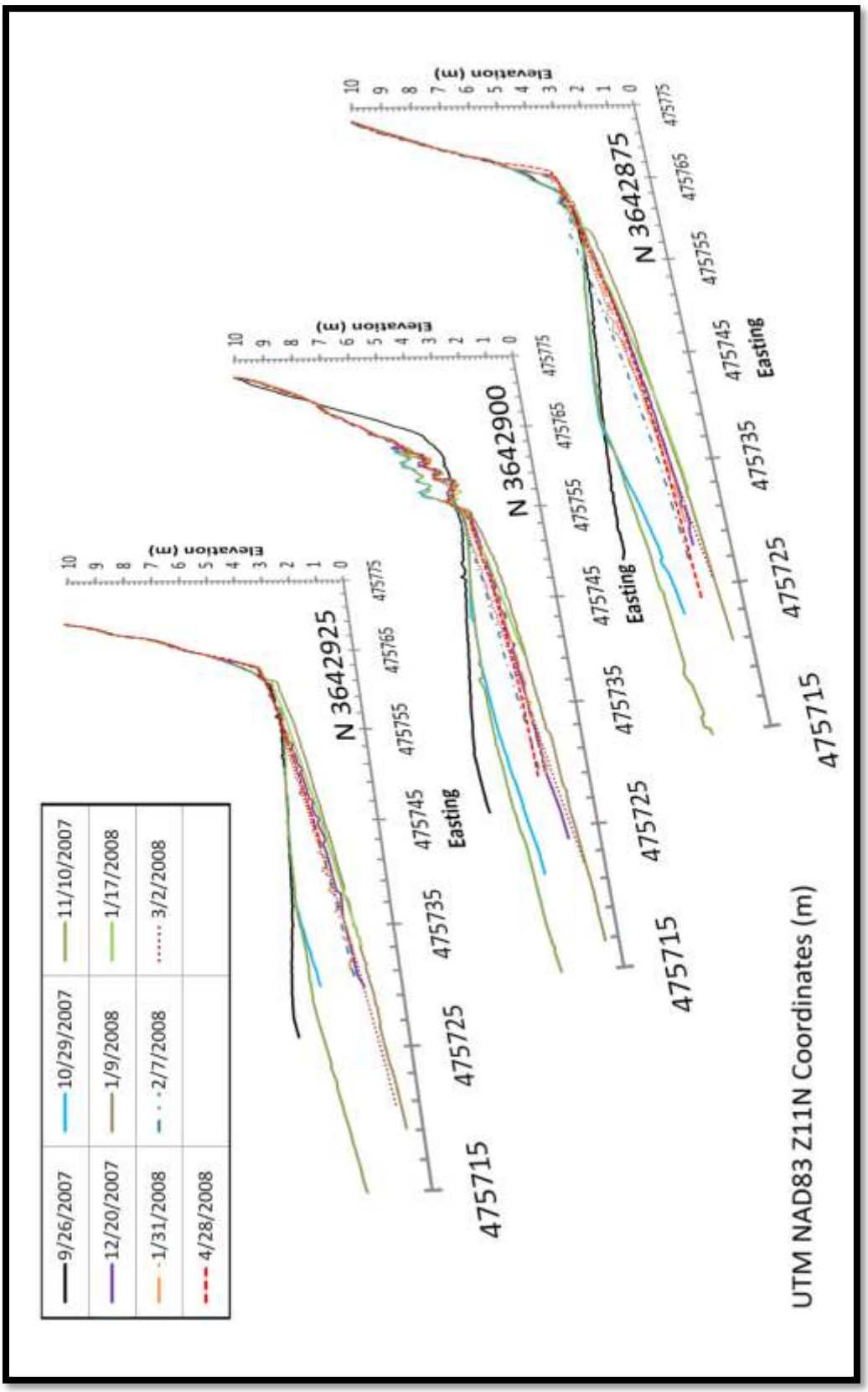
9/26/2007
10/29/2007
11/10/2007
12/20/2007
1/9/2008
1/17/2008
1/31/2008
2/7/2008
3/2/2008
4/28/2008
Elevation (m)
N 3642925
N 3642900
N 3642875
Easting
475715
475725
475735
475745
475755
475765
475775
UTM NAD83 Z11N Coordinates (m)

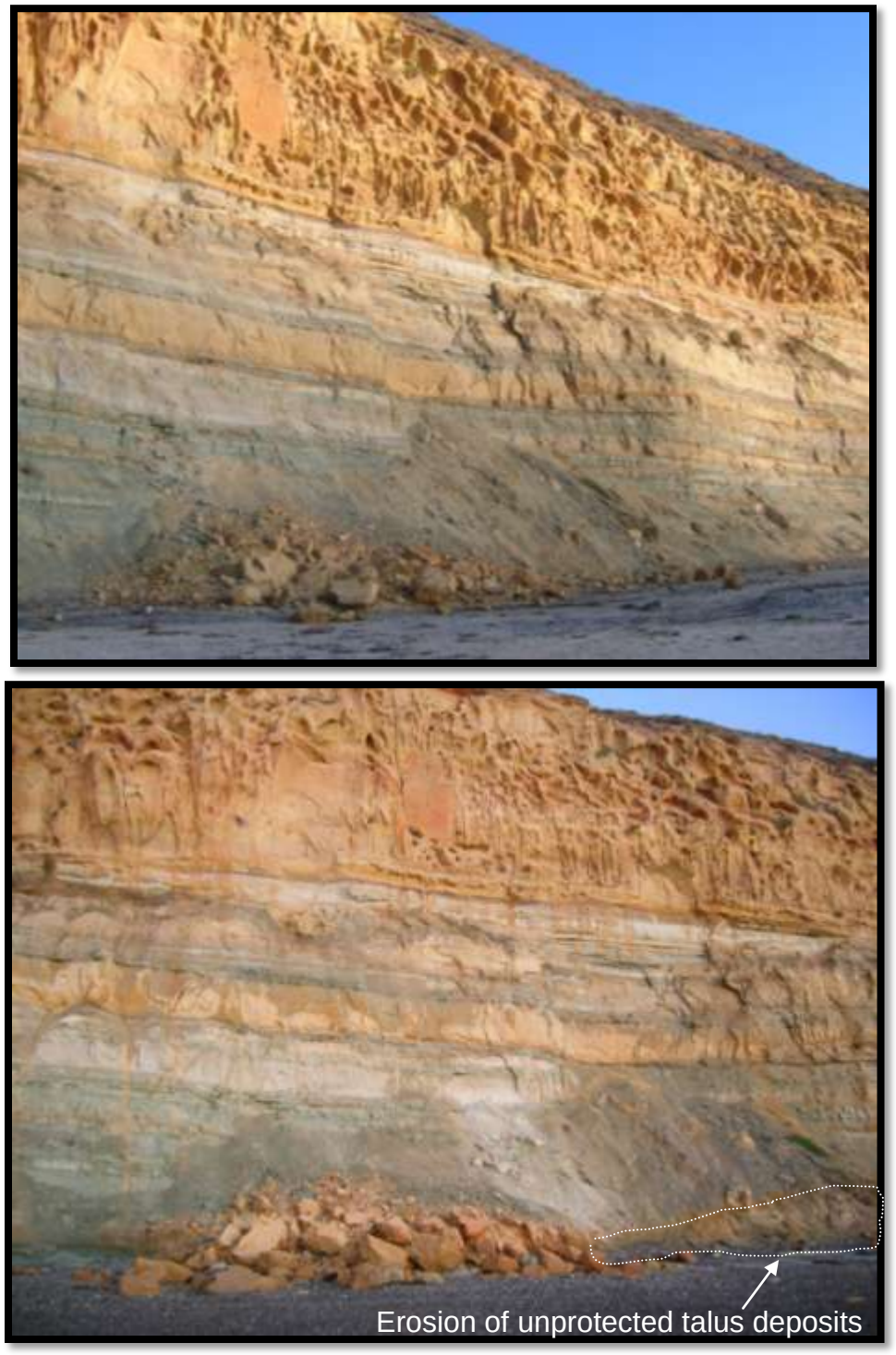

Figure 5-27. Failure Site TP4 (A) before (Nov 11, 2007) and (B) after (Jan 9, 2008) winter storms showing failure stabilizing talus deposits with erosion of talus deposits away from failure

TP6

Site TP6 occurred in June 2008 on the unstable upper cliff (Figure 5-28), completing an arch formation. Several tree roots have created joints in the rock and are strong evidence for biological weathering. The vegetation also implies the presence of groundwater in the rock.

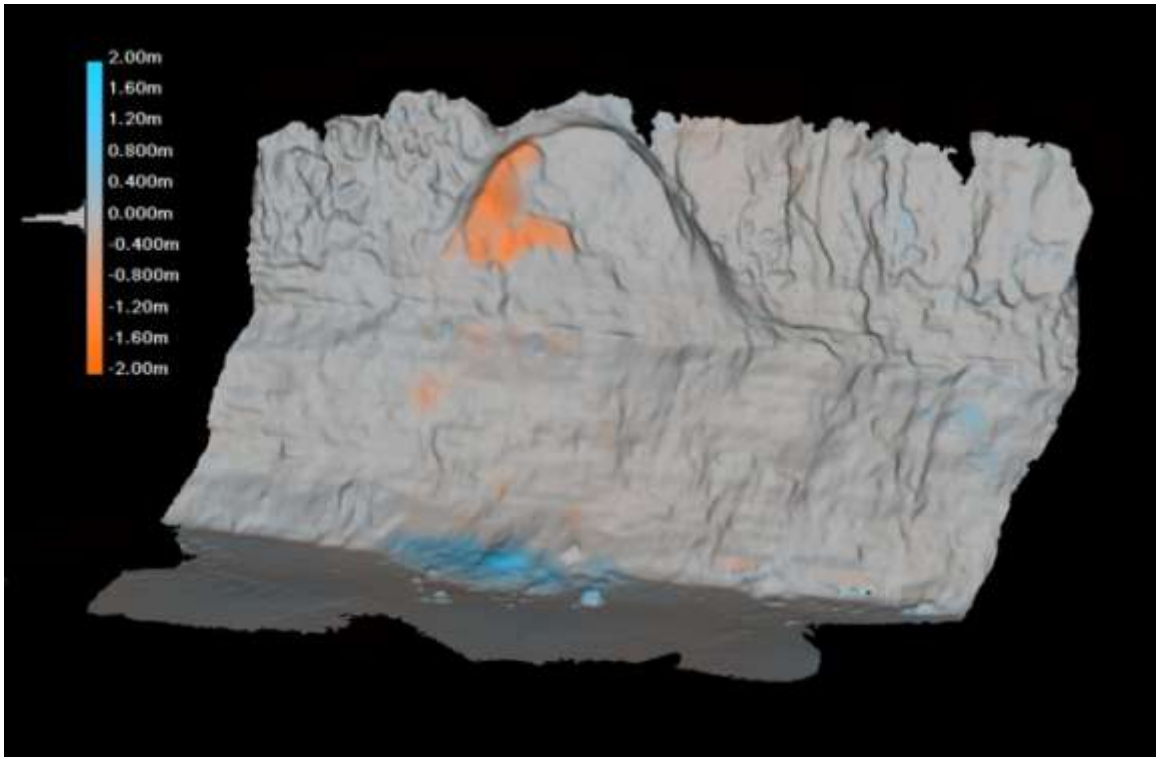

Figure 5-28. Surface change analysis for site TP6 comparing the post failure, June 18, 2008 survey to the pre-failure, April 28, 2008 survey

Type D Failure Sites

DM1

The failure at Site DM1 occurred mid-August 2007 in an unstable area undergoing a substantial amount of erosion due to groundwater sapping and surface runoff from a storm drain. Previous failures at this site are discussed in Young and Ashford (2007). Repeat scans showed minimal change in the failure volume ($88m^3$) at the site because the majority of the failure mass has been resting on a platform.

SIO1

This 30 m^3 failure occurred approximately 250 m north of the pier at Scripps Institution of Oceanography in September 2007 and landed on a platform approximately 3m in elevation. Some undercutting has previously occurred above the platform (Figure 5-29). Waves generally were unable to reach the failure because it is perched on a platform (Figure 5-30), thus there was minimal change in the failure mass. During precipitation events, a small amount (< 1 m^3) of the failure mass was washed off the platform. During the winter season, approximately 8 m^3 of sediment was removed from the failure, most of which was in the center of the failure where the platform does not extend as far seaward. The failure cannot be compared to the TWL calculated from wave runup because the Stockdon et al. (2006) equation was developed for sloping beach profiles, not for platform sites which would have different energy dissipations.

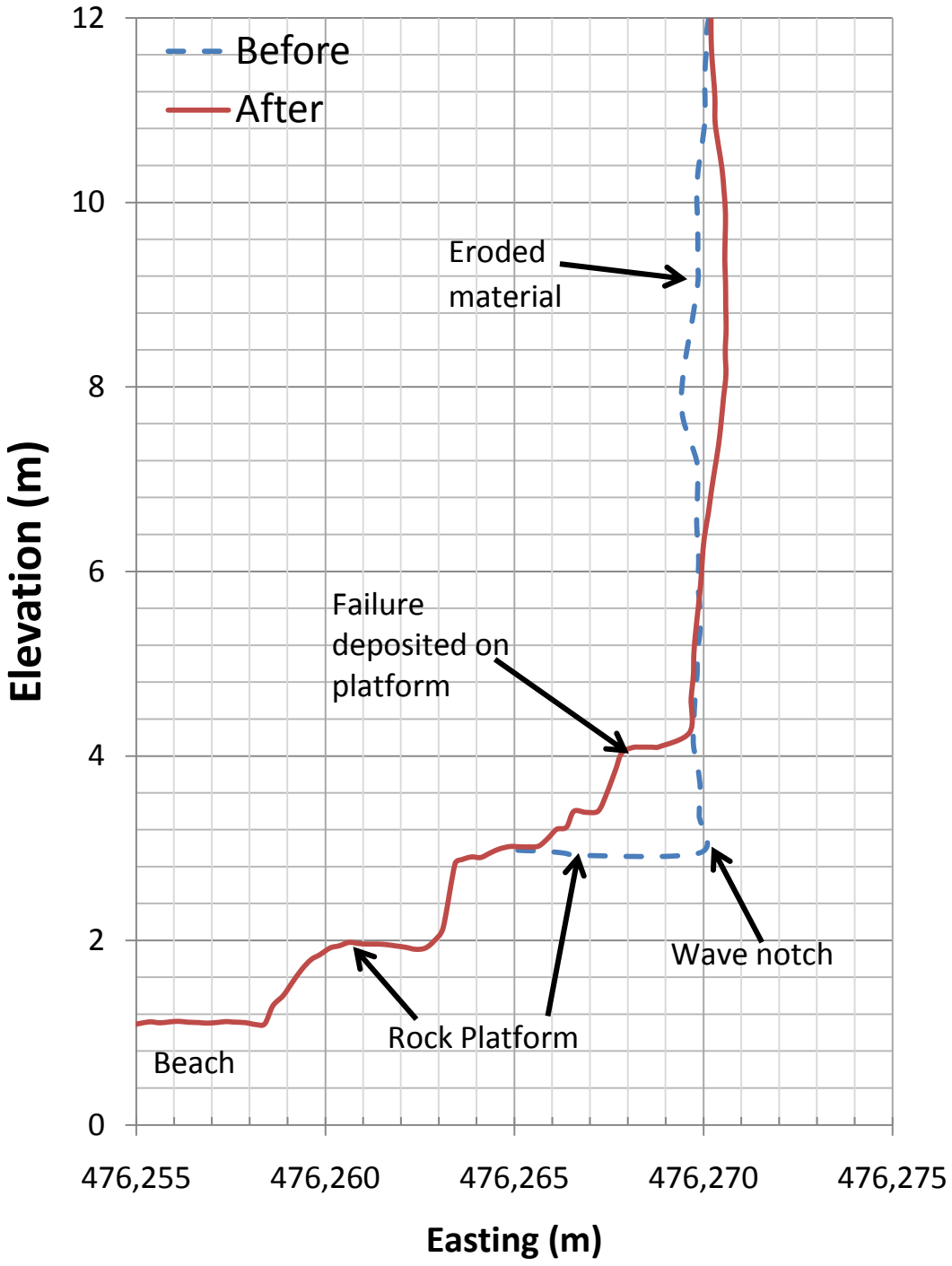

Figure 5-29. Cross section analysis for site SIO1 showing failure mass atop rock platform

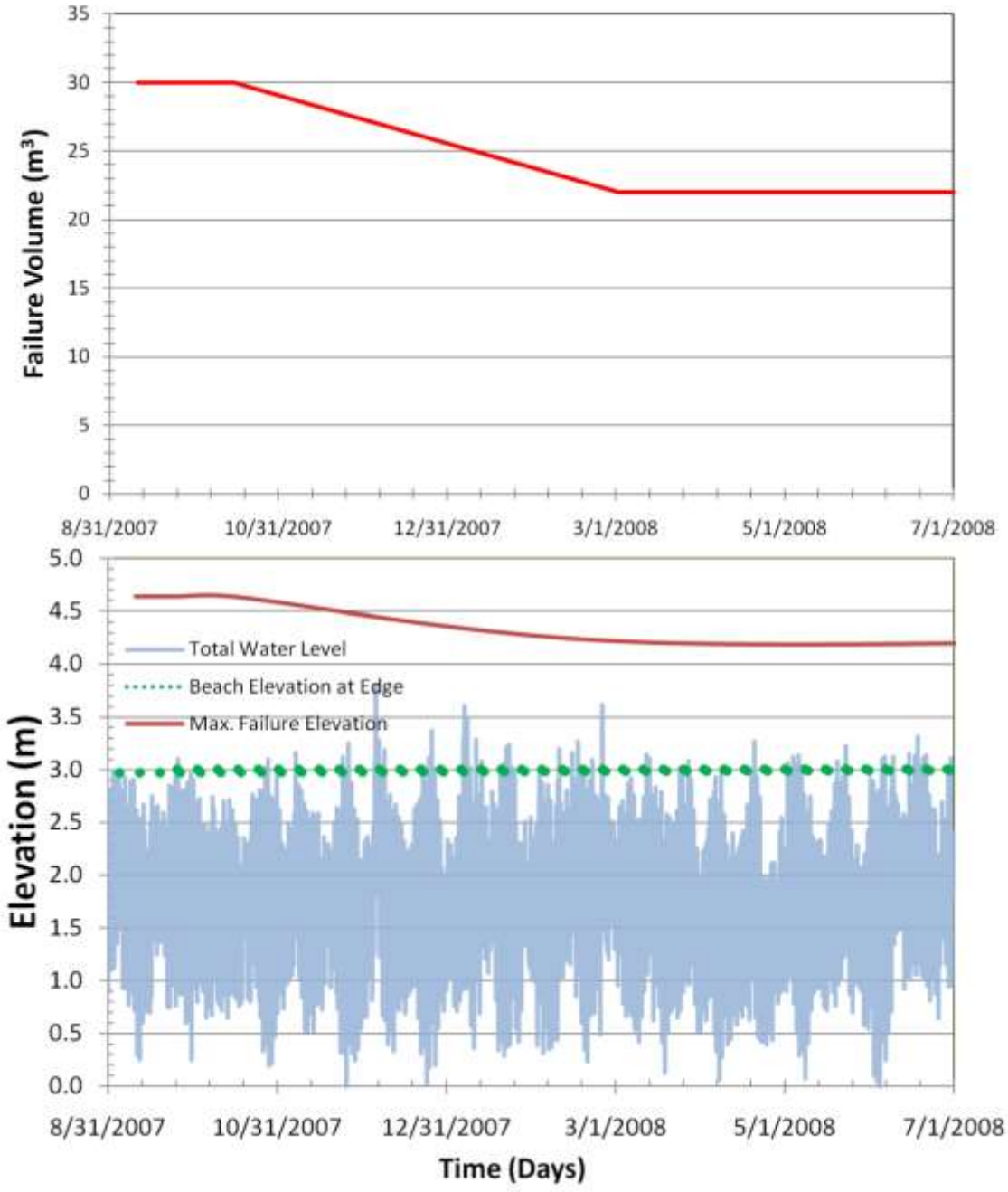

Figure 5-30. (A) Failure volume change at site SIO1, and (B) comparison of Platform elevation with Total water level. Note that Total water level is for reference only because the waves would dissipate differently upon impact with the platform compared to runup on a beach.

DISCUSSION OF RESULTS

This study places important new constraints on the rate of wave reworking of cliff failures. Failure sites (Types A, B, and C) that are exposed to waves showed removal of sediment with wave impact. Type A sites (EN1) show that the lower energy summer waves are sufficient to rework loose sediment and small rocks from the failure. Type B sites (i.e., TP5) showed storm events quickly redistribute the sediment. Most other sites (i.e., TP1, TP4, and DM1) required major storm waves to reach the failure volume or erode a protective beach berm. Type D failures obviously showed minimal loss of sediment that would only be reworked during very large storm events, which did not occur during the study period. As discussed in Young and Ashford (2007), several small seacliff failures can account for a large portion of the sediment contributed to the beach. This study shows that this sediment derived from these seemingly insignificant failures requires minimal energy to be reworked and contribute sand to the beach system. Additionally, note in Figure 5-2 that for the Torrey Pines section, Type C failures occurred in locations with talus deposits to protect the seacliffs from wave based erosion. The demarcation line occurs immediately to the south of site TP1. To the South, Type B failures occurred from wave based erosion. In the southern portion, sea caves and wave undercutting are much more dominant because of the lack of talus deposits protecting the cliffs.

Additionally, the failures can act as rip rap and minimize local cliff erosion provided the failure material consists of large boulders that trap talus deposits.

Erosion continues to occur adjacent to the failure mass. Smaller rocks from the failure mass can be hurled by waves at the adjacent cliff that would serve to accelerate the wave-based erosion. The failed sediment also can cause abrasion on the unprotected cliff. Site TP4 shows a clear example of this phenomenon, where talus deposits grew slightly near the failure during the winter months, the cliff was protected from wave erosion and undercutting. In contrast, talus deposits adjacent to the failure, were eroded and exposed the cliff to wave activity during the winter months. Site TP1 also shows similar behavior where the talus deposits at the site of the failure remain in place during the winter because of the larger stabilizing rocks. Adjacent to the failure mass, the talus deposits are not present, which allowed wave energy to cause the collapse of a sea cave (Figure 5-7H). At site TP2, talus deposits were not present. However, the second failure occurred adjacent to the first failure as wave energy was concentrated on the cliff to the sides of the failure mass. The importance of talus deposits in protecting the cliffs from wave-based erosion is illustrated in Table 1, which shows that wave-based failures and undercutting only occurred at sites without talus deposits. This phenomenon will be important as sea level rise accelerates cliff erosion, this second order feedback will actually protect some sections of the cliff and may accelerate erosion and undercutting of the adjacent cliffs. This may provide a nucleation site and feedback that acts to cause cliff erosion and undercutting to radiate out away from regions with failed material on the beach.

Failures with large boulders (>1/3 m) in areas of dynamic beach changes can contribute to the beach volume because during winter storms, the sand below them is eroded away and they are on the beach level, but the summer waves do not have sufficient power to rework or move the large boulders. Thus new sand is deposited on top of the old boulders as their elevation changes with beach fluctuations. During winter, the boulders are then re-exposed and can act as protective mechanisms, or destructive mechanisms depending on the wave energy and size of the boulders. This was observed at sites EN1 and TP5.

Insights into beach system dynamics were also derived by this repeat study, that is seasonal beach inflation and deflation is asymmetric. Beach sand levels changed drastically with the onset of the first major winter storm, and beach berms eroded within a few weeks. In contrast, the beach build-up during the summer season was gradual and over a period of a few months. Site TP1 and TP4 both had a large beach berm that was only slightly eroded during the start of the winter season. As soon as the major winter storms hit in late November and December, the waves quickly reworked and eroded the beach berm. Interestingly, some sites that did not have a beach berm (EN1,TP5) showed an increase in beach elevation during the winter months, probably as a result of sediment being redistributed from sites with large sediment supply to sites with less sediment from the high energy winter waves.

CONCLUSIONS

TLS provides a valuable tool to understand and quantify geologic processes using efficient, high resolution techniques. Comparing the TLS data with available environmental data allows us to assess various triggering mechanisms for seacliff failures. Several failures occurred in association with major and minor storm wave events. Frequent site observations and repeated mapping following a collapse provides new insights on sediment reworking processes. First, minimal wave energy is required to rework unconsolidated failures into the beach system. Thus, seemingly small erosion over the entire cliff face is continually transported vertically to the beach. Second, feedback mechanisms occur from seacliff failures, protecting the cliff directly behind the failure and accelerating erosion adjacent to the failure. This pattern might explain the general, long-term linear retreat patterns of the coastline. Third, most sand on the beach is removed rapidly during the first winter storms and then is gradually replaced on the beach during the lower energy summer months. These observations show the importance of seacliff erosion in providing sand and stabilization to beaches. Additionally, the classification system developed here assists in the prioritization of study sites for repeat surveys. It additionally provides insights on the failure mechanisms where Type A and B failures tend to be wave-based failures and Type C and D tend to be subaerial based failures.

ACKNOWLEDGEMENTS

This research was supported by California Seagrant (Project #R/OE-39) and the Coastal Environmental Quality Initiative (CEQI) under award #04-T-CEQI-06-0046. Pat Rentz and Jessica Raymond of Scripps Institution of Oceanography assisted in the LIDAR surveys. Adam Young provided the 2005 scans of site EN1 and assisted in the initial survey of site EN1. Gary Samad alerted us to the locations of several failures during this study. Scott Schiele and John Dolan from I-Site provided technical assistance for this work. Travis Thompson of CALVRS assisted in using the CALVRS GPS network.

Chapter 5, in part, is being prepared for submission for publication of the material. Olsen, M.J., Johnstone, E., Driscoll, N., Kuester F., and Ashford, S.A. The dissertation author was the primary investigator and author of this paper.

CHAPTER 6. TOPCAT: TOPOGRAPHICAL CHANGE ANALYSIS TOOLS FOR ARCGIS®

OVERVIEW

The coastal zone is a complex and dynamically changing environment, which significantly impacts coastal communities and resources. Therefore, understanding the processes and rates that drive coastal change are important for coastal planning and management. Recent advances in remote sensing techniques provide high resolution spatial and temporal coastal information, and Geographic Information Systems (GIS) provide a tool to analyze and display the impacts of coastal change. This chapter discusses a new GIS extension named the Topographic Compartment Analysis Tool (TopCAT) which compares sequential digital elevation models (DEMs) and provides a quantitative and statistical analysis of the alongshore topographical change. TopCAT was specifically designed for the morphological analysis of seacliffs and beaches but may be applied to other elongated features which experience topographical change, such as stream beds, river banks, coastal dunes, etc. To demonstrate the capabilities of TopCAT two case studies are further described herein. The first case examines the cliff face retreat of a 500 m section of seacliffs in Del Mar, California, showing that two large failures dominated the seacliff erosion in the study area and that retreat rate averages do not provide a good estimate of what can potentially occur. The second case investigates the alongshore volumetric beach and dune sand change caused by hurricanes Bonnie (1998) and Dennis (1999) for a 3,800 m section in the Cape Hatteras National Seashore, North Carolina. This investigation showed significantly different erosional patterns for

both hurricane events. The dune system experienced similar erosional patterns in Hurricane Bonnie and in Hurricane Dennis; whereas, the beach system experienced opposing erosional patterns from Hurricane Bonnie to Hurricane Dennis. The case studies show the added insights into the nature of coastal erosion available by performing a small-scale analysis using TopCAT.

INTRODUCTION

The coastal zone is a complex, dynamic system which can experience significant morphological change thereby affecting coastal communities, infrastructure and public resources. Therefore, understanding the processes and rates of coastal change is critical for proper coastal management and planning. This chapter presents a new Geographic Information Systems (GIS) extension named the Topographical Compartment Analysis Tool (TopCAT) for analyzing topographical change. The main function of TopCAT is to divide the study region into discrete "compartments" from which the alongshore topographic and volumetric change may be quantified. This method was originally developed and demonstrated by Young and Ashford (2006b, 2006c, 2007) in a manual GIS environment. TopCAT is designed to assist GIS analysis of topographical data using this method in an automated, user friendly workflow and is available for free download at *http://lidarweb.ucsd.edu/TopCAT.*

A GIS provides a powerful environment for analyzing Digital Elevation Models (DEMs) obtained from various remote sensing techniques. Comparing sequential DEMs of an area reveals the topographic change over time and

therefore provides insight into the processes and rates that drive morphological change. Although many remote sensing techniques can be used to produce DEMs, this chapter focuses on topographical data derived from LIght Detection and Ranging (LIDAR) which pulses a high frequency laser at a target surface to obtain a swath of topographical point data. Although some tools in TopCAT are specifically designed for LIDAR data, TopCAT is not limited to working solely with LIDAR data but can be applied to any data that can produce continuous DEMs.

BACKGROUND

Several GIS tools have been previously developed to assist in the calculation of coastal change rates. Duffy and Dickson (1995) produced an ArcInfo® Macro Language (AML) program, SHOREGRID, to calculate shoreline erosion rates from digitized 2D shorelines (from DEMs or aerial photographs, etc.) for two time intervals. The digitized shorelines are then converted to grids with a value of “1” in each grid cell that would intersect the shoreline. SHOREGRID then determines the shortest distance between two shoreline grids and divides that by the time difference to determine the shoreline erosion rate. SHOREGRID also can be used to predict future shorelines based on a linear projection of the calculated erosion rates. SHOREGRID has been successfully implemented to investigate seacliff retreat (Moore et al., 1999; Moore and Griggs, 2002).

Similar to the SHOREGRID program, the Digital Shoreline Analysis System (DSAS, Thieler et al., 2005; previous version (DSMS/DSAS, Danforth

and Thieler, 1992)) utilizes digitized shorelines in a GIS environment to quantify shoreline change. This tool uses regression techniques to calculate the linear change rates at specified locations between multiple digitized shorelines by casting perpendicular transects from the original shoreline. The DSAS tool has been applied successfully to evaluate seacliff top retreat (Hapke and Reid, 2007) and various beach shoreline proxies (Esteves et al, 2006; Morton et al, 2006; Harris et al, 2005; Himmelstoss et al., 2006; Pendleton et al, 2004).

The SHOREGRID and DSAS tools are primarily aimed at analyzing 2-D shoreline data; however recent advances in coastal remote sensing now provide high resolution 3-D topographical data. Therefore, the TopCAT GIS extension was developed to build upon the SHOREGRID and DSAS tools to incorporate the use of a 3-D environment. Working with TopCAT and 3-D data provides several advantages compared to 2-D data. First, TopCAT works with the entire data grid, not just transects, therefore the data between transects is accounted for. Second, transects at close intervals can overlap around bends in the coastline, which forces the user to use a larger interval which eliminates the ability to study localized phenomena. Additionally, TopCAT allows for volumetric analysis which provides valuable information for sediment budget analysis. However, because high resolution topographic datasets have only become recently available, TopCAT may not be applicable to historical shoreline analysis which relies on 2-D data sets.

METHODOLOGY

Procedure

The TopCAT program (Figure 6-1) runs through Visual Basic for Application (VBA) routines created within ArcView® GIS 9.1 Software (ESRI, 2005), and is upward compatible. Prior to running TopCAT, the user creates ESRI® DEM grid files of two sequential topographical datasets for the area of interest. Once the user has created the DEM grids, TopCAT routines can be easily and quickly implemented through the following steps (1-5) for beach studies with a few additional steps (6-7) for seacliff erosion studies:

1. Create a volume change grid by differencing two digital elevation models using the *Elevation Change Grid Creation Tool*
2. Define boundaries to remove unwanted or erroneous data (i.e. vegetation, waves, data outside the boundary of interest, etc)
3. Draw a centerline through the data or use the *Centerline Creation Tool*
4. Run the *Compartment Creation Tool* (Figure 6-2)
5. Calculate the compartmental volume differences using the *Compartment Analysis Tool*
6. Run the *Height Finder Tool* to obtain cliff heights (seacliff analysis only).
7. Calculate the average cliff face retreat rate using the *Retreat Rate Calculator Tool* (seacliff analysis only)

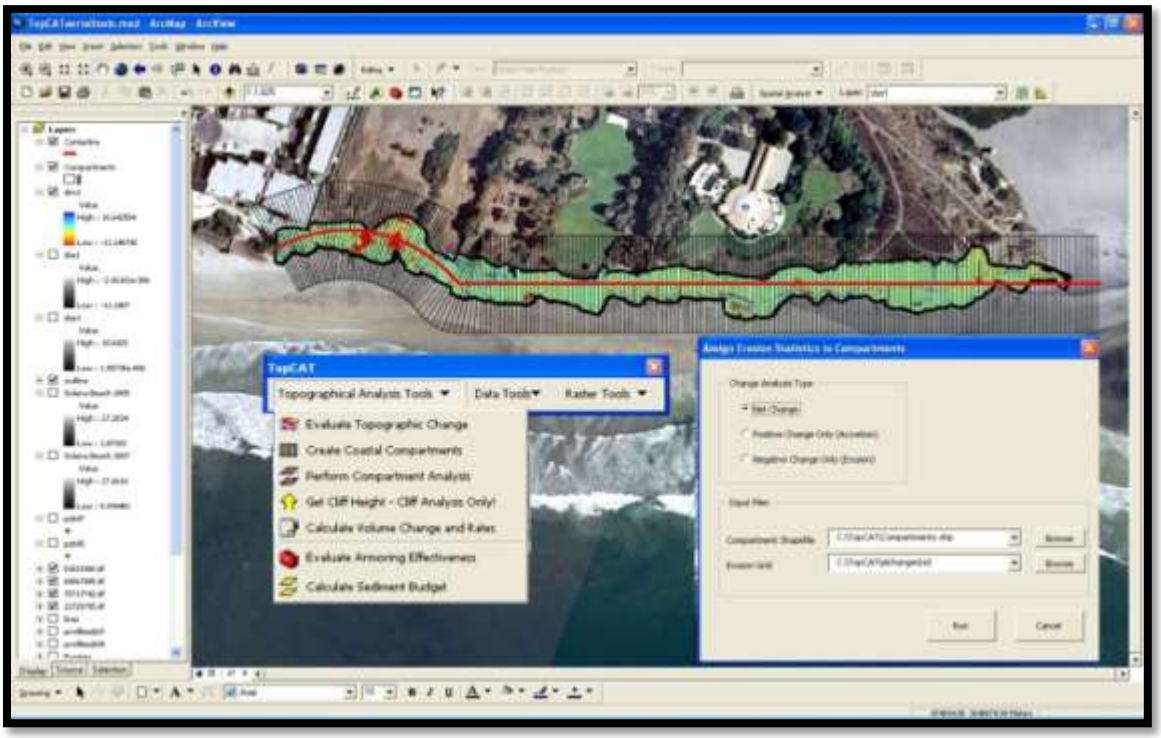

Figure 6-1. TopCAT toolbar and user interface run through ESRI's ArcGIS®

From the output results of TopCAT, the user can then plot the data and perform statistical analysis using the results for the individual compartments or do further comparisons.

Additional tools

TopCAT provides other useful tools to increase productivity while working with DEM's and LIDAR data, including:

- *Profile Extraction Tool* - Creates profiles of DEMs perpendicular to centerline spaced at equal intervals, through the center of compartments, or through custom lines drawn by the user

- *Pulse Extraction Tool* - Extracts a specific return pulse from a in a multi point return file
- *Aerial LIDAR coloring Tool* - Applies photographic color from orthoimagery to aerial LIDAR datasets
- *Grid Converter* Tool - Converts floating point ASCII grids into ESRI grids
- *RMS Calculator* Tool - Calculates the overall RMS change between two grids which is useful in examining error
- *Grid Clipper Tool* - Clips a grid extents based on a polygon

Mechanics

This section is not necessary to implement the program but provides helpful information on how the routines were developed. The TopCAT program was designed to automate the procedure described in Young and Ashford (2006b) for topographical change analysis of seacliffs. This method divides the coastline into compartments based off of a centerline (Figure 6-2) which allow for statistical and discretized analysis.

The accuracy of the results depends on the quality of the elevation change grid that is created from the elevation grids of the two datasets. To minimize error, the two grids should be the same cell size, have their cells aligned by starting from a common origin, and be of the same projection. In addition, because one dataset may capture data in one area where another does not, the user must verify that the other data has interpolated or estimated values for that area if it is of interest for the analysis. For example, if the top of the cliff was not

obtained from terrestrial LIDAR scanning, the user needs to make sure that there are cell values to represent the top of the cliff in both datasets in active areas of erosion, otherwise, the erosional rates will be erroneously low. This miscalculation can occur because in the first dataset, the cliff top will occur seaward of the second dataset. Thus, the first dataset needs to extend to the cliff top of the second dataset to quantify the erosion in those areas.

Other adjustments that will need to be made to the erosion grid include the elimination of areas of vegetation and beach sand (for a seacliff study) which can cause erroneous calculations. If areas of vegetation are included in the analysis, these areas can be mistaken as accretion of sediment rather than vegetation growth. These areas can usually be quickly identified as areas of highly variable pixel values. Because areas of beach sand seasonally change and do not reflect overall erosion, they should be removed for the seacliff analysis.

The centerline, stored as a polyline in an ESRI shapefile, determines how to create the compartments. The ideal centerline should parallel the coastline equidistant between the seaward and landward analysis boundaries. To produce the best results in creating the compartments, the centerline should be simple, avoiding jagged edges and sharp turns. This procedure can be automated via a C*enterline Creation Tool* which traces the contour at the elevation of the average cliff height on the DEM from one of the datasets.

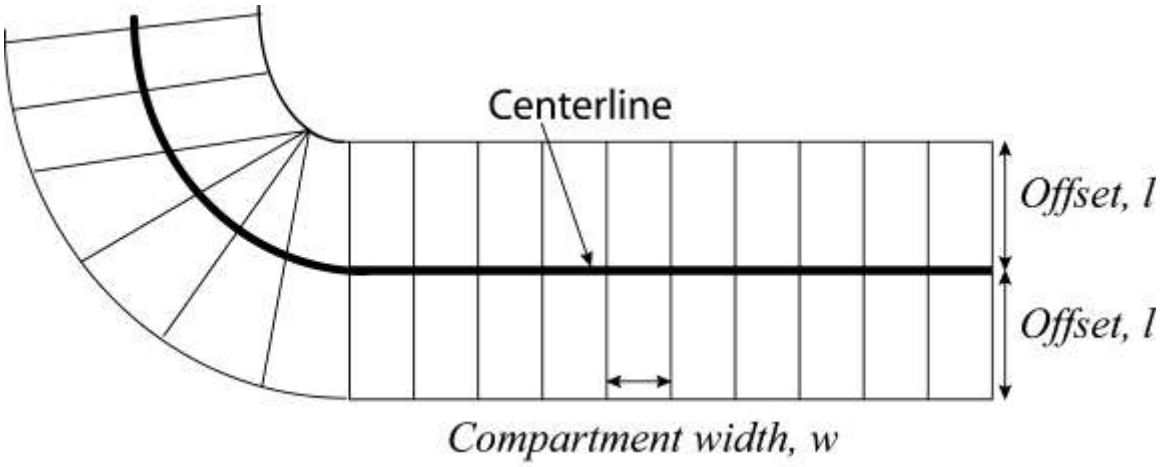

Figure 6-2. Schematic for compartment creation

After a centerline is created, the user runs the *Compartment Creation* Tool. The basic inputs to this routine are the desired compartment width, (*w*) and the offset distance (*l*) (Figure 6-2). To create these compartments, the routine creates a copy of the centerline on the left and on the right of the centerline by the specified offset distance. The routine then marches along the centerline by subdividing the centerline to the specified compartment width and finds the nearest points on the lines copied on the left and the right for the subdivision's start and end nodes. These four new points along with the line segments between these points are used to create a polygon compartment whose area is checked to ensure equal area compartments (within a typical tolerance of 1%), which is particularly important at rounded corners where the compartments must fan around a vertex (Figure 6-2). If the compartment area is within the tolerance, the routine moves on to the next segment and repeats the process. If the area is

not within the tolerance, then the routine will increase or decrease the centerline segment size accordingly until the compartment area complies.

In areas where the coastline may have sharp corners and bends, TopCAT has custom options to find and smooth these sections of the centerline. The smooth line option in ArcGIS® can be performed as part of the routine, thus the user does not need to manually run this processing step separately. If a large offset distance is used, the centerline can be densified to use more vertices thereby producing smoother curves. This option may be necessary because ArcGIS® uses a series of lines with vertices to approximate curves. In addition, an advanced option can be enabled to find areas where there is a sharp corner and fan the compartments as triangles around that point rather than have a sharp kink in the middle of the compartment (Figure 6-2). The compartment creation routine was designed to avoid as much interaction as possible in the creation of the compartments and in general, these options are not necessary. However, after the compartments are created the user can then perform manual edits or change the parameters to recreate the compartments if desired.

Following the compartment creation, the user runs the *Compartment Analysis Tool* which utilizes the ArcGIS® Zonal Statistics functions in the Spatial Analyst extension to determine volume change statistics from the elevation change grid such as the sum, average, range, maximum and minimum volume change per cell within each compartment. The total compartment volume change is calculated by:

$$E = A_{cell} \times \sum_{i=0}^{i=n_{cell}} dz_i \qquad \textbf{(6-1)}$$

where:

E = the eroded compartment volume, m^3,

A_{cell} = the area of a grid cell, m^2,

n_{cell} = the number of cells in the compartment, and

d_{zi} = the value of elevation difference, m, of the i^{th} cell in the compartment from the elevation change grid.

These values are then normalized by the width of the compartment to get the alongshore volumetric change per unit width. With this data available for each compartment as opposed to the entire dataset, small scale change and alongshore analysis can be performed.

Following the volumetric analysis, two additional steps are required for a seacliff analysis that are not run for a beach or coastal dune analysis. By running the *Height Finder Tool*, the user can assign a seacliff height each compartment. The routine finds the highest value on a DEM in each compartment to represent the seacliff height. Alternatively, in developed areas where buildings are on top of the seacliff and would be the highest value on the DEM for the compartment, the user can use a digitized polyline representing the top of the seacliff to guide the assignment of the seacliff height from the DEM. Once height values are obtained, the user then runs the *Retreat Rate Calculation Tool* which calculates the average cliff face retreat rate (Figure 6-3, Young and Ashford 2006c) from:

$$\boldsymbol{R = E/(h * w * t)} \quad \textbf{(6-2)}$$

where:

R = the average cliff face retreat rate (m/year)

E = the eroded compartment volume (m^3), calculated in Eq. 6-1,

h = the height of the cliff in the compartment (m),

w = the compartment width along the centerline (m), and

t = the time difference between the datasets (yr).

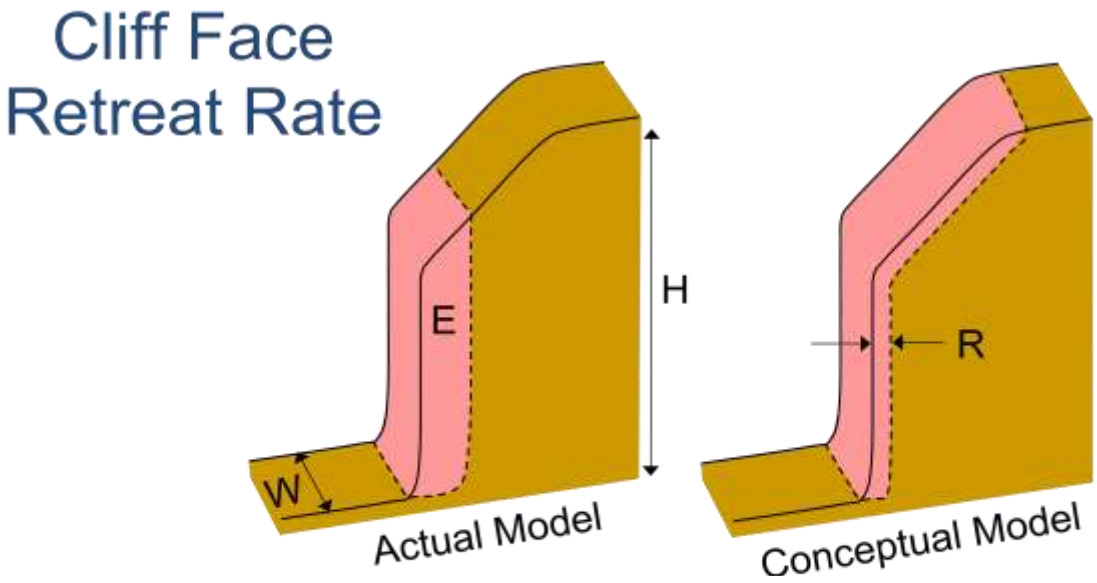

Figure 6-3. Geometric relationship between average seacliff face retreat and the eroded compartment seacliff volume (figure modified from Young and Ashford, 2006c)

In regions where seacliffs provide sediment to the littoral system, the coarse sediment yield may also be calculated using TopCAT. Coarse grained sediment (diameter larger than the littoral cutoff diameter, LCD) contributes to the sediment to the littoral system (Hicks, 1985) while finer sediment (diameter less than the LCD) will not remain on the beach. The percentage of coarse material within the seacliffs may be evaluated using the littoral cutoff diameter (Hicks, 1985) and sieve analysis. The seacliff coarse sediment yield is determined by reducing the total eroded volume to the percentage of coarse material within the cliff forming material (Equation 6-3). The routine calculates the annual seacliff coarse sediment yield for each compartment using the equation:

$$\boldsymbol{Q_{Si} = E_i \times \%coarse/t} \qquad \textbf{(6-3)}$$

where:

Q_S = the rate of seacliff coarse sediment yield (m^3/year),

i = the i^{th} compartment,

E_i = the total volume change for the seacliffs (m^3),

%coarse = the percent of coarse sediment in the seacliffs, and

t = time period (years)

Categorization Analysis

Change rates often are dependent on many variables such as soil types, groundwater conditions, erosion control, development, etc. To compare the effects of these variables, a TopCAT tool was developed to automate

compartment categorization and then determine the influence of those variables on topographic change. In this procedure the user creates digitized polylines delineating the different features and assigns categories to each polyline. If a polyline intersects a compartment, the routine assigns the corresponding category to the compartment. The tool outputs a table showing the compartmental change for each category and the percent contribution of that category to the overall change. For example, many areas of the coastline have portions which are protected by various methods such as seawalls, rip-rap, notch-fills, etc. whose effectiveness can be evaluated by the following equation (Young and Ashford 2006b):

$$\boldsymbol{PE = [(R_U - R_V)/R_U] \times 100\%} \qquad \textbf{(6-4)}$$

where:

PE = Percent Effectiveness,

R_U = the rate for the unclassified (natural) portions, and

R_V = the rate for the specific variable, *V*, (i.e. type of protection for this example).

To implement this comparison using the *Categorization Analysis Tool*, the user delineates polylines representing areas protected by each type of protection and assigns a category identifier for each type. The TopCAT routine then determines what type of erosion control is present in each of the compartments, if any, and evaluates the overall effectiveness of each type by a comparison with unprotected compartments.

RESULTS

Case Study 1 – Dog Beach, Del Mar, CA

To demonstrate the applicability of TopCAT to seacliff erosion analysis, TopCAT was used to evaluate a 500 m segment of Dog Beach in Del Mar, California (Figure 6-4). Topographic data collected from terrestrial LIDAR surveys in October 2005 and March 2007 were gridded into DEMs at 0.5 m resolution. The vertical RMS error between the datasets was evaluated by comparing the elevation differences between the two DEMs on a control surface (a concrete covered slope immediately north of the study area) and was found to be 13 cm. To evaluate the data accuracy, volumes calculated using the gridded data in TopCAT were compared to volumes calculated using 3D surfacing methods available in I-Site Studio 3.0 for failure sites F1,F2, and F3 (Table 6-1). The gridded data, as previously stated, were created by inverse distance weighted interpolation. I-Site Studio 3.0 creates surfaces by triangulating the data points to from a 3-D model.

TopCAT was then implemented with a compartment width of 2 m to evaluate the alongshore (Figure 6-5) and overall (Table 6-2) morphology. The results for the entire section (Table 6-2) show an average cliff face retreat rate of 4.9 cm/year and an average loss of 1 m^3 of sediment per year per meter of coastline. The total volume of sediment loss for the study area during the 1.5 year period was 745 m^3, or approximately 500 m^3 of sediment per year.

Figure 6-4. Location map for case study #1: Dog Beach, Del Mar, California (Elevation basemap from ESRI®)

Table 6-1. Comparisons of erosional volumes using 3D volumetric analysis and TopCAT compartmental analysis

Failure	I-Site 3D Vol (m^3)	TopCAT Vol (m^3)	% Difference
F1	263	251	-4.6
F2	312	346	11.1
F3	42	46	10.0
Sum	**617**	**644**	**4.3**

Table 6-2. Compartmental Analysis from TopCAT for Dog Beach, Del Mar CA (Oct 2005- March 2007)

Statistic	Average Cliff Face Retreat Rates (cm/year)	Volume per Unit Length per year (m^3/m-yr)
Average	**-4.90**	**-1.0**
Max Erosion	**-144**	**-32.7**
Max Accretion	13.9	3.4
Std Dev	17.7	3.8

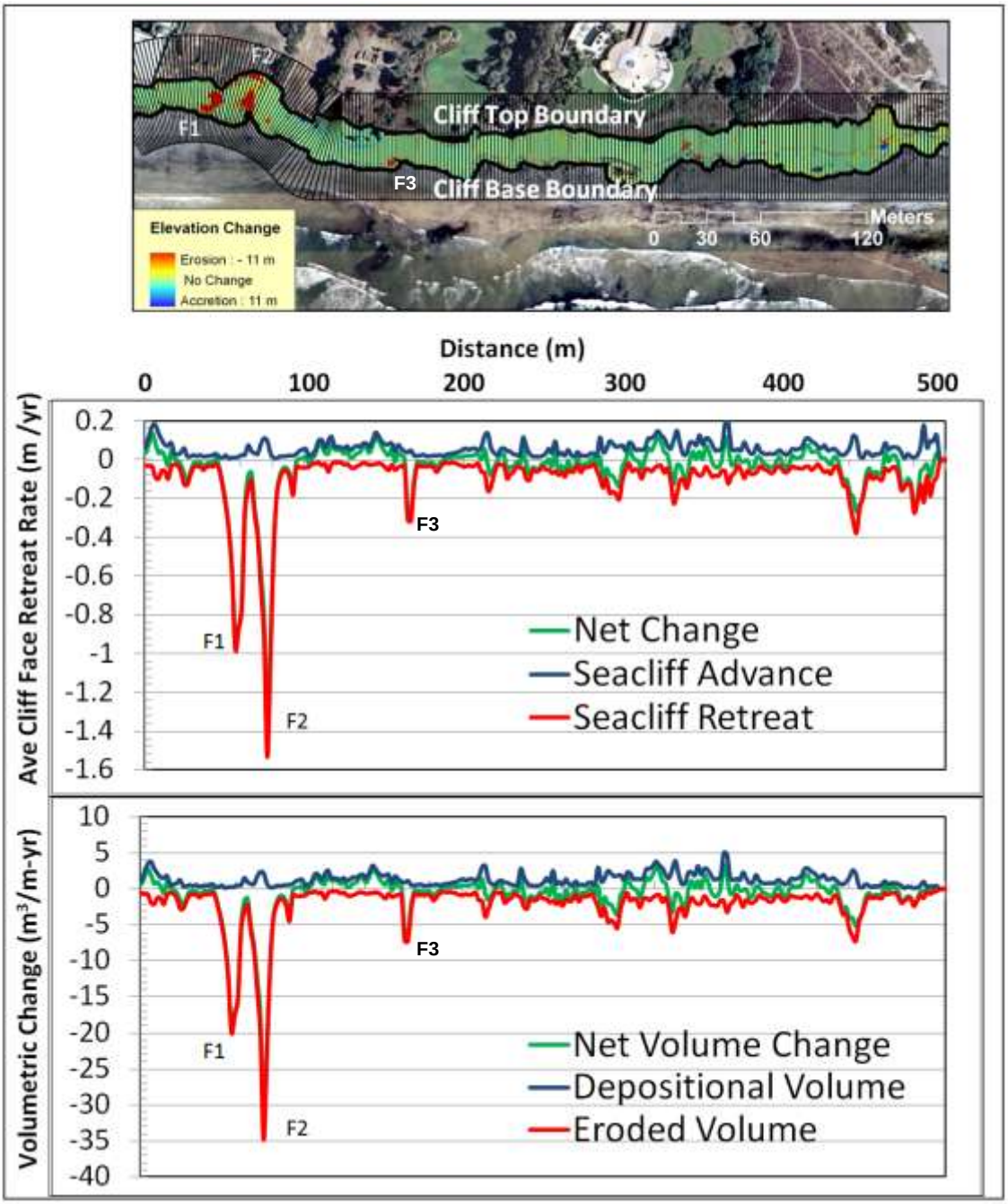

Figure 6-5. Elevation change grid and compartment analysis for Dog Beach, Del Mar, CA (October 2005 – March 2007)

Case Study 2 – North Cape Hatteras National Seashore, North Carolina

To demonstrate the application of TopCAT to volumetric beach and dune change, TopCAT was applied to a 3.8 km segment of Cape Hatteras National Seashore in North Carolina (Figure 6-6) immediately south of the Oregon Inlet. Airborne LIDAR datasets of the region from Fall 1997, Fall 1998 (post Hurricane Bonnie), and Fall 1999 (post Hurricane Dennis) were obtained from NOAA (*http://maps.csc.noaa.gov/TCM/*, NOAA - LDART, 2007) to analyze the volumetric change induced by Hurricanes Bonnie (August 19-30, 1998) and Dennis (August 24 to September 7, 1999) for the beaches, dunes, and combined beaches and dunes. These datasets have a vertical accuracy of 15 cm (NOAA – LDART, 2007). For this study, DEM's were created at 1 m resolution, and boundaries (Figure 6-7) were set at the approximate waterline, the initial beach-dune line, and the coastal highway to isolate the beach and dune regions.

Elevation change grids were evaluated for each hurricane (Bonnie: 1997 to 1998 datasets and Dennis: 1998 to 1999 datasets) and TopCAT was implemented with 5 m wide compartments. The alongshore volumetric change for a portion of the analysis is shown in Figure 6-8. The total sediment volume loss for the combined beaches and dunes was approximately 318,300 m^3 (Table 6-3) between 1997 and 1999. The average volumetric change in the study area was a sediment loss of 84 m^3/m (Table 6-4) from the beach and the dunes combined from 1997 to 1999, showing an average change of 42 $m^3/m\text{-}yr$.

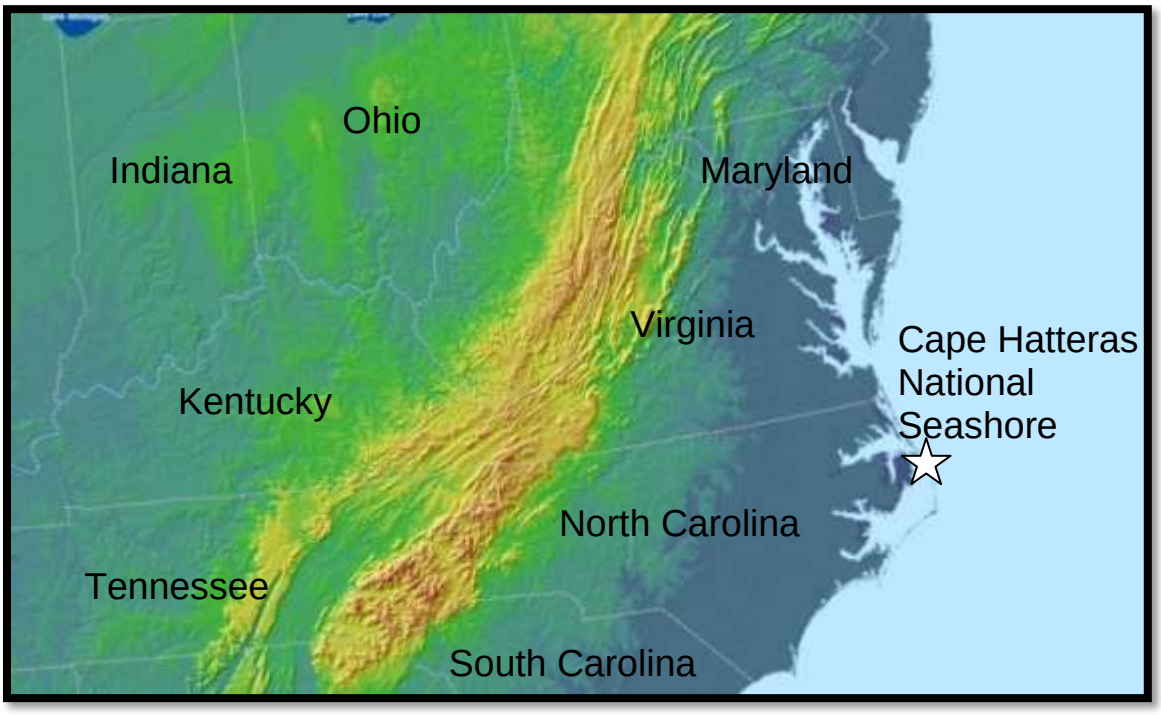

Figure 6-6. Location Map for Case Study #2 at Cape Hatteras National Seashore, North Carolina (Elevation basemap from ESRI®)

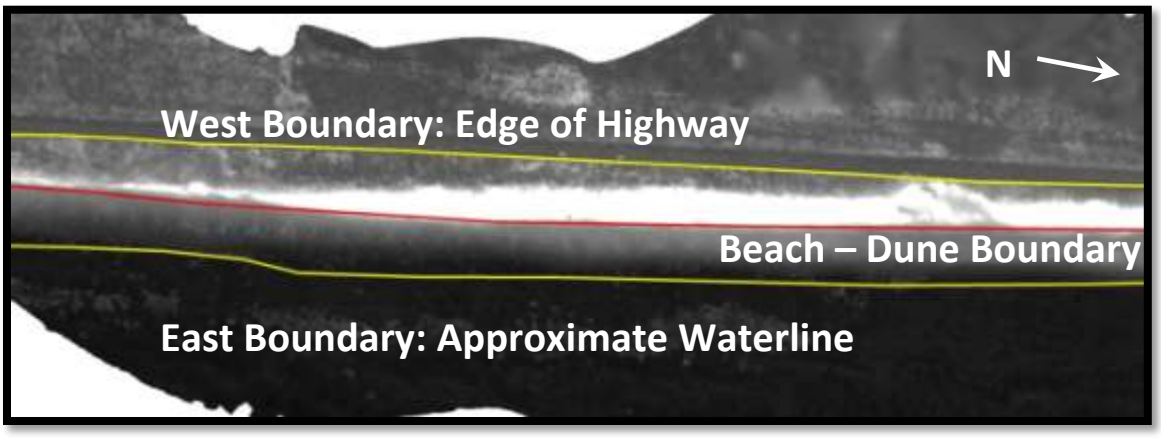

Figure 6-7. Analysis boundaries of DEM for Cape Hatteras National Seashore, North Carolina

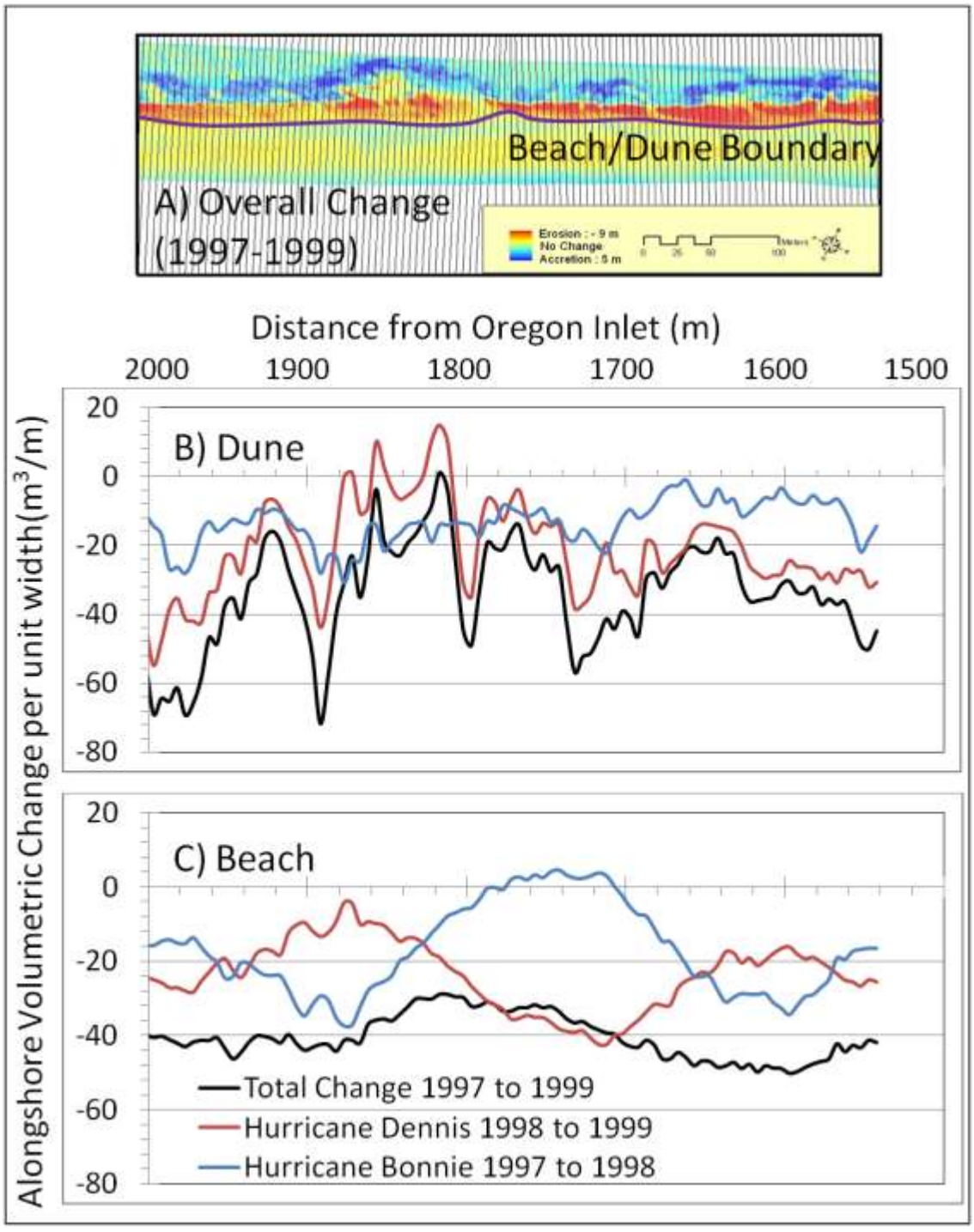

Figure 6-8. A) A portion of the elevation change grid for North Cape Hatteras National Seashore, North Carolina (Fall 1997 to Fall 1999) and alongshore B) dune and C) Beach volumetric changes induced by Hurricanes Dennis and Bonnie.

Table 6-3. Total volume change analysis from TopCAT for 3.8 km of Cape Hatteras National Seashore, North Carolina (1997-1999).

	Total Volume Change (m^3)		
	1997 to 1998 (Bonnie)	**1998 to 1999 (Dennis)**	**1997 to 1999 (Both)**
Dune	57,700	77,000	134,700
Beach	118,800	64,800	183,600
Combined	176,500	141,800	318,300

Table 6-4. Compartmental Analysis from TopCAT for volumetric alongshore erosion rates for 3.8 km of Cape Hatteras National Seashore, North Carolina (1997-1999)

	Volume per Unit Length (m^3/m)								
	1997 to 1998 (Bonnie)			**1998 to 1999 (Dennis)**			**1997 to 1999 (Both)**		
Statistic	**Dune**	**Beach**	**Combo**	**Dune**	**Beach**	**Combo**	**Dune**	**Beach**	**Combo**
Average	-15	-31	-46	-21	-17	-38	-36	-48	-84
Max Erosion	-55	-120	-141	-116	-62	-132	-135	-112	-186
Max Accretion	31	18	30	56	31	82	87	24	111
Std Dev	12	24	31	22	16	29	27	21	42

Uncertainty Analysis

To evaluate the quality of the digital elevation models used in this study, the results from the comparisons of the 1997 to 1999 datasets were compared to the sum of the results from the 1997 to 1998 and 1998 to 1999 dataset comparisons (Table 6-5) which would agree exactly if there were no interpolation or instrument error in the analysis. The results agreed well for the total eroded volume and average volumetric erosion rates with a 3.08% error between estimates for the entire length. Another method to evaluate the error within the individual compartments themselves, the root mean square of the errors (RMSE) of the 1997 to 1998 and 1998 to 1999 comparisons and the volumes of the 1997 to 1999 comparison for each compartment. The RMSE was found to be 16 m^3 for the total volumes of the individual compartments, or 3.3 m^3 for the volume per unit length for each compartment. When compared to the average erosional volumes of the compartments, this translates to an average error of 3.8% which agrees well with 3.08% error found in the total volume uncertainty analysis (Table 6-5). The percent error from this method is higher than looking at the entire area because in the total area, some of the areas of negative error can be cancelled out by areas of positive error in the total volume analysis. The RMSE method eliminates this problem, but does not allow for examination of specific statistics as can be done in the total volume analysis.

Table 6-5. Uncertainty Analysis of total volume from TopCAT for Oregon Inlet, North Carolina (1997 to 1999)

	1997 to 1998 and 1998 to 1999		1997 to 1999		Compartment Volume Comparisons	
Statistic	Volume per Compartment (m^3)	Volume per Unit Length (m^3/m)	Volume per Compartment (m^3)	Volume per Unit Length (m^3/m)	Volumetric Difference (m^3)	Percent Difference (%)
Average	-420	-84	-434	-87	-13	3.08
Max Erosion	-928	-186	-941	-188	-13	1.42
Max Accretion	557	111	552	110	-5	-0.92
Std Dev	211	42	212	42	1	0.22
Total	-318,281	-	-328,380	-	-10,098	3.08

DISCUSSION

Case Study 1 – Dog Beach, Del Mar, CA

Performing a regional analysis for this study area could lead to the conclusion that seacliff retreat occurs relatively slowly in Dog Beach (4.9 cm/year). However, TopCAT reveals that the erosion was dominated by two large (>250m^3) failure events (F1& F2 in Figure 6-5) which accounted for over 80% of the volume change for the study area. Site F2 is an exposure of a fault, which has led to increased localized erosion. Figure 6-5 shows localized retreat rates as high as 1.4 m/year in Dog Beach, showing that the average does not provide a complete understanding of the erosional patterns, but further statistics in addition to the average value paint a more comprehensive picture of what has actually occurred. Thus, TopCAT provides insight on the variable and episodic

nature of seacliff retreat and shows the enhanced understanding of geologic processes available by performing a small scale analysis.

Case Study 2 – North Cape Hatteras National Seashore, North Carolina

An examination of Tables 2 and 3 shows that Hurricane Bonnie produced more volume change on the beaches (118,800 m^3) than on the dunes (57,700 m^3), whereas Hurricane Dennis produced similar volume change on the beaches (64,800m^3) as on the dunes (77,000 m^3). Further, Hurricane Dennis shows more dune erosion (77,000 m^3) than Hurricane Bonnie (57,700m^3), whereas Hurricane Bonnie (118,800 m^3) shows almost double the volumetric beach change as Hurricane Dennis (64,800m^3).

Meridith et al. (1999) previously studied the Cape Hatteras National Seashore as part of a large scale analysis of volumetric change in North Carolina after Hurricane Bonnie using sections 22 km in length. Meridith et al. (1999) calculated an average volumetric sediment loss per unit length of shoreline of 38 m^3/m, similar to the value of 46 m^3/m calculated in this study using TopCAT for only 3.8 km of that 22 km section (Figure 6-8). TopCAT, however, provides new insights on the erosional patterns that can only be observed in a small scale investigation. For example, by analyzing the compartmental trends (Figure 6-8), it is seen that the dune system experienced similar erosion trends during the two hurricane events. However, the beach system appears out of phase in its erosional patterns between the two hurricanes where the areas with largest volumetric change during the first hurricane event show minimal change during

the second and vice versa. This response appears to be a trend of shoreline adjustment during the second event which would be averaged out in a large scale analysis. This example illustrates TopCAT's ability to enhance understanding of system response to natural disasters.

CONCLUSIONS

This chapter presents a new GIS based tool (TopCAT) which provides a user-friendly interface for automated volumetric change analysis of large topographical datasets along with several tools to enhance DEM and LIDAR data processing. The tool was developed to provide high resolution visual and statistical morphological change using a discrete compartmentalization method. Performing a change analysis in TopCAT provides the same useful information (overall volumetric change and retreat rates) as performing a large-scale regional analysis, but in addition, TopCAT provides new insights on the smaller scale where localized events can be further analyzed and provides a statistical background on the large scale regional information. For example, using TopCAT reveals erosional hot spots and alongshore coastal change trends which are not readily visible when performing overall and average change detection for a region. This information leads to an enhanced understanding of the hazard which can be underestimated in a large scale analysis. While TopCAT was successfully applied to the examples presented in this chapter for seacliff face retreat rate analysis and beach and dune volumetric erosion analysis, TopCAT can be a beneficial tool for many other types of statistical change analysis of

elongated features that experience topographical change. TopCAT will be publically available for free download at *http://lidarweb.ucsd.edu/TopCAT/*.

ACKNOWLEDGEMENTS

The authors would like to thank Elizabeth Johnstone for performing LIDAR survey work in Del Mar, CA, NOAA for the Aerial LIDAR datasets for North Carolina, and Scott Schiele and John Dolan of I-Site for technical assistance.

Chapter 6, in part, is being prepared for submission for publication of the material. Olsen, M.J., Young, A.P., and Ashford, S.A. The dissertation author was the primary investigator and author of this paper.

CHAPTER 7. CONCLUSIONS AND CONTRIBUTIONS

OVERVIEW

This dissertation develops and unifies techniques from a variety of disciplines including geomatics, geotechnical engineering, geology, and computer science to create methodologies to provide new insights about the complex mechanisms governing coastal erosion, sediment distribution, and feedback mechanisms.

New surveying techniques have been developed through this research to apply TLS to large-scale dynamic environments. These methods substantially increase efficiency compared to previous control methods which are limited in application to localized sites. Thus, TLS can now be performed on a regional scale, which allows for an improved analysis of geologic processes which occur on a larger scale. Through the implementation of calibration surveys, optimal scanning parameters of setup spacing, distance from cliff, and sampling ratio were obtained and verified in multiple field surveys. Calibration testing showed how these parameters affect scan quality from instrumental error and topographical occlusions. The numerous repeat surveys completed during this work provide a large database with a wealth of information about the coastline and sediment dispersal. These datasets can be used to determine development setbacks and identify hazard areas. Because they are georeferenced, they can easily be integrated with other coastal datasets.

Advances in the field of computer science and visualization include the understanding of the necessity of constraints in the alignment of point clouds and

the use of multiple neighboring point clouds to avoid propagation of detrimental misalignments on a regional scale. This new method does not require fixed reference models or external data for alignment, but is self-sufficient. Additionally, previous methods fix one of the scans to provide the global coordinate system, whereas, this method allows all scans to be placed in real-world coordinates. Also, a workflow for the scan alignment procedure was developed and made publically available, eliminating the tedious user interaction required with previous techniques. Methodologies of data verification through RMS error calculations, 2D cross sections, GPS comparisons on “fixed” structures, and repeat surveys were also presented. These ensure that errors are minimized and change assessment highlights actual change as opposed to misalignments. Finally, the methodology was developed for long, linear, topographic features, which presents new challenges not found when scanning conventional objects or sites for which point cloud alignment algorithms were initially developed.

These TLS surveys collected using this new methodology provide valuable geologic and geotechnical information on sediment reworking processes and slope stability. Rapid response endeavors provide the unique ability to analyze the sequence of events from before the failure to showing the failure sediment dispersal at an unprecedented scale. Correlation of the TLS data with wave, climate, and tidal data shows the relationship of extreme wave events and precipitation with cliff failures. It also quantifies the speed at which waves can

rework the sediment provided by these cliff failures. A classification system distinguishing failure sites based on wave action was developed to prioritize the study area and highlight differential sediment dispersal rates. Further, the classification system helps determine the causes and conditions leading to failure. Finally, the ability of a seacliff failure to act as a protection and stabilizing mechanism was also discovered from repeat surveys using high resolution TLS data. Such a feedback causes failures due to wave undercutting and notching to migrate laterally and begins to explain the long-term linear retreat of the seacliffs that minimizes the development of embayments and promontories.

The automation of statistical topographical change analysis in a GIS environment was presented, showing new insights by looking at both small scale and large scale change for datasets along large coastal sections. Application of these tools to seacliffs showed the importance of erosional hotspots in short term erosion rates. These tools were also used to illustrate the differences in sediment dispersal between beach and dune systems during hurricane events. In addition, several new tools to assist in performing time-consuming processes with LIDAR datasets were developed and effectively implemented.

A website has been created (*http://lidarweb.ucsd.edu/coastalstudy/*) to disseminate these results and data to the public and inform about the dangers and effects of seacliff erosion. Such information will allow coastal managers and policy makers to have reliable data and information to determine the optimal utilization of the valuable coastline.

ADDITIONAL APPLICATIONS OF TLS

Although this dissertation focused on the application of TLS to coastal studies, the dissertation author also worked on several other projects to develop TLS techniques including deformation analysis of structural specimens (Figures 7-1 and 7-2), historical preservation projects (Figure 7-4 and 7-5), and archeological sites.

Application of TLS to these projects has produced several unique challenges, as well. These scans were performed at high resolution and close range, producing large datasets which require substantial computational power to display, query, and analyze. In the case of the Palazzo Vecchio scanning project (Figure 7-4), a database of over 1.5 billion points was collected during the surveys, each with XYZ coordinates, RGB color values and an intensity signature value. The dissertation author worked with computer scientists toward developing new algorithms to not only process the data, but display the cumbersome datasets in real time. Figure 7-6 shows the display on a high resolution (286 million pixels) wall (Hiperspace) which allows researchers to visually interrogate and discuss large datasets that cannot be fully visualized on conventional display systems. Figure 7-7 shows a CAVE environment where users can interact with the data a full 3D environment allowing for new insights and the ability to edit and classify the data in a more intuitive way.

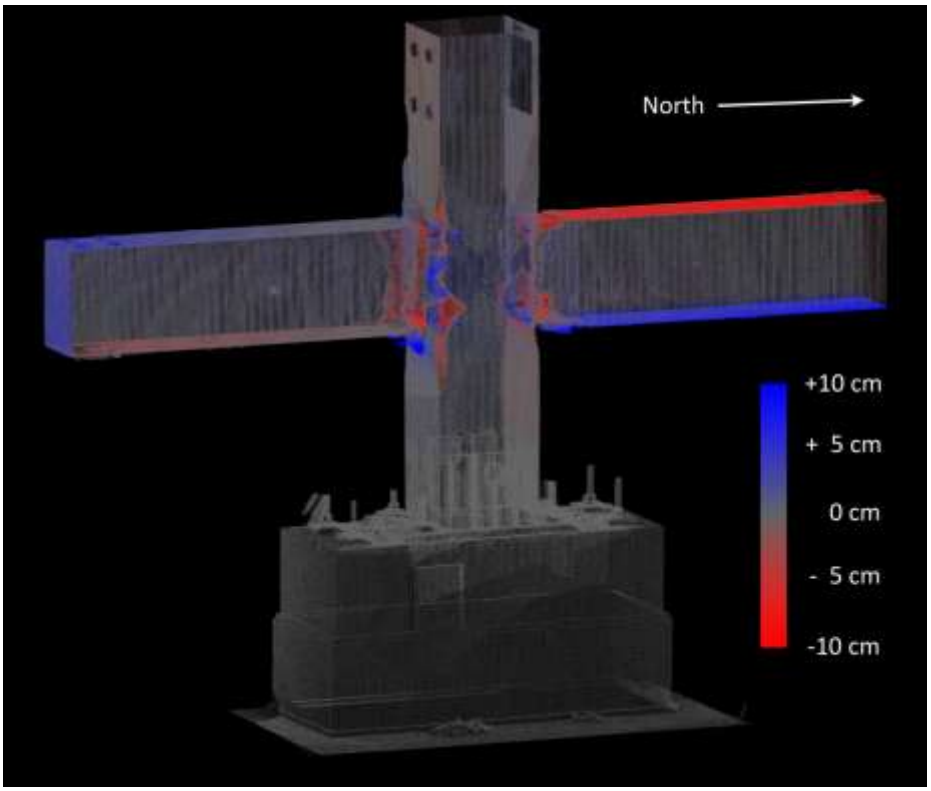

Figure 7-1. Structural specimen point cloud after failure

Figure 7-2. Close-up of surface mesh of failed structural specimen with overlaid texture map.

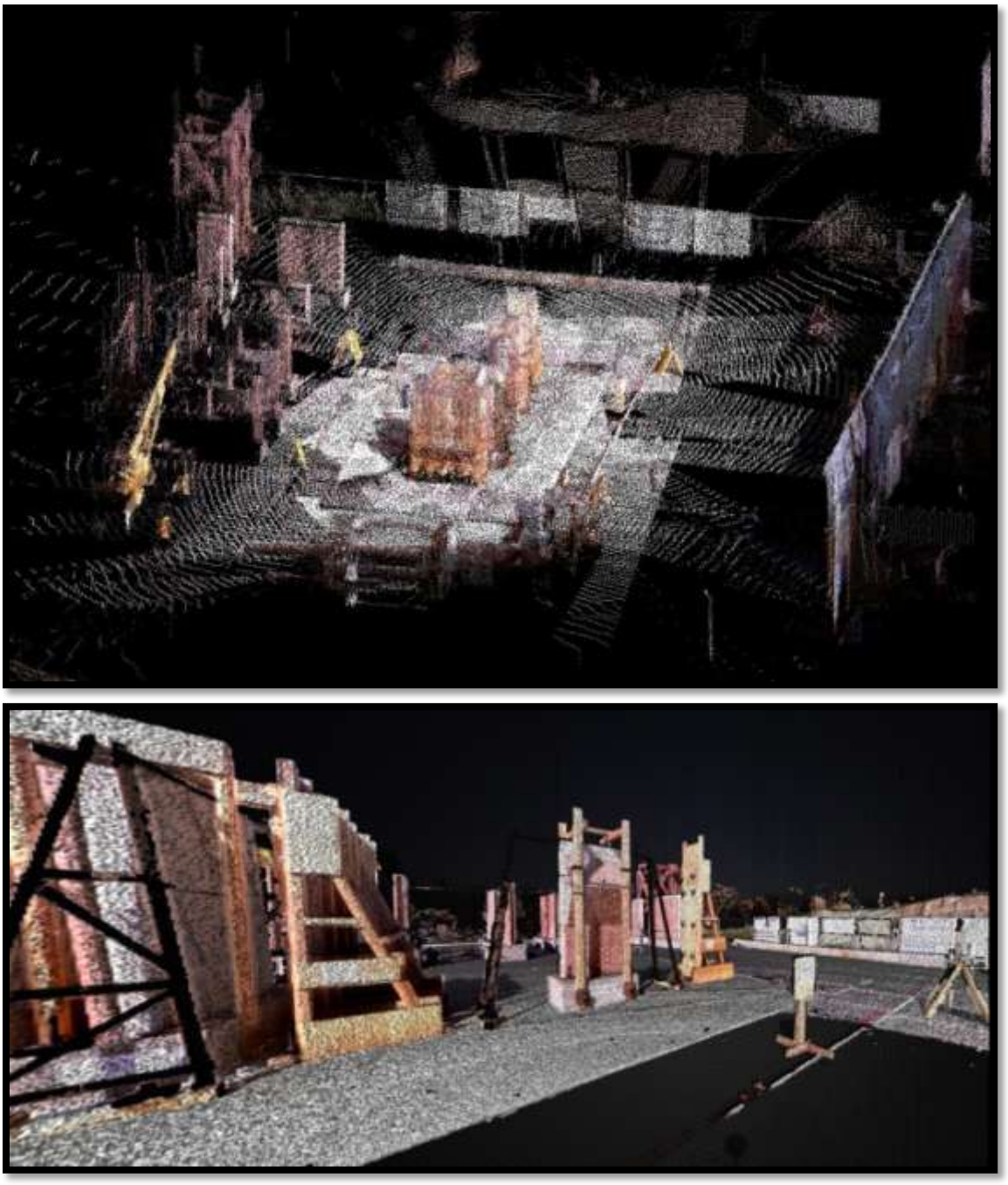

Figure 7-3. (A) LIDAR point clouds of structural specimens on the UCSD Outdoor Shake Table (B) with photodraped surface mesh

Figure 7-4. Point cloud dataset for the Hall of the 500 in the Palazzo Vecchio in Florence Italy

Figure 7-5. Garden Courtyard of the Palazzo Medici in Florence Italy.

Figure 7-6. Display of coastal dataset on Hiperspace tile display wall, a 286 Million Pixel Display

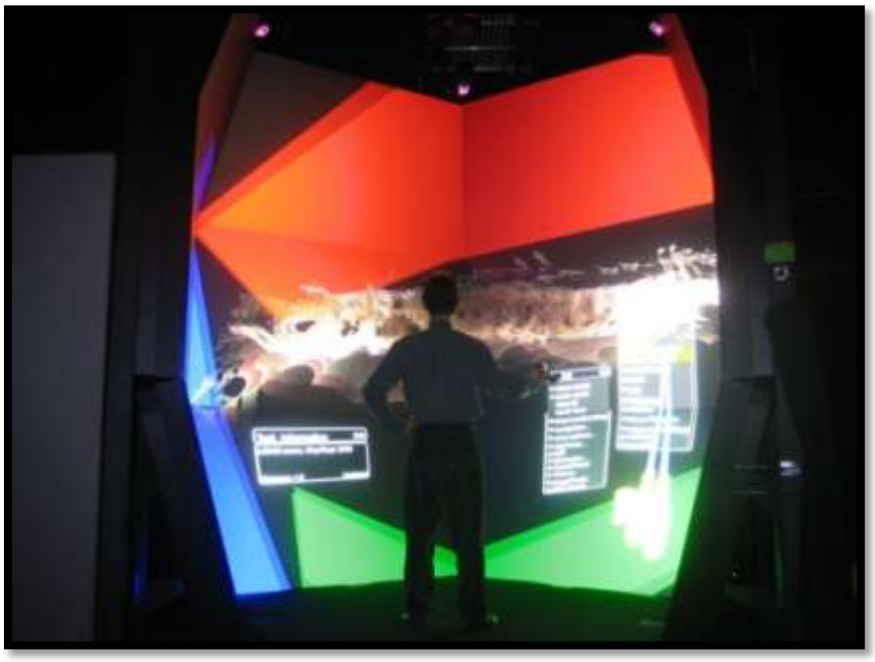

Figure 7-7. Display of coastal dataset in a CAVE Virtual Reality Environment (from Hsieh et al. 2007)

FUTURE RESEARCH

While TLS has been successfully applied to a wide range of projects, several difficulties arise in its application. Because data is collected rapidly, TLS datasets can become very large which is very taxing on data processing and visualization. Additionally, point clouds are usually triangulated to produce surface meshes for analysis. Developing an optimal surface that removes redundancy and preserves features can be an immense challenge. Development of point based change analysis tools help speed up the analysis. Furthermore, intensity values obtained by laser scanners can be a valuable tool in the automation of classification of soil types and vegetation in the scans. These intensity values are dependent on the range, the angle at which the laser is reflected off of the surface, the type of laser pulse, and the surface material. Hence, a model to normalize the intensity values so that the only variance in the values is because of material properties is requisite to provide accurate classification results based off of intensity. RMS values between scans can also be used to highlight vegetated areas.

Further optimization of TLS surveying can be performed by using a baseline model as a reference while performing field scans. An algorithm can then highlight data gaps in current surveys and predict the optimal location for the next survey to fill in those gaps. Additionally, as technology is further developed to mobile scanning platforms, the optimal scanning parameters from

this work can be modified and/or normalized to use the newer methods for optimal coverage.

Furthermore, substantial time series data from repeat TLS of the coastal sections will be instrumental in determining erosional rates and patterns. Such data will allow for predictive mechanisms to be developed to determine the areas with the highest hazards. These datasets can be used in conjunction with other datasets such as aerial LIDAR and nearshore mapping to produce a more complete model of the coast to understand the processes shaping the coastline (Figure 7-8).

Technology changes rapidly. Although these techniques were developed for terrestrial laser scanning, which is currently the state of the art for such mapping, they will be applicable to new technologies as well because the new technologies face similar challenges. For example, advancements in photogrammetry now allow point clouds to be created from a series of photographs (Vergauwen and Van Gool, 2006; Snaveley, et al., 2008) for 3D reconstruction. These novel techniques not only will allow for rapid data collection with inexpensive, lightweight equipment but will also allow for the exploitation of a wealth of previous photographic datasets of the coastline. Currently, accuracy and georeferencing limitations need to be resolved for these new 3D reconstruction techniques to be implemented for coastal studies, and the methods presented herein will provide a guide to assist in these tasks to ensure optimal spatial and temporal modeling for coastal studies.

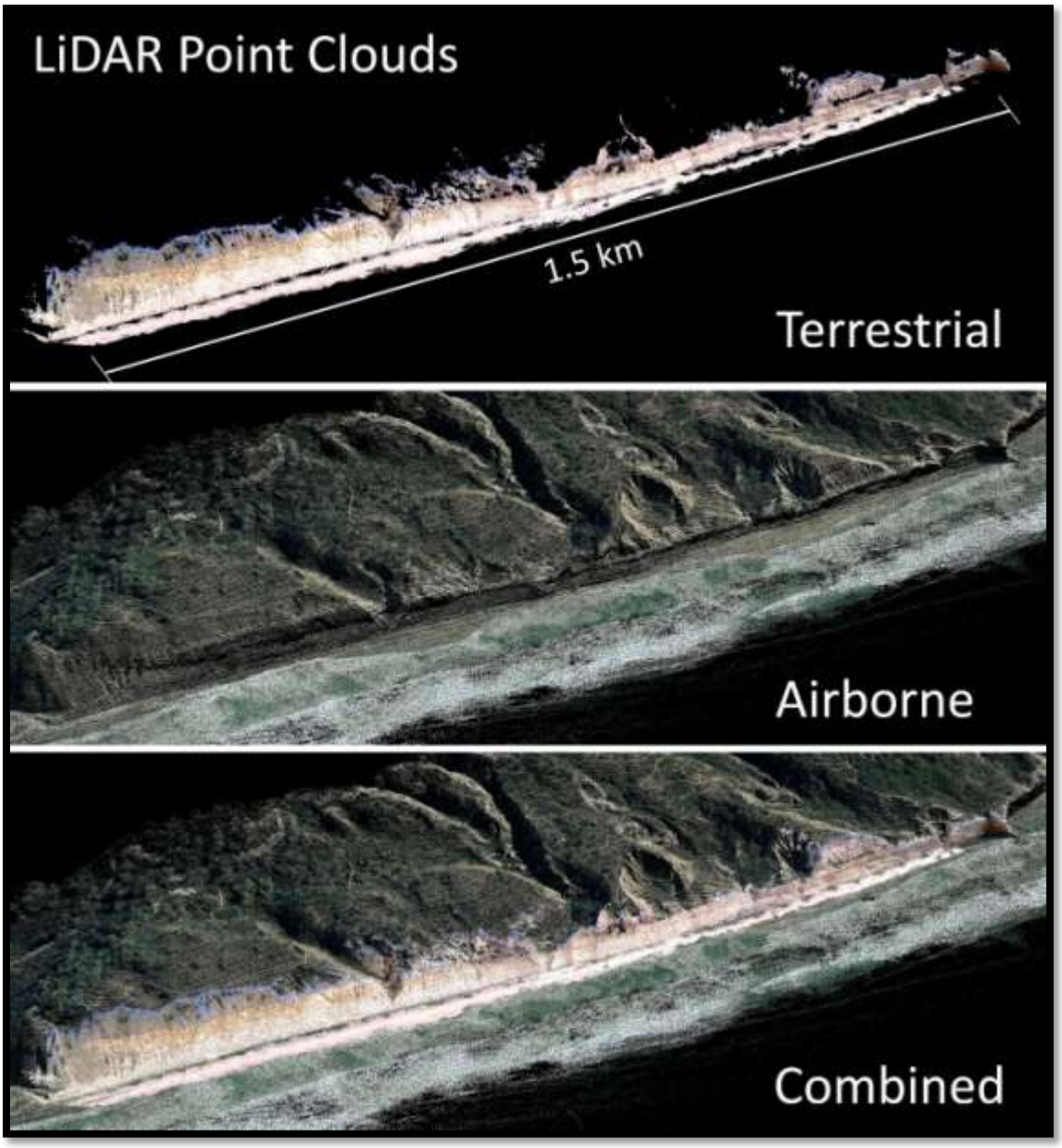

Figure 7-8. Comparison of (A) Aerial LIDAR dataset (NOAA - LDART 2007 with photographic coloring from photographs from USGS 2008). (B) Terrestrial LIDAR dataset (Feb 2008), and (C) combined for Torrey Pines State Reserve. Note the poor coverage of the airborne LIDAR data on the cliff face and the lack of coverage of the terrestrial LIDAR on the cliff top.

APPENDIX A: Calculating RMS using the point to plane technique

After, selecting a point from scan A, the three nearest points from scan B can be used to obtain the plane. First, the normal (**n**) of the three points can be calculated by the cross product of the vectors from a point (p_1) in scan B to the other two points (p_2 and p_3):

$$\vec{\boldsymbol{n}} = (\boldsymbol{a}, \boldsymbol{b}, \boldsymbol{c}) = (\boldsymbol{p3} - \boldsymbol{p1}) \times (\boldsymbol{p2} - \boldsymbol{p1}) \qquad \textbf{(A.1)}$$

where *a, b, c* are the components of the normal to the plane. Then, the individual components of the normal can be substituted into the plane equation:

$$\boldsymbol{ax} + \boldsymbol{by} + \boldsymbol{cz} + \boldsymbol{d} = \boldsymbol{0} \qquad \textbf{(A.2)}$$

where *d* is a constant based on the points in the plane. Using any of the 3 points and substituting in the *x, y, z* values of that point and the values of *a*, *b*, and *c* calculated from equation A.1 into equation A.2, the constant *d* is obtained to complete the equation for the plane. The shortest distance from the point (p_A) to the plane is found by projecting that point (p_A) onto the plane by taking the dot product of the vector (***v***) formed by the nearest point on that plane (p_B = *(x, y, z))* to the point p_A and the normalized normal vector of the plane obtained in equation A.1. This yields:

$$\boldsymbol{D_i} = \vec{\boldsymbol{n}} \cdot \vec{\boldsymbol{v}} = \frac{|\boldsymbol{a}(\boldsymbol{x} - \boldsymbol{x_a}) + \boldsymbol{b}(\boldsymbol{y} - \boldsymbol{y_a}) + \boldsymbol{c}(\boldsymbol{z} - \boldsymbol{z_a})|}{\sqrt{\boldsymbol{a^2} + \boldsymbol{b^2} + \boldsymbol{c^2}}} \qquad \textbf{(A.3)}$$

where D_i is the minimum distance from the point to the plane. Substituting the plane equation (equation A.2) into equation A.3 yields:

$$\boldsymbol{D_i} = \frac{|\boldsymbol{a}(\boldsymbol{x_a}) + \boldsymbol{b}(\boldsymbol{y_a}) + \boldsymbol{c}(\boldsymbol{z_a}) + \boldsymbol{d}|}{\sqrt{\boldsymbol{a^2} + \boldsymbol{b^2} + \boldsymbol{c^2}}} \qquad \textbf{(A.4)}$$

The RMS is obtained by summing up the distances calculated for all *n* of the selected point pairs using the following equation:

$$\boldsymbol{RMS = \sqrt{(\sum_{i=1}^{n} D_i^2)/n}} \qquad \textbf{(A.5)}$$

APPENDIX B: Least squares approach to solve for the optimal α_B for a given value of α_A

First, define matrices to represent the 2D coordinates of the matching points of scans A and B. Because the scan alignment optimization has been reduced to one parameter per scan (rotation about the Z axis) from the constraints, we do not need the other translation and rotation values. We also do not include Z values because a rotation about the Z axis does not change the Z values. However, as shown in appendix A, when evaluating the RMS, we use a full 3D formulation because we have error in the Z direction. Note that the matching points of scan A are found by method described in the previous section by finding the nearest point on the plane of scan A to the selected point of scan B:

$$X_A = \begin{Bmatrix} x_{A1} & y_{A1} \\ x_{A2} & y_{A2} \\ \vdots & \\ x_{An} & y_{An} \end{Bmatrix} \quad X_B = \begin{Bmatrix} x_{A1} & y_{A1} \\ x_{A2} & y_{A2} \\ \vdots & \\ x_{An} & y_{An} \end{Bmatrix} \quad \textbf{(B.1A,B.1B)}$$

Then, define matrices to represent the 2D coordinates of the origins of scans A and B:

$$X_{AO} = \begin{Bmatrix} X_{A0} & Y_{A0} \\ X_{A0} & Y_{A0} \\ \vdots & \\ X_{A0} & Y_{A0} \end{Bmatrix} \quad X_{BO} = \begin{Bmatrix} X_{B0} & Y_{B0} \\ X_{B0} & Y_{B0} \\ \vdots & \\ X_{B0} & Y_{B0} \end{Bmatrix} \quad \textbf{(B.2A,B.2B)}$$

Next, define rotational matrices for the rotations of scans A and B about their respective axes:

$$R_A = \begin{bmatrix} \cos \propto_A & \sin \propto_A \\ -\sin \propto_A & \cos \propto_A \end{bmatrix} \quad R_B = \begin{bmatrix} \cos \propto_B & \sin \propto_B \\ -\sin \propto_B & \cos \propto_B \end{bmatrix} \quad \textbf{(B.3A,B.3B)}$$

Now, define matrices to represent the 2D coordinates of the points of scans A and B after the rotations have been completed and the scans are at their optimal

position. Note that because we want to perform the rotations about the scan origin, we must translate the entire scan so that it has an origin at (0,0), perform the rotation, and translate the scan origin back to its original position.

$$X_{Af} = (X_A - X_{AO})R_A + X_{AO} \quad \textbf{(B.4A)}$$

$$X_{Bf} = (X_B - X_{BO})R_B + X_{BO} \quad \textbf{(B.4B)}$$

Lastly, define the error matrix,

$$V = \begin{Bmatrix} v_{x1} & v_{y1} \\ v_{x2} & v_{y2} \\ & \vdots \\ v_{xn} & v_{yn} \end{Bmatrix} \qquad \textbf{(B.5)}$$

Now, formulate the least squares condition when both scans are rotated to the optimal fit:

$$X_{Bf} = X_{Af} + V \qquad \textbf{(B.6)}$$

We have two unknown variables α_A and α_B, which we need to solve for by finding the optimal values to minimize the sum of the squares of the errors. We will use an iterative approach to estimate α_A and then use a least squares approach to solve directly for the optimal α_B given for each value for α_A. By evaluating the RMS for each pair using the method in Appendix A, we can find the combination that produces the lowest RMS. Substituting equation B.4B into equation B.6 to include the R_B matrix containing the unknown variable α_B, we have:

$$(X_B - X_{BO})R_B + X_{BO} = X_{Af} + V \qquad \textbf{(B.7)}$$

If we make the assumption that the angle is very small ($cos \propto \approx 1$ and $sin \propto \approx \propto$), and solve equation B.7 for V, we have:

$$\begin{Bmatrix} v_{x1} & v_{y1} \\ v_{x2} & v_{y2} \\ \vdots & \\ v_{xn} & v_{yn} \end{Bmatrix} = \begin{Bmatrix} x_{B1} - X_{B0} & y_{B1} - Y_{B0} \\ x_{B2} - X_{B0} & y_{B2} - Y_{B0} \\ \vdots & \\ x_{Bn} - X_{B0} & y_{Bn} - Y_{B0} \end{Bmatrix} \begin{bmatrix} 1 & \propto_B \\ -\propto_B & 1 \end{bmatrix} + \begin{Bmatrix} X_{B0} & Y_{B0} \\ X_{B0} & Y_{B0} \\ \vdots & \\ X_{B0} & Y_{B0} \end{Bmatrix} - \begin{Bmatrix} x_{Af1} & y_{Af1} \\ x_{Af2} & y_{Af2} \\ \vdots & \\ x_{Afn} & y_{Afn} \end{Bmatrix} \quad \textbf{(B.8)}$$

To apply the least squares method, we need to calculate the sum of the squares of the errors:

$$V_{SS}^2 = v_{x1}^2 + v_{y1}^2 + v_{x2}^2 + v_{y2}^2 + \cdots + v_{xn}^2 + v_{yn}^2 \qquad \textbf{(B.9)}$$

To minimize, we can differentiate B.9 and set it equal to zero:

$$\frac{\partial V_{SS}^2}{\partial \propto_B} = \frac{\partial v_{x1}^2}{\partial \propto_B} + \frac{\partial v_{y1}^2}{\partial \propto_B} + \frac{\partial v_{x2}^2}{\partial \propto_B} + \frac{\partial v_{y2}^2}{\partial \propto_B} + \cdots + \frac{\partial v_{xn}^2}{\partial \propto_B} + \frac{\partial v_{yn}^2}{\partial \propto_B} = 0 \qquad \textbf{(B.10)}$$

Reducing equation B.11 for only the i^{th} terms produces:

$$\frac{\partial v_{xi}^2}{\partial \propto_B} + \frac{\partial v_{yi}^2}{\partial \propto_B} = 0 \qquad \textbf{(B.11)}$$

Looking at the errors from the i^{th} matching pair in B.8, we can formulate:

$$v_{xi} = x_{Bi} - (y_{Bi} - Y_{BO}) \propto_B - x_{Afi} \qquad \textbf{(B.12A)}$$

$$v_{yi} = y_{Bi} + (x_{Bi} - X_{BO}) \propto_B - y_{Afi} \qquad \textbf{(B.12B)}$$

So differentiating $v_{xi}^2$and v_{yi}^2 (squaring equations B.12A and B.12B) with respect to α_B:

$$\frac{\partial v_{xi}^2}{\partial \propto_B} = 2\big(x_{Bi} - (y_{Bi} - Y_{BO}) \propto_B - x_{Afi}\big)(Y_{BO} - y_{Bi}) \qquad \textbf{(B.13A)}$$

$$\frac{\partial v_{yi}^2}{\partial \propto_B} = 2\big(y_{Bi} + (x_{B1} - X_{BO}) \propto_B - y_{Afi}\big)(X_{BO} - x_{Bi}) \qquad \textbf{(B.13B)}$$

Substituting the expressions from B.13A and B.13B into equation B.11 and solving for α_B yields:

$$\propto_B = -\frac{x_{Afi}y_{Bi} - x_{Afi}y_{BO} + x_{Bi}y_{BO} - y_{Afi}x_{Bi} + y_{Afi}x_{BO} - y_{Bi}x_{BO}}{(y_{Bi} - y_{BO})^2 + (x_{Bi} - x_{BO})^2} \qquad \textbf{(B.14)}$$

Finally, using superposition to expand the solution to use all matching point pairs found in the scans and factoring to minimize computations produces:

$$\propto_B = -\frac{\sum_{i=1}^{n} x_{Afi}y_{Bi} - \sum_{i=1}^{n} y_{Afi}x_{Bi} + y_{BO}(\sum_{i=1}^{n} x_{Bi} - \sum_{i=1}^{n} x_{Afi}) + x_{BO}(\sum_{i=1}^{n} y_{Afi} - \sum_{i=1}^{n} y_{Bi})}{\sum_{i=1}^{n} y_{Bi}^2 + \sum_{i=1}^{n} x_{Bi}^2 - 2(y_{BO}\sum_{i=1}^{n} y_{Bi} + x_{BO}\sum_{i=1}^{n} x_{Bi}) + n(y_{BO}^2 + x_{BO}^2)} \quad \textbf{(B.15)}$$

which represents the optimal rotational angle for scan B using an assumed value of α_A. We can then continue to iterate values of α_A and select the combination which produces the lowest RMS using the method discussed in Appendix A. We can then set up a tri-diagonal matrix to store the rotation angles found by matching each scan with its neighbors:

$$\propto = \begin{bmatrix} \propto_{0,0} & \propto_{0,1} & Null & & & & \\ \propto_{1,0} & \propto_{1,1} & \propto_{1,2} & \cdots & & Null & \\ Null & \propto_{2,1} & \propto_{2,2} & & & & \\ & \vdots & & \ddots & & \vdots & \\ & & & & \propto_{n-2,n-2} & \propto_{n-2,n-1} & Null \\ & Null & & \cdots & \propto_{n-1,n-2} & \propto_{n-1,n-1} & \propto_{n-1,n} \\ & & & & Null & \propto_{n,n-1} & \propto_{n,n} \end{bmatrix} \quad \textbf{(B.16)}$$

where $\alpha_{i,j}$ represents the rotation angle of scan *i* based on correspondence with scan *j* for i≠j and $\alpha_{i,j}$ = 0.5*($\alpha_{j,j+1}$ + $\alpha_{j,j-1}$) for *i* = *j*. If desired, a weighting can be assigned to the terms in the average. A weighting was not used for this study because the warping was uniform on both sides of the scan. The matrix is tridiagonal because there is very limited correspondence between scans other than between adjacent scans when scanning long, linear features. Although not implemented in *PointReg*, when scanning targets that would not be considered linear features, the tridiagonal matrix could be expanded to a full matrix. Then rotation ($\alpha_{i,i}$) for the i^{th} scan could then be found by averaging all of the non-null

and non-diagonal elements in row *i.* This average would need to be weighted so that the overall value from the scans on the left of a scan *i* have equal weight to the overall value from those on the right to minimize warping.

REFERENCES

Akca, D., and Gruen, A., (2005). "Fast correspondence search for 3D surface matching," *Int. Arch. of the Photogrammetry, Remote Sensing and Spatial Information Sciences*, 36(3/W52), Enschede, the Netherlands, 186-191.

Akca D. and Gruen A., (2007). "Generalized least squares multiple 3D surface matching," *Int. Arch. of Photogrammetry and Remote Sensing*, 36(3/W52), Finland.

Alba, M., Longoni, L., Papini M., Roncoroni, F., and Sacioni, M. (2005). "Feasibility and problems of TLS in modeling rock faces for hazard mapping," *Int. Arch. of Photogrammetry and Remote Sensing*, 36(3/W19), Enschede, Netherlands.

Alba, M., and Scaioni, M. (2007). "Comparison of techniques for terrestrial laser scanning data georeferencing applied to 3-D modeling of cultural heritage," *Int. Arch. Of Photogrammetry and Remote Sensing*, 36(5/W47), Zurich, Switzerland.

Aman, R.L. (2004). "A minimal surface perturbation method for global surface registration of unstructured point cloud data," MS Thesis, Industrial Engineering, North Carolina State University.

American Association of Stratigraphic Palynologists (AASP), 1973. "Coastal Area Geology at Torrey Pines State Preserve, and La Jolla, San Diego County, California," 6th Annual Meeting Field Trip Guidebook, October 18, 1973.

Barber, D., Mills, J., and Smith-Voysey, *S.,* 2008. "Geometric validation of a ground-based mobile laser scanning system,*" ISPRS Journal of Photogrammetry and Remote Sensing,* 63(1), Theme Issue: Terrestrial Laser Scanning, 128-141.

Benumof, B.T. and Griggs, G.B., 1999. "The dependence of seacliff erosion rates, cliff material properties, and physical processes: Sand Diego County, California." Shore and Beach, 67(4), 29-41.

Benumof, B.T., Storlazzi, C.D., Seymour, R.J., and Griggs, G.B, 2000. "The relationship between incident wave energy and seacliff erosion rates: San Diego County, California," Journal of Coastal Research, 16(4), 1162-1178.

Bernardini, F., Martin, I., Mittleman, J., Rushmeier, H., Taubin, G., 2002. "Building a Digital Model of Michelangelo's Florentine Pieta'." IEEE Computer Graphics & Applications, 59-67.

Bernardini F., and Rushmeier, H., (2002). “The 3D model acquisition pipeline,” *Computer Graphics Forum*, 21 (2), 149–172.

Besl, P.J., and McKay, N.D., (1992). “A method for registration of 3D shapes,” *IEEE PAMI*, 14(2), 239-256.

California Virtual Reference Station, CALVRS (2008). “CALVRS: a real-time California cooperative.” <http://www.calvrs.net> (Last Accessed: August 7, 2008).

Chen, Y. and Medioni, G. G., (1992). “Object modeling by registration of multiple range images,” *Image and Vision Computing*, 10(3), 145–155.

Collins, B., and Sitar, N. (2004). “Application of high resolution 3d laser scanning to slope stability studies.” *Proc., 39th Annual Symposium on Engineering Geology and Geotechnical Eng*., Butte, MT, 79–92.

Collins, B., Kayen, R., Reiss, T., and Sitar, N. 2007. “Terrestrial LIDAR investigation of the December 2003 and January 2007 activations of the Northridge Bluff Landslide, Daly City, California.” *U.S. Geologic Survey, Open File Report 2007-1079*, 32pg.

Colorado Center for Astrodynamics Research, 2008. “University of Colorado Global Mean Sea Level,” <http://sealevel.colorado.edu>, (Last Accessed: Nov. 3, 2008)

Crowell, M. Honeycutt, M., and Hatheway, D., 1999. “Coastal erosion hazards study: phase one mapping.” *Journal of Coastal Research*, SI(28), 10-20. Royal Palm Beach (Florida), ISSN 0749-0208.

Dal Piaz, V., Guaranieri, A., Pirotti, F. Vettore, A., 2007. Stability control of an historical structure with TLS survey, *Int. Arch. Of Photogrammetry and Remote Sensing*, 36(5/W47), Zurich, Switzerland.

Danforth, W.W., and Thieler, E.R., 1992. “Digital Shoreline Analysis System (DSAS) User’s Guide, Version 1.0,” *US Geological Survey Open-File Report 92-355*, 42pg.

Duffy, W. and S.M. Dickson 1995. “Using Grid and Graph to Quantify and Display Shoreline Change,” *Proceedings of the 1995 ESRI International User Conference*, p. 74.

Emery, K.O. and Kuhn, G.G., 1982. “Sea cliffs: their processes, profiles, and Classification,” Geological Society of America Bulletin, 93, 644-654.

Earth Science Research Institution, ESRI, 2008. “ESRI- The GIS software leader,” <http://www.esri.com>, (Last Accessed: December 20, 2008)

Esteves, L.S.; Williams J.J., and Dillenburg, S.R., 2006. “Seasonal and interannual influences on the patternsof shoreline changes in Rio Grande do Sul, southern Brazil,” *Journal of Coastal Research,* 22(5), 1076–1093, West Palm Beach (Florida), ISSN 0749-0208.

Flick, R.E.,1994. “Shoreline Erosion Assessment and Atlas of the San Diego Region, 2 volumes,” Sacramento, California: California Department of Boating and Waterways.

Gastil, G., and Higley, R., 1977. “Guide to San Diego Stratigraphy,” American Association of Petroleum Geologists (AAPG), December 17, 1977.

Girardeau-Montaut, D., Roux, M., Marc, R., and Thibault, G., 2005. “Change Detection on points cloud data acquired with a ground laser scanner,” *Int. Arch. Of Photogrammetry and Remote Sensing*, 36(3/W19), Enschede, Netherlands.

Griggs, G.B., Patsch, K., and Savoy, L.E., 1985. “Living With the California Coast*.” Duke University Press*, Durham, North Carolina, 393 pp.

Griggs, G.B., Patsch, K., and Savoy, L.E., (2005). “Living With the Changing California Coast,” *University of California Press*, 540 pp.

Grine, D. 2005 “Geology of Torrey Pines State Reserve,” Torrey Pines State Reserve, <http://www.torreypine.org/geology/geology.html>, (Last Accessed: March 3, 2005).

Gruen A., and Akca D., 2004. “Least squares 3D surface matching,” *Int. Arch. of Photogrammetry and Remote Sensing*, 34(5/W16), Dresden, Germany.

Guarnieri, A., Pirotti, F., Pontin, M., and Vettore, A. (2005). “Combined 3D surveying techniques for structural analysis,” *Int. Arch. Of Photogrammetry and Remote Sensing*, Vol. 36(5/W17), Mestre-Venice, Italy

Haas, J., 2005. “Grain size and mineralogical characteristics of beach sand with implications for sediment provenance in the Oceanside Littoral Cell.” MS Thesis, University of California, San Diego (UCSD), San Diego, CA, 126 p.

Hapke, C., and Richmond, B., 2000. “Monitoring beach morphology changes using small-format aerial photography and digital softcopy photogrammetry*.” Environmental Geosciences,* Special Issue on Coastal Hazard Mapping Techniques, 7(1), 32-37.

Hapke, C. 2004. "The measurement and interpretation of coastal cliff and bluff retreat," In Formation, Evolution and Stability of Coastal Cliffs-Status and Trends, USGS Professional Paper 1963, Editors: Hampton, M.A. and Griggs, G.B., <http://pubs.usgs.gov/pp/pp1693/pp1693.pdf>

Hapke, C.J. and Reid D., 2007. “National Assessment of Shoreline Change Part 4: Historical Coastal Cliff Retreat along the California Coast,” *US Geological Survey Open File Report 2007-1133*.

Harris, M., Brock, J., Nayegandhi, A., and Duffy, M. 2005. “Extracting shorelines from NASA airborne topographic Lidar-derived digital elevation models,” *US Geological Survey Open File Report 2005-1427.*

Hicks, D. M., 1985. “Sand dispersion from an ephemeral delta on a wave-dominated coast,” Unpub. Ph.D. dissertation. Earth Sciences Dept., University of California, Santa Cruz, 210pp.

Himmelstoss, E.A.; Fitzgerald, D.M.; Rosen, P.S., and Allen, J.R., 2006. “Bluff evolution along coastal drumlins: Boston Harbor Islands, Massachusetts,” *Journal of Coastal Research,* 22(5), 1230–1240, West Palm Beach (Florida), ISSN 0749-0208.

Hori, Y., Ajioka, O., and Hanghai, A., 2007. “Laser scanning in Pompeian city wall a comparative study of accuracy of the drawings from 1930s to 40s,” *Int. Arch. Of Photogrammetry and Remote Sensing*, Vol. 36(5/W47), Zurich, Switzerland.

Hsieh, T., Olsen, M. J., Johnstone, E., Young, A. P., Driscoll, N., Ashford, S. A., and Kuester, F., 2007. “VR-based visual analytics of LIDAR data for cliff erosion assessment,” *Proceedings of the 2007 ACM Symposium on Virtual Reality Software and Technology* (Newport Beach, California, November 05 - 07, 2007), S. N. Spencer, Ed., VRST '07, ACM, New York, NY, 249-250.

Ikemoto, L.; Gelfand, N.; Levoy, M., 2003. "A hierarchical method for aligning warped meshes," *Proceedings on 3-D Digital Imaging and Modeling, 3DIM,* pp. 434-441

Inman, D.L., and Masters, P.M., 1991 "Budget of sediment and prediction of the future state of the coast," Coast of California Storm and Tidal Waves Study “State of the Coast” Report, San Diego Region, Chapter 9, US Army Corps of Engineers, Los Angeles District.

Innovemetric (2008). “Polyworks Software,” <http://www.innovemetric.com> (Last Accessed: Aug. 7, 2008).

I-Site (2008). “Maptek I-Site 3D laser scanning.” <http://www.isite3d.com> (Last Accessed: August 7, 2008).

Kayen, R., Pack, R.T., Bay, J., Sugimoto, S., and Tanaka, H., 2006. “Terrestrial-LIDAR visualization of surface and structural deformations of the 2004 Nigata Ken Chuetsu Japan, Earthquake,” *Earthquake Spectra*, EERI, 22(S1), pp. S147-S162.

Kennedy, M.P., 1973. “Bedrock Lithologies, San Diego Coastal Area, California,” Studies on the Geology & Geologic Hazards of the Greater San Diego Area, California, San Diego Association of Geologists, May 1973.

Kennedy, M.P., 1975. “Geology of the San Diego metropolitan area, western area,” California Division of Mines and Geology Bulletin 200, 56p.

Kennedy, M.P. and Tan S.S., 2005. “Geologic Map of the San Diego 30’ x 60’ Quadrangle, California,” California Department of Conservatism.

Khun, G.G., and Shepard, F.P., 1980. “Coastal Erosion in San Diego County,” *Proceedings of Coastal Zone '80 Conference*, Amer. Soc. Civil Engineers, Hollywood, Florida, November 17–20, 1980, 1899-1918.

Leica Geosystems (2008). “Cyclone Software,” <http//www.leica-geosystems.com> (Last Accessed: Aug. 7, 2008).

Leuliette, E. W, R. S. Nerem, and G. T. Mitchum, 2004. “Calibration of TOPEX/Poseidon and Jason altimeter data to construct a continuous record of mean sea level change,” *Marine Geodesy*, 27(1-2), 79-94.

Levoy, M., Pulli, K., Curless, B., Rusinkiewicz, S., Koller, D., Pereira, L., Ginzton, M., Anderson, S., Davis, J., Ginsberg, J., Shade, J., and Fulk, D, 2000.

"The Digital Michelangelo Project: 3D Scanning of Large Statues," *Proc. Of Siggraph 2000*.

Lichti, D.D., Gordon, S.J., and Tipdecho, T., 2005. "Error models and propagation in directly georeferenced terrestrial laser scanner networks." *J. Surv. Eng*.. 131(4), 135-142.

Lim, M., Petley, D.N., Rosser, N.J., Allison, R.J., and Long, A.J., 2005. "Combined digital photogrammetry and time-of-flight laser scanning for monitoring cliff evolution," *The Photogrammetric Record*, 20(110), 109-129.

Meridith, A., Eslinger, D., and Aurin, D., 1999. "An evaluation of hurricane-induced erosion along the North Carolina Coast using airborne LIDAR surveys," CSC Technical Report NOAA/CSC/99031-PUB.

Miller, P., Mills, J., Edwards, S., Bryan, P., Marsh, S., Mitchell, H., and Hobbs, P., 2008. "A robust surface matching technique for coastal geohazard assessment and management," *ISPRS Journal of Photogrammetry and Remote Sensing*, 63(5), Theme Issue: Remote Sensing of the Coastal Ecosystems, September 2008, 529-542, ISSN 0924-2716, DOI: 10.1016/j.isprsjprs.2008.02.003.

Monserrat, O., and Crosetto, M., 2008. Deformation measurement using terrestrial laser scanning data and least squares 3D surface matching, *ISPRS Journal of Photogrammetry and Remote Sensing*, 63(1), Theme Issue: Terrestrial Laser Scanning, 142-154.

Moore, L.J., Benumof, B., and Griggs, G.B., 1999. "Coastal erosion hazards in Santa Cruz and San Diego Counties, California," In: *Coastal Erosion Mapping and Management,* Crowell, M. and Leatherman, S.P. (eds.), *Journal of Coastal Research*, SI 28*,* 121-139.

Moore, L.J. and Griggs, G.B., 2002. "Long-term cliff retreat and erosion hotspots along the central shores of the Monterey Bay National Marine Sanctuary," *Marine Geology*, 181(1) p. 265-283.

Morton, R.A.; Miller, T., and Moore, L., 2005. "Historical shoreline changes along the US Gulf of Mexico: A summary of recent shoreline comparisons and analyses," *Journal of Coastal Research,* 21(4), 704–709. West Palm Beach (Florida), ISSN 0749-0208.

National Oceanographic and Atmospheric Administration, NOAA, 2008a. "Sea Level Trends," <http://tidesandcurrents.noaa.gov/sltrends/sltrends.shtml>, (Last Accessed: July 15, 2008).

National Oceanographic and Atmospheric Administration, NOAA, 2008b. "NOAA Tides and Currents," <http://tidesandcurrents.noaa.gov/>, (Last Accessed: July 15, 2008).

National Oceanographic and Atmospheric Administration, NOAA, 2008c. "National Climatic Data Center (NCDC)," <http://www.ncdc.noaa.gov/oa/ncdc.html>, (Last Accessed: July 15, 2008).

National Oceanographic and Atmospheric Administration, NOAA LDART (2007). <http://maps.csc.noaa.gov/TCM/>, Last Accessed: December 28, 2007

Nordsrtom, C.E., and Inman, D.L., 1973. "Beach and Cliff Erosion in San Diego County, California," Studies on the Geology & Geologic Hazards of the Greater San Diego Area, California, San Diego Association of Geologists, May 1973.

Olsen, M.J., Johnstone, L., Young, A.P., Hsieh, T.J., Ashford, S.A., Driscoll, N., and Kuester, F., (2008). "Rapid Response to Seacliff Erosion in San Diego County using Terrestrial LIDAR." *Proc. Solutions to Coastal Disasters Conference*, ASCE, Oahu, Hawaii (April 13-16, 2008), 573-583.

Olsen, M. J., Johnstone, E., Ashford, S.A., Driscoll, N., and Kuester, F. (2009, In Press). "Terrestrial laser scanning of extended cliff sections in dynamic environments: a parameter analysis," ASCE *Journal of Surveying Engineering*.

Olsen, M. J., Johnstone, E., Kuester, F. Ashford, S.A., and Driscoll, N., (Under Review). "Automated, constrained point-cloud alignment minimizing warping effects in mapping long coastal sections," submitted to the *ISPRS Journal of Photogrammetry and Remote Sensing*.

Olsen, M. J., Johnstone, E., Driscoll, N., Kuester, F., and Ashford, S.A., (In Prep). "Fate and transport of cliff failure material in the southern Oceanside littoral cell," to be submitted to *Marine Geology*.

Olsen, M.J., Young, A.P., and Ashford, S.A., (In Prep). "TopCAT: Topographical Change Analysis Tools for ArcGIS®, to be submitted to the *ASPRS Journal of Photogrammetry and Remote Sensing*.

Pendleton, E.A., Williams, S.J., and Thieler, E.R., 2004. "Coastal vulnerability assessment of Assateague Island National Seashore (ASIS) to sea-level rise," *U.S. Geological Survey Open-File Report 2004-1020*.

Pulli, K., 1999. "Multiview registration for large data sets," *Proc. of the 2nd Int. Conf. on 3D Digital Imaging and Modeling,* 3DIM, Ottawa, Canada, Oct. 1999, 160–168.

Reed, L.D., 1990. "Normal Heights Mudstones: A New Upper Pleistocene Marine Sedimentary Unit, San Diego, California," Geotechnical Engineering Case Histories in San Diego County, San Diego Association of Geologists, October 20, 1990.

Robinson, B.A., 1988. Coastal cliff sediments-San Diego region, Dana Point to the Mexican border (1887-1947), Coast of California Storm and Tidal Wave Study 88-8, U.S. Army Corps of Engineers, Los Angeles District, 275p.

Rosser, N.J., Petlety, D.N., Lim, M., Dunning, S.A., and Allison, R.J., 2005. "Terrestrial laser scanning for monitoring the process of hard rock coastal cliff erosion." *Quarterly J. of Eng. Geology and Hydrology*, 38, 363-375.

Rosser, N.J., Lim, M., Norman, E., and Petley, D.N., 2008. "Exploring variations in and controls upon cliff, platform and coastline geometry." *Geophysical Research Abstracts, Vol. 10, European Geosciences Union,* EGU2008-A-10318.

Ruggiero, P., Komar, P.D., McDougal, W.G. and Beach R.A., 1996. "Extreme water levels, wave runup, and coastal erosion," *Proc. 25th Coastal Engineering Conf.*, ASCE, 2793-2805.

Ruggiero, P., Komar, P.D., McDougal, W.G, Mara, J.J., and Beach R.A., 2001. "Wave runup, extreme water levels and the erosion of properties backing beaches." *J. of Coastal Research,* 17(2), 407-419.

Ruggiero, P., 2008. "Impacts of Climate Change on Coastal Erosion and Flood Probability In the Pacific Northwest." *Proc. Solutions to Coastal Disasters Conference*, ASCE, Oahu, Hawaii (April 13-16, 2008), 158-169.

Sallenger, A.H, Krabill, W.B., Swift, R.N., Brock.J, List, J., Hansen, M., Holman, R.A., Manizade, S., Sontag, J., Meredith, A., Morgan, K., Yunkel, J.K., Frederick, E.B., and Stockdon, H., 2003. "Evaluation of airborne topographic LIDAR for quantifying beach changes," *Journal of Coastal Research*, 19(1), 125-133.

Scaoini, M., 2004. "Direct georeferencing of TLS in surveying of complex sites." *Proc. Of 3D-ARCH, Virtual Reconstruction and Visualization of Complex Architectures*, Int. Society of Photogrammetry and Remote Sensing, ISPRS, Mestre-Venice, Italy.

Scaioni M., Giussani A., Roncoroni F., Sgrenzaroli M., Vassena G., 2004. "Monitoring of Geological sites by laser scanning techniques," *Int. Arch. Of Photogrammetry and Remote Sensing*, 35(B7), Istanbul, Turkey, 708-713.

SCANALYZE, 2002. "Scanalyze: a system for aligning and merging range data," <http://graphics.stanford.edu/software/scanalyze/>, (Last Accessed: September 8, 2008).

Schuhmacher, S., and Bohm, J., 2005. "Georeferencing of laser scanner data for applications in architectural modeling," *Int. Arch. Of Photogrammetry and Remote Sensing*, 36(5/W17), Mestre-Venice, Italy

SCRIPPS Institution of Oceanography, 2008. "The Coastal Data Information Program (CDIP)," Integrative Oceanography Division, Scripps Institution of Oceanography, San Diego. <http://cdip.ucsd.edu/>, (Last Accessed: July 15, 2008).

Snavely, N., Seitz, S. M., and Szeliski, R., 2008. "Modeling the World from Internet Photo Collections," *Int. J. Comput. Vision* 80, 2 (Nov. 2008), 189-210. DOI= http://dx.doi.org/10.1007/s11263-007-0107-3

Son, S., Park, H., and Lee, K.H., 2002. "Automated laser scanning system for reverse engineering and inspection," *International Journal of Machine Tools and Manufacture*, 42(8), 889-897.

Stockdon, H.F., Holman, R.A., Howd,P.A., and Sallenger, A.H., 2006. "Empirical parameterization of setup, swash, and runup." *Coastal Engineering*, 53(7), 573-588.

Sunamura, T. (1992). Geomorphology of Rocky Coasts, John Wiley and Sons, New York, NY.

Thieler, E.R., Himmelstoss, E.A., Zichichi, J.L., and Miller, T.L., 2005, "Digital Shoreline Analysis System (DSAS) version 3.0: An ArcGIS extension for calculating shoreline change," *U.S. Geological Survey Open-File Report 2005-1304.*

US Geologic Survey, USGS, 2008. "The National Map Seamless Server," <http://seamless.usgs.gov>, (Last Accessed: August 15, 2008).

Vergauwen, M. and Van Gool, L., 2006. “Web-based 3D Reconstruction Service,” *Mach. Vision Appl.* 17, 6 (Oct. 2006), 411-426. DOI= http://dx.doi.org/10.1007/s00138-006-0027-1

Weissel, J.K., and Driscoll N.W. 1998. “Landslides: An Onshore-Offshore Comparison.” AGU 1998 Fall Meeting, H32G-06.

Weisstein, Eric W. (2007a) "Point-Plane Distance." From MathWorld--A Wolfram Web Resource. <http://mathworld.wolfram.com/Point-PlaneDistance.html> (Last Accessed: April 1, 2008).

Weisstein, Eric W. (2007b) "Root-Mean-Square." From MathWorld--A Wolfram Web Resource. <http://mathworld.wolfram.com/Root-Mean-Square.html> (Last Accessed: April 1, 2008).

Young, A.P. and Ashford, S.A., 2006a. “Application of airborne LIDAR for seacliff volumetric change and beach sediment budget contributions,” *J. of Coastal Research*, 22(2), 307-318.

Young, A.P., and Ashford, S.A., 2006b. Performance Evaluation of Seacliff Erosion Control Methods*, Shore and Beach*, 74(4), 16-24

Young, A.P., 2006c. “Quantifying Short-Term Seacliff Morphology of a Developed Coast: San Diego County, California.” PhD Dissertation, University of California, San Diego (UCSD), San Diego, CA, 208pg.

Young, A.P. and Ashford, S.A., 2007. “Quantifying sub-regional seacliff erosion using mobile terrestrial LIDAR.” Shore and Beach, 75(3), 38-43.

Young, A.P. and Ashford, S.A., 2008. “Instability investigation of cantilevered seacliffs,” Earth Surface Processes and Landforms 33, 1161-1677.

Zhang Z. 1994. “Iterative point matching for registration of free-form curves and surfaces,” *International Journal of Computer Vision*, 13(2), 119–152.